Communauté UNIVERSITÉ Grenoble Alpes

THÈSE

Pour obtenir le grade de

DOCTEUR DE LA COMMUNAUTE UNIVERSITE GRENOBLE ALPES

Spécialité : **Cosmologie et astroparticules**

Arrêté ministériel : 7 août 2006

Présentée par

Alessia Ritacco

Thèse dirigée par **Juan-Francisco MACÍAS-PÉREZ**
et codirigée par **Alessandro Monfardini**

préparée au sein du **Laboratoire de physique subatomique et de cosmologie (LPSC)**
dans **l'École Doctorale de Physique de Grenoble Alpes**

Polarimétrie aux longueurs d'onde millimétriques avec les instruments NIKA et NIKA2

Thèse soutenue publiquement le **14 Octobre 2016**,
devant le jury composé de :

Ken GANGA
APC Paris, Rapporteur
Olivier PERDEREAU
LAL Orsay, Rapporteur
Alessandro MONFARDINI
Institut Néel Grenoble, Co-Directeur de thèse
Paolo DE BERNARDIS
La Sapienza Roma, Examinateur
Laurent DEROME
LPSC Grenoble, Président
Juan-Francisco MACÍAS-PÉREZ
LPSC Grenoble, Directeur de thèse
Nicolas PONTHIEU
IPAG Grenoble, Invité
Andrea CATALANO
LPSC Grenoble, Invité

To my best friend and partner, Alessandro, who offered me unconditional love and has always been there along the way. I couldn't have done this without you. Thank you.

Contents

Introduction **1**

Introduction générale **3**

I Polarisation at millimetre wavelengths **5**

1 Polarisation at millimetre wavelengths **7**
1.1 Motivations 8
1.2 CMB results 9
1.2.1 Cosmological standard model 9
1.2.2 Thermal history of the Universe 10
1.2.3 Inflation 11
1.2.4 CMB anisotropies 13
1.2.5 CMB polarisation 15
1.3 Diffuse Galactic emissions 17
1.3.1 Synchrotron emission 17
1.3.2 Dust emission 20
1.3.3 Anomalous microwave emission 24
1.3.4 Free-free emission 24
1.3.5 CO emission 25
1.4 Extragalactic polarised radio sources 26
1.4.1 Quasars 26
1.5 Star forming regions 27
1.5.1 Star formation physics overview 27
1.5.2 Magnetic fields 28
1.5.3 A schematic scenario of early star formation 30
1.6 Summary 31

2 Polarisation of the light **33**
2.1 Formalism of the polarised light 34
2.2 Jones formalism 34
2.2.1 Ideal polariser 35
2.2.2 Ideal Half Wave Plate 36
2.3 Stokes formalism 37
2.3.1 Polarimetry: basics and conventions 39
2.4 Mueller formalism 40

2.4.1 Mueller matrix of a polariser . . . 41
2.4.2 HWP Mueller matrix . . . 41
2.5 Conclusions . . . 42

II NIKA and NIKA 2 instruments 43

3 The *NIKA* and *NIKA2* instruments 45
3.1 The telescope . . . 46
3.2 Cryogenic detectors . . . 47
3.2.1 Context . . . 47
3.2.2 Fundamentals of superconductivity . . . 48
3.3 Kinetic Inductance Detectors: KIDs . . . 49
3.3.1 Kinetic inductance and optical power . . . 49
3.3.2 Detector response . . . 50
3.3.3 Natural frequency multiplexing . . . 50
3.4 *NIKA* & *NIKA2* general description . . . 52
3.4.1 *NIKA* detectors: Lumped Element KIDs . . . 53
3.4.2 Readout electronics . . . 55
3.4.3 Cryostat . . . 56
3.4.4 Optics . . . 56
3.4.5 *NIKA* and *NIKA2* polarisation setup . . . 58
3.4.6 The output polarised signal . . . 58
3.5 Scientific goals of *NIKA2* . . . 60

4 Instrumental characterisation of the *NIKA* polarisation setup 63
4.1 *NIKA* HWPs . . . 64
4.1.1 First HWP version: single plate of sapphire . . . 64
4.1.2 Multi-plate HWP solutions . . . 65
4.1.3 Mesh-HWP . . . 65
4.2 Laboratory characterisation . . . 67
4.2.1 Martin-Puplett Interferometer (MPI) . . . 69
4.2.2 Characterisation of the single plate sapphire HWP . . . 70
4.2.3 Instrumental stray polarisation . . . 73
4.2.4 Characterisation of the *NIKA* final HWP . . . 76
4.2.5 Propagating uncertainties on the HWP parameters to the output polarised signal . . . 80
4.3 Conclusions . . . 82

III The NIKA polarimeter on the sky 83

5 Observations at the IRAM 30-meter telescope 85
5.1 Observational strategies . . . 85
5.2 Opacity determination and calibration . . . 86
5.2.1 Skydip . . . 87
5.2.2 Polarised Skydip . . . 88

5.3 Realtime observations . . . 88
5.3.1 Focal plane reconstruction . . . 88
5.3.2 Focus determination . . . 90
5.3.3 Pointing correction . . . 93
5.4 Polarisation setup at the telescope . . . 94
5.5 Conclusions . . . 95

6 A dedicated polarisation data analysis 97
6.1 Unpolarised TOI processing . . . 98
6.1.1 Correlated noise . . . 99
6.1.2 Uncorrelated noise: intrinsic detector noise . . . 100
6.1.3 Glitches . . . 100
6.1.4 Noise decorrelation methods . . . 100
6.2 Polarized demodulation map making . . . 101
6.2.1 *NIKA*'s polarised timelines: simulation . . . 101
6.2.2 Demodulation of the polarised signal: the lock-in procedure . . . 102
6.2.3 Link with the classical maximum likelihood map making . . . 104
6.2.4 Covariance of the estimated Stokes parameters . . . 107
6.3 Polarised timelines: observations . . . 111
6.3.1 HWP Synchronous Signal correction: HWPSS . . . 112
6.3.2 Map making and demodulation: validation on observed data . . . 115
6.3.3 Decorrelation methods applied to an extended polarised source . . . 117
6.3.4 Noise correlation in the decorrelated maps . . . 119
6.4 Instrumental polarisation IP . . . 124
6.4.1 Intensity to polarisation leakage correction . . . 125
6.4.2 Leakage correction on point and extended sources . . . 130
6.5 Conclusions . . . 131

7 Polarisation observations of the NIKA instrument 135
7.1 *NIKA* intensity calibration procedure . . . 136
7.2 Polarised observations . . . 140
7.2.1 Polarisation reconstruction accuracy . . . 144
7.2.2 Validation of the polarisation reconstruction on QUASARS . . . 147
7.2.3 Estimation of the *NIKA* sensitivity in polarisation observations . . . 151
7.3 Observations of compact and extended sources . . . 153
7.3.1 M87 . . . 153
7.3.2 Cygnus-A . . . 157
7.3.3 Orion OMC-1 molecular cloud . . . 159
7.3.4 Spectral index maps . . . 167
7.4 Summary and conclusions . . . 167

IV Polarisation properties of the Crab nebula 169

8 Millimeter polarisation properties of the Crab nebula 171
8.1 Polarisation angle calibration in CMB experiments . . . 171
8.2 *NIKA* observations . . . 172

8.2.1 Total intensity map estimation 172
8.2.2 Polarisation maps 175
8.2.3 Polarisation degree and angle estimation 178
8.2.4 A calibrator for CMB experiments 180
8.2.5 Extension to other frequencies 181
8.2.6 Polarisation intensity SED 182
8.2.7 Spectral index 183
8.3 Conclusions 184

9 Conclusions **187**

Acknowledgements

Sometimes during a PhD thesis we feel like racing against time. This worry, even if fatiguing, makes the challenge more stimulating. The people I met during these last three years helped me to overcome difficulties, by pushing my limits. I would like to thank those people and of course sincerely thank all the people who are part of my life from long time. They are there for me even if they live thousands of kilometers away.

First of all, I would like to sincerely thank all the members of the thesis jury. In particular, Olivier Perdereau and Ken Ganga who accepted to report this thesis. I am very grateful for their advises and questions, which have improved the quality of the manuscript.

Juan, muchas gracias. Thanks for advising me on my thesis and for all the times you read it. Thank you also for pushing me to give it all, specially during the last months before the thesis submission. Thank you for the pleasant moments we spent together, I will kindly remember the coffee breaks at the telescope and the promenades around Pico Veleta. I would like to thank you also for your kindness, in particular moments it was crucial for me having your moral support. You are a very "e-"special person and it has been an honour for me working with you. *Tu es le meilleur chef du monde.*

Nico, for you I will write something in french to thank you for all the time you spent teaching me this beautiful language. Je voudrais te remercier de tout coeur de la patience, la dévotion et la passion avec lesquelles tu m'as appris tout ce que tu pouvais sans aucune réserve. Je te remercie aussi de ton infinie disponibilité jusqu'à la fin. La force a été avec moi.

Andrea, thank you for all the nice memories in the laboratory in Grenoble and at the telescope. I would like to thank you for our discussions, which have helped me to get the head out of the sand. Thank you for believing in my capacities and for supporting my choices in particular moments of my work.

To the *NIKA* team many thanks for welcoming me in the group. Thank you for the nice time we shared during the telescope campaigns and the coffee breaks at the LPSC.

A special thank you to the "bureau 333" and its guests: Céline, Rémi, Florian, Vincent, Nico for the funny time, the special carnet, the discussions about physics and above all for the precious french lessons.

I want to say an authentic big thank you to my best friends for their support. Thank you for always being there for me and for all the wonderful moments we spent together. Thanks to my Calabrian sisters: Giusy, Margherita, Grazia, Francesca; you are part of my family. Thanks to my favorite astrophysicists Simona, Davide and Donatella for sharing with me the university years in Rome and this PhD experience, even while being in different places in the world.

Thanks to my "exotic-french" family, Mónica, Armando, Bhaskar, Angelo for sharing with me this experience "grenobloise" and for all the nice international dinners and trips around the Rhone-Alpes region and the world. It was amazing to meet you and to learn more about your culture. This contributed to make this experience unforgettable.

Thank you to all members of the Grenoble swing association, who experienced with me several dancing nights and strenuous but amazing week-ends of Lindy-hop workshops.

Thanks to the extraordinary family I have, who support me on every decision I make. Grazie "Mamma e Papà" for your infinite love and for the effort you made that allowed me pursuing my dreams. To my fabulous brother Ilario and Egle for being my enthusiastic fans and for everything. You are very special for me. Thanks to Romana, Giuseppe and Dario for making me feel at home with you.

Thanks to the magic night where the snow painted Rome and put you on my way. Thank you Alessandro for following me in this french adventure, for believing in me above all others and for everything you do every day for me.

Introduction

Technological progress in the last decades has improved our understanding of the Universe's evolution. One of the most powerful cosmological probes is the Cosmic Microwave Background (CMB). The study of temperature anisotropies by satellite missions like COBE [Boggess *et al.*, 1992], *WMAP* [Hinshaw *et al.*, 2013] and *Planck* [Planck Collaboration *et al.*, 2013] as well as previous ground-based and balloon-born experiments, has reached high levels of sensitivity and angular resolution, allowing the determination of the main cosmological parameters with accuracies close to 1%. The CMB polarisation anisotropies also encode a wealth of cosmological information. Not only the E-mode polarisation has allowed us to tighten the cosmological constraints by breaking degeneracies between parameters [Planck Collaboration *et al.*, 2015i], but also the detection of the B-mode polarisation may provide a confirmation of the existence of primordial gravitational waves created by inflation, the epoch of the exponential expansion in the primordial Universe [Zaldarriaga et Seljak, 1997].

Specifically-targeted experiments like SPTpol [Austermann *et al.*, 2012], BICEP2 [BICEP2 Collaboration *et al.*, 2014], *Planck* [Planck Collaboration *et al.*, 2015h], POLARBEAR [The Polarbear Collaboration: P. A. R. Ade *et al.*, 2014], ACTPOL [van Engelen *et al.*, 2015] have already started to put constraints on the tensor-to-scalar ratio r, the parameter used to parametrise the amplitude of the B-mode signal. Recently, the first primordial B-mode detection was claimed by BICEP2 at 150 GHz [Ade *et al.*, 2014]. However, high frequency data from the *Planck* satellite have shown that the level of polarised dust emission in the region of the sky covered by BICEP2 is a significant component of the measured signal [BICEP2/Keck and Planck Collaborations *et al.*, 2015].

Nowadays, it is widely recognised that any unambiguous detection of the B-mode anisotropy requires a detailed, multi-frequency study of foreground contamination levels. The whole sky maps collected by *Planck* show a diffuse Galactic emission consisting of a number of distinct components, that emit via different emission mechanisms: synchrotron, *free-free*, anomalous microwave emission (AME) and thermal dust emission. In particular, *Planck* maps at 353 GHz [Planck Collaboration *et al.*, 2015e] are dominated by thermal dust emission display filaments distributed over the whole sky [Planck Collaboration *et al.*, 2014a].

The filamentary structure of the diffuse interstellar matter is also a striking feature of dust observations at higher angular resolution, such as performed by *Herschel* [Griffin *et al.*, 2010], and of spectroscopic HI observations (e.g. [André *et al.*, 2014; Clark *et al.*, 2014]). The analysis of *Planck* dust polarisation data in the diffuse interstellar medium (ISM), at low and intermediate Galactic latitudes, indicates that the interstellar matter structures tend to be aligned with the plane-of-the-sky (POS) magnetic field structures (B_{POS}, [Planck Collaboration *et al.*, 2014b]). Tracing magnetic fields via dust thermal

emission provides a unique window for revealing magnetic fields in diffuse interstellar gas and molecular clouds. Resolving the remaining uncertainties related to grain alignment as well as obtaining high-density maps of magnetic fields in dense gas, and, importantly, in high latitude diffuse gas, will shed light on the many astrophysical effects of magnetic fields. In particular, the understanding of the star formation process at small angular scales (0.01-0.1) pc is one of the outstanding challenges of modern astrophysics.

Therefore, many technological efforts are needed to open new scientific windows towards the understanding of processes at play both at Cosmological and Galactic scales. In this context a better overall mapping speed and sensitivity is required. This can only be obtained with large, photon noise limited, detector arrays.

One of the scientific purposes of the *NIKA2* instrument, a multi-thousand pixel dual-band camera installed at the IRAM 30 m telescope, is mapping observations of linearly polarised continuum emission from magnetically-aligned dust grains at 1.15 mm. This is a powerful tool to measure the morphology and structure of magnetic field lines in star-forming clouds and dense cores.

The aim of this Ph.D work has been the development of the *NIKA* polarisation system and consequently that of *NIKA2*. Here, a new approach to the measurement of the polarisation of the sky has been investigated. First, using a recently developed technology of detectors, the KIDs (Kinetic Inductance Detectors) and then, using a continuously rotating, achromatic Half-Wave-Plate. Along this thesis we will discuss the advantages and disadvantages of this solution for a ground-based experiment.

The thesis is organised as follows. Chap. 1 presents the context in which polarisation studies are particularly interesting, mainly for CMB polarisation purposes, foreground emissions and star formation study. Chap. 2 briefly gives the classical formalism adopted to manipulate polarisation vectors. Chap. 3 presents the *NIKA* and *NIKA2* instruments and we mainly discuss their instrumental characteristics. Chap. 4 discusses the characterisation of the *NIKA* polarimeter in laboratory: the first prototype used at the telescope had a single plate of sapphire HWP optimised to work at 230 GHz, while the final *NIKA* polarimeter had a mesh HWP optimised to transmit the polarised signal at each frequency in the large *NIKA* bandwidth, this configuration has been chosen also for the *NIKA2* polarimeter. These two prototypes have been characterised in the laboratory at the Néel Institute. Chap. 5 presents the procedures of realtime observations at the telescope. Chap. 6 details the dedicated polarisation data reduction pipeline specifically developed during my PhD. Chap. 7 discusses the validation of the polarisation detection on point, compact and extended sources. Chap. 8 presents the results obtained on the Crab nebula, which is the absolute calibrator used for CMB polarisation measurements. Finally I present my conclusions and perspectives in Chap. 9.

Introduction générale

Les progrès technologiques de ces dernières années ont amélioré notre compréhension de l'évolution de l'Univers, et le Fond Diffus Cosmologique (*Cosmic Microwave Background* CMB) est l'une des principales sondes d'investigations cosmologiques. L'étude de ses anisotropies en température fournie par les satellites COBE [Boggess *et al.*, 1992], *WMAP* [Hinshaw *et al.*, 2013] et *Planck* [Planck Collaboration *et al.*, 2013] ainsi que d'autres expériences basées au sol ou en ballon, ont atteint un haut niveau de sensibilité et couvrent une large gamme d'échelles angulaires. Ceci a permis une mesure des paramètres cosmologiques avec une précision de l'ordre du pour-cent.

Les anisotropies de la polarisation du CMB sont elles aussi riches d'information. Si la détection des modes E a permis de mieux contraindre les paramètres cosmologiques [Planck Collaboration *et al.*, 2015i], la détection des modes B pourrait confirmer l'existence d'ondes gravitationnelles primordiales créées au moment de l'inflation, cette époque correspondant à une expansion accélérée de l'Univers primordial. Des expériences comme BICEP2 [BICEP2 Collaboration *et al.*, 2014], *Planck* [Planck Collaboration *et al.*, 2015h], POLARBEAR [The Polarbear Collaboration: P. A. R. Ade *et al.*, 2014], ACTPOL [van Engelen *et al.*, 2015] ont déjà commencé à mettre des contraintes sur le paramètre r qui est relié à l'amplitude de ces ondes gravitationnelles. Récemment, BICEP2 [Ade *et al.*, 2014] a déclaré avoir détecté pour la première fois ces modes B à 150 GHz. Cependant, comme a pu le montrer *Planck* en particulier, l'émission diffuse de la Galaxie couvre quasiment tout le ciel et résulte de plusieurs composantes : le rayonnement synchrotron, le free-free, l'émission anormale (AME) et thermique de la poussière. Une seconde analyse conjointe des données de BICEP2 et de *Planck* a alors montré que la contribution de l'émission polarisée de la poussière dans le champ observé par BICEP2 était plus importante qu'estimée lors de la première étude et invalidait la significance de la détection des modes B primordiaux. Ceci confirme qu'une mesure précise de la polarisation du CMB nécessite une bonne soustraction des avant-plans polarisés, et que pour cela une étude approfondie multifréquence et multi-échelles de ces émissions est nécessaire.

Les cartes *Planck* obtenues à 353 GHz [Planck Collaboration *et al.*, 2015e], dominées par l' émission thermique de la poussière, montrent des structures filamentaires distribuées sur tout le ciel [Planck Collaboration *et al.*, 2014a]. C'est aussi une caractéristique remarquable des observations à haute résolution du satellite *Herschel* [Griffin *et al.*, 2010] et des observations spectroscopiques HI (*e.g.* [André *et al.*, 2014; Clark *et al.*, 2014]). Les grains de poussière sont asymétriques et émettent un rayonnement polarisé dans la direction de leur grand axe, lequel s'aligne principalement perpendiculairement au champ magnétique. La mesure de la polarisation permet donc en principe de cartographier les lignes de champ magnétique et une analyse simultanée de la polarisation et de l'intensité totale permet alors de mieux comprendre le rôle du champ magnétique

dans la formation de ces filaments, puis dans la formation stellaire.

Une mesure précise de la polarisation du ciel, dans le domaine millimétrique, répond donc à la fois à des enjeux cosmologiques et à des enjeux astrophysiques. *NIKA2* offre la possibilité de mesurer la polarisation du ciel à 260 GHz, à une résolution de 12 arcsec et sur un champ de vue de 6 arcmin. *NIKA2* observe également à 150 GHz. Les plans focaux sont constitués de matrices d'environ 1000 *Kinetic Inductance Detectors* chacun, des détecteurs de nouvelle génération développés à l'institut Néel de Grenoble. *NIKA2* est installée au télescope de 30 m de l'IRAM depuis octobre 2015 et se trouve actuellement en phase de caractérisation. La mesure de la polarisation consiste en une détection quasi-simultanée des paramètres de Stokes Q et U, grâce à la rotation rapide et continue d'une lame demi-onde devant un polariseur, les deux étant placés devant l'entrée de l'instrument.

Le travail effectué lors de cette thèse a consisté à caractériser ce module polarimétrique et à développer une chaîne d'analyse des données permettant de reconstruire les cartes du signal astrophysique polarisé. Pour cela, mon travail a porté sur le prototype *NIKA* et s'est composé de tests en laboratoire et d'observations au télescope. Le prototype *NIKA* est le premier instrument à observer le ciel avec des KIDs. D'autre part, la rotation rapide d'une lame demi-onde pour moduler la polarisation est une stratégie employée par une seule expérience jusqu'à présent. C'est cette double originalité que je développe principalement dans ce manuscrit qui est organisé comme suit : le chapitre 1 présente le contexte scientifique dans lequel la mesure de la polarisation est particulièrement intéressante, en privilégiant la polarisation du fond diffus cosmologique, les avant plans polarisés et la formation stellaire. Le chapitre 2 décrit brièvement le formalisme classique adopté pour manipuler les vecteurs de polarisation. Le chapitre 4 présente la caractérisation du polarimètre de *NIKA* au laboratoire : le premier prototype utilisé au télescope avait une seule plaque de saphir optimisé pour fonctionner à 230 GHz, tandis que la version finale de la lame demi-onde est composée de grilles métalliques qui permettent de transmettre le signal polarisé à chaque fréquence de la bande passante de *NIKA*. C'est la configuration qui a été retenue pour le polarimètre de *NIKA2*. Ces deux prototypes ont été caractérisés au laboratoire de l'Institut Néel. Le chapitre 5 présente les procédures d'observation en temps réel au télescope. Le chapitre 6 détaille la réduction des données polarisées développée pendant ma thèse. Le chapitre 7 discute la validation de la détection de la polarisation en utilisant des observations de sources compactes et diffuses. Le chapitre 8 enfin, présente les résultats obtenus sur une source considérée comme un calibrateur primaire pour les expériences CMB : la nébuleuse du Crabe. Le chapitre 9 résume les principaux résultats de ce travail et en présente quelques perspectives.

Part I

Polarisation at millimetre wavelengths

1

Polarisation at millimetre wavelengths

Contents

1.1 Motivations **8**

1.2 CMB results **9**

1.2.1 Cosmological standard model 9

1.2.2 Thermal history of the Universe 10

1.2.3 Inflation 11

1.2.4 CMB anisotropies 13

1.2.5 CMB polarisation 15

1.3 Diffuse Galactic emissions **17**

1.3.1 Synchrotron emission 17

1.3.2 Dust emission 20

1.3.3 Anomalous microwave emission 24

1.3.4 Free-free emission 24

1.3.5 CO emission 25

1.4 Extragalactic polarised radio sources **26**

1.4.1 Quasars 26

1.5 Star forming regions **27**

1.5.1 Star formation physics overview 27

1.5.2 Magnetic fields 28

1.5.3 A schematic scenario of early star formation 30

1.6 Summary **31**

1.1 Motivations

The measurement of the polarisation of the Cosmic Microwave Background (CMB) constitutes one of the remaining major challenges of modern cosmology. In particular, the next generation of CMB experiments aims at measuring the primordial CMB B-modes [Zaldarriaga, 2004]. Such a signal is generated by primordial gravitational waves during inflationary epoch according to the standard cosmological model. For that purpose, a large number of background limited detectors ($\sim 1000 - 20000$) increasing the sensitivity of the instrument ($S/N \propto \sqrt{n_{det}}$) and covering the range 20 GHz-1 THz is required. Full sky coverage is highly preferable for CMB studies. This motivation, with the addition of reduced low-frequency noise contamination and understanding of systematics, makes favorable space missions for CMB studies. Recently, results obtained by BICEP2 and *Planck* [BICEP2/Keck and Planck Collaborations *et al.*, 2015], [Planck Collaboration *et al.*, 2016b], [Keck Array *et al.*, 2016], established an upper limit on the parameter that describes the amplitude of the CMB B-modes. The observations also showed the importance of an accurate determination of the foreground contributions that contaminate the CMB signal. *Planck* [Planck Collaboration *et al.*, 2015e], WMAP [Gold *et al.*, 2009] and Archeops [Benoît *et al.*, 2004] observations, have shown that the strong contribution of the galactic thermal dust emission to the CMB polarised signal at the frequencies of interest for CMB observations. The Galactic synchrotron radiation also imparts a strong polarised foreground at galactic scales. As a consequence, the galactic emission is a major contaminant to constrain the inflationary epoch [Planck Collaboration *et al.*, 2015a]. The understanding of these contributions to the polarised signal represents a fundamental step to ensure an accurate determination of the polarised CMB signal.

Within our Galaxy, high angular resolution experiments have been designed to measure the interstellar medium (ISM), with a particular focus on probing the physics inside the core of molecular clouds where star formation occurs. The Galactic magnetic field has a regular component characterised by intensity, direction, and a turbulent component. While the intensity of the magnetic field can be measured via the Zeeman effect, synchrotron polarisation measurements provide additional, often tighter, constraints on the strength and orientation of the regular component [Beck, 2012; Beck, 2007; Houde *et al.*, 2013]. Finally, dust polarisation provides us with information on the direction of the magnetic field lines within the thin disk of the Galaxy where most of the matter is located [Crutcher, 2012]. The dynamics of magnetic fields in the star formation process is very poorly constrained and requires high resolution polarisation sensitive experiments.

Thus, the interest in developing new sensitive polarisation experiments is twofold: on the one hand to probe the inflation predicted by the Big Bang theory, through the detection of the primordial B-modes, and on the other hand to investigate the mechanism at play in star forming clouds. In the next sections I briefly review the CMB physics, the diffuse Galactic emissions, and focus the attention on the current understanding of the star formation process. The understanding of the latter is indeed the main scientific goal of the *NIKA2* polarisation channel.

1.2 CMB results

Here, I will briefly review the CMB physics to arrive at the current status of the experiments in this field.

1.2.1 Cosmological standard model

The Big Bang theory describes the expansion of the Universe, for a review see [Linde *et al.*, 1994]. This theory includes the assumptions of a homogeneous and isotropic Universe that expands from a very high density and temperature state, and offers an exhaustive explanation for many phenomena: the abundance of light elements (*i.e.* Primordial Nucleosynthesis), the CMB radiation, large scale structures with inflation and the Hubble's Law (*i.e.* redshift of the galaxies). According to this theory, the Universe was born 13.8 billion years ago [Planck Collaboration *et al.*, 2013; Planck Collaboration *et al.*, 2015i] and after expanding sufficiently to allow the formation of subatomic particles, and later atoms [Gamow, 1946]. Giant clouds of these primordial elements later coalesced through gravity to form stars, galaxies and clusters of galaxies.

General relativity provides the connection between the evolution of the Universe and its energy content. The Friedmann equations [Friedmann, 1922; Friedmann, 1924] describe the evolution of the Universe:

$$\left(\frac{\dot{a}}{a}\right)^2 = \frac{8\pi G}{3}\rho_{tot} - \frac{kc^2}{a^2} \tag{1.1}$$

and

$$\frac{\ddot{a}}{a} = -\frac{4\pi G}{3}\left(\rho_{tot} + \frac{3p_{tot}}{c^2}\right); \tag{1.2}$$

where $a(t)$ is the scale factor (at the present reference time t_0 $a(t_0) = 1$), which represents the expansion of the Universe. G is the Newton's gravitational constant and c the speed of light in vacuum. The expansion rate $\left(\frac{\dot{a}}{a}\right)$ is also called Hubble parameter [Hubble, 1929], first measured locally by Hubble when he discovered that distant galaxies are in fact receding from us. The total density ρ_{tot} is written as:

$$\rho_{tot} = \rho_\Lambda + \rho_m + \rho_r, \tag{1.3}$$

where ρ_Λ represents the dark energy density, which may be in the form of cosmological constant Λ [Einstein, 1916], ρ_m accounts for a baryonic, (ρ_b), and non-baryonic, (ρ_c), components, the latter representing the dark matter. The radiation density ρ_r is composed of ultra-relativistic particles (photons and neutrinos). The k parameter determines the curvature of the Universe. Each component has its own equation of state, characterised by the parameter w, which links pressure and density:

$$w_i = \frac{p_i}{\rho_i c^2}. \tag{1.4}$$

The normalised energy density components:

$$\Omega_i = \frac{\rho_i}{\rho_{cr}}, \tag{1.5}$$

are widely used; $\rho_{cr} = \frac{3H^2}{8\pi G}$ is the critical universe density for which the spatial geometry is flat ($k = 0$).

At early times, radiation dominated the dynamics of the Universe providing an evolution of the scale factor $a \propto t^{1/2}$. At later times, the density of matter exceeded both the density of radiation and the dark energy and the dependence on the scalar factor switches to $a \propto t^{\frac{2}{3}}$. The CMB radiation offers a powerful way to investigate the origin of fluctuations, the geometry and time evolution of the Universe and to constrain the matter content.

The COsmic Background Explorer (COBE) [Boggess *et al.*, 1992] satellite discovered the anisotropies in the CMB. Improvements in the precision and resolution of the measurements of CMB anisotropies were made with the Wilkinson Microwave Anisotropy Probe (WMAP) satellite [Hinshaw *et al.*, 2013]. The subsequent, and still current mission, *Planck* [Planck Collaboration *et al.*, 2013] has shown that the temperature power spectrum could be extremely well reproduced with a spatially flat Cold Dark Matter with cosmological constant Λ (ΛCDM) cosmology specified by six parameters. Recently a more precise analysis [Planck Collaboration *et al.*, 2015i] shows a quasi-Euclidean[1] Universe ($\Omega_k \equiv 1 - \Omega_{tot} \simeq 0$), in accelerated expansion, and dominated by dark energy. Among the other parameters *Planck* measures the Hubble constant (z=0) value of 67.74 ± 0.46 km s^{-1} Mpc^{-1} and the age of the Universe equals to 13.799 ± 0.021 Gyr. The values of the energy density components as measured by *Planck* [Planck Collaboration *et al.*, 2015i] are:

$$\begin{cases} \Omega_\Lambda &= [69.11 \pm 0.62]\%, \\ \Omega_\mathrm{m} &= [30.89 \pm 0.62]\%, \\ \Omega_\mathrm{c} h^2 &= [11.88 \pm 0.10]\%, \\ \Omega_\mathrm{b} h^2 &= [2.230 \pm 0.014]\%, \\ \Omega_\mathrm{r} &\simeq 5 \times 10^{-3}\%, \\ \Omega_k &= [0.00 \pm 0.50]\%. \end{cases} \tag{1.6}$$

The factor h^2 (where h is the Planck constant) removes the degeneracy with the Hubble constant today in the density of baryons and cold dark matter (*i.e.* Ω_c and Ω_b), such as $H_0 = 100\ h$ km/s/Mpc (where $h = 0.6774 \pm 0.0046$). Given the success of the current model of cosmology in cataloging the content of the universe, CMB studies are now pushing to new frontiers, of which there is much excitement for the earliest stages in the Universe (*i.e.* the inflationary epoch).

1.2.2 Thermal history of the Universe

The CMB has a black body spectrum with a well measured temperature $T(t_0) = 2.7255 \pm 0.0006K$ [Fixsen, 2009]. A photon with an energy $k_B T$ today has a wavelength $\hbar c / k_B T(t_0)$, where k_B is the Boltzmann constant and $\hbar$ the Dirac constant. Early on, when the scale factor was smaller than it is today, this wavelength would have been correspondingly smaller. Since the energy of a photon is inversely proportional to its wavelength, the photon energy would have been larger than today by a factor of $1/a$. This argument applied to the thermal bath of photons implies that the temperature of the plasma as a

[1] Two initially parallel light rays will remain parallel when travelling freely in the Universe

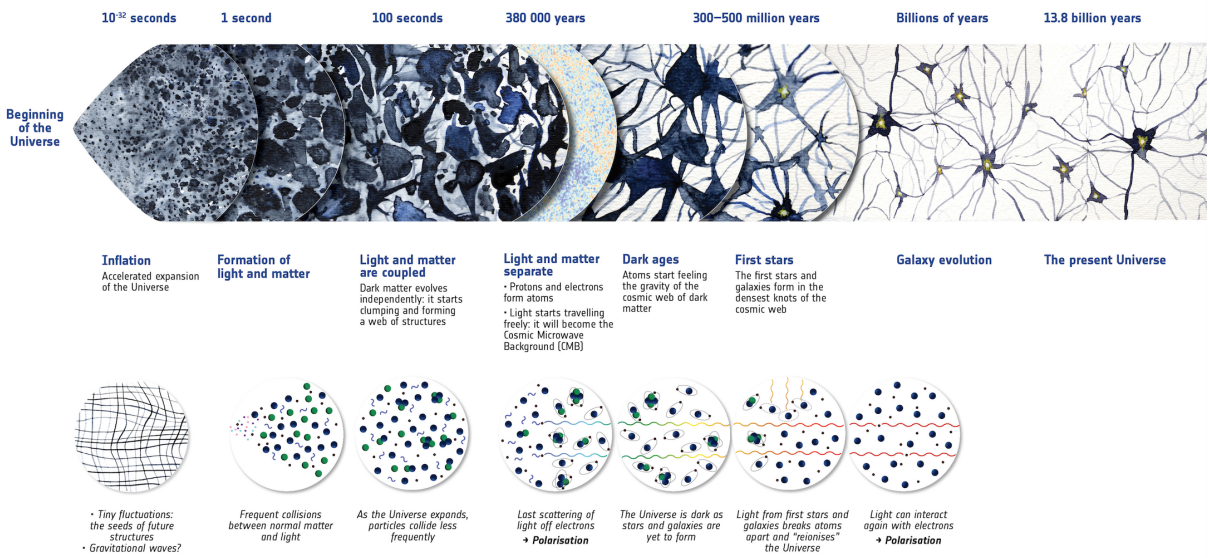

Figure 1.1: *Summary of the almost 14 billion year history of the Universe, showing in particular the events that contributed to the Cosmic Microwave Background. Credits: ESA.*

function of time is:

$$T(t) \propto (1/a(t) = 1 + z), \tag{1.7}$$

where z is the redshift. At the beginning of the Universe the plasma is in thermal equilibrium and it consists of relativistic particles with high interaction rate. With the expansion of the Universe, this rate decreases and the particles leave the thermal bath. When the temperature reaches ~ 100 keV, the nuclear interactions between photons and neutrons allow the formation of deuterium, helium and heavy metals. This epoch is called primordial nucleosynthesis [Gamow, 1946]. At a redshift of ~ 1000 corresponding to $T \sim 3000$ K, electrons and protons combine and the Universe becomes neutral. This epoch is called "recombination". After recombination, photons travel from the "Last Scattering Surface" (LSS) to us today and the Universe enters a matter-dominated epoch. The dark matter, which interacts via gravity, collapses, forming filamentary structures and halos. At z $\sim$ 7-8, star formation starts emitting ultraviolet radiation that carves out ionised regions around stars. After a sufficient number of ionising sources have formed, the ionised fraction of the gas in the Universe rapidly increases until hydrogen becomes fully ionised. This period, during which the cosmic gas went from neutral to ionised, is known as the Universe's epoch of reionization. During this matter-dominated epoch, the structure formation leads to the formation of galaxy clusters at the intersections of filaments. Finally, later than $z \sim 0.5$, dark energy starts to dominate and the expansion of Universe accelerates. An illustration of Universe's history is shown on Fig. 1.1.

1.2.3 Inflation

The Big Bang model, although it is very successful, presents many observational problems (see [Liddle et Lyth, 2000] for a review). An additional paradigm is needed to solve these

problems. Inflation solves these problems[Starobinsky, 1982; Guth, 1981; Linde, 1982; Linde, 2014]:

- the *singularity problem*: the assumptions on which the model is based break down long before the singularity is reached and therefore the model cannot be used to explain the earliest moments of the evolution of the Universe.

- The *horizon* problem: within the Big Bang model there is no explanation for the observed homogeneity and isotropy of the CMB [Smoot *et al.*, 1992] as the observed large angular scales (larger than 1 degree or so) today were not in casual contact at recombination.

- The *flatness problem*: the current Universe seems to be Euclidean flat (see results in 1.6). However, in the Big Bang model the flat solution is unstable and therefore to explain the current flatness of the Universe, the initial spatial curvature had to have been tuned to very high accuracy (Ω_{tot} -1 $< 10^{-60}$ at the Planck time).

- The *seed-fluctuations problem*: the Big Bang model does not provide an explanation for the primordial density fluctuations at the origin of the CMB anisotropies [Smoot *et al.*, 1992] and that gave rise to the large scales structures in the Universe today [Planck Collaboration *et al.*, 2013; Planck Collaboration *et al.*, 2015i].

Inflation introduces a superluminal expansion of space-time [Starobinsky, 1982; Guth, 1981]. Based on the solutions of the Friedmann equations, accelerated expansion requires $w < -\frac{1}{3}$. Since inflation must be limited in time, we thus need a mechanism to switch from exponential expansion to a radiation dominated universe. These two properties can be obtained using one or more scalar fields. The scalar field associated with inflation is called the *inflaton* field. Following [Liddle et Lyth, 2000], the density and pressure of a scalar field, ϕ, can be written as, $\rho_\phi = \frac{1}{2}\dot{\phi}^2 + \frac{(\nabla\phi)^2}{2a^2} + V(\phi)$ and $p_\phi = \frac{1}{2}\dot{\phi}^2 - \frac{(\nabla\phi)^2}{6a^2} - V(\phi)$ where $V(\phi)$ is the potential associated to the scalar field. To obtain accelerated expansion the *slow-roll* conditions, $\dot{\phi} << V(\phi)$ and $\ddot{\phi} << 3H\phi$, need to be satisfied, so that the equation of state is $p \sim -\rho$. These conditions can be expressed conveniently in terms of slow-roll parameters, $\epsilon = \frac{m_{Pl}^2}{2}\left(\frac{V'}{V}\right)^2 << 1$ and $\eta = m_{Pl}^2\left(\frac{V''}{V}\right) << 1$ where m_{Pl} is the reduced Planck mass. It is important to notice that under the *slow roll* conditions $H \simeq \frac{3\pi G}{3}V(\phi) \simeq$ constant and $a(t) \propto \exp(Ht)$ (exponential expansion). A successful inflation model needs to last long enough to solve the horizon and flatness problems. Typically, the amount of inflation is measured in terms of the number of *e-foldings* defined as $N = \int_{t_i}^{t_f} Htdt$ where t_i and t_f are the time inflation starts and ends respectively. The minimum required number of *e-foldings* is of the order of 60 [Starobinsky, 1982].

Any scalar field will have quantum fluctuations $\delta\phi$. During the inflationary phase fluctuations will be expanded to sizes many orders of magnitude larger than Hubble radius [Starobinsky, 1982]. When the wavenumber, k, satisfies $k > aH$, the quantum fluctuations become classical perturbations described by general relativity. According to these ideas, the fluctuations seen in the universe today would have originated from these quantum fluctuations. The fluctuations $\delta\phi$ generate scalar perturbations that grow to produce the structure that we observe today. In addition, gravitational waves are generated during inflation which introduce a tensor contribution to the fluctuations. The power spectra of the fluctuations in scalar and tensor components at the end of inflation can be expressed

as $P_S(k) = \left(\frac{H^2}{2\pi\dot{\phi}^2}\right)^2 \left(\frac{k}{aH}\right)^{n_S-1}$ and $P_T(k) = \frac{8}{m_{Pl}^2}\left(\frac{H^2}{2\pi}\right)\left(\frac{k}{aH}\right)^{n_T}$, respectively. The scalar and tensor spectral indices are given by $n_S - 1 = -6\epsilon + 2\eta$ and $n_T = -2\epsilon$ respectively [Liddle et Lyth, 2000]. We can define the tensor-to-scalar ratio as the ratio between the amplitude of tensor and scalar perturbations:

$$r = \left.\frac{P_{\rm t}}{P_{\rm s}}\right|_{k=k_\star} \tag{1.8}$$

Notice that both contributions have the same dependance on k, so usually we define $r_{0.002} = r(k_\star = 0.002\ \mathrm{Mpc}^{-1})$. The tensor-to-scalar ratio measures the energy scale, V, associated with inflation $r = 0.001\left(\frac{V}{10^{16}Gev}\right)^2$ [Liddle et Lyth, 2000].

During the inflationary period, the energy density of the Universe is completely dominated by the energy of the inflaton field. The density of regular matter is exponentially diluted. An essential part of any inflationary model is the so-called *reheating process*, by which the energy density is transformed to regular matter at the end of the period of inflation. After inflation, the evolution of the cosmological perturbations can be obtained by perturbative expansion to linear order, of the Einstein equations about the background metric. Metric perturbations can be classified in scalar, tensor and vector fluctuations. The most important fluctuations are the scalar ones which couple to matter inhomogeneities. These scalar modes lead to density perturbations which grow by gravitational collapse and form stars, that merge into galaxies and those into clusters of galaxies. Density and tensor perturbations at the time of recombination leave their imprint on the CMB photons producing CMB anisotropies as discussed in the following sections.

1.2.4 CMB anisotropies

On the celestial sphere, the CMB temperature field can be decomposed into spherical harmonics:

$$T(\hat{n}) = \sum_{l=0}^{\infty}\sum_{m=-l}^{l} a_{T,lm} Y_{lm}(\hat{n}), \tag{1.9}$$

where $\hat{n}$ is an unit direction vector and a_T refers to the temperature field. Likewise, the Q and U Stokes parameters for linear CMB polarisation can be decomposed into complex spin-2 harmonics [Newman et Penrose, 1966; Goldberg *et al.*, 1967]:

$$(Q \pm iU)(\hat{n}) = \sum_{l=0}^{\infty}\sum_{m=-l}^{l} a_{\pm 2lm}\ {}_{\pm 2}Y_{lm}(\hat{n}). \tag{1.10}$$

The spin-2 coefficients can then be combined to represent polarisation modes that have no curl (E-modes) and modes that have no divergence (B modes). These are given by the coefficients [Zaldarriaga et Seljak, 1997]:

$$a_{E,lm} = -\frac{a_{2lm} + a_{2lm}}{2}, \tag{1.11}$$

$$a_{B,lm} = i\frac{a_{2lm} - a_{2lm}}{2}. \tag{1.12}$$

The angular power spectra are related to these modes according to:

$$C_l^{XY} = \frac{1}{2l+1} \sum_{m=-l}^{l} a_{lm}^X a_{lm}^{*Y}, \tag{1.13}$$

where $X, Y = T$, E, or B. Therefore, there are six independent power spectra than can be constructed from the temperature and polarisation data, TT, TE, TB, EE, EB, and BB, though in theories which parity is conserved, TB and EB are expected to be zero.

The dipole

The largest CMB anisotropy is the dipole ($l = 1$), the first spherical harmonic with amplitude 3.3645 ± 0.0008 mK [Planck Collaboration *et al.*, 2015b]. The dipole is interpreted as the Doppler shift caused by the solar system motion relative to the nearly isotropic black body field.

Temperature anisotropies

CMB temperature anisotropies at recombination are generated by four main physical processes.

- **Sachs-Wolfe effect**. The horizon scale at the LSS corresponds to $l \sim$200. Anisotropies at large angular scales have not evolved significantly, and hence directly reflect the primordial fluctuations, $\frac{\Delta T}{T_{\rm CMB}} \simeq \frac{\delta\phi}{3}$ where ϕ is the perturbation to the gravitational potential, evaluated on the LSS. This is a result of the combination of gravitational redshift and intrinsic temperature fluctuations, and is usually referred to as the Sachs-Wolfe effect [Sachs et Wolfe, 1967; White et Hu, 1997].

- **Tensor anisotropies**. Primordial tensor fluctuations generate temperature anisotropies through the integrated effect of the locally anisotropic expansion of space. Since tensor modes also redshift away as they enter the horizon, they contribute only to angular scales above one degree [Hu et White, 1997].

- **Acoustic oscillations of the baryon-photon fluid**. Before recombination, photons are tightly coupled to electrons, by Thomson (Compton) scattering; the electrons are in turn tightly coupled to the baryons by Coulomb interactions. As a consequence, any bulk motion of the photons must be shared by the baryons. Primordial scalar fluctuations induce matter density anisotropies at the LSS, leading to over-density regions. The radiation pressure will oppose to the baryon gravitational collapse leading to acoustic oscillations of the baryon-photon fluid. The pattern of acoustic oscillations on the LSS seen by the observer becomes the acoustic peaks in the temperature anisotropy. Assuming inflationary adiabatic primordial fluctuations, we have $\frac{\Delta T}{T_{\rm CMB}} \propto \frac{\delta\rho}{3\rho}$. Acoustic oscillations also imply that the plasma is moving relative to the observer.

- **Damping**. Above we have assumed that photons and baryons respond to pressure and gravity as a single perfect fluid. However, fluid imperfections are related to the Compton mean free path of photons. Thus Compton scattering induces dissipation,

and thus the damping of the acoustic oscillations, becomes strong at the diffusion scale which is the distance a photon can randomly walk in a given time. Damping can be thought of as the random walk in the baryons that takes photons from hot regions into cold ones and vice-versa [Silk, 1968]. The damping is enhanced due to the finite duration of recombination. Only fluctuations with wavelengths shorter than the thickness of the LSS are measured [Hu et White, 1997].

1.2.5 CMB polarisation

Polarisation of the CMB photons is due to Thomson scattering with electrons in the primordial plasma[2]. By symmetry, we can show that only a quadrupole anisotropy of the incident radiation on an electron can produce polarisation. The Thomson scattering differential cross section of an electron (assumed at rest) illuminated by an unpolarised photon flux is given by:

$$\frac{d\sigma}{d\Omega} = \frac{3\sigma_T}{8\pi} \left|\epsilon \cdot \epsilon'\right|^2 . \tag{1.14}$$

The scalar product $|\epsilon \cdot \epsilon'|$ implies the absorption of the components parallel to the polarisation of the incident flux. If the flow is less intense in one direction, then the received radiation is linearly polarised. Let us consider the following cases:

- if the incident radiation is isotropic (*i.e.* monopole) then the total resulting polarisation for the observer is zero;
- if the incident intensity of the incident radiation follows a dipole pattern then each component of the polarisation is compensated and there is no resulting polarisation;
- if the incident intensity is quadrupolar, then there is no more compensation and a non zero resulting polarisation appears.

So, from a non-polarised incident flux but having a quadrupolar anisotropy, a linearly polarised radiation can be generated. There are three types of metric perturbations, related to three different physical sources, that give rise to quadrupole anisotropies: the scalar (from density fluctuations), the vector (due to vortices) and the tensor anisotropies (related to the passage of gravitational waves).

1. **scalar perturbations**: let us consider an electron near an over-density (see Fig. 1.2). In its reference frame, the other plasma particles aligned along the same radius go away. By contrast, those that belong to the same isocontour of density (left and right sides of the electron) come closer. The same reasoning applies to matter under-densities. This phenomenon produces quadrupole anisotropies on the LSS.

[2] In the low-energy limit, the electric field of an incident electric wave accelerates the charged particle, here an electron, causing it to emit radiation at the same frequency as the incident wave, and thus scatter this later. The particle moves in the direction of the oscillating electric field, resulting in an electromagnetic dipole radiation. The moving particle radiates most strongly in a direction perpendicular to its motion and that radiation will be polarised along the direction of its motion.

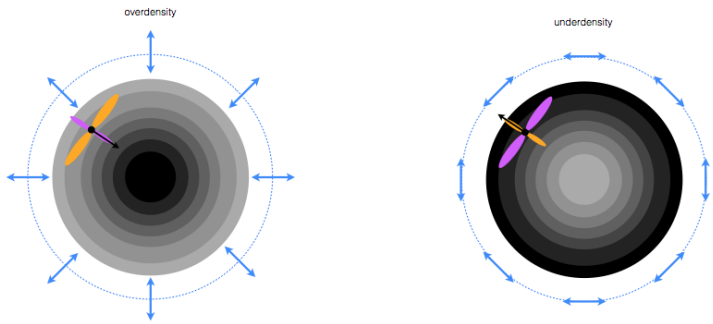

Figure 1.2: *Illustration of an electron falling into an over-density (left panel) or going away from an under-density (right panel). Resulting polarisation patterns are shown on the external blue dashed circle. The electron and its speed are depicted in grey-scale and the associated quadrupole is depicted in orange (hot direction) and purple (cold one). Credits:[Errard, 2012].*

2. **vector perturbations**: movements of vortices in the primordial plasma can produce quadrupole anisotropies. They are not necessarily related to density fluctuations. However, in most of the inflationary models, vector perturbations are negligible.

3. **tensor perturbations**: a gravitational wave passing through a density fluctuation changes the shape of the potential well. Density contours are no longer circular but become elliptical, thus forming quadrupole perturbations and loosing their symmetric properties.

At the recombination epoch, the inflationary gravitational waves (IGW) contribute to the anisotropy of the CMB in both total intensity and linear polarisation. We usually decompose the polarisation patterns into two geometrical components named E- and B-modes (see 1.2.4), which are a combination of the Stokes parameters Q and U, see [Zaldarriaga, 1998] for detailed calculations. This decomposition allows us to distinguish physical causes generating those geometrical patterns: in fact, primordial density or scalar perturbations (see Fig. 1.2) only generate polarisation E-modes. Primordial tensor perturbations lead to both E and B modes of polarisation. The amplitude of the tensor perturbations is conventionally parametrised by r, the tensor-to-scalar ratio. Primordial B-modes discovery would correspond to an indirect detection of primordial gravitational waves and would constrain the energy scale of inflation.

Planck [Planck Collaboration *et al.*, 2015i] measured the six fundamental cosmological parameters of the ΛCDM model and together with BICEP2 [BICEP2/Keck and Planck Collaborations *et al.*, 2015] set an upper limit for r which involves an inflationary model and corresponding to $r < 0.12$ (95% C.L.), recently updated by [Keck Array *et al.*, 2016] to $r < 0.07$ (95% C.L.).

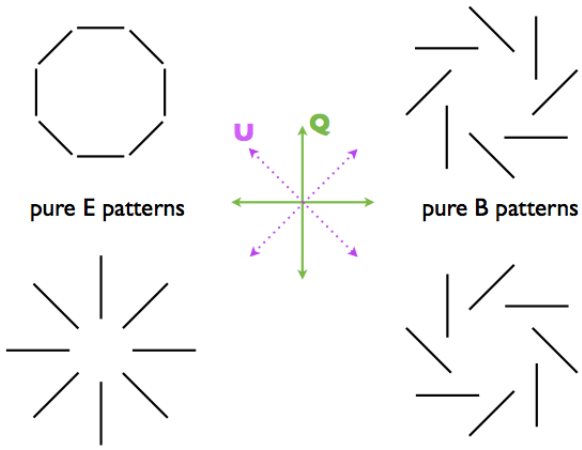

Figure 1.3: *Illustration of pure E- (left) and B-patterns (right) which are a combination of Stokes parameters Q and U. Credits:[Errard, 2012].*

1.3 Diffuse Galactic emissions

The microwave sky in total intensity exhibits very rich astrophysics [Planck Collaboration *et al.*, 2015f]. Apart from the CMB, different Galactic diffuse emissions are observed:

- synchrotron emission generated by cosmic-ray electrons spiralling in the Galactic magnetic field;
- thermal dust emission primarily dominating at frequencies above 100 GHz;
- Anomalous Microwave Emission (AME), which may be due to spinning dust due to the rotation of dust grains;
- *free-free* emission, or bremsstrahlung, resulting from electron-ion collisions;
- CO transition line emission at 115, 230 and 345 GHz.

The thermal Sunyaev-Zeldovich (SZ) effect, which is caused by CMB photons scattering off hot free electrons in galaxy clusters [Sunyaev et Zeldovich, 1972], adds to the extragalactic component. While the signal in total intensity has been well investigated, at the sensitivity of current experiments, only three diffuse components have been clearly detected in polarisation, CMB, Galactic and extragalactic synchrotron and thermal dust. In the next sections I will detail mainly the synchrotron and dust emission which are particularly interesting for the observations performed in polarisation with *NIKA* and I will briefly review the other diffuse mechanisms of emission of interest at Galactic scales.

1.3.1 Synchrotron emission

At low frequencies ($\leq$ 10 GHz), synchrotron radiation form ultra-relativistic electrons spiralling in the Galactic magnetic field dominates the sky. This process is also responsible for the radio emission from supernova remnants and extragalactic radio sources. It is also

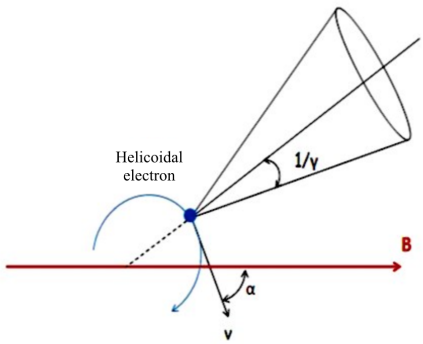

Figure 1.4: *Synchrotron emission by an electron gyrating around the magnetic fields lines with an angle α. The radiation is restricted in a cone of angular size of $1/\gamma$.*

responsible for the non-thermal optical and X-ray emission observed in the Crab Nebula and possibly for the optical and X-ray continuum emission of quasars. The radiation of a relativistic electron gyrating around the magnetic fields lines is contained in a cone as represented in the Fig. 1.4. The electrons emit jets of radiation with a frequency ν_B as:

$$\nu_B = \frac{e \mid \overrightarrow{B} \mid}{2\pi\gamma m_e c}, \tag{1.15}$$

where $\mid \overrightarrow{B} \mid$ is the norm of the magnetic field, e and m_e are the charge and the mass of the electron. The relativistic factor γ is called the *Lorentz factor* and it is defined as:

$$\gamma = \frac{1}{\sqrt{1 - \frac{v^2}{c^2}}}. \tag{1.16}$$

The opening angle of the emission cone is $1/\gamma$ (Fig. 1.4). The time window for each jet is less than the rotation period of the electron about the magnetic field lines. The critical frequency ν_c, where the synchrotron emission has the maximum intensity is defined by:

$$\nu_c = \frac{3}{2}\gamma^3 \nu_B \sin(\alpha), \tag{1.17}$$

where α is the angle between the electron velocity vector and the magnetic field $\overrightarrow{B}$. The radiated power of the synchrotron emission can be expressed as:

$$P_\nu = \sqrt{3}\frac{e^3 \mid \overrightarrow{B} \mid \sin(\alpha)}{mc^2} F\left(\frac{\nu}{\nu_c}\right), \tag{1.18}$$

where $F\left(\frac{\nu}{\nu_c}\right)$ is an integral over a modified Bessel function [Ginzburg et Syrovatskii, 1965] and reads:

$$F\left(\frac{\nu}{\nu_c}\right) \simeq \frac{4\pi}{\sqrt{3}\Gamma(1/3)}\left(\frac{\nu}{2\nu_c}\right)^{1/3}, \qquad \frac{\nu}{\nu_c} << 1 \tag{1.19}$$

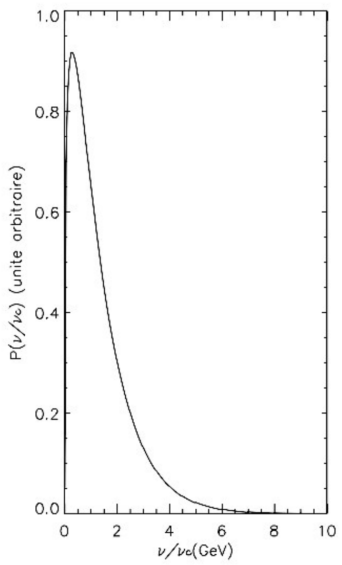

Figure 1.5: *Frequency spectrum ν of the synchrotron emission for an electron with ν_c = 1 GHz, obtained considering the function $F\left(\frac{\nu}{\nu_c}\right)$ reported in [Ginzburg et Syrovatskii, 1965].*

$$F\left(\frac{\nu}{\nu_c}\right) \simeq \left(\frac{\pi}{2}\right)^{1/2} \exp -\frac{\nu}{\nu_c}\left(\frac{\nu}{\nu_c}\right)^{1/2}, \qquad \frac{\nu}{\nu_c} >> 1. \tag{1.20}$$

Fig. 1.5 presents the spectrum of emission by a single electron versus frequency. Let's consider now a population of ultra-relativistic electrons with energies between E and $E + dE$. We assume that their energy distribution can be represented by a power law:

$$N(E)dE = C(\alpha)E^{-p}dE, \qquad E_1 < E < E_2. \tag{1.21}$$

Consequently

$$N(\gamma)d\gamma = C(\alpha)\gamma^{-p}d\gamma, \qquad \gamma_1 < \gamma < \gamma_2, \tag{1.22}$$

The radiated power per unit of volume and frequency is obtained by:

$$P_{tot}(\nu) = C\int_{\gamma_1}^{\gamma_2} P(\nu)\gamma^{-p}d\gamma \propto \int_{\gamma_1}^{\gamma_2} F\left(\frac{\nu}{\nu_c}\right)\gamma^{-p}d\gamma \tag{1.23}$$

Defining x $\equiv \frac{\nu}{\nu_c}$ and noticing that $\nu_c \propto \gamma^2$ then:

$$P_{tot}(\nu) \propto \nu^{-(p-1)/2}\int_{x_1}^{x_2} F(x)x^{(p-3)/2}dx, \tag{1.24}$$

where x_1 and x_2 correspond to the limits γ_1 and γ_2 depending of ν. If the energy range of the electrons considered is large enough, $x_1 \approx 0$ and $x_2 \approx \infty$. The integral in the previous equation is then approximately constant and we can write:

$$P_{tot}(\nu) \propto \nu^{-s}, \tag{1.25}$$

where s is the spectral index defined by:

$$s = \frac{p-1}{2}. \tag{1.26}$$

We can define the antenna temperature or Rayleigh-Jeans temperature T_{RJ} of the synchrotron emission as:

$$P_{tot}(\nu) = \frac{2k\nu^2}{c^2} T_{RJ} \propto \nu^{-s} \tag{1.27}$$

and then:

$$T_{RJ} \propto \frac{c^2}{2k} \nu^{\beta_s} \tag{1.28}$$

$$\beta_s = -(s+2) \tag{1.29}$$

β_s defines the spectral index of the synchrotron emission in the case of Rayleigh-Jeans approximation. If the slope p equals 3, s = 1 and $\beta_s = -3$. Estimations of the energy distribution set this spectral index value between -2.7 and -3.3 [Kogut *et al.*, 2007; Gold *et al.*, 2009].

Synchrotron radiation is intrinsically highly polarised up to around 100 GHz. Hence, for a power-law distribution of electron energies $N(E) \propto E^{-p}$ propagating in a uniform magnetic field, the resulting emission is partially polarised with fractional linear polarisation:

$$f_s = \frac{s+1}{s+7/3} \tag{1.30}$$

aligned perpendicular to the magnetic field. See [Rybicki et Lightman, 1979] for more details.

1.3.2 Dust emission

The ISM fills the regions between stars in a Galaxy like the Milky Way. It is made of gas, dust, magnetic fields and charged particles. Interstellar gas itself is made of hydrogen (about 70%) and helium (about 28%), with traces of heavier elements called "metals", mostly carbon, silicon, oxygen and nitrogen. Interstellar dust grains are small particles, which are mostly composed of silicon, carbon, metal inclusions and ice mantles. There exist different types of the interstellar grains, classified as: large molecules called Polycyclic Aromatic Hydrocarbons (PAHs), very small grains (VSGs) and big grains (BGs) [Meny *et al.*, 2007; Desert *et al.*, 1990]. Their size ranges from a few Angströms to a micrometer: PAH are of the order of few Angströms, the VSG size is of the order of few nanometers and the BG size ranges between 10 and 100 nm. Current models [Compiègne *et al.*, 2011] aim at reproducing the observed extinction and emission [Desert *et al.*, 1990] of ISM.

Gas appears primarily in two forms, as cold clouds of atomic or molecular hydrogen and hot ionised hydrogen near hot young stars. The clouds of cold molecular and atomic hydrogen represent the raw material from which stars can be formed in the disk of the Galaxy if they become gravitationally unstable and collapse. Although such clouds do not emit visible light, they can be detected by their radio frequency emission. The ionising radiation from the central O/B stars produces ionised hydrogen cloud regions (HII), the surrounding dust is heated by radiation at optical wavelengths originating

from the central stars and as a consequence radiates at sub-millimetre and infrared (IR) wavelengths. The flux density of the radiation from these two components was found to be equal in the wavelength range 1-3 mm (100 to 300 GHz) by [Kurtz *et al.*, 1994] for a selection of compact HII regions.

The ensemble of dust particles having a broad size range ensures a smooth extinction curve from the infrared to the far-UV, with smaller particles absorbing light more efficiently at smaller wavelengths. In general, small dust grains cause attenuation of the stellar light passing through interstellar space. At IR wavelengths dust particles cause very little extinction. The temperature of the interstellar grains causes them to emit radiation in the infrared.

In the microwave sky at frequencies ≥ 70 GHz, thermal emission from interstellar dust grains mostly made of graphites, silicates, and PAHs (Polycyclic Aromatic Hydrocarbons) dominates the diffuse Galactic emission. We can model the intensity of the thermal dust emission using a simple grey body spectrum of the form:

$$I_\nu = I_0 \nu^{\beta_d} B_\nu(T_d), \tag{1.31}$$

where β_d is the spectral index of the thermal dust emission and T_d is the dust temperature and $B_\nu(T_d)$ is the Planck spectrum:

$$B_\nu(T) = \frac{2h\nu^3}{c^2} \frac{1}{e^{\frac{h\nu}{k_B T}} - 1}. \tag{1.32}$$

We can also define the dust emissivity cross section $k_\nu \propto \nu^{\beta_d}$. If most hydrogen is in molecular form, the optical depth is related to the column density of molecular hydrogen [Kauffmann, 2005]:

$$N_{H_2} = 2.14 \times 10^{25} \mathrm{cm}^{-2} \tau_\nu \left(\frac{k_\nu}{0.01 \mathrm{cm}^2 \mathrm{g}^{-1}} \right)^{-1}. \tag{1.33}$$

As typical H_2 column densities are below 10^{23} cm^{-2}, the optical depth τ_ν is expected to be much smaller than 1. Thermal dust emission in the (sub-)millimetre regime is therefore optically thin. As the optical depth is related to the column density, Eq. 1.31 relates the observed intensity to the column density. The dust temperature, T_d, is determined by the equilibrium between interstellar radiation field (heating) and efficiency of emitting far-infrared light (cooling) of the dust grains. The spectral index, β_d, depends on the dust composition and grain size distribution. Smaller grains have larger opacity indices, leading to steeper spectra at longer wavelengths, whereas larger grains such as those found in circumstellar or protoplanetary disks exhibits flatter spectra with low index of β_d. Detailed all-sky maps of dust intensity revealed the strong emission due to dust within our Galaxy [Planck Collaboration *et al.*, 2014e], see Fig. 1.6.

Interstellar dust polarisation

Polarisation of starlight arise from absorption and scattering by elongated dust grains that are at least partially aligned by a magnetic field. Several observations of the interstellar dust extinction [Hiltner, 1949; Hall, 1949] and more recently [Heiles, 2000] have confirmed

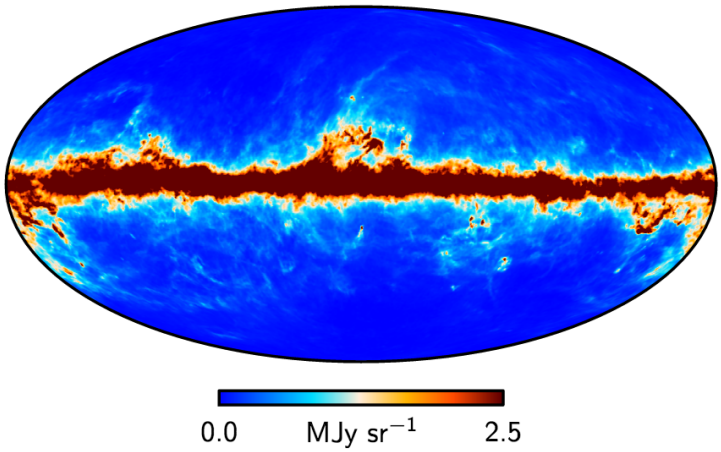

Figure 1.6: *Thermal dust emission map at 353 GHz estimated by the Planck experiment [Planck Collaboration* et al.*, 2014e].*

that. This phenomenon is explained by considering that dust grains are asymmetric and aligned with respect to the magnetic field lines. Aligned grains absorb more light along their longer direction. The situation is reversed if grain emission is considered: more emission emanates in the direction of the grain's longer axis.

Interstellar extinction Following [Mathis, 1990], the absolute extinction A_λ defines the amount of light, in units of stellar magnitude, absorbed or scattered out of the line of sight at a specific wavelength λ. Stellar radiation is attenuated by interstellar dust trough absorption and scattering. The interstellar extinction A_λ is defined as the difference between the observed apparent magnitude and the apparent magnitude if there is no extinction:

$$A_\lambda = m_{obs} - m_0. \tag{1.34}$$

Let's consider the initial radiation flux $I_{0,\lambda}$ which passes through a dust cloud with optical depth τ_λ. The outcoming radiation will then be:

$$I_\lambda = I_{0,\lambda} e^{-\tau_\lambda}. \tag{1.35}$$

The interstellar extinction can be expressed in terms of fluxes as,

$$A_\lambda = -2.5 \log_{10} \left(\frac{I_\lambda}{I_{0,\lambda}} \right), \tag{1.36}$$

using Eq. 1.35 we obtain:

$$A_\lambda = -2.5 \log_{10}(e^{-\tau_\lambda}) = 1.086 \tau_\lambda. \tag{1.37}$$

The interstellar extinction depends on wavelength: shorter wavelengths correspond to higher A_λ [Patriarchi et Perinotto, 1999].

For an ensemble of aligned grains the extinction perpendicular and parallel to the direction of alignment are different. Therefore the initially unpolarised starlight acquires polarisation while passing through a volume with aligned dust grains. If the extinction

in the direction of alignment is $\tau_{\parallel}$ and in the perpendicular direction is $\tau_{\perp}$ one can write the polarisation [Lazarian, 2003], P_{abs}, by selective extinction of grains as:

$$P_{abs} = \frac{e^{-\tau_{\parallel}} - e^{-\tau_{\perp}}}{e^{-\tau_{\parallel}} + e^{-\tau_{\perp}}} \approx -(\tau_{\parallel} - \tau_{\perp})/2 \tag{1.38}$$

where the latter approximation is valid for $\tau_{\parallel} - \tau_{\perp} << 1$, $\tau_{\parallel} << 1$ and $\tau_{\perp} << 1$. The difference in $\tau_{\parallel}$ and $\tau_{\perp}$ results in emission of aligned grains being polarised:

$$P_{em} = \frac{(1-\tau_{\parallel}) - (1-\tau_{\perp})}{(1-\tau_{\parallel}) + (1-\tau_{\perp})} \approx \frac{\tau_{\parallel} - \tau_{\perp}}{\tau_{\parallel} + \tau_{\perp}}, \tag{1.39}$$

where both optical depths $\tau_{\parallel}$ and $\tau_{\perp}$ were assumed to be small. Taking into account that both P_{em} and P_{abs} are functions of wavelength λ and combining 1.38 and 1.39, one gets for $\tau = (\tau_{\parallel} + \tau_{\perp})/2$:

$$P_{em}(\lambda) \approx -P_{abs}(\lambda)/\tau(\lambda) \tag{1.40}$$

which establishes the relation between polarisation in emission and absorption. The minus sign reflects the fact that emission and absorption polarisation are orthogonal.

Planck maps of total intensity and polarised emission display filamentary structure of the ISM [Planck Collaboration *et al.*, 2015c] with the maximum fraction of dust polarisation $p_{max} > 18\%$.

Dust grains alignment

Davis-Greenstein mechanism To explain the alignment of dust grains with respect to the magnetic field lines, Davis-Greenstein [Davis et Greenstein, 1951] proposed a mechanism (D-G mechanism) based on the paramagnetic dissipation that is experienced by a rotating dust grain. Paramagnetic materials contain unpaired electrons, which get oriented by the interstellar magnetic field, **B**. The orientation of spins causes grain magnetisation and the latter varies as the vector of magnetisation rotates in grain-body coordinates. This causes paramagnetic loses at the expense of grain rotation energy. Note that if the grain rotational velocity, ω, is parallel to **B**, the grain magnetisation does not change with time and therefore no dissipation takes place. Thus the paramagnetic dissipation acts to decrease the component of ω is perpendicular to **B** and one may expect that eventually grains will tend to rotate with ω is parallel to **B** provided that the time of relaxation t_{D-G} is much shorter than t_{gas}, the time of randomisation through chaotic gaseous bombardment. In practice, the last condition is difficult to satisfy. For more details on this mechanism see [Davis et Greenstein, 1951; Lazarian et Hoang, 2007]. [Jones et Spitzer, 1967] found that the loss of energy due to para- or ferromagnetic relaxation leads the grain to have its shortest axis of inertia perpendicular to the symmetry axis, which, for prolate grains, corresponds to alignment of the shortest axis with the magnetic field and which is consistent with the results of D-G. The field strength required for such a scenario is of order of 10^{-5} to 10^{-8} G, which is consistent with the observed strength of the Galactic Magnetic Field (GMF).

Radiative torques Further study of the statistical mechanisms of grain alignment [Jones et Spitzer, 1967; Purcell et Spitzer, 1971] raised questions about the ability of the

interstellar magnetic field to achieve the degree of observed alignment. The effect of grain alignment induced by radiative torques was discovered by [Dolginov et Mitrofanov, 1976]. Several mechanisms were proposed and elaborated upon, to various degrees, to account for the observed grain alignment, see the review [Lazarian et Hoang, 2007]. The mechanism of radiative torque alignment may be more promising as it can align grains within subsonic flows. They considered a grain that exhibited a difference in the cross-section for right-handed and left-handed photons. They noticed that the scattering of unpolarised light by such a grain resulted in its spin-up. However, they could not quantify the effect and therefore their pioneering work was mostly neglected for the next 20 years. [Draine et Weingartner, 1996; Draine et Weingartner, 1997; Weingartner et Draine, 2003] demonstrated that the magnitude of torques is substantial for irregular shapes. They predict that irregular dust grains are subject to radiative torques when irradiated by interstellar starlight. Radiative torques arising from anisotropy of the starlight background can act directly to alter the grain alignment on much shorter timescales, and are therefore central to the process of interstellar grain alignment. Later, [Abbas *et al.*, 2004] demonstrated the spin-up of grains by radiative torques in laboratory conditions. See [Andersson *et al.*, 2015; Lazarian *et al.*, 2015] for a review on radiative torques and dust grain alignment.

1.3.3 Anomalous microwave emission

Anomalous microwave emission (AME) is an additional Galactic emission that has been detected at frequencies 10-60 GHz [Planck Collaboration *et al.*, 2014d]. It could be explained by spinning dust grains [Draine et Lazarian, 1998]. Very small grains (*e.g.* PAHs) can get spin up by gas collisions, radiative torques, and other processes. If grains have a dipole moment, this rotation causes them to radiate. Current measurements place upper limits on the polarisation of AME at a few per cent or below [Dickinson *et al.*, 2011; Macellari *et al.*, 2011; Rubiño-Martín *et al.*, 2012].

1.3.4 Free-free emission

Thermal bremsstrahlung from an HII region is often called free-free emission because it is produced by free electrons scattering off ions without being captured. HII regions occur around massive stars and massive stars are preferentially formed in dense cores of molecular clouds. Photons emitted by stars beyond the Lyman continuum limit ($\lambda \leq$ 912 Angstroms) ionise the surrounding gas, which emits the absorbed energy as free-free [Beckert *et al.*, 2000]. This mechanism operates when charged particles (*e.g.* electrons) are accelerated by encountering another charged particle. Consequently, radio free-free emission is expected to manifest in any environment populated by an ionised plasma. The distribution and energy cutoff for scattering in such a plasma are characterised by the Gaunt factor $\langle g_{ff} \rangle$ [Nozawa *et al.*, 1998], which allows one to work out the absorption coefficient, k_ν, for the plasma:

$$k_\nu \propto N_e N_i T_e^{-3/2} \nu^2 \langle g_{ff} \rangle. \tag{1.41}$$

Integration of this quantity along the line of sight $\int k_\nu dl$, gives the optical depth for the free-free emission often approximated as [Dickinson *et al.*, 2003]:

$$\tau_\nu \approx 3.28 \times 10^{-7} \left(\frac{T_e}{10^4\mathrm{K}}\right)^{-1.35} \times \left(\frac{\nu}{\mathrm{GHz}}\right)^{-2.1} \left(\frac{EM}{\mathrm{cm}^{-6}\mathrm{pc}}\right), \tag{1.42}$$

where T_e is the electron temperature, EM is the emission measure, defined by the integral $\int N_e N_i dl$. The brightness temperature, T_b, from such emission is given by:

$$T_b = T_e(1 - e^{-\tau_\nu}). \tag{1.43}$$

In the Rayleigh-Jeans region of the spectrum, where $S_\nu = 2k_B T_b/\lambda^2$ in units of W m^{-2} Hz^{-1} sr^{-1}, and assuming emission extended relative to the resolution of the telescope, the resulting flux density from such emission [Ichiki, 2014] is then given as:

$$\left(\frac{S_\nu}{\mathrm{Jybeam}^{-1}}\right) = 3.07 \times 10^4 \left(\frac{\nu}{\mathrm{GHz}}\right)^2 \times \left(\frac{T_e}{\mathrm{K}}\right)(1 - e^{-\tau_\nu}) \left(\frac{\Omega_b}{sr}\right), \tag{1.44}$$

where Ω_b is the beam size. Where the plasma giving rise to the free-free emission is reasonably uniform in density, this leads to a characteristic radio spectrum which has two components delineated by the frequency at which the optical depth equals unity ($\tau_\nu = 1$), marking the transition from optically thick behaviour to optically thin. In the optically thick regime, the optical depth term in 1.44 becomes approximately unity and the flux density spectrum rises as ν^2; in the optically thin regime, the optical depth term becomes $\sim \tau_\nu$ and the frequency dependence of τ_ν (see 1.42) cancels in 1.44 resulting in a flux spectrum which varies as $\nu^{-0.1}$. The frequency at which an ionised plasma becomes optically thick/thin depends on its size, density and temperature. The emission measure of an ionised plasma surrounding a massive young star can be used to establish the relative age of the object with denser, higher emission measure objects corresponding to younger systems. This emission is very weakly polarised, averaged over the full sky, the free-free emission is observationally constrained to be less than 1% polarised [Macellari *et al.*, 2011].

1.3.5 CO emission

The ISM represents about 10-15% of the total mass of the Milky Way. The ISM contains atomic and molecular gas; the cold neutral gas is confined close the Galactic disk mid-plane in clouds with varying molecular-to-atomic ratios. Molecular clouds, where hydrogen is molecular, are the sites of star formation, and play a pivotal role in the interstellar matter cycle, see [Ferriere, 2001] for a review. Molecular clouds were discovered via rotational emission line $J = 1 \rightarrow 0$ of carbon moxide in its fundamental electronic and vibrational levels [Wilson *et al.*, 1970]. Because CO is abundant, easily excited by collisions with H_2, and easily observable from the ground, it is considered a good tracer of the molecular component of the ISM. *Planck* CO survey [Planck Collaboration *et al.*, 2014c] reveals the lowest CO rotational transition lines at 115, 230 and 345 GHz that contributes to the signal of the 100 GHz, 217 and 353 GHz *Planck* HFI (High-Frequency-Instrument) broadband channels, respectively. The *Planck* CO emission maps show that the bulk of the Galactic CO emission originates in a diffuse component.

1.4 Extragalactic polarised radio sources

In this section I briefly introduce the physics of Active Galactic Nuclei (AGN), which have been observed with *NIKA* to verify the good reconstruction of the polarised signal.

1.4.1 Quasars

Quasars (*QUASi-stellAR radio source*) are the most energetic and cosmological distant galaxies of a class of objects called AGN, containing active, supermassive black holes at their centres. The accretion disks of these black holes, composed of interstellar gas, dust, and stars, are heated to very high temperatures and radiate from the radio to the X-ray (see [Netzer, 2013] for a review on the physics of AGN). The central engines of AGNs can form collimated jets of material, in which particles are accelerated to nearly the speed of light, probably by the magnetic field of the black hole itself [Comastri et Brusa, 2007]. These particles (e.g. electrons, protons, and heavier nuclei) encounter the Galactic and extragalactic magnetic fields and the interstellar and intergalactic media, and can produce radiation at nearly all wavelengths. Some of this radiation is synchrotron emission, generated by ultra-relativistic electrons when they spiral around the magnetic field lines they encounter. Synchrotron emission is responsible for the radio emission in these objects, but can generate also optical and X-ray emission in the most powerful jets [Lacki et Thompson, 2010; Hlavacek-Larrondo *et al.*, 2012]. Spectral and behavioural properties of AGN and quasars depend on the orientation of their central engine and jet with respect to us. It is believed that AGN will be brighter the closer the jet is pointed in the line of sight direction. Quasars are AGNs for which the jet is nearly aligned with the line of sight. In cases where the jet is almost exactly aligned with the line of sight, we see the most extreme example of AGN, a blazar [Urry et Padovani, 1995].

Short millimetre observations of radio-loud AGN offer an excellent opportunity to study the physics of their synchrotron-emitting relativistic jets, from which the bulk of radio and millimetre emission is radiated [Krolik, 1999]. On one hand, AGN jets and their emission cores are significantly less affected by Faraday rotation (see next paragraph) and depolarisation than at longer wavelengths [Jorstad *et al.*, 2005; Matthews *et al.*, 2001]. On the other hand, the millimetre emission of AGN is dominated by the compact innermost regions in the jets, where the jets can not be seen at longer wavelengths due to synchrotron opacity [Omont *et al.*, 2001]. The AGNs spectra was originally interpreted as a quite flat spectrum type following a power law

$$F_\nu \simeq \nu^{-\alpha} \tag{1.45}$$

where F_ν describes the source flux density. The reality is now known to be more complicated with a spectral index α taking values between 0.5 and 2 that generally increases with frequency. At a transition frequency, the spectrum turns over and varies as $\nu^{\frac{5}{2}}$ corresponding to a spectral index $\alpha = -2.5$. This occurs because the plasma of spiraling electrons becomes opaque to its own synchrotron radiation, an effect known as *synchrotron self-absorption* [Carroll et Ostlie, 2007].

Faraday rotation

The emission from extragalactic and Galactic radio sources, such as quasars is linearly polarised. When the polarised light passes through the interstellar medium undergoes Faraday rotation [Gaensler *et al.*, 2005]. The faraday rotation angle is given by:

$$\Delta\chi = RM\lambda^2 \tag{1.46}$$

where

$$RM \propto \int n_e B_{\|} dl \tag{1.47}$$

is the rotation measure, $B_{\|}$ is the component of the total magnetic field parallel to the line of sight, n_e is the electron density. Faraday rotation is significant at wavelengths larger than a few centimetres. By measuring the RM at two wavelengths one can determine the strength and the direction of $B_{\|}$.

1.5 Star forming regions

1.5.1 Star formation physics overview

Stars are a primary source of astronomical information and, hence, are essential for our understanding of the Universe and the physical processes that govern its evolution. At optical wavelengths almost all the light we observe in the sky originated from stars. When we look at the sky on a clear night, we can also note dark patches of obscuration along the band of the Milky Way. These are clouds of dust and gas that block the light from stars further away. We know now, that these clouds give birth to stars. In the last century the advent of new observational instruments made it possible to observe astronomical objects at wavelengths ranging from γ-rays to radio frequencies. Especially useful for studying the dark clouds are radio, sub-millimetre and far-infrared wavelengths, at which they are fairly transparent. Observations now show that all star formation occurring in the Milky Way is associated with the dark clouds of molecular hydrogen and dust. The mass of the Galactic disk plus bulge is about $6 \times 10^{10} M_\odot$ [Dehnen et Binney, 1998], where 1 $M_\odot = 1.99 \times 10^{33} g$ is the mass of the Sun. Thus assuming standard values for the stellar mass distribution, there are $\sim 10^{12}$ stars in the Milky Way.

Stars form continuously, 10 % of the Milky Way disk mass is in the form of gas, which is forming stars at a rate of about 1 $M_\odot$ yr^{-1}. In the absence of any obstacles, the gas then collapses gravitationally to form stars on a free-fall time [Jeans, 1902]:

$$T_{ff} = \left(\frac{3\pi}{32G\rho}\right)^{1/2} = 140 Myr \left(\frac{n}{0.1\mathrm{cm}^{-3}}\right)^{-1/2}, \tag{1.48}$$

where n is the number density of the gas. Interstellar gas in the Milky Way consists of one part helium for every ten parts of hydrogen. The mass density is $\rho = \mu n$, where we take the Galactic value for the mean mass per particle in neutral atomic gas $\mu = 2.11 \times 10^{-24} g$ and G is the gravitational constant. The free-fall time T_{ff} is very short compared to the age of the Milky Way, about 10^{10} yr. In the past the stars were forming at a faster rate than today (*e.g.* [Lilly *et al.*, 1996], [Madau *et al.*, 1996], [Baldry *et al.*, 2002], [Lanzetta

et al., 2002]), with as much as 80 % of star formation in the Universe being complete by redshift $z = 1$. We are interested to know which mechanisms allowed rapid star formation in the past, but suppress its rate today.

For many years it was thought that support by magnetic pressure against gravitational collapse offered the best explanation for the slow rate of star formation. In this theory developed by [Shu, 1977; Shu *et al.*, 1987; Mouschovias et Morton, 1991] and others, the interstellar magnetic field prevents the collapse of gas clumps with insufficient mass to flux ratio, leaving dense cores in magneto hydrostatic equilibrium. The magnetic field couples only to electrically charged ions in the gas, though, so neutral atoms can only be supported by the field if they collide frequently with ions.

The classical theory of gravitational collapse balanced by pressure did not take into account the conservation of angular momentum and magnetic flux during collapse.
It became clear from observations of polarised starlight [Hiltner, 1949] that substantial magnetic fields thread the interstellar medium. This forced the magnetic flux problem to be addressed, but also raised the possibility that the solution to the angular momentum problem might be found in the action of magnetic fields.

1.5.2 Magnetic fields

Magnetic fields are currently considered one of the key components that regulate star formation [Shu, 2007]. Observations of polarisation in star forming regions have shown that the magnetic fields (B-fields) are often well-ordered on scales from ~ 100 pc down to ~ 1 pc [Heiles, 2000], which suggests that large scale B-fields are dynamically important. One usually distinguishes between the ordered component of the magnetic field and the turbulent component. The ordered magnetic field is coherent in orientation though can exhibit changes in direction. The turbulent field arises from turbulent gas flows. The observed polarisation generally traces the general behaviour of the ordered field, because the turbulent component depolarises the signal.
There exist mainly two theories explaining the magnetic field role in the star formation process:

1. **ambipolar diffusion**: this theory can solve the question of how magnetically supported gas can fragment if it allows neutral gas to gravitationally condense across field lines. The local density can then increase without also increasing the magnetic field, thus lowering the critical mass for gravitational collapse [Spitzer, 1968]. Ambipolar diffusion reduces support in cores and hence drives star formation (*e.g.*, [Mouschovias et Ciolek, 1999]), this is the so-called strong magnetic field theory. In this case, the ideal MHD (Magneto HydroDynamic) conditions are usually assumed to be satisfied in astrophysical plasmas: ionised particles are coupled to the magnetic field, while neutrals, which constitutes the majority of a cloud mass, are not. During gravitational collapse, neutrals can move across field lines. Although rapid collapse is prevented by the collisions between neutrals and ions, which are supported by magnetic field lines. Thus, the magnetic field supports the cloud against collapse, depending on the ratio between the strength of the magnetic field, the core density and the ionisation fraction of the gas.

2. **Turbulence**: another interpretation shows the molecular clouds as intermittent phenomena in an interstellar medium dominated by turbulence, and the problem of cloud support for long time periods is irrelevant (e.g., [Elmegreen, 2000]). In this paradigm, clouds form and disperse by the operation of compressible turbulence, with clumps sometimes becoming gravitationally bound. Turbulence then dissipates rapidly, and the cores collapse to form stars. Turbulence and magnetic field are likely both present and dynamically important for star formation theories and it has been very recently addressed by magnetic reconnection diffusion theory [Lazarian *et al.*, 2014].

These two main theories have different predictions for the magnetic field morphology and strength that can be observationally tested.

1. Ambipolar diffusion tends to keep magnetic field lines smooth, not dominated by irregular structure.

2. A turbulence-dominated medium will have a chaotic magnetic field, with field lines stretched along low-density matter filaments and more regular structure close to the centre of the forming core, in spite of its density structure.

The role of the magnetic field in the ISM dynamics depends on the field strength with respect to gravitational and turbulent energies. In the diffuse ISM, the magnetic energy is observed to be comparable with the turbulent kinetic energy of the gas ([Heiles et Troland, 2005; Basu et Roy, 2013]) and to dominate its self-gravity [Crutcher *et al.*, 2010], while stars form where and when gravity prevails.
Observations towards dense clouds [Crutcher *et al.*, 2010] are not well explained via ambipolar diffusion, whereas simulations of core formation by turbulence in the presence of weak magnetic field are in better agreement with the observations.

Polarisation in dense regions, such as interstellar clouds, is of particular interest. One of the most important objectives of polarimetric studies in these media is to investigate the role of the magnetic field in structuring the interstellar matter. To probe dust polarisation in high density clouds it is necessary to extend extinction measurements from the visible to the infrared wavelengths, and to perform observations of the polarised emission continuum in the sub-millimetre range. Recent 1.3 mm observations performed with CARMA on star forming cores and regions have shown that we can see the so-called "polarisation-hole" effect even at $\sim 2.5''$ resolution, with a significant drop of the polarisation fraction near the total intensity peak [Hull *et al.*, 2014]. The trend of decreasing polarisation with increasing density is predicted by the theory of dust grain alignment: in the absence of internal sources of radiation, few photons penetrate deep into the cloud, thus grain alignment is less efficient, which leads to low polarisation. Moreover, if one considers ambipolar diffusion to take place during cold cores formation, one would expect the big grain population to grow in the centre of the collapsing cloud because big grains are not frozen to the magnetic field lines while small grains are [Ciolek et Mouschovias, 1996]. Efficiency of big grain alignment by radiative torques is more important than for the small ones, so polarisation inside dark clouds would not be zero [Cho et Lazarian, 2005].

More recently, observations with *Herschel* and *Planck* satellites have provided with unprecedented sensitivity maps of the star forming complexes in the Galaxy. By measuring intensity and polarisation from Galactic dust over the whole sky as well as scales as

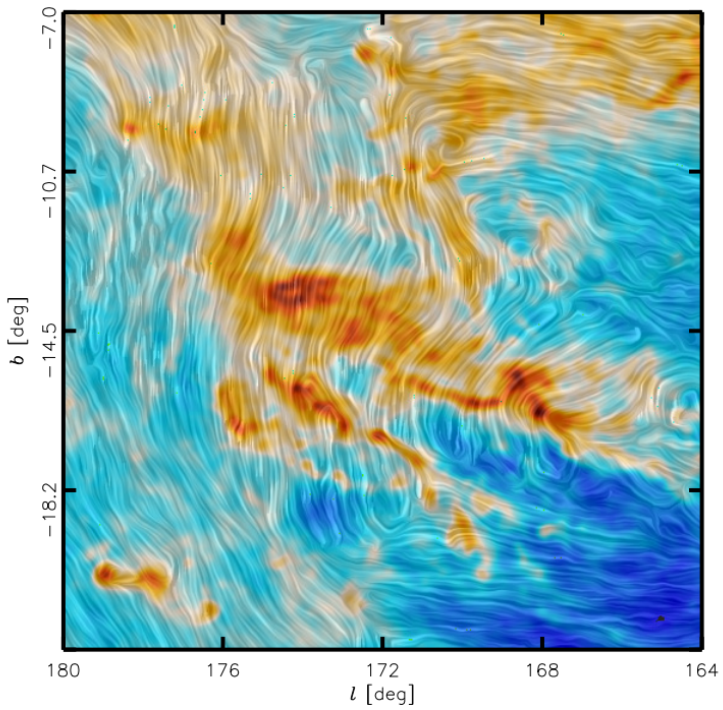

Figure 1.7: *Magnetic field and column density measured by Planck towards the Taurus Molecular Cloud. The colours represent column density. The "relief" pattern, indicates the orientation of the magnetic field lines, assumed to be orthogonal to the measured orientation of the submillimetre polarisation. Credits: [Planck Collaboration* et al.*, 2016a].*

small as the cores of nearby Molecular Clouds (MCs), *Planck* provides an unprecedented data set to study the morphology of the magnetic field and the surrounding ISM, as illustrated for the Taurus region in Fig. 1.7 (more details in [Planck Collaboration *et al.*, 2016a]). Dust grains tend to align their longest axis at right angles to the direction of the field. As a result, the light emitted by dust grains is partially "polarised" and it vibrates in a preferred direction. High angular resolution *Herschel* observations demonstrate that filaments are ubiquitous in the cold ISM [Palmeirim *et al.*, 2013]. These maps reveal large scale filamentary structures as the preferential sites of star formation [Arzoumanian *et al.*, 2011], [Pereyra et Magalhães, 2004]. These filamentary structures are associated with organised magnetic field topology at scales larger than 0.5 pc. This indicates that magnetic fields may play a major role in star formation and that they need to be explored in detail on scales of 0.01 to 0.1 pc. At smaller scales ambipolar diffusion or turbulent magnetic reconnection diffusion are thought to allow dense cores to become "supercritical" [Crutcher, 2012] at which point gravity overwhelms magnetic support and allows the formation of a central protostar.

1.5.3 A schematic scenario of early star formation

The formation and evolution of MCs and their substructures, from filaments to cores and eventually to stars, is regulated by interstellar turbulence and its interplay with gravity [McKee et Ostriker, 2007]. MHD turbulence sets the initial conditions to large scale for

the formation of filaments of MCs. *Herschel* observations of active star-forming regions support a scenario according to which core formation occurs in two main steps (*e.g* [André *et al.*, 2010]). First, large-scale MHD turbulence gives rise to a web-like network of filaments in the ISM. In a second step, gravity takes over and fragments the densest filaments into prestellar cores via gravitational instability. Indirect arguments suggest that dense, self-gravitating filaments, which are expected to undergo radial contraction [Inutsuka et Miyama, 1997], can maintain a constant central width of 0.1 pc if they accrete additional mass from their surroundings while contracting [Arzoumanian *et al.*, 2011]. *Planck* observations of the polarisation dust, combined with high angular resolution intensity observations from *Herschel*, outline this scenario for star forming region.

High angular resolution polarisation observations can probe the physics acting at small angular scales and complete the current understanding of the star formation process: this is one of the main objectives of the *NIKA2* instrument/collaboration/science program.

1.6 Summary

Diffuse Galactic microwave emission in intensity and polarisation carries important information about fundamental properties of the Interstellar Medium (ISM), but it also constitutes a major foreground for the study of the Cosmic Microwave Background (CMB) experiments [Planck Collaboration *et al.*, 2015d]. In polarisation, the Galaxy represents the cradle of different emission mechanisms, namely: synchrotron, anomalous microwave emission (AME) and interstellar dust. These correspond to the main foreground contaminations for the reconstruction of the CMB polarisation spectrum, which peaks at 150 GHz. On a different topic, high resolution studies of the nearest star-forming clouds can provide a detailed view on the physics controlling the earliest phases of the star formation [André *et al.*, 2010]. The *Herschel* satellite has revealed an intricate network of filamentary structures in every interstellar cloud, with the images showing prestellar cores in the densest filaments [Peretto *et al.*, 2012]. Such filaments are striking features in numerical simulations of the diffuse ISM and molecular clouds (*e.g.* [Heitsch *et al.*, 2005; Nakamura *et al.*, 2008; Gong et Ostriker, 2011; Hennebelle, 2013]). They are present in both hydrodynamic and magnetohydrodynamic (MHD) simulations, but they are more conspicuous in the latter. These studies relate the filamentary appearance of the ISM to compression and shear driven by turbulence, and the anisotropic infall of gravitationally unstable structures. [Soler *et al.*, 2013] find that, statistically, the orientation changes from parallel to perpendicular for gravitationally bound structures in simulations where the magnetic field is dynamically important.

The study of magnetic field orientation within the molecular clouds is possible through the observation of polarised thermal emission from dust. Far-infrared and sub-millimetre polarimetric observations have been limited to small regions up to hundreds of square arcminutes within clouds [Matthews *et al.*, 2014], or to large sections of the Galactic plane at a resolution of several degrees [Bierman *et al.*, 2011]. *NIKA2*, with its polarised channel at 260 GHz, can probe the critical scales $\sim$ 0.01 - 0.05 pc in the nearest clouds, at which magnetic field lines channel the matter of interstellar filaments into growing dense cores. The scope of this thesis has been the characterisation of the polarisation system for *NIKA2* taking advantage of its prototype *NIKA*.

2

Polarisation of the light

Contents

2.1 Formalism of the polarised light **34**

2.2 Jones formalism **34**

2.2.1 Ideal polariser 35

2.2.2 Ideal Half Wave Plate 36

2.3 Stokes formalism **37**

2.3.1 Polarimetry: basics and conventions 39

2.4 Mueller formalism **40**

2.4.1 Mueller matrix of a polariser 41

2.4.2 HWP Mueller matrix 41

2.5 Conclusions **42**

The polarisation of light is due to the orientation of the electrical field vector. The more common description of incoherent or partially polarised radiation is given by the Stokes formalism. A matrix method to manipulate Stokes vectors is provided by Mueller calculus. In this technique, the effect of a particular optical element is represented by a Mueller matrix, a 4×4 matrix that is an overlapping generalisation of the *Jones* matrix. In this chapter I will introduce the formalism of the polarised light and how to represent it using the *Jones* and Mueller matrix. In the context of the *NIKA* experiment, the optical elements, which modulate the incoming polarised light and allow to separate it from the total intensity signal, are a Half Wave Plate (HWP hereafter) and a polariser as described in Sec. 3.4.5.

2.1 Formalism of the polarised light

Since an electromagnetic wave is a three dimensional object, it can be described by the superposition of its two orthogonal components orientated in a plane perpendicular to the propagation direction. If we consider a Cartesian coordinate system (x, y, z), where z is for convenience the light propagation axis, the oscillation of the electromagnetic field has to satisfy the $D'Alembert$ equation:

$$\nabla^2 E(r,t) = \frac{1}{c^2}\frac{\partial^2 E(r,t)}{\partial t}. \tag{2.1}$$

Solving Eq. 2.1 considering the isofrequency solutions yields:

$$\begin{aligned} E_x(z,t) &= A_x(t)\cos(\omega t + \phi_x), \\ E_y(z,t) &= A_y(t)\sin(\omega t + \phi_y). \end{aligned} \tag{2.2}$$

We can derive the locus described by the resultant vector as:

$$\frac{E_x^2}{A_x^2} + \frac{E_y^2}{A_y^2} - 2\frac{E_x}{A_x}\frac{E_y}{A_y}\cos\phi = \sin\phi^2, \tag{2.3}$$

where $\phi = \phi_x - \phi_y$. Eq 2.3 is defined as the *polarisation ellipse* and it represents, in a general form, any polarisation states of light. Depending on particular values of ϕ or/and E_{0xy} the polarisation ellipse falls into particular forms.

- **Linear Polarisation** x direction if $A_x \neq 0$, $A_y = 0$ and y direction if $A_x = 0$, $A_y \neq 0$;
- **Linear Polarisation** (45 degrees): if $\phi = 0$ or $\phi = \pi$ and $A_x = A_y = E_0$;
- **Cicular Polarisation** (clockwise or anticlockwise): if $\phi = \frac{\pi}{2}, \frac{3}{2}\pi$ and $A_x = A_y = E_0$.

In general, the polarisation state can be changed by modifying the orthogonal amplitudes A_x, A_y and the phase ϕ. Only two polarising elements are needed to change the three parameters of the polarisation state. The amplitude can be changed using a polarised element, also called polariser. Wave plates introduce a predetermined phase difference between the two perpendicular polarisation components changing the polarisation state of an incident wave.

2.2 Jones formalism

It is possible to describe polarised light by a *Jones* vector, and linear optical elements by *Jones* matrices. When light crosses an optical element the resulting polarisation of the

emerging light is found by taking the product of the *Jones* matrix of the optical element and the *Jones* vector of the incident light as follows:

$$\begin{pmatrix} E_a(t) \\ E_b(t) \end{pmatrix} = \begin{pmatrix} J_{00} & J_{01} \\ J_{11} & J_{12} \end{pmatrix} \begin{pmatrix} E_x(t) \\ E_y(t) \end{pmatrix}. \tag{2.4}$$

For many applications, it is interesting to deal with rotated active optical elements. Indeed, the rotation by an angle α as illustrated on Fig. 2.1 of an element induces a variation of the polarisation status. Consequently changing the Cartesian coordinates system we obtain:

$$\begin{aligned} E_a &= E_x \cos\alpha + E_y \sin\alpha, \\ E_b &= -E_x \sin\alpha + E_y \cos\alpha. \end{aligned} \tag{2.5}$$

The *Jones* matrix of a rotated system will be:

$$R_\alpha = \begin{pmatrix} \cos\alpha & \sin\alpha \\ -\sin\alpha & \cos\alpha \end{pmatrix}. \tag{2.6}$$

Finally, in order to efficiently estimate the outgoing polarisation, it is necessary to transform the coordinate system forward to the initial reference frame. From the above equations we obtain the signal S:

$$S = R_\alpha^T \times \ M_{el} \times R_\alpha, \tag{2.7}$$

where M_{el} represents the generic optical element.

2.2.1 Ideal polariser

A linear polariser (also called analyser) consists of a regular array of fine parallel lithographic or metallic wires, placed in front of an incident beam. In the ideal generalisation the electromagnetic wave which has a component of the electric field aligned parallel to the wires is fully reflected backwards along the incident beam. On the other hand, the perpendicular component is fully transmitted. The *Jones* matrix describing a linear polariser is represented by:

$$J_{pol} = \begin{pmatrix} p_x & 0 \\ 0 & p_y \end{pmatrix}. \tag{2.8}$$

The real values $0 \leq p_x \leq 1$ and $0 \leq p_y \leq 1$ are transmission factors for the x and y components of the electric field $E_x^{'} = p_x E_x$, $E_y^{'} = p_y E_y$.

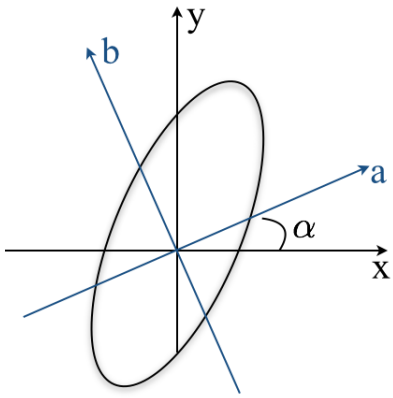

Figure 2.1: *Stokes parameters change with respect to a change of reference frame.*

2.2.2 Ideal Half Wave Plate

By far the most commonly used wave plate is the Half Wave Plate (HWP). Let's assume a monochromatic light of wavelength $\lambda = 2\pi c/\omega$ and the electric field components defined by the Eq. 2.2. Let's consider only one component for now, *e.g.* $A_x e^{i\omega t}$. The optical refraction index of the plate is defined as $n = c/v$ where c is the light speed in vacuum and v the light speed in the material. While passing through a plate of optical index n and of thickness d, the field is therefore shifted by $\omega t = \omega d/v = 2\pi n d/\lambda$. For a birefringent crystal, like a single sapphire plate, two orthogonal directions define the "ordinary axis" and the "extraordinary axis" which have different optical indices n_o and n_e. An incident electric field has components along both directions. Thus, while passing through the plate, they are shifted differently, this induces a rotation of the polarisation. The phase shift induced by the plate depends on both optical indices and plate's thickness. The refraction indices vary with the angle of incident ray with respect to the plate (See Fig. 2.2) so that:

$$\begin{aligned} n_o(\theta) &= n_o, \\ n_e(\theta) &= \frac{1}{\sqrt{\frac{1}{n_e^2}\cos^2\theta + \frac{1}{n_o^2}\sin^2\theta}}. \end{aligned} \tag{2.9}$$

Where θ is the angle between the ellipse axis and the incident ray. The effective thickness of the plate as seen by an incoming ray at different incident angles is different as well. The length can be computed from refraction equations $n_{air}\sin\theta = n\sin\theta_1$. We will not detail this relation because the relevant factor is $d(n_e(\theta) - n_o)$. Let's assume that x is the ordinary axis and y the extraordinary axis, then, after going through the plate, the electric field reads:

$$\overrightarrow{E}_{out} = e^{i\omega t}\begin{pmatrix} E_x e^{i2\pi d n_o/\lambda} \\ E_y e^{i2\pi d n_e/\lambda} \end{pmatrix}. \tag{2.10}$$

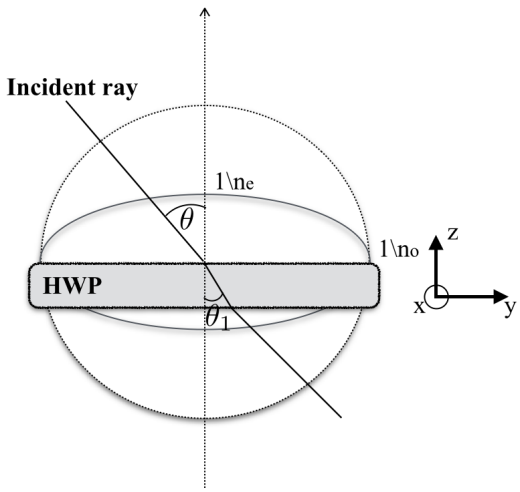

Figure 2.2: *The HWP and the optical index surfaces are represented in the lab reference frame. The ordinary index n_o (dash circle) is constant, the extraordinary index n_e must be read from the solid ellipse for an incident ray at angle θ.*

The plate can therefore be described by the following *Jones* matrix:

$$J = e^{i2\pi d n_o/\lambda} \begin{pmatrix} 1 & 0 \\ 0 & e^{i2\pi d(n_e - n_o)/\lambda} \end{pmatrix} \equiv J = e^{i2\pi d n_o/\lambda} \begin{pmatrix} 1 & 0 \\ 0 & e^{i\phi} \end{pmatrix}. \tag{2.11}$$

The pre-factor is common to both components and has therefore no observable effect on polarisation. It will be discarded in the following. A perfect HWP has $\phi = \pi$.

2.3 Stokes formalism

The Stokes formalism is a measurable representation of the electromagnetic field by using time averages of $\langle |E_x(t)| \rangle$ and $\langle |E_y(t)| \rangle$. Starting from Eq. 2.3 we can obtain four Stokes parameters S_0, S_1, S_2, S_3 also called I, Q, U, V, by averaging over a period of electromagnetic oscillation:

$$\begin{aligned} S_0 &= I = \langle |A_x|^2 \rangle + \langle |A_y|^2 \rangle \\ S_1 &= Q = \langle |A_x|^2 \rangle - \langle |A_y|^2 \rangle \\ S_2 &= U = 2\langle |A_x| \rangle \langle |A_y| \rangle \cos\phi \\ S_3 &= V = 2\langle |A_x| \rangle \langle |A_y| \rangle \sin\phi \end{aligned} \tag{2.12}$$

where the $\langle \cdot \rangle$ indicates that each component is time-averaged assuming that the radiation is in steady state at the time scale of averaging. The fully polarised electromagnetic wave at a given time and wavelength is fully described by the horizontal and vertical amplitudes A_x and A_y, and the phase difference ϕ between orthogonal components of the electric fields. In addition to these three parameters, we need an extra parameter p to

describe the degree of polarisation defined as the ratio between the polarised intensity over the total intensity of a given beam of light. As a result, four free parameters can fully describe the light polarisation. By introducing two geometrical parameters, the orientation of polarisation ψ and the ellipticity χ, the above equation can be written in terms of intensity as:

$$\begin{bmatrix} I \\ Q \\ U \\ V \end{bmatrix} = \begin{bmatrix} I_{\mathrm{p}} \\ I_{\mathrm{p}} \cos(2\psi)\cos(2\chi) \\ I_{\mathrm{p}} \sin(2\psi)\cos(2\chi) \\ I_{\mathrm{p}} \sin(2\chi) \end{bmatrix} + \begin{bmatrix} I_{\mathrm{u}} \\ 0 \\ 0 \\ 0 \end{bmatrix}, \tag{2.13}$$

where I_{u} and I_{p} are the unpolarised and polarised intensity, respectively. Alternatively,

$$\begin{bmatrix} I \\ Q \\ U \\ V \end{bmatrix} = I \begin{bmatrix} 1 \\ p\cos(2\psi)\cos(2\chi) \\ p\sin(2\psi)\cos(2\chi) \\ p\sin(2\chi) \end{bmatrix}, \tag{2.14}$$

with

$$p \equiv \frac{\sqrt{Q^2 + U^2 + V^2}}{I} = \frac{I_{\mathrm{p}}}{I_{\mathrm{p}} + I_{\mathrm{u}}}. \tag{2.15}$$

In these equations,

- I represents the total intensity;
- Q is the amount of horizontal and vertical linear polarisation;
- U represents the linear polarisation at 45° with respect to the original reference frame;
- V represents the clockwise and anti clockwise circular polarisation.

The degree of polarisation $p = 1$ corresponds to the case of fully polarised light and $p = 0$ corresponds to an unpolarised light. Therefore:

$$0 \leq p \leq 1. \tag{2.16}$$

This translates a relation between the Stokes parameters:

$$I^2 \geq Q^2 + U^2 + V^2, \tag{2.17}$$

where the equality indicates the completely polarised state of the light and the sign $>$ corresponds to partially polarised light. The angle ψ is the polarisation angle in a given coordinate system, defined as:

$$\psi \equiv \frac{1}{2}\arctan(\frac{U}{Q}), \tag{2.18}$$

and the angle χ is the ellipticity, defined as:

$$\chi \equiv \arctan(\frac{A_y}{A_x}) = \frac{1}{2}\arcsin(\frac{V}{I_p}), \tag{2.19}$$

where $0 \leq \psi \leq \pi$ and $-\frac{\pi}{4} \leq \chi \leq \frac{\pi}{4}$. Non-zero χ indicates that the light is elliptically polarised. For the *NIKA* astrophysical aims we are interested only on linear polarisation, and hereafter, we therefore account only for the first 3 Stokes parameters I, Q and U.

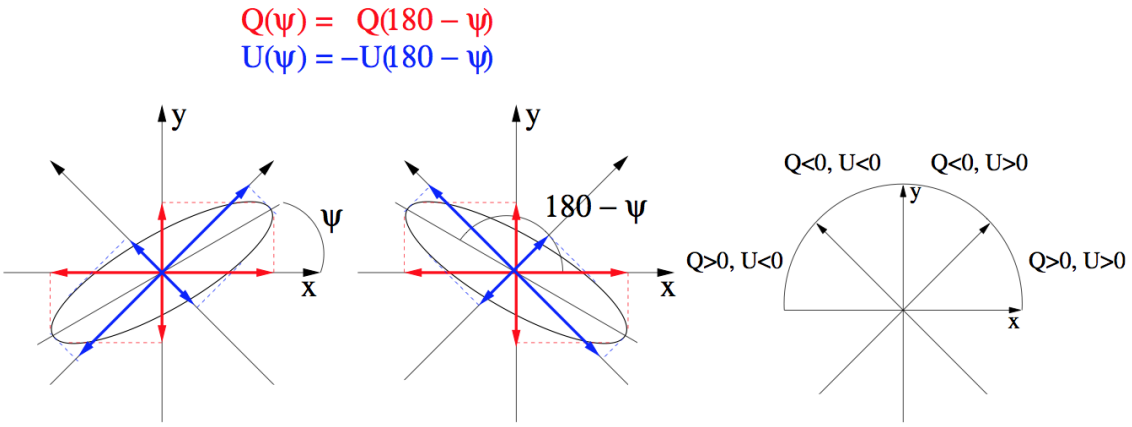

Figure 2.3: *Left, centre: projection of the polarisation ellipse on the x and y axes. The Stokes Q parameter is identical in two panels. Right: overview of the Q and U sign respect to the position of the polarisation ellipse, represented by Eq. 2.3, on the x, y plane.*

2.3.1 Polarimetry: basics and conventions

Let's see how the Stokes parameters transform if we change the reference frame. From Eq. 2.12 we can re-define I, Q, U in a more intuitively form as:

$$\begin{aligned} I &= I_x + I_y, \\ Q &= I_x - I_y, \\ U &= I_x^{45} - I_y^{45}, \end{aligned} \tag{2.20}$$

where $I_x = \langle |A_x|^2 \rangle$ and $I_y = \langle |A_y|^2 \rangle$; the exponent 45 indicates a basis oriented at 45° with respect of the x axis. The U parameter is measured from the electric field components of the wave in the two orthogonal axes oriented at 45° with respect to the original reference frame:

$$\begin{aligned} U &= I_x^{45} - I_y^{45} = \langle |\frac{1}{\sqrt{2}}(E_x + E_y)^2| \rangle - \langle |\frac{1}{\sqrt{2}}(-E_x + E_y)^2| \rangle \\ &= \frac{1}{2}|A_x + A_y e^{i\phi}|^2 - \frac{1}{2}|-A_x + A_y e^{i\phi}|^2 \\ &= \frac{1}{2}|A_x + A_y \cos\phi + iA_y \sin\phi|^2 + \qquad (2.21) \\ &- \frac{1}{2}|-A_x + A_y \cos\phi + iA_y \sin\phi|^2. \qquad (2.22) \end{aligned}$$

Doing calculations we finally obtain:

$$U = 2A_x A_y \cos\phi. \tag{2.23}$$

Let's suppose a change of reference frame as described by Eq 2.5, the Stokes parameter Q in the reference frame results in[1]:

$$\begin{aligned} Q_{ab} &= \langle |E_a|^2 \rangle - \langle |E_b|^2 \rangle \\ &= |\cos\alpha A_x + \sin\alpha A_y e^{i\phi}|^2 - |-\sin\alpha A_x + \cos\alpha A_y e^{i\phi}|^2 \\ &= (A_x^2 - A_y^2)\,\cos 2\alpha + 2A_x A_y \cos\phi\,\sin 2\alpha \\ &= Q_{xy}\,\cos 2\alpha + U_{xy}\,\sin 2\alpha. \end{aligned}$$

Similarly for U_{ab} we can write by replacing α with $\alpha + \pi/4$:

$$U_{ab} = -Q_{xy}\,\sin 2\alpha + U_{xy}\,\cos 2\alpha.$$

Thus, we have:

$$\begin{pmatrix} I \\ Q \\ U \end{pmatrix}_{ab} = \begin{pmatrix} 1 & 0 & 0 \\ 0 & \cos 2\alpha & \sin 2\alpha \\ 0 & -\sin 2\alpha & \cos 2\alpha \end{pmatrix} \begin{pmatrix} I \\ Q \\ U \end{pmatrix}_{xy} \tag{2.24}$$

$$= \mathcal{R}_\alpha \begin{pmatrix} I \\ Q \\ U \end{pmatrix}_{xy}. \tag{2.25}$$

2.4 Mueller formalism

The Stokes formalism describes polarisation and intensity with a 4-vector. Operator acting on this vector, and describing for instance optical systems, are 4 x 4 matrices, called the Muller matrices. It is common to use the Mueller formalism to describe the Stokes parameters components and the *Jones* formalism for describing the electric field components. We discuss here the basic conventions to easily link the two formalisms. Let's define the Pauli matrices as:

$$\sigma_0 \equiv \begin{pmatrix} 1 & 0 \\ 0 & 1 \end{pmatrix} \quad \sigma_1 \equiv \begin{pmatrix} 1 & 0 \\ 0 & -1 \end{pmatrix} \quad \sigma_2 \equiv \begin{pmatrix} 0 & 1 \\ 1 & 0 \end{pmatrix} \quad \sigma_3 \equiv \begin{pmatrix} 0 & -i \\ i & 0 \end{pmatrix} \tag{2.26}$$

Using these matrices we define the Muller matrix M of an optical system from its Jones matrix J:

$$\begin{aligned} M_{kl} &= \frac{1}{2} Tr\left(\sigma_k J \sigma_l J^\dagger\right) \\ &= \frac{1}{2}\begin{pmatrix} |J_{00}|^2 + |J_{01}|^2 + |J_{10}|^2 + |J_{11}|^2 & |J_{00}|^2 - |J_{01}|^2 + |J_{10}|^2 - |J_{11}|^2 & 2Re(J_{00}J_{01} + J_{10}J_{11}) \\ |J_{00}|^2 + |J_{01}|^2 - |J_{10}|^2 - |J_{11}|^2 & |J_{00}|^2 - |J_{01}|^2 - |J_{10}|^2 + |J_{11}|^2 & 2Re(J_{00}J_{01} - J_{10}J_{11}) \\ 2Re(J_{00}J_{10} + J_{01}J_{11}) & 2Re(J_{00}J_{10} - J_{01}J_{11}) & 2Re(J_{00}J_{11} + J_{01}J_{10}) \end{pmatrix} \end{aligned} \tag{2.27}$$

$J_{00}, J_{01} \cdots$ are components of the *Jones* matrix (see Eq. 2.4) and † indicates the transpose and conjugate. Here the Mueller matrix is a 3 x 3 matrix (instead of 4 x 4) because we do not consider circular polarisation.

[1]The factor $e^{-i\omega t}$ is omitted to avoid too much complexity in the notation

2.4.1 Mueller matrix of a polariser

Using Eq. 2.28 an 2.8 for a polariser reads:

$$M_{pol} = \begin{pmatrix} p_x^2 + p_y^2 & p_x^2 - p_y^2 & 0 \\ p_x^2 - p_y^2 & p_x^2 + p_y^2 & 0 \\ 0 & 0 & 2p_x p_y \end{pmatrix} \tag{2.28}$$

Since we are free to choose the x reference axis, we will take it as the transmission direction of the polariser. Hence Eq. 2.28, transmitting only a polarisation, is reduced to:

$$M_{pol} = \frac{1}{2} \begin{pmatrix} 1 & 1 & 0 \\ 1 & 1 & 0 \\ 0 & 0 & 0 \end{pmatrix}. \tag{2.29}$$

2.4.2 HWP Mueller matrix

When the optical element that changes the polarisation state is a HWP, after passing it the linearly polarised light having an incident angle θ with respect to the HWP optical axis ("ordinary" see Fig. 2.4), will be rotated by an angle 2θ. A realistic representation of a HWP is given by [Savini *et al.*, 2006]:

$$\begin{aligned} M_{HWP} &= \frac{1}{2} \begin{pmatrix} \alpha^2 + \beta^2 & (\alpha^2 - \beta^2)\cos 2\theta & (\alpha^2 - \beta^2)\sin 2\theta \\ (\alpha^2 - \beta^2)\cos 2\theta & (\alpha^2 + \beta^2)\cos^2 2\theta + 2\alpha\beta \sin^2 2\theta \cos\phi & (\alpha^2 + \beta^2 - 2\alpha\beta\cos\phi)\cos 2\theta \sin 2\theta \\ (\alpha^2 - \beta^2)\sin 2\theta & (\alpha^2 + \beta^2 - 2\alpha\beta\cos\phi)\cos 2\theta \sin 2\theta & (\alpha^2 + \beta^2)\sin^2 2\theta + 2\alpha\beta\cos^2 2\theta \cos\phi \end{pmatrix} \\ &= \frac{1}{2} \begin{pmatrix} \alpha^2 + \beta^2 & (\alpha^2 - \beta^2)\cos 2\theta & (\alpha^2 - \beta^2)\sin 2\theta \\ (\alpha^2 - \beta^2)\cos 2\theta & A & B \\ (\alpha^2 - \beta^2)\sin 2\theta & B & D \end{pmatrix}, \end{aligned} \tag{2.30}$$

where α and β are the transmission coefficients along the ordinary and extraordinary axis respectively. In the ideal case, where the transmission along the ordinary and extraordinary axis of the HWP is perfect and equals to 1 and the angle phase shift is π, we can write:

$$M_{HWP} = \begin{pmatrix} 1 & 0 & 0 \\ 0 & \cos^2 2\theta - \sin^2 2\theta & \cos 2\theta \sin 2\theta \\ 0 & 2\cos 2\theta \sin 2\theta & \sin^2 2\theta - \cos^2 2\theta \end{pmatrix}. \tag{2.31}$$

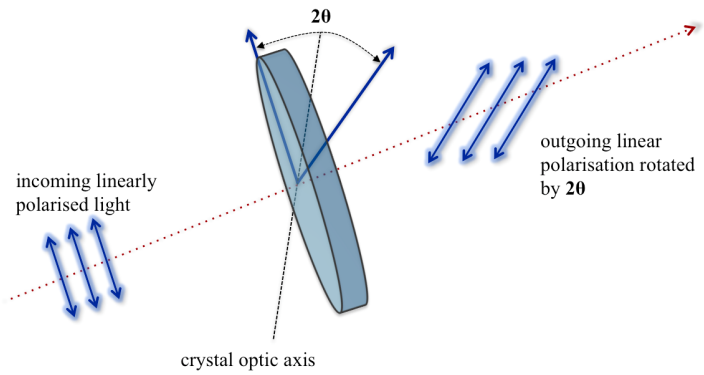

Figure 2.4: *Plane-polarised wave normally incident on a half wave plate with an angle θ with respect to the optical systems axis. The outgoing polarised light will be rotated by 2θ.*

2.5 Conclusions

This chapter presented the formalism adopted to describe the polarisation of light. The Stokes formalism is commonly adopted to represent the polarisation as a 4-vector. Operators acting on this vector, and describing optics, are 4×4 matrices, called Mueller matrices. For *NIKA* we neglect Stokes circular polarisation parameter V obtaining 3×3 matrices. In order to measure each component of the linear polarisation we can use optical elements that modify the amplitude and the phase of a polarisation state. For *NIKA* and *NIKA2* it has been chosen a polarisation system consisting of a continuously rotating HWP and a polariser. This permits to have a quasi-simultaneous measurement of the three Stokes parameters I, Q, U. Next chapter will present first the instruments *NIKA* and *NIKA2* and then the outgoing signal from the *NIKA* polarised system derived using the formalism described here. Further, Chap. 4 will discuss the characterisation of this system in terms of its transmission efficiency.

Part II

NIKA and NIKA 2 instruments

3

The *NIKA* and *NIKA2* instruments

Contents

3.1 The telescope **46**

3.2 Cryogenic detectors **47**

3.2.1 Context 47

3.2.2 Fundamentals of superconductivity 48

3.3 Kinetic Inductance Detectors: KIDs **49**

3.3.1 Kinetic inductance and optical power 49

3.3.2 Detector response 50

3.3.3 Natural frequency multiplexing 50

3.4 *NIKA* & *NIKA2* general description **52**

3.4.1 *NIKA* detectors: Lumped Element KIDs 53

3.4.2 Readout electronics 55

3.4.3 Cryostat 56

3.4.4 Optics 56

3.4.5 *NIKA* and *NIKA2* polarisation setup 58

3.4.6 The output polarised signal 58

3.5 Scientific goals of *NIKA2* **60**

In the last years, millimetre wave astronomy has opened new opportunities to study the evolution of stars, galaxies, and the Universe. Indeed, the composition of the interstellar medium, the earliest stages of star formation, the internal kinematics of the galaxies are uniquely revealed at millimetre wavelengths. At these wavelengths, the atmosphere is overall very opaque but with some atmospheric windows, so that most of the experiments in this region of the spectrum have to be carried out on satellites. Given the high cost of space missions, ground-based telescopes located in high and dry places represent

an excellent alternative. The IRAM 30 m telescope is located in Pico Veleta in the Sierra Nevada, in Spain, at an altitude of 2850 m. This location is ideal to deploy the atmospheric windows centred at 2.05 mm and 1.15 mm. Furthermore, with a 30 m main dish, the telescope is one of the largest facilities in the world for these wavelengths.

In order to explore the universe at high resolution and high sensitivity, large detector arrays are required. Since the current detectors are photon noise limited, the only way to increase the sensitivity of an instrument is to scale up the number of detectors n_{det}. By increasing n_{det}, we improve the mapping speed and, as a consequence, the signal-to-noise ratio (S/N) in the final map for an equivalent integration time and sky area. In this context, the *NIKA* project proposes a recent developed detector technology: the Kinetic Inductance Detectors (KIDs) proposed by [Day *et al.*, 2003]. Their natural multiplexing capability make them one of the best candidates for large size detector array development. The *NIKA* instrument as well as *NIKA2* is a dual-band imaging camera operating with KIDs and designed to cover the field of view of 6.5 arc-minutes of the IRAM 30 m telescope. In the first section of this chapter I will describe the main characteristics of the IRAM telescope. Then, I will describe the main characteristics of the *NIKA* instruments starting from their fundamental feature, the detectors.

3.1 The telescope

The IRAM telescope consists of a classic single dish parabolic antenna (M1) with a 30 meter diameter and a focal length of 10.5 meter (see picture on Fig. 3.1). The secondary hyperbolic mirror (M2) has a 2 meter diameter. The system is installed on a large alt-azimuth mounting. The incident beam is directed into the receiver cabin through a hole in M1 using a standard Cassegrain configuration. A rotating tertiary (M3) provides a fixed focal plane (Nasmyth focus). The optical axis, in order to conform to the dimensions of the cabin, is deviated by two flat mirrors (M4 and M5). M4 can rotate between two fixed positions, selecting either heterodyne or continuum instruments. The angular response of the telescope, the beam, is crucial in the exploration of cosmic objects such as nearby galaxies and interstellar clouds. The telescope resolution can be limited mainly by image diffraction. In general the angular resolution of an optical system can be estimated, from the diameter of the aperture and the wavelength of the light, by the *Rayleigh* criteria. Accordingly, two point sources are resolved when the principal diffraction maximum of one image coincides with the first minimum of the other. Considering the diffraction through a circular aperture, this translates into $\theta_0 = 1.22\frac{\lambda}{D}$, where D represents the diameter of the telescope and λ the considered wavelength. For *NIKA*, θ_0 corresponds to 17 arcsec at 150 GHz and 10 arcsec at 260 GHz. Deformations of the primary mirror can affect the beam and produce secondary lobes. These deformations can be accentuated by the wind or temperature variations. The IRAM telescope has a temperature control system to control such problems.

Furthermore, the angular resolution of an instrument depends not only on the main telescope mirrors but also on the optics of the instrument itself. The characterisation of the angular resolution of *NIKA* has been performed using observations of strong sources. A summary of main characteristics of *NIKA* is reported in Tab. 3.1.

Figure 3.1: *IRAM 30 meter telescope.*

3.2 Cryogenic detectors

3.2.1 Context

High resolution and sensitivity experiments demand the development of a new generation of arrays with large number of detectors. All the experiments working over the last decades at millimetre wavelengths have taken advantage of detectors working at cryogenic temperatures, typically 300 mK or less. The detector technology prevalently used has consisted of bolometers. In a bolometer, an incoming flux of radiation is absorbed by a thermistor that has a very strong dependance of the resistance with temperature. The low temperature allows the decrease of the thermal *Johnson Noise* $\propto \sqrt{4k_BTR\Delta f}$ of the bolometers and, for the most recent detectors, have become an even more fundamental requirement, since these rely on the phenomenon of superconductivity.

The latest generation of detectors takes full advantage of the peculiar properties of superconductors. Superconducting materials have a transition at a critical temperature T_c. If the thermal energy is low enough, electrons can bind via a phonon mediated interaction in boson-like particles called *Cooper pairs*, which have a perfectly ordered and non-dissipative motion. The binding energy plays a role analogous to the gap energy of semiconductors, but its value is typically of a few or a fraction of one meV, 1000 times lower than the band gap of semiconductors. Thus, using superconductors one can reach the direct detection limit even for millimetre radiation, or have bolometric sensors with a much higher responsivity. The most widespread kind of superconducting detectors are *Transition Edge Sensors* (TES) [C.Hunt, 2003]. TES sensors are bolometers that exploit the very fast change of resistivity between the normal and superconducting state of the material. Medium-sized arrays of TES sensors, with $\sim$ 1000 pixels, are feasible, but moving to larger arrays gets extremely complicated, both for technical and economical reasons.

3.2.2 Fundamentals of superconductivity

A theory that explains many properties of superconductors has been stated by *Bardeen*, *Cooper* and *Schrieffer*, who in 1957 showed that below a critical temperature T_c electrons can bind to form Cooper Pairs [Bardeen *et al.*, 1957]. In a superconductor, the surface impedance $Z_s = R_s + j\omega L_s$ is determined by the resistive contribution, R_s, of the quasiparticles and the inductive contribution of Cooper pairs, L_s[1]. The latter that can store energy of both magnetic and kinetic origin. The Z_s values vary if the quasiparticles density n_{qp} increases, because the Pauli exclusion principle prevents the Cooper pairs from occupying previously available energy states. In order to measure this variation of n_{qp}, the superconducting sensor is used as the inductance of a high Q (merit factor) resonator. The pairs are held together by an electron phonon interaction with binding energy equals to $2\Delta \simeq 3.52\ k_B T_c$, where k_B is the Boltzmann constant, Δ and T_c are the energy gap and the critical temperature of the superconductor, respectively. An intuitive explanation of this is that an electron moving through the ion lattice distorts slightly the lattice itself. As a consequence, after its passage there is a slight excess of positive charge that tends to attract another electron, which is therefore bound to the first one as shown in Fig. 3.2. The number of quasiparticles is given by the empirical formula which describes its variation with temperature [Gorter et Casimir, 1957]:

$$\frac{n - n_{qp}}{n} = 1 - \left(\frac{T}{T_c}\right)^4, \tag{3.1}$$

where n is the total density of carrier charge. Therefore, photons with energy greater than the energy gap 2Δ break Cooper pairs that causes an excess of quasiparticle density as schematically illustrated on the right panel of Fig. 3.2.

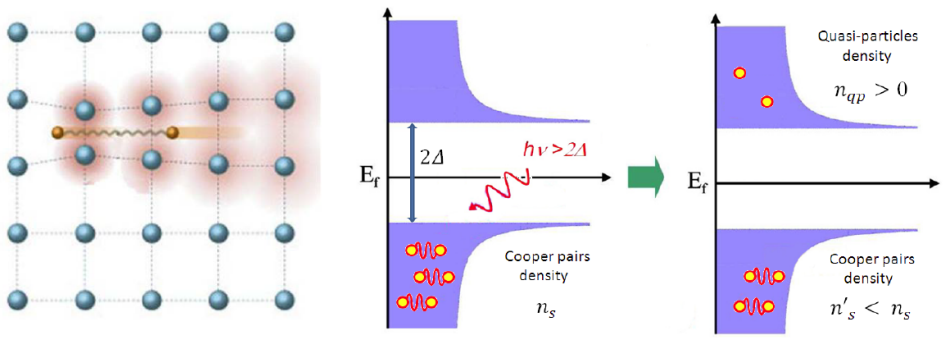

Figure 3.2: **Left**: *Representation of the interaction between two electrons bound in a Cooper Pair. The blue spheres represent the ions of the lattice, the orange ones the electrons.* **Right**: *When a photon of appropriate frequency ($h\nu > 2\Delta$) is absorbed, it breaks Cooper Pairs (Cps), which become quasiparticles (QPs). The total CPs and QPs densities are therefore altered. Credits:[Calvo, 2008].*

[1] $L_s = L_k + L_m$ where L_k and L_m are respectively the kinetic and magnetic component of the internal inductance. For thin films, $L_k >> L_m$, so it is practice to speak in terms of kinetic inductance only.

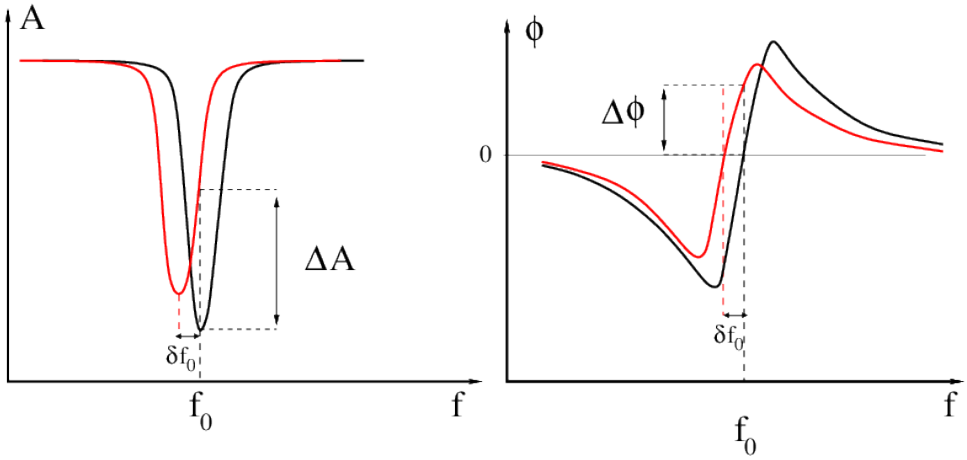

Figure 3.3: *Schematic representation of a KID resonance in terms of its amplitude (left) and phase (right), function of the excited tone injected in the feedline. The absorption of a photon with enough energy shifts the resonance frequency and this is directly proportional to the power received.*

3.3 Kinetic Inductance Detectors: KIDs

Kinetic inductance detectors (KIDs) are RLC superconducting resonators usually fabricated from thin metal films that change their electromagnetic properties in response to incoming radiation. When photons of sufficient energy[2] are absorbed by the superconducting film, the ratio of paired (*Cooper pair*) and unpaired (*quasi-particles*) charge carriers changes. This modifies the surface impedance of the superconducting strip that can be parametrised by a complex conductance with an inductive and a resistive component. In particular, the breaking of *Cooper pairs* increases the *quasi-particles* density, which causes a change in the kinetic inductance L_k. This produces a shift of the resonant frequency of the KID. The operating principle is schematically represented in Fig. 3.3.

3.3.1 Kinetic inductance and optical power

Resonant circuits are used to respond selectively to signals of a given frequency while discriminating against signals of different frequencies. If the response of the circuit is more narrowly peaked around the chosen frequency, we say that the circuit has higher "selectivity". A "quality factor" Q is a measure of that selectivity, and we speak of a circuit having a "high Q" if it is more narrowly selective. As discussed before the surface impedance of the superconductor excited by an electromagnetic field of angular frequency ω is represented as $Z_s = R_s + j\omega L_k$. The kinetic inductance, L_k is proportional to Cooper pair density [D'Addabbo, 2014] such as:

$$\delta L_k \propto -\delta\left(n - n_{qp}\right) \propto \delta n_{qp}. \tag{3.2}$$

The quasiparticle lifetime, τ_{qp}, is a measure of the average time that a quasiparticle takes before the recombination with another quasiparticle emitting energy under the form of phonons. Its value plays a key role especially in the case of a continuum flux of low energy

[2]Energy exceeding the superconducting cut-off.

photons, where the signal to be measured is due to the average excess of quasiparticles that the incoming power causes, which is proportional to τ_{qp}. Thus:

$$\delta n_{qp} \propto \delta P_{opt}. \tag{3.3}$$

Since a KID is a RLC resonator, it consists of a capacity C, an inductance L and a residual resistance R. The capacity depends on the material permittivity ϵ and the inductance accounts the magnetic (L_m) and kinetic (L_k) contribution. In the following we consider the approximation $L_k >> L_m$ which is valid for thin films of superconducting material. Thus the resonance frequency is given by:

$$f_0 = \frac{1}{2\pi\sqrt{L_k * C(\epsilon)}}. \tag{3.4}$$

If we differentiate Eq. 3.4 with respect to the kinetic inductance we obtain a linear equation between the variation of kinetic inductance L_k and the resonance frequency:

$$\delta f_0 = \delta L_k \frac{\partial f_0}{\partial L_k} = -\frac{1}{2} C(\epsilon) f_0^3 \delta L_k. \tag{3.5}$$

Combining Eqs. 3.2, 3.3 and 3.5 we obtain a linear correlation between the flux energy of the source absorbed by the detector and the optical power related to the change of the resonance frequency,

$$\delta f_0 \propto -\delta P_{opt}. \tag{3.6}$$

3.3.2 Detector response

In order to read a KID circuit we need to couple it with a transmission feedline as shown on Fig. 3.4. Usually, the transmission is expressed through the S_{21} parameter, which is the quantity measured by a circuit vector analyser and represents the transfer function of the signal measured:

$$S_{21}(f) = \mathcal{I} + j\mathcal{Q}, \tag{3.7}$$

where $\mathcal{I}$ and $\mathcal{Q}$ give the real (*in-phase*) and imaginary (*quadrature*) part, respectively, of the ratio between the input and output signal of the feedline transmission. Fig. 3.3 represents the amplitude $A = \sqrt{\mathcal{I}^2 + \mathcal{Q}^2}$ and phase $\phi = \text{atan}\left(\frac{\mathcal{Q}}{\mathcal{I}}\right)$ of the transfer function of a KID. The absorption of the optical power produces a shift of the resonance frequency. The quality factor or Q factor is a dimensionless parameter that describes how under-damped a resonator is, and characterises the resonator's bandwidth relative to its central frequency. Higher Q indicates a lower rate of energy loss relative to the stored energy of the resonator. Fig. 3.5 shows the feedline transmission ($|S_{21}|$) as a function of the excitation frequency for 2.05 mm array of *NIKA*. Each resonance corresponds to a single detector, which shifts when the flux absorbed increases.

3.3.3 Natural frequency multiplexing

The main characteristic that makes the KIDs attractive for next generation of instruments is their natural multiplexability. KIDs are made of a lithographic aluminium on a silicon substrate. Each resonator coupled to the feedline will affect the bias signal only at

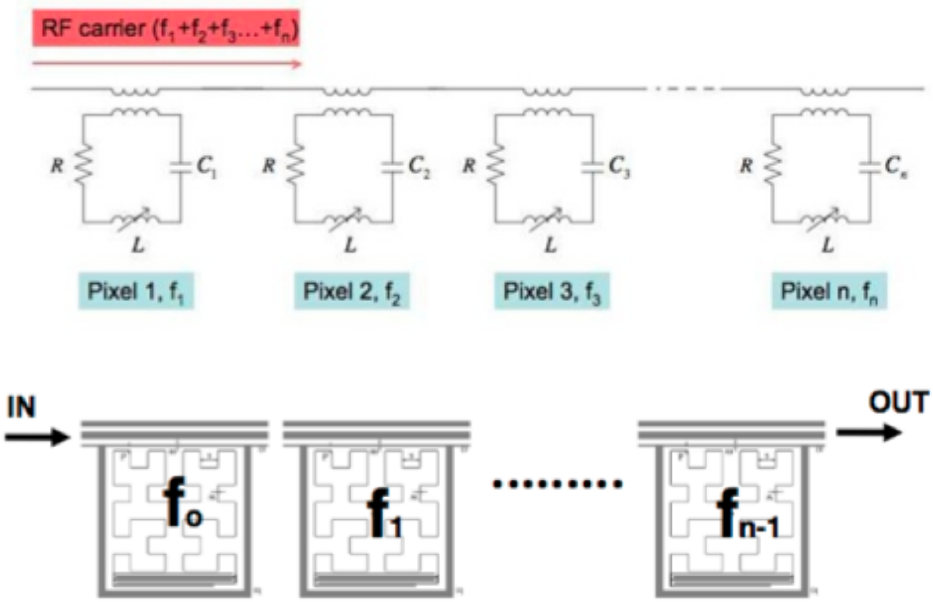

Figure 3.4: *Typical multiplexing configuration, with n pixels shunting the same line and a bias signal given by the superposition of n frequencies, corresponding to the resonances of all the KIDs (Frequency Domain Multiplexing). The resonant RLC circuits are inductivly coupled with the feedline. Credits:[D'Addabbo, 2014].*

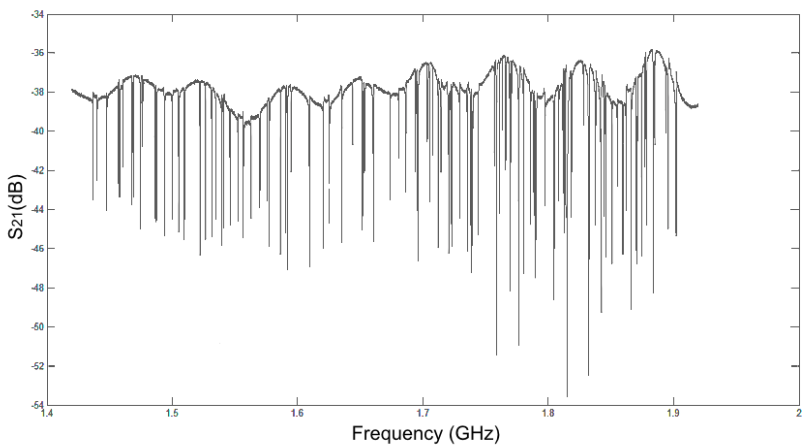

Figure 3.5: *Feedline transmission (S_{21}) frequency scan showing the resonances for a 2 mm NIKA array. 129 resonances identified out of 132 KIDs in the array. Credits: [Monfardini et al., 2014]*

frequencies very close to its resonant frequency f_0. On the contrary away from f_0, the signal will be transmitted without any distortion or loss. Thus, a large number, n_{det}, of resonators can be coupled to the same feedline, each one resonating at a different frequency f_0^i (See Fig. 3.4), see details in [Calvo, 2008].

3.4 *NIKA* & *NIKA2* general description

The New IRAM Kids Array (*NIKA*) camera has been the test-bench of *NIKA2*. The latter has been successfully installed at the IRAM telescope in October 2015. The *NIKA* instrument, as well as *NIKA2*, is based on KIDs array technology. The other main components of these camera are: a dilution cryostat, a readout electronics and a warm and cold optics. The cryostat permits to cool down the detector arrays at their optimal working temperature of ∼100 mK and the readout electronics allows to read all detectors simultaneously. These tools are discussed in detail in the next sections. A summary of the technical characteristics of *NIKA* and *NIKA2* is reported in Tab. 3.1. The main characteristics of an instrument operating at a telescope are defined by the circular Field of View (FOV), the angular resolution FWHM and the sensitivity. The FOV describes the angular extent of a given sky area imaged by a camera. The angular resolution is measured by reconstructing the main beam from the radial profile of bright point sources and the sensitivity of the instrument is defined by its capability to map faint sources.

NIKA has been operating at the telescope in the period 2012-2015. During this period, successive technical runs and three observational campaigns opened to astronomers have been performed. The quality of the *NIKA* observations has been demonstrated in mapping high redshift galaxies, quasars and star forming clouds [Catalano *et al.*, 2014]. Moreover, *NIKA* obtained scientific results via Sunyaev-Zel'dovich (SZ) effect observations of galaxy clusters [Adam *et al.*, 2014b; Adam *et al.*, 2014a; Adam *et al.*, 2015].

The *NIKA* polarimeter consisting of a Half Wave Plate (HWP) and a polariser placed in front of the *NIKA* cryostat window has been mounted at the telescope for the first time in January 2014, after the characterisation of its performance in laboratory. The laboratory characterisation of the polarimeter will be discussed in Sec. 4.

Table 3.1: *NIKA measured performance and NIKA2 technical characteristics and goals.*

	NIKA		*NIKA2*	
	150 GHz	260 GHz	150 GHz	260 GHz
Wavelenghts	2.05 mm	1.15 mm	2.05 mm	1.15 mm
Field of View (FoV)	1.8'	1.8'	6.5'	6.5'
Detectors number	128	196	1020	2 × 1140
Valids detectors	114	136	90% (goal)	90% (goal)
FWHM	17.5"	12"	16" (goal)	10" (goal)
Bandpass (GHz)	137–172	220–270	125-170	240-280
Sensitivity (mJy $\sqrt{s}$)	14	40	–	–

NEFD The noise equivalent flux density (NEFD) gives an estimation of the sensitivity of the instrument per frequency band. It is equivalent to the rms flux calculated on one

second of integration. It involves the time $t_{\rm ps}$, effectively spent on the source. It is defined by:

$$\mathrm{NEFD} = \Delta A_{\rm ps} \times \sqrt{t_{\rm ps}} \times \frac{d^2_{\rm array}}{S_{\rm pix}}, \tag{3.8}$$

where $A_{\rm ps}$ represent the amplitude measured by a 2D Gaussian fit on the source. $d^2_{\rm array}$ represents the average distance between the pixel of the same array and $S_{\rm pix}$ the pixel surface. For intensity observations, [Catalano *et al.*, 2014] reports values of NEFD estimated in good weather conditions on a point source map and equivalent to 40 and 14 mJys$^{1/2}$ at 1.15 and 2.05 mm, respectively.

3.4.1 *NIKA* detectors: Lumped Element KIDs

LEKID (Lumped Element Kinetic Inductance Detectors) [Doyle *et al.*, 2008] are a particular implementation of the more generic KID principle, based on planar superconducting resonators. In a LEKID, the inductive and capacitive parts of the resonator are separated by design. This feature allows the shaping of the inductor, in which the current distribution is at first order homogeneous, to directly absorb the incoming radiation. For *NIKA* a particular kind of LEKID has been adopted: the Hilbert LEKID. It consists of a LEKID, where the classical meander geometry of the inductor is replaced by a Hilbert-like fractal pattern of the 3rd order [Roesch *et al.*, 2012]. The Hilbert LEKID has an absorbing area uniformly filled. Fig. 3.6 shows the design of a classical device LEKID on left and of the Hilbert geometry design on the right. While the first is sensitive to one polarisation orientation of the light only, the second is sensitive to the two orientations, with no preferential direction in absorption. Fig. 3.7 shows the comparison between the two polarisations as the response of the KIDs in terms of the frequency shift. The figure shows the same behaviour in both polarisation orientations (horizontal and vertical). Keeping the same performances for each of the two polarisations, a factor 2 in quantum efficiency is achievable by using a dichroic instead of a wire grid analyser to split the beam. However, this property makes necessary the use of a polariser to select the orientation of the polarisation. In *NIKA* the polariser is placed at ambient temperature allowing the transmission of a single polarisation for both channels. In *NIKA2*, it has been conceived as part of the cold optics and placed within the 100 mK stage of the cryostat. It transmits one polarisation on a 1.15 mm array and reflects the other one on a second 1.15 mm array. This scheme permits to entirely recover the polarised light and consequently improves the sensitivity of the instrument in polarisation.

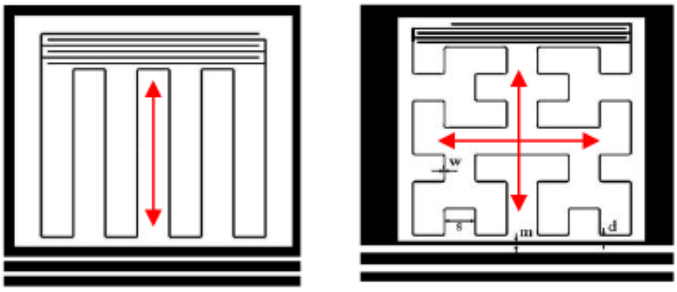

Figure 3.6: **Left**: *standard LEKID design, sensitive only to a single polarisation.* **Right**: *Hilbert LEKID design, sensitive to the two polarisations. Black: thin (e.g. 20 nm) Aluminium; white: Silicon substrate. The pixel size is about 2 mm. Credits: [Roesch et al., 2012].*

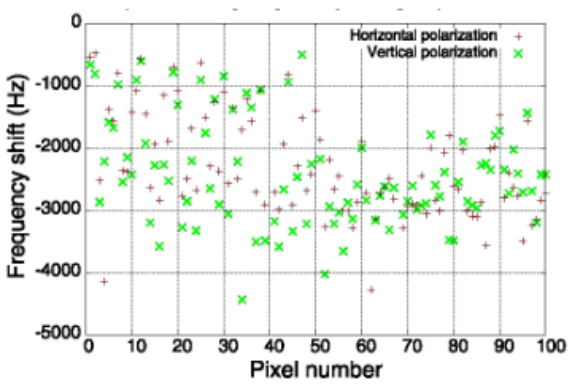

Figure 3.7: *Comparison of the two polarisation responses for an Hilbert LEKID array. For each pixel of the array the response in resonance frequency shift are plotted. The green and the red crosses correspond to the horizontal and vertical linear polarization, respectively.Credits: [D'Addabbo et al., 2013].*

For illustration purpose Fig. 3.8 shows the 132 pixel array for the 2.05 mm band of *NIKA* on left and a 1020 pixel array for the same millimetre band of *NIKA2*.

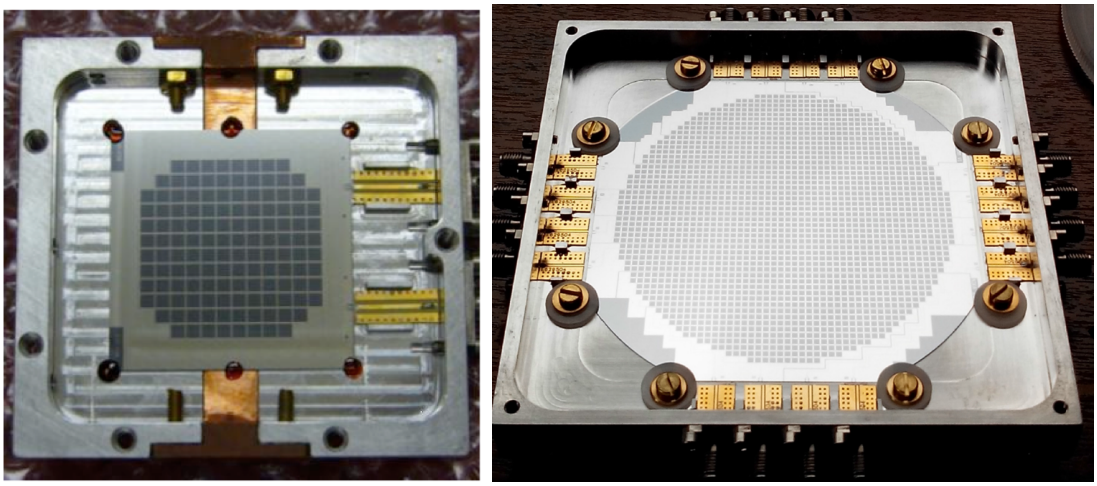

Figure 3.8: *132 pixel array of NIKA (left) and 1020 pixel array of NIKA2 (right). The pixel size is 2.3 mm in both arrays with a diameter of 12 pixels in the NIKA array and of 36 pixels in NIKA2 one.*

3.4.2 Readout electronics

The multiplexed readout of a KID is achieved by using a dedicated electronic board called NIKEL [Bourrion *et al.*, 2011; Bourrion *et al.*, 2012], specifically developed for *NIKA* and shown on Fig. 3.9. This board can excite and readout up to 400 pixels over a 500MHz bandwidth, and apply a Direct Down Conversion method on the acquired output signal to determine the variations of amplitude and phase of each tone. These tones are up and down converted by mixing them with a local oscillator carrier signal (LO) of frequency f_{LO}. The operating principle is schematically illustrated in Fig. 3.9. Briefly the excitation frequency of the detectors is the tool to compare the input and output signal in order to reconstruct the astrophysical signal.

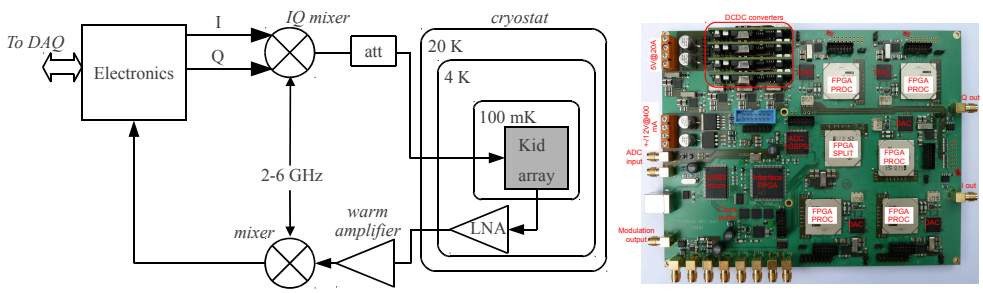

Figure 3.9: *Functioning scheme and picture of a NIKEL board. Credits: [Bourrion* et al.*, 2011; Bourrion* et al.*, 2012].*

In *NIKA2* a number of detectors comprised between 150 and 250 is multiplexed on the same pair of coaxial lines providing the excitation and the readout. The excitation line is made by stainless steel cables running from 300 K down to base temperature. They are properly isothermal at each cryostat stage and 20 NIKEL boards are needed in order to simultaneously read all the 3300 detectors. The complete electronics configuration has been installed at the telescope during the 3rd technical campaign of *NIKA2*.

Automated tuning procedure The standard way to read a pixel out is to excite it with a fixed tone at f_0 (reference frequency) and to monitor how the In-phase ($\mathcal{I}$) and in-Quadrature ($\mathcal{Q}$) components of the transmitted signal are modified by the changes in the resonance frequency of the KID, f_0. For *NIKA* and *NIKA2* we adopted a more complex strategy. Instead of using an excitation at a fixed frequency, we rapidly modulate between two different readout tones, f^+ and f^-, just above and just below f_0. The tones are separated by $df = f^+ - f^-$. This modulation technique allows to measure, for each acquired data sample, both the values of $\mathcal{I}$ and $\mathcal{Q}$ and the variation $d\mathcal{I}$, $d\mathcal{Q}$ that is dependent on a given frequency shift df. When the optical power on the detectors changes by an amount ΔP_{opt}, a variation $\Delta\mathcal{I}$, $\Delta\mathcal{Q}$ is observed between successive data samples. The $d\mathcal{I}$, $d\mathcal{Q}$ values can then be used as a calibration factor to associate to the observed $\Delta\mathcal{I}$, $\Delta\mathcal{Q}$ the corresponding change in the resonance frequency Δf_0, and thus to measure ΔP_{opt}. More details on the modulated readout technique can be found in [Calvo *et al.*, 2012] and [Catalano *et al.*, 2014]. The advantage of this solution is that the $d\mathcal{I}$, $d\mathcal{Q}$ values are evaluated for every data sample. If the load on the detectors changes (*e.g.* due to variations in the atmospheric opacity), the exact shape of the resonance feature of each pixel will change, but since the calibration factor $d\mathcal{I}$, $d\mathcal{Q}$ is updated in real time it will take this effect into account. The use of this technique strongly improve the photometry accuracy of the instrument (see [Catalano *et al.*, 2014] for details).

3.4.3 Cryostat

In order to ensure an optimal operation of the detectors and to optimally suppress the in-band stray-light, the focal plane arrays and the last portion of the optics, are cooled down to a base temperature of around 150 mK by a He^3–He^4 dilution fridge. Fig. 3.10 shows the *NIKA* cryostat with a mirror of the warm optic chain while Fig. 3.11 shows the scheme of the *NIKA2* cryostat. While in *NIKA* only a dichroic separated the incoming light into two channels at 150 (2.05 mm) GHz and 260 GHz (1.15 mm), in *NIKA2* two arrays in the 260 GHz channel collect the two components of the linear polarisation of the light. The polariser mounted between them transmits and reflects the vertical and horizontal polarisation. The 150 GHz channel in NIKA2 is not polarised.

3.4.4 Optics

Fig. 3.12 shows the coupling between warm optics of the telescope with the cold optics inside the cryostat. *NIKA* re-images the large telescope focal plane onto the sensitive area covered by the KIDs. This is accomplished using two flat mirrors (M6, M7), one bi-conical mirror (M8) and three high-density polyethylene (HDPE) corrugated lenses (L1, L2, L3). A dichroic separates the light in the two mm channels observing in two bands at 150 and 260 GHz. In *NIKA2* the optics is similar, but a polariser is added to measure both polarisation orientations, for the 260 GHz channel.

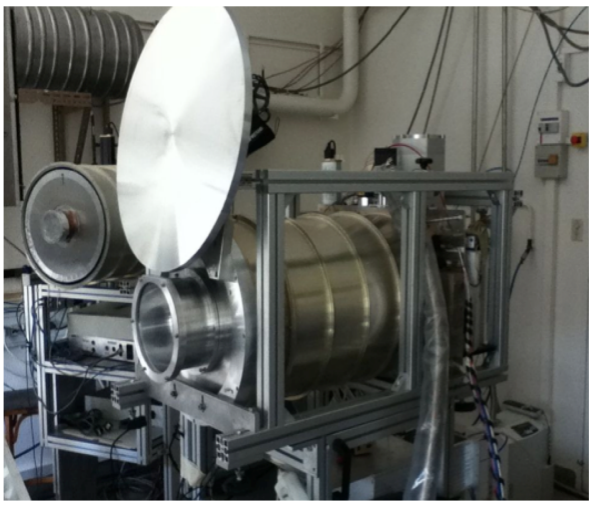

Figure 3.10: *NIKA cryostat at 30m telescope Nasmyth cabin. A cryogenic machine is used to achieve the 4 K stage.*

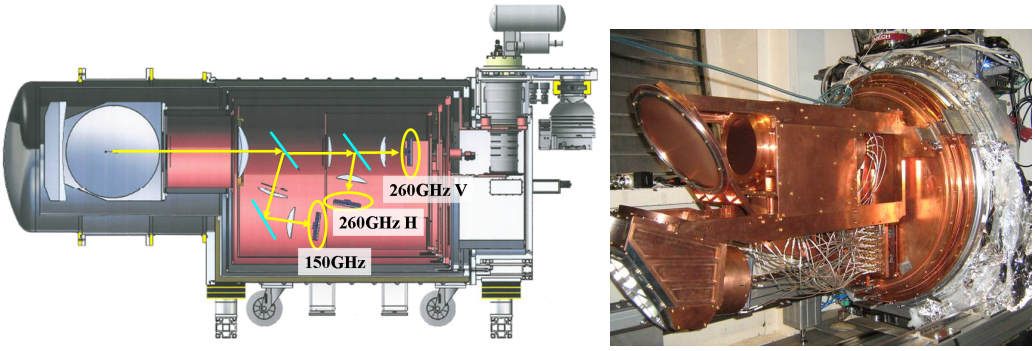

Figure 3.11: **Left***: NIKA2 cryostat scheme, a first dichroic separates the two mm channels and a polariser splits the linear polarisation orientation in two arrays at 260 GHz.* **Right***: Optics at 100 mK stage of the cryostat, picture taken during the first commissioning run done in October 2015.*

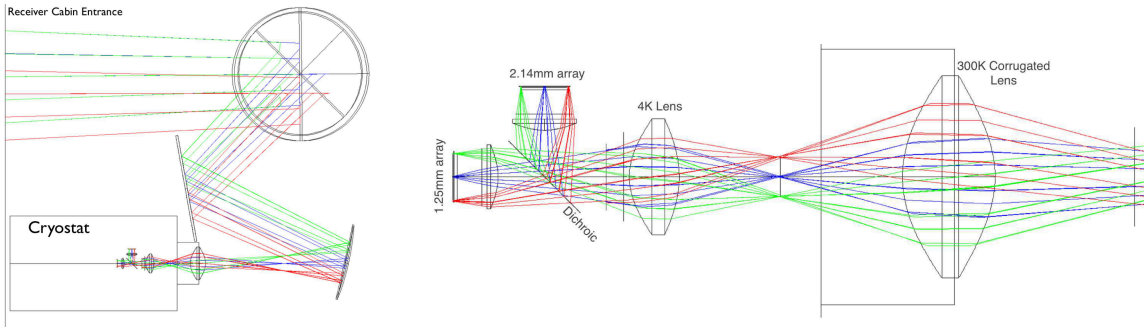

Figure 3.12: *Schematic view of the NIKA optics.* **Left**: *full optical chain from the second mirror of the telescope.* **Right**: *Cold optics inside the cryostat. Credits: [Catalano et al., 2014].*

3.4.5 *NIKA* and *NIKA2* polarisation setup

The *NIKA* polarisation setup consists of a continuously rotating multi-mesh hot pressed Half-Wave Plate (HWP) [Savini *et al.*, 2006] and of a polariser to select the direction of the polarisation. Fig. 3.13 schematically shows the linear polarisation detection strategy. The direction of polarisation of the incident polarised light is rotated depending on the angle of the HWP with respect to the optical axis. Then, it passes through the polariser and finally is detected by the detectors mounted inside the cryostat. The expected signal shown in Fig. 3.13 will be modulated at four times the HWP rotational frequency. As discussed in Sec. 3.3 the design adopted for the KID detectors allows the detection of both linear polarisations (horizontal and vertical). For this reason we adopt a polariser to select the orientation of the polarised signal. In *NIKA* the HWP and the polariser are placed in front of the pupil at ambient temperature (300 K), outside the cryostat (see the left panel of Fig. 3.14). In *NIKA2* only the HWP is placed at 300 K. In both instruments the HWP is mounted inside a holder coupled with a step motor, which permits the fast rotation of the wave plate. The picture on the right panel of Fig. 3.14 shows the holder of the HWP for *NIKA2*, in this case the polariser is placed in the 100 mK stage inside the cryostat where two 1.15 mm arrays absorb both directions of the incoming polarisation (see Fig. 3.11).

3.4.6 The output polarised signal

In order to calculate the output polarised signal expected to be detected by the KIDs we set the basis xy as the Nasmyth reference frame (*i.e.* telescope cabin) and ω the angle between the telescope cabin x axis and the HWP ordinary axis. The polarised light coming from the sky (reference frame ab) is $(I, Q, U)_{in} = I(1, p\cos 2\psi, p\sin 2\psi)$, when the polarisation of the source observed makes an angle ψ with x. In such a case, the incoming radiation expressed by the Stokes parameters in the telescope reference frame is given by:

$$\begin{pmatrix} I \\ Q \\ U \end{pmatrix}_{xy} = \begin{pmatrix} 1 & 0 & 0 \\ 0 & \cos 2\psi & -\sin 2\psi \\ 0 & \sin 2\psi & \cos 2\psi \end{pmatrix} \begin{pmatrix} I \\ Q \\ U \end{pmatrix}_{ab} . \tag{3.9}$$

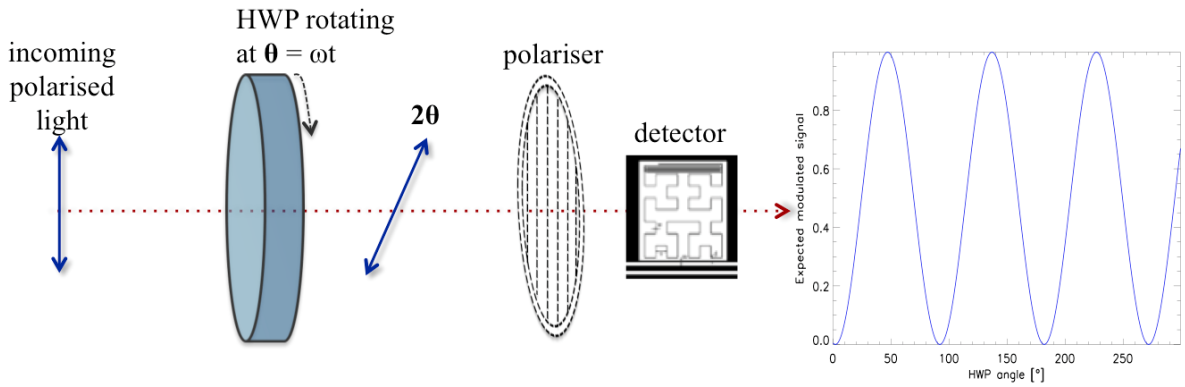

Figure 3.13: *Schematic view of the NIKA polarisation detection strategy. From left to right, the incoming light passes through a rotating Half-Wave Plate (HWP) and a polariser, used to select the orientation of the linear polarisation. The polarised signal is finally detected by the KIDs mounted inside the cryostat and it is expected to be modulated.*

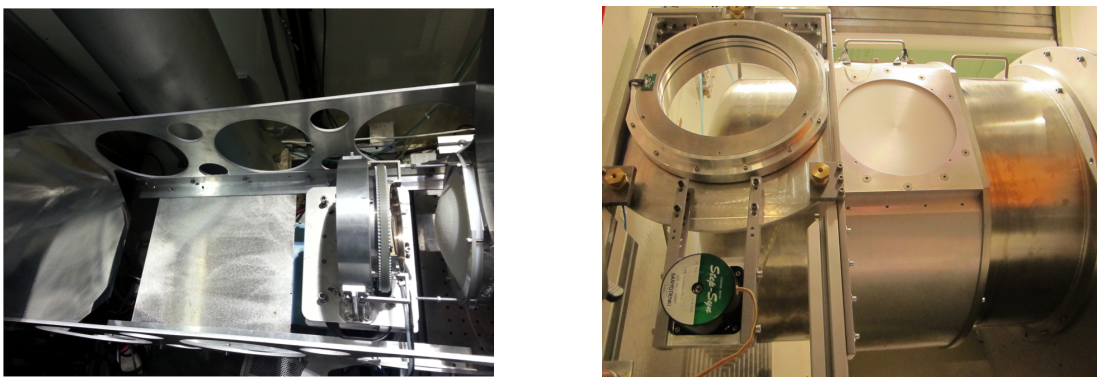

Figure 3.14: *Pictures of the polarisation setup mounted in the cabin of the IRAM 30 m telescope.* **Left***: NIKA setup mounted during the first technical campaign in January 2014. The incoming light from the last mirror propagates through the HWP mounted in the step motor and a polariser tilted by ∼ 10 degrees to avoid standing waves with the cold optical filters inside the cryostat.* **Right***: NIKA2 polarisation setup mounted during the first commissioning campaign in October 2015. The polarization setup shifts automatically in front of the cryostat entrance when required. In this picture the HWP was not yet mounted in the step motor.*

The radiation absorbed by the detector $\mathbf{S}_{out} = (I, Q, U)_{out}$ in the Nasmyth reference frame (xy basis) is described by:

$$\begin{pmatrix} I \\ Q \\ U \end{pmatrix}_{out} = M_{pol} \times M_{HWP} \begin{pmatrix} I \\ Q \\ U \end{pmatrix}_{xy}, \tag{3.10}$$

where M_{HWP} is given by Eq. 2.30 and M_{pol} is different from Eq. 2.29. Thus, resolving Eq. 3.10 and considering $\theta = \omega t$ in Eq. 2.30 we can derive the signal measured by a KID detector, k:

$$\begin{aligned} m_k &= \frac{1}{4}\{I_{in}[(\alpha^2+\beta^2)+(\alpha^2-\beta^2)\cos(2\omega t)] \\ &+ (\alpha^2-\beta^2)\cos(2\omega t)[Q_{in}\cos(2\psi)-U_{in}\sin(2\psi)]+[Q_{in}\sin(2\psi)+U_{in}\cos(2\pi)](\alpha^2-\beta^2)\sin(2\omega t) \\ &+ (\alpha^2-\beta^2)\cos(2\omega t)+A[Q_{in}\cos(2\psi)-U_{in}\sin(2\psi)]+B[Q_{in}\sin(2\psi)+U_{in}\cos(2\psi)]\}. \end{aligned} \tag{3.11}$$

Where:

$$\begin{aligned} A &= (\alpha^2+\beta^2)\cos^2 2\theta + 2\alpha\beta\sin^2 2\theta\cos\phi, \\ B &= (\alpha^2+\beta^2-2\alpha\beta\cos\phi)\cos 2\theta\sin 2\theta. \end{aligned} \tag{3.12}$$

In the ideal case, in which the transmission coefficients $\alpha = \beta = 1$ and the phase shift $\phi = \pi$, the total polarisation amount will be totally located at the HWP fourth harmonic component. Therefore, using trigonometrical relations Eq. 3.11 reduces to:

$$\begin{aligned} m_k &= \frac{1}{2}\{I_{in}+Q_{in}\cos(4\omega t)\cos(2\psi)-U_{in}\cos(4\omega t)\sin(2\psi)+Q_{in}\sin(4\omega t)\sin(2\psi)+U_{in}\sin(4\omega t)\cos(2\psi)\} \\ &= \frac{1}{2}\{I_{in}+Q_{in}\cos(4\omega t-2\psi)+U_{in}\sin(4\omega t-2\psi)\}. \end{aligned} \tag{3.13}$$

The transmission characterisation of this system is crucial for a correct determination of the polarimeter efficiency. In chapter 4 I will discuss the measurements performed in laboratory at *Néel Institute* in Grenoble. These measurements have been fundamental to fix the HWP reference frame and to determine the transmission coefficients α and β.

3.5 Scientific goals of *NIKA2*

The *NIKA2* collaboration has 1300 hours of observation guaranteed time that will focus on five science cases:

1. **Galaxy clusters via Sunyaev Zel'dovich effect**
   The Sunyaev Zel'dovich (SZ hereafter) effect results from the interaction between the cosmic microwave background (CMB) photons and free electrons of the Intra-Cluster Medium (ICM). After this interaction a fraction of the CMB photons are boosted to higher energies, with a resulting flux decrement (increment) at frequencies below (above) 217 GHz. The SZ effect allows us to probe and study clusters of galaxies. A total of 300 hours of *NIKA2* observation guaranteed time will be dedicated to high resolution observations of clusters of galaxies at intermediate and high redshift via the thermal SZ (tSZ) effect. *NIKA2* is well adapted for those observations because of its large number of highly sensitive detectors at two frequency bands (150 and 260 GHz) and its large field of

view (6.5 arcmin) given the 30 m resolution (20 and 12 arcsec for the *NIKA2* frequencies). The purpose is to observe a large sample of clusters of galaxies (about 50) with redshift between 0.5 and 1.0 to study the relationship between the mass of the cluster and the tSZ emission.

2. **Deep Field**
   The high angular resolution, sensitivity and Field of View (FOV) makes *NIKA2* an instrument of choice for the observations of large regions of the sky. Observing very deeply the sky with two frequency bands will permit the identification and characterisation of dusty galaxies at high redshift. This will give a crucial information on the link between large scale structures formation and star formation.

3. **Mapping the interstellar medium**
   The stellar *Initial Mass Function* (IMF) is a fundamental global output of the star formation process, and the question about its origin and universality has been a long-standing open issue (*e.g.* [Bastian *et al.*, 2010; Offner *et al.*, 2014]). While the base of the IMF ($\sim$ solar-type stars) is likely inherited from the prestellar core mass function (*e.g.* [Motte *et al.*, 1998; André *et al.*, 2010]) and may result from gravo-turbulent cloud fragmentation (*e.g.* [Hennebelle et Chabrier, 2008]), the problem of how the most extreme stellar objects (high-mass stars and brown dwarfs) build up their masses is completely unsetted. *NIKA2* will provide a unique tool to address this problem.

4. **Nearby galaxies**
   The mm region of the spectrum is one of the least explored areas of the galaxies SEDs spectral energy. Since it contains emission from three fundamentally important physical processes: thermal emission from dust (see 1.3.2), free-free emission (see 1.3.4) from ionised gas and synchrotron emission (see 1.3.1) from relativistic charged particles moving in the galactic magnetic field; the simultaneous observations in two millimetre bands provided by *NIKA2* will permit the investigation of the physical processes at play.

5. **Polarisation measurements of Galactic regions**
   Magnetic fields have been proved to play a predominant role in a large number of astrophysical processes from galactic to cosmological scales. In particular, recent observations with the *Herschel* and *Planck* satellites have provided us with complete, sensitive maps of the star forming complexes in the galaxy. These maps reveal large scale filamentary structures as the preferential sites of star formation [Molinari *et al.*, 2010; André *et al.*, 2010]. These filamentary structures are associated with organised magnetic field topology at scales larger than 0.5 pc. This indicates that magnetic fields may play a major role in star formation and they need to be explored in details on scales of 0.01 to 0.1 pc [André *et al.*, 2014]. This will be the aim of the polarised channel of *NIKA2* that will observe the sky at 260 GHz. The building and the calibration of a system able to detect the linear polarisation of the diffuse galactic emission with high performances is the ambition of this thesis.

4

Instrumental characterisation of the *NIKA* polarisation setup

Contents

4.1 *NIKA* HWPs **64**

4.1.1 First HWP version: single plate of sapphire 64

4.1.2 Multi-plate HWP solutions 65

4.1.3 Mesh-HWP 65

4.2 Laboratory characterisation **67**

4.2.1 Martin-Puplett Interferometer (MPI) 69

4.2.2 Characterisation of the single plate sapphire HWP 70

4.2.3 Instrumental stray polarisation 73

4.2.4 Characterisation of the *NIKA* final HWP 76

4.2.5 Propagating uncertainties on the HWP parameters to the output polarised signal 80

4.3 Conclusions **82**

The *NIKA* prototype and *NIKA2* final instrument polarisation facilities (see Fig. 3.14) consist of a continuously spinning Half Wave Plate (HWP), a wire-grid polariser and the *NIKA* cryostat containing two KID array at millimetre wavelengths. A polariser is necessary to select the orientation of the incoming polarised light because the *NIKA* detectors KIDs are not sensitive to the polarisation of the light. In both instruments, the HWP is mounted outside the cryostat, with a consequently working temperature of 300 K. It is therefore easy to remove it during total intensity observations avoiding any absorption effect of the plate material.

One of the most important improvements between *NIKA* and *NIKA2* consisted in displacing the wire-grid polariser from 300 K working temperature to the 100 mK cryogenic stage. A cryogenic polariser avoids the reflection of the high temperature optical background signal into

the cryostat, which constitutes a disadvantage in *NIKA* prototype measurements. Furthermore, thanks the two 260 GHz arrays mounted in the 100 mK stage of *NIKA2* (see Fig. 3.11) the totality of photons is recovered. While this configuration improves the sensitivity of *NIKA2* in polarisation, the polarised signal is only detected at 260 GHz.

The aim of this chapter is to report the results obtained by the laboratory characterisation of the *NIKA* prototype polarimeter. The polariser can be considered as "ideal" for our purposes and we focus on the characterisation of the HWP. The chapter is organised in two main sections: Sec. 4.1 discusses the characteristics of the *NIKA* HWPs configurations chosen. Sec. 4.2 discusses their instrumental characterisation performed in laboratory at Néel Institute.

4.1 *NIKA* HWPs

In this section we will be presenting the main features of the Half Wave Plates we chose for *NIKA* polarisation facilities. For the initial configuration a mono-chromatic HWP was preferred to a more sophisticated achromatic one in order to minimise and better control systematic errors linked to the plate. This HWP has been used during the first polarisation run at the IRAM telescope in January 2014. Theoretically, a HWP made of a birefringent crystal (*e.g.* sapphire) can correctly dephase the linear polarisation only at a single frequency. This can cause efficiency losses and systematic effects in large band frequency instruments. To solve this limitation the traditional way is to use multi plate devices with three or more plates rotated by a defined set of angles to achieve an achromatic performance over the broad band [Pisano *et al.*, 2006; Savini *et al.*, 2006]. [Pisano *et al.*, 2008] studied an alternative method using the metal mesh technology. This technology solves the limitations imposed by the availability of birefringent materials and their associated performance losses. A metal mesh HWP has been chosen as solution for the second *NIKA* HWP mounted at the IRAM telescope during the second (October 2014) and third (February 2015) polarisation runs, and also for the final instrument *NIKA2*. The following sections detail the two different optical systems adopted.

4.1.1 First HWP version: single plate of sapphire

A polarised plane wave passing through a single birefringent plate HWP will have its polarisation orientation rotated by $\Delta\psi = 2\theta$ (see Fig. 4.1), where θ is the angle between the incident polarisation and one of the optical crystal axes. As explained in Sec. 2.2.2 the two orthogonal axes are defined as "ordinary axis" and "extraordinary axis" with different optical indices n_o and n_e.

Quantitatively, the birefringence of a material is defined as $n_e - n_o$. Since the light speed within the crystal is inversely proportional to the index, one polarisation will travel faster than the other defining a slow and fast axis. The highest refractive index corresponds to the lowest speed of light inside the material. We can define the refractive indices as:

$$n_e = \frac{c}{v_\parallel}, \tag{4.1}$$

$$n_o = \frac{c}{v_\perp}, \tag{4.2}$$

where v is the light speed in the medium and c in the vacuum. The phase-shift introduced by a birefringent material depends on the plate thickness d of the material, the wavelength λ of the incident light and the birefringence value:

$$\phi = 2\pi d(n_e - n_o)\lambda. \tag{4.3}$$

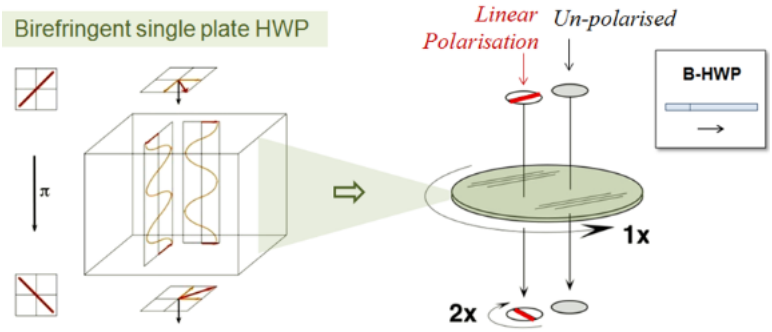

Figure 4.1: *Working principle of a birefringent HWP [Pisano, 2000]. The outgoing signal will be rotated by twice the angle between the incident light and the optical axis.*

The maximum transmission at a given wavelength is achieved by a phase-shift $\phi = \pi$. The dependance on the wavelength makes impossible to optimise the transmission of the polarised light with a phase-shift constant in a large frequency band. Moreover, since sapphire has a high refractive index $n_o \simeq 3.05$ along the ordinary axis and $n_e \simeq 3.39$ along the extraordinary axis (values measured at 140 GHz by [Savini *et al.*, 2006]), the reflective loss R and transmission T on each surface of the plate is given by the *Snell* equations:

$$R = \left(\frac{1 - n_s}{1 + n_s}\right)^2, \tag{4.4}$$

$$T = 1 - R - A. \tag{4.5}$$

In Eq. 4.4 "1" corresponds to the refractive index of the air. Here, we consider for simplicity n_s the averaged refraction index. Since sapphire is transparent at the wavelengths considered, the absorption coefficient A can be neglected in Eq. 4.5. As a consequence taking $n_s = 3.27$ we obtain a reflective loss on each surface of 28%. This effect can be greatly reduced by the use of broadband anti-reflection (ARCs) coatings. Thin film ARCs work by producing two reflections which interfere destructively with each other. In the case of sapphire there are no natural materials that have this property, so they have to be artificially synthesised [Pisano *et al.*, 2014].

4.1.2 Multi-plate HWP solutions

The efficiency of a single layer HWP for broadband applications such as *NIKA* camera can be increased using the theory developed by Pancharatnam [Pancharatnam, 1955]. The multi-plate method suggested involves the stacking of different birefringent HWPs and rotating their axes by specific angles (see Fig. 4.2). However, this kind of plate demands the use of very broadband multi-layer ARCs, which can represent an important limitation. Another problem is the limited availability of large diameter crystal plates [Pisano *et al.*, 2014]. This implies that birefringent HWPs are not suitable for large diameter detector arrays applications.

4.1.3 Mesh-HWP

The metal-mesh technology is the standard method for providing optical filtering at far infrared and millimetre wavelengths [Ulrich, 1967; Tucker et Ade, 2006; Ade *et al.*, 2006]. The concept of a HWP is visualised as capacitive and inductive geometries that invoke opposite frequency

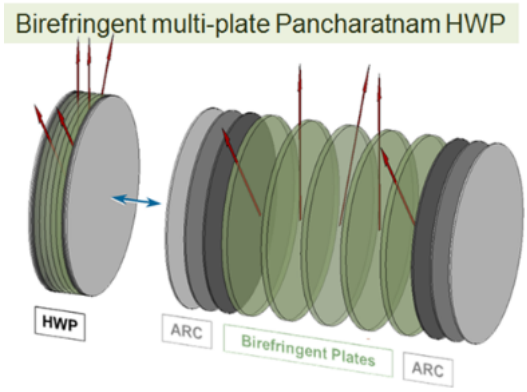

Figure 4.2: *Broadband HWPs consisting of a combination of birefringent plates.*

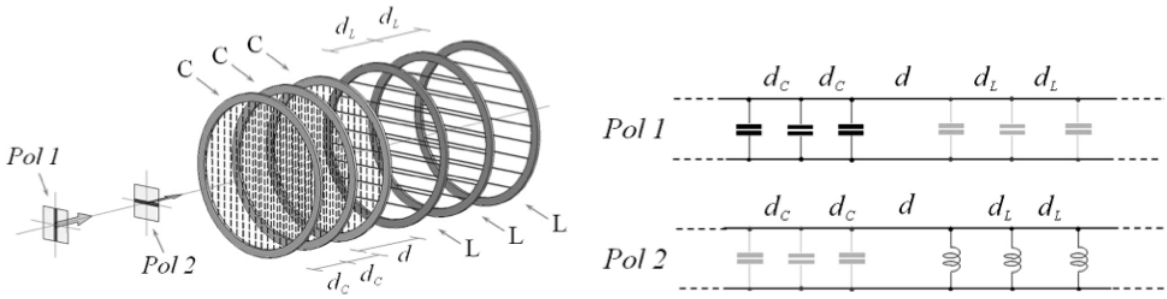

Figure 4.3: **Left***: Example of a HWP made with three capacitive and three inductive grids.* **Right***: transmission line equivalent circuits for the device [Pisano* et al.*, 2008].*

dependent phase shifts. Indeed, it is possible to design metal grids that exhibit capacitive or inductive behaviour in one polarisation direction and that are almost transparent in the orthogonal one [Pisano *et al.*, 2008]. This kind of grids are called air-gap mesh HWP. An example of three capacitive grids coupled to three inductive grids device is represented on the left panel of Fig. 4.3. The transmission line equivalent circuit is presented on the right panel. The *Pol-1* signal interacts with the first three capacitive grids and then propagates through the remaining inductive grids almost unaffected. Similarly, *Pol-2* interacts only with the inductive grids. In this way, the capacitive and inductive grids introduce phase shifts with opposite signs making it possible to achieve large differential phase shifts between the orthogonal polarisations. The inconveniece of this device is the fragility of the thin dielectric substrates necessary to hold the metal grids.

The fragility problem of the air-gap mesh HWP can be solved embedding all the grids inside the same dielectric material. Therefore, the grid-substrates are thermally bonded with each other. This kind of HWP allows a quasi-total (> 90 %) transmission of the polarised signal along a large bandwidth. This solution has been finally chosen for *NIKA* and it is shown on Fig. 4.4 (right panel).

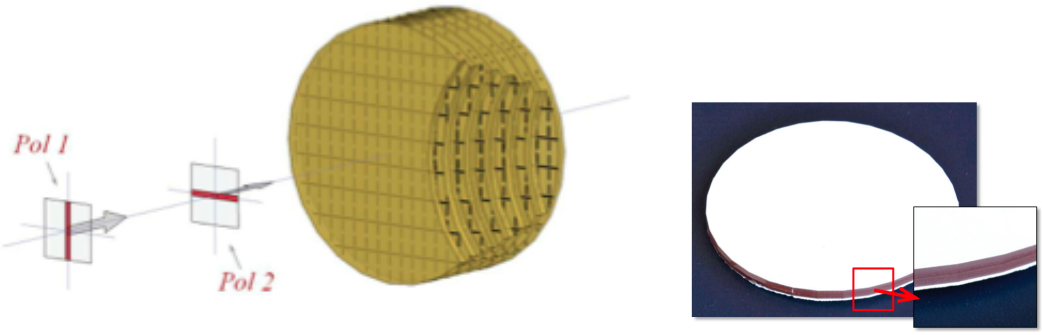

Figure 4.4: **Left**: *Sketch of the dielectrically embedded six grids Mesh-HWP internal structure. Credits:[Pisano et al., 2008].* **Right**: *Picture of the NIKA final HWP.*

4.2 Laboratory characterisation

A first characterisation of the properties of HWP was carried out during its fabrication at Cardiff University. The two *NIKA* HWPs, made in Cardiff, have been characterised in the laboratory at the Néel Institute. The Mueller matrix of a HWP, described by Eq. 2.30 shows that the determination of the relative difference between the transmission coefficients α and β defines the performance of the system. Indeed, if they are both equal to unity the HWP is ideal and no performance losses are expected. Non-idealities can transform a certain amount of unpolarised signal into polarised that will be modulated at the second harmonic of the HWP rotation frequency ω and higher its harmonics. In addition, it can cause performance losses of the polarised signal expected to be located only at fourth harmonic of ω.

In order to check the polarisation efficiency of the HWP measured in Cardiff during its fabrication and the level of the instrumental stray polarisation in the whole instrumental chain of *NIKA* we performed two session of measurements:

(i) spectral transmission measurements using a Martin-Puplett interferometer. The main parameters of the HWP, the transmission coefficients α and β, polarisation efficiency $\rho_{\rm pol}$ and the phase shift ϕ in the *NIKA* band are then derived;

(ii) total power measurements with rotating HWP in an environment close to the telescope conditions.

In order to perform spectral measurements we have used a source 100% polarised coming from a Martin-Puplett Interferometer, the HWP in a fixed position and a lithographic kapton coper polariser. The optical configuration used for these measurements is schematically shown on Fig. 4.5 and Fig. 4.6 shows a picture of the instrumental setup. For the second session of measurements (ii) the HWP is mounted in a rotating wheel coupled to a step motor and placed in front of the cryostat window at room temperature. The polariser, not shown in this picture, works also at room temperature at a distance of 6 cm from the HWP. Its substrate plane was tilted by 10 degrees with respect to the HWP optical axis to avoid standing waves with the cold optical filters inside the cryostat.

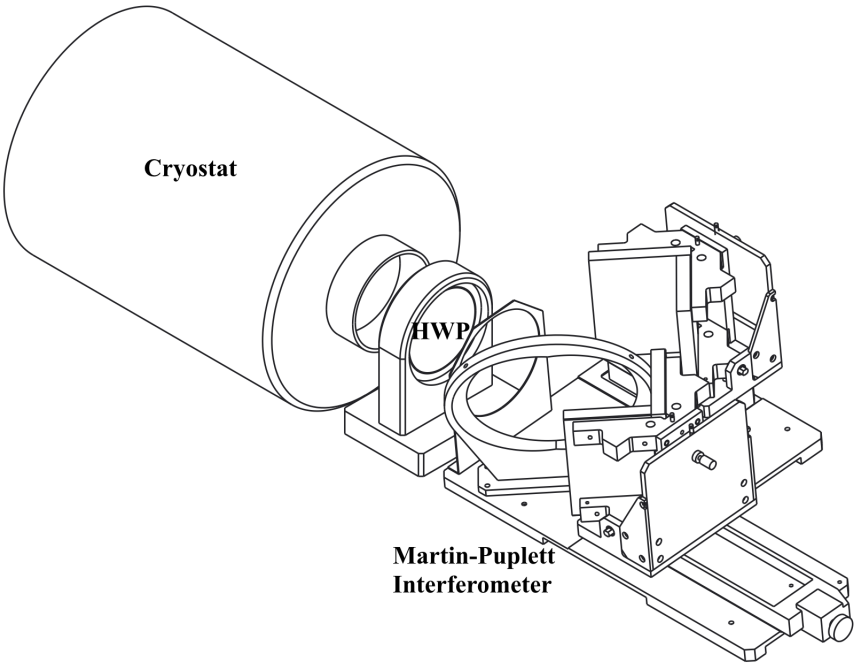

Figure 4.5: *From left to right, the NIKA dilution cryostat, the HWP mounted in the rotating wheel and the Martin-Puplett interferometer.*

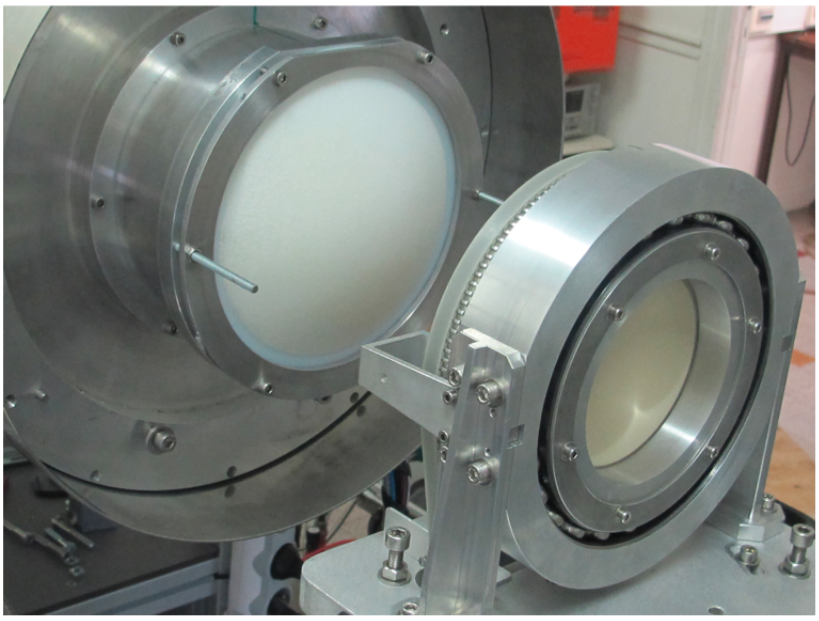

Figure 4.6: *Picture of the instrumental setup for polarisation measurements. The single plate sapphire HWP mounted in a rotating wheel coupled to a step motor is placed in front of the NIKA cryostat window. The subsequent polariser is not shown in this picture.*

4.2.1 Martin-Puplett Interferometer (MPI)

The Martin Puplett Interferometer is a differential Fourier transform spectrometer (FTS), which measures the difference between the spectral brightness of two input sources (see [Martin et Puplett, 1970] for details). In our instrumental setup these two sources are represented by two black bodies with different temperatures (ambient ECCOSORB and warmed ECCOSORB).

The working principle of a MPI is shown on Fig. 4.7. A MPI employs three Wire-Grids (WGs): the first one transforms an unpolarised radiation into a totally polarised radiation; the second WG is placed at 45° with respect to the first one and between the two roof mirrors. It acts as a beam splitter separating the linearly polarised signal in two orthogonal components that, after having undergone a polarisation rotation of 90° caused by the reflection in the roof mirrors, recombine again on the same WG. Finally the third WG allows a modulation of the output signal in order to obtain the typical interference fringes when one of the two roof mirrors is moved with respect to the other. The phase-shift produced by the movement of the roof mirror is:

$$\varphi = \frac{2\pi\delta}{\lambda} \tag{4.6}$$

where δ is the mechanical shift of the roof mirror and λ the wavelength. The Mueller formalism can be used to describe a MPI considering a combination of a phase-shift element and a beam splitter WG:

$$\mathbf{M}_{MP} = \begin{pmatrix} 1 & 0 & 0 & 0 \\ 0 & \cos\varphi & 0 & \sin\varphi \\ 0 & 0 & -1 & 0 \\ 0 & \sin\varphi & 0 & -\cos\varphi \end{pmatrix} \tag{4.7}$$

Adding the last WG we obtain the typical interference signal which is absorbed by the detectors:

$$I_R = \frac{1}{2}(I_0 + I_1) + \frac{1}{2}(I_0 - I_1)\cos\varphi \tag{4.8}$$

$$I_T = \frac{1}{2}(I_0 + I_1) - \frac{1}{2}(I_0 - I_1)\cos\varphi \tag{4.9}$$

where I_0 and I_1 are the intensity of the two input sources (ECCOSORB and warmed ECCOSORB) and I_R, I_T are the final reflected and transmitted intensity that arrives on the detectors. This output signal allows us to extract the difference frequency spectrum of the two input unpolarised beams through Fourier transform. From Eq. 4.6 we can derive the spectral resolution and the maximum accessible frequency of the final spectrum. In the case of our laboratory tests, we performed interferograms with steps of 250 μm for a total excursion of the roof mirror of 44 mm. This allows us to reach a maximum accessible frequency of about 1 THz and a spectral resolution of about 3.5 GHz.

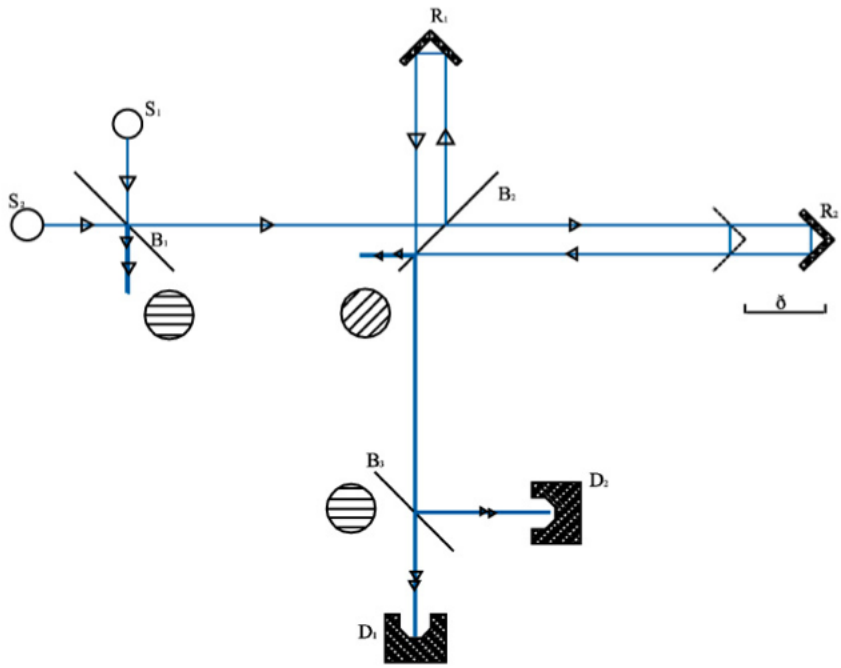

Figure 4.7: *Schematic view of a Martin-Puplett interferometer. The signal coming from the two sources is transmitted and reflected by the first wire-grid B_1. Then the central grid B_2 acts as beam splitter and separates the beam in two. The radiation is then double reflected by the roof mirrors R_1 and R_2 and reaches the beam splitter B_2. The beams are then recombined and transmitted to the last wire-grid B_3.*

4.2.2 Characterisation of the single plate sapphire HWP

The HWP was designed to have the maximum transmission in the 1.15 mm *NIKA* band. It had a 100 mm diameter and a thickness of 1.97 mm and as a consequence a working frequency of 230 GHz, obtained by inverting Eq. 4.3 and considering a phase shift of π. The plate was anti-reflection coated on both sides with a single dielectric substrate in order to minimise surface reflections.

The calibration of the polarisation angle required an accurate determination of the HWP zero position angle, which has been performed in laboratory during the tests. In order to fix the reference frame of the HWP, prior to any measurement we rotated the *NIKA* HWP to find a zero point initial position, which maximised the measured LEKID signal. This characterisation allowed us to mark on the HWP the exact position of the zero and to fix the reference frame at the telescope. Using the power spectrum at zero position as reference we performed the characterisation of the spectral transmission of the HWP for different relative angle with respect to the initial position. As the polariser was kept at a fixed position, this induced an attenuation of the signal measured.

The characterisation of the HWP parameters is crucial for the determination of the polarisation efficiency of the polarimeter. From Eq. 3.11 we see that the term $(\alpha^2 - \beta^2) \neq 0$ can induce a modulation of the signal at the second harmonic of ω producing a loss of the polarised signal normally detected at 4 ω. The "non-idealities" of the HWP can induce a distortion of the spectrum. Figure 4.8 shows the measured power spectrum at the reference zero position (red

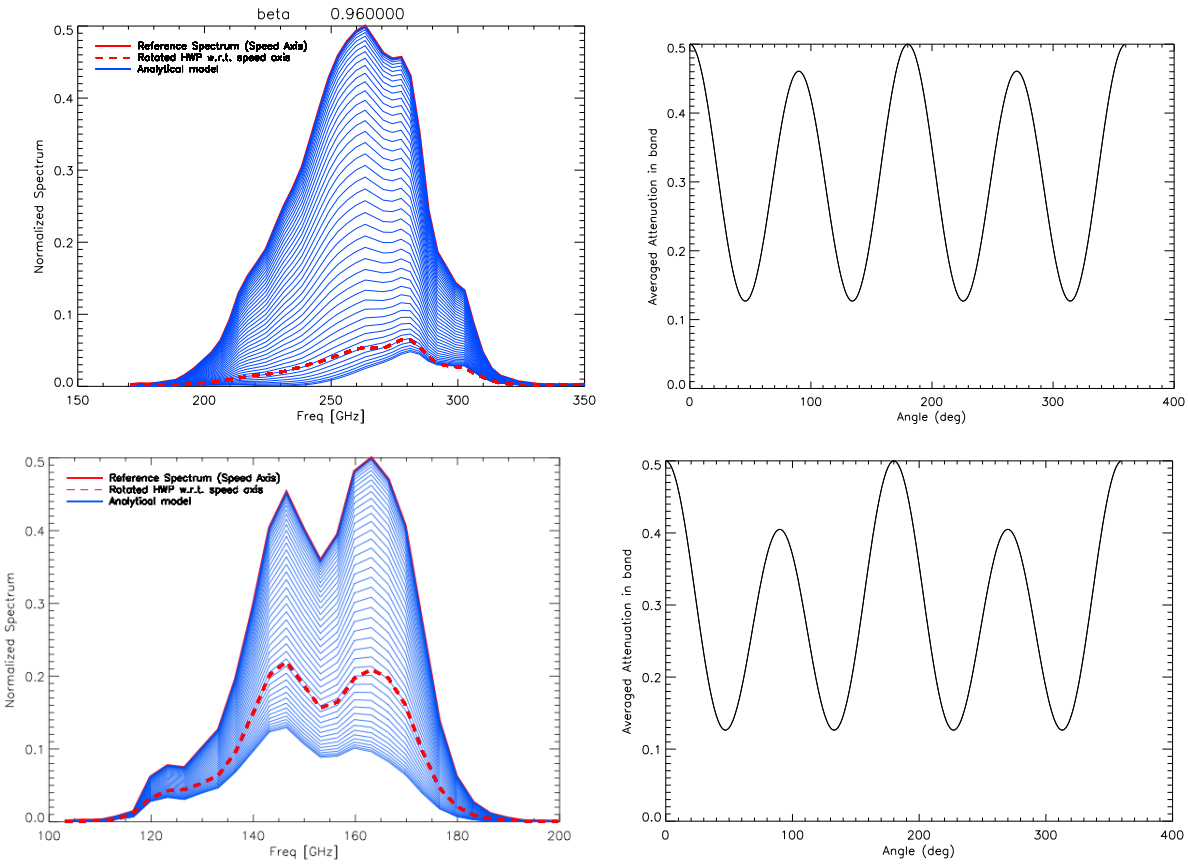

Figure 4.8: **Left**: *maximum transmission spectrum (red solid line). Analytical model for 1.15 mm (top) and 2.05 mm (bottom) channel for different HWP angles (blue line) with respect to the first wire-grid of Fig. 4.7. The measured spectrum for a rotated angle of the HWP (red dotted line) shows a distortion of the spectrum.* **Right**: *expected signal attenuation for a full HWP turn.*

solid line) and at a relative angle (red dotted line) for both channels.

In order to derive the difference between α and β we developed an analytical model. The model accounts for the Mueller matrices of an ideal polariser (see Eq. 2.29) and the "real" HWP (see Eq. 2.30). Since we are interested to the relative difference between α and β we fixed one of the coefficients to unity keeping the second one as a free parameter. The phase shift ϕ for this HWP configuration is directly estimated by the Eq. 4.3. Fig. 4.8 shows the attenuation of the power spectrum for different angles of the HWP obtained from the model (blue curves). The best-fit value for β is estimated considering a maximum likelihood. The model is given by:

$$\zeta = \frac{S_{RF}}{MAX_{RF}} \times M(\theta, \beta), \tag{4.10}$$

where $\frac{S_{RF}}{MAX_{RF}}$ represents the normalised maximum transmission spectrum and $M(\theta, \beta)$ is the Mueller matrix that describes the expected output signal from the HWP+polariser system. $M(\theta, \beta)$ is calculated for each angle θ in the range [0-360]° and β in the range [0-1]. In order to

estimate the value of β we calculate the Chi-square function χ^2 defined as:

$$\chi^2 = \sum_{i=1}^{N} \frac{(S(\theta)_i - \zeta_i(\theta, \beta))^2}{\sigma_i^2}, \tag{4.11}$$

where $S(\theta)_i$ represents the spectrum measured for a given HWP rotated angle θ and the model $\zeta_i(\theta, \beta)$. The errors σ_i are estimated as the dispersion of the measured signal by all the detectors. We can approximate the likelihood function L as:

$$L(\theta, \beta) \simeq exp(-\chi^2(\theta, \beta)/2). \tag{4.12}$$

The most probable β value corresponds to the maximum of the L function. The best fit results and uncertainties are presented in Tab. 4.1. As expected by the requirements, *i.e.* maximum transmission in the 1.15 mm channel, the incoming polarised light is quasi-totally transmitted in this channel. Furthermore, we can derive the HWP polarisation efficiency from the Eq. 2.30 as:

$$\rho_{pol} = (1 - 2\gamma)/2, \tag{4.13}$$

where:

$$\gamma = \frac{\alpha\beta\cos(\phi)}{\alpha^2 + \beta^2}. \tag{4.14}$$

Since $\alpha = 1$ the resulting formula for the parameter ρ_{pol} is:

$$\rho_{pol} = \frac{1}{2} - \frac{\beta\cos\phi}{1 + \beta^2}. \tag{4.15}$$

And the associated uncertainty can be computed as:

$$\sigma_{\rho_{pol}} = \frac{\cos\phi(1 + \beta^2) - 2\beta^2\cos\phi}{(1 + \beta^2)^2}\sigma_\beta, \tag{4.16}$$

where we assume Gaussian uncertainties in β. From the equations above we can estimate ρ_{pol} in the two *NIKA* millimetre channels. The results are reported in Tab. 4.1 showing that performance losses, for sapphire HWP, are particularly important at 2.05 mm. For this analysis we considered the value of the averaged in-band HWP phase angle, ϕ, also reported in Tab. 4.1 . By multiplying ρ_{pol} for the intensity spectral bandpass we obtain the polarisation spectral bandpass defined as $Q - U$ spectrum on Fig. 4.9. The figure shows a better transmission of the polarised light in the 1.15 mm *NIKA* band than at 2.05 mm, as expected.

	α	β	Total transmission	ρ_{pol}	Avg in-band ϕ
			Sapphire HWP		
Channel 1.15 mm	1	0.96±0.01	96%	0.963±0.004	202°
Channel 2.05 mm	1	0.90±0.01	90 %	0.749±0.005	120°
			Metal mesh HWP		
Channel 1.15 mm	1	0.999±0.005	99%	0.9956±0.0002	179°
Channel 2.05 mm	1	0.924±0.005	93 %	0.9941±0.0002	188°

Table 4.1: *Transmission parameters obtained from the characterisation of the single layer sapphire HWP and the metal mesh final NIKA HWP.*

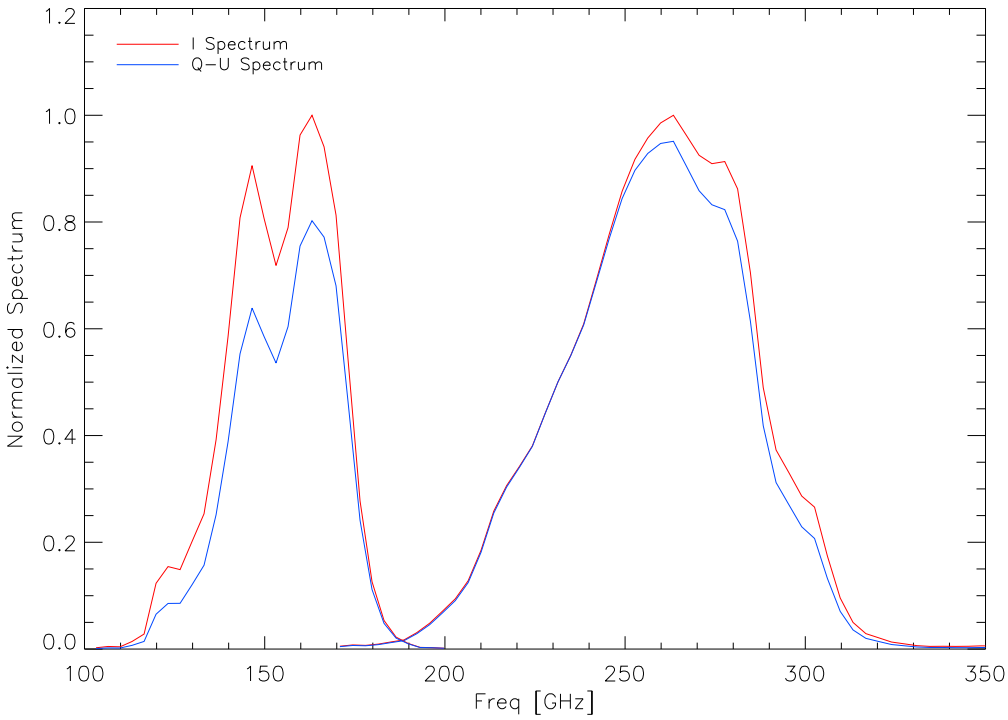

Figure 4.9: *NIKA spectral transmission (red). Polarisation transmission of the sapphire HWP across the bandwidth of NIKA (blue).*

4.2.3 Instrumental stray polarisation

In the second session of the laboratory tests, we wanted to characterise the whole optical chain of the *NIKA* polarimeter in a configuration close to telescope conditions. For this purpose we used a sky simulator built at the Néel Institute, a mechanical holder to rotate the HWP with a subsequent polariser mounted in front of the *NIKA* cryostat window, *NIKA*. A picture of the sky simulator is shown on Fig. 4.10 (a). It consists of a pulse tube cryostat with a 24 cm absorber cold plate in it. The absorber is cooled down to 50 K, which corresponds to the atmospheric background we have at the telescope. The simulator is equipped with a resistance

to heat the cold plate. In order to simulate an astrophysical source, we put a high-emissivity sphere (diameter of about 5 mm) in front of the sky simulator at room temperature. This virtual source is mounted in a XY stage in order to simulate an OTF (*On The fly*) scan similar to what is performed at the telescope.

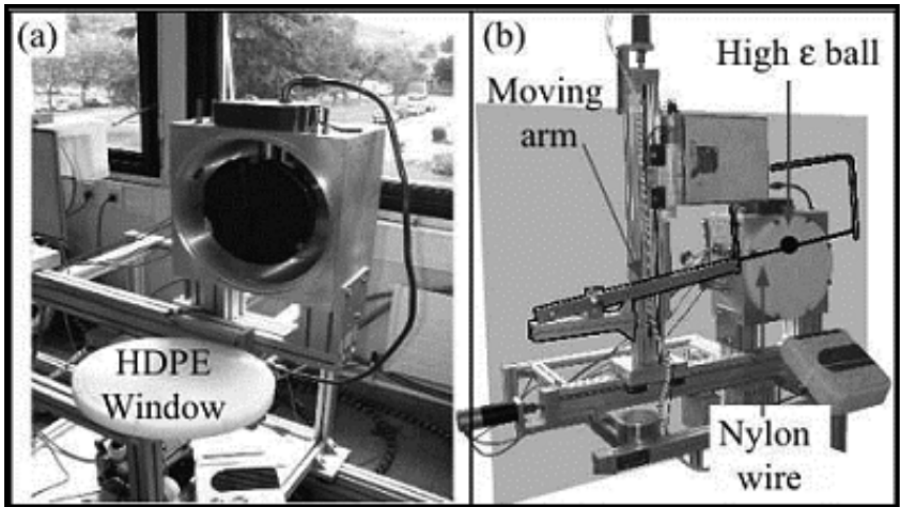

Figure 4.10: *Picture of the sky simulator used for laboratory measurements. a) Open pulse tube cryostat with view to the 24 cm absorber cold plate. b) Complete system with a ball used to simulate the planet.*

In order to estimate the level of any spurious signal due to the mechanical modulation of the HWP we performed tests in three configurations:

(a) only mechanical holder running at $\omega = 1.9$ Hz without HWP;

(b) HWP mounted inside the holder and rotating at $\omega = 1.9$ Hz ;

(c) HWP rotating at $\omega = 1.9$ Hz + polariser mounted facing the *NIKA* cryostat window.

Fig. 4.11 and 4.12 show a zoom of the observed time ordered data in the three configurations (left panels) for a single detector of the *NIKA* 1.15 mm and 2.05 mm array, respectively. On right of the figure it is shown the corresponding power spectrum. From the power spectra we note a 1/f noise spectrum due to temperature fluctuations of the sky simulator. Adding the HWP to the setup (central plots) we observe a modulation of the background signal probably due to some reflections of the signal in the laboratory room. Finally adding the polariser to the configuration, the polarised signal shifts at the fourth harmonic of ω. A parasitic signal due to imperfections of the HWP is observed peaked at harmonics of ω. Such a parasitic signal has been already observed by the EBEX experiment [Johnson *et al.*, 2007] and it will be treated and subtracted from the observations using a dedicated data analysis software, see Sec. 6.3.1. Additional parasitic signals induced by the fast rotation of the holder are not observed.

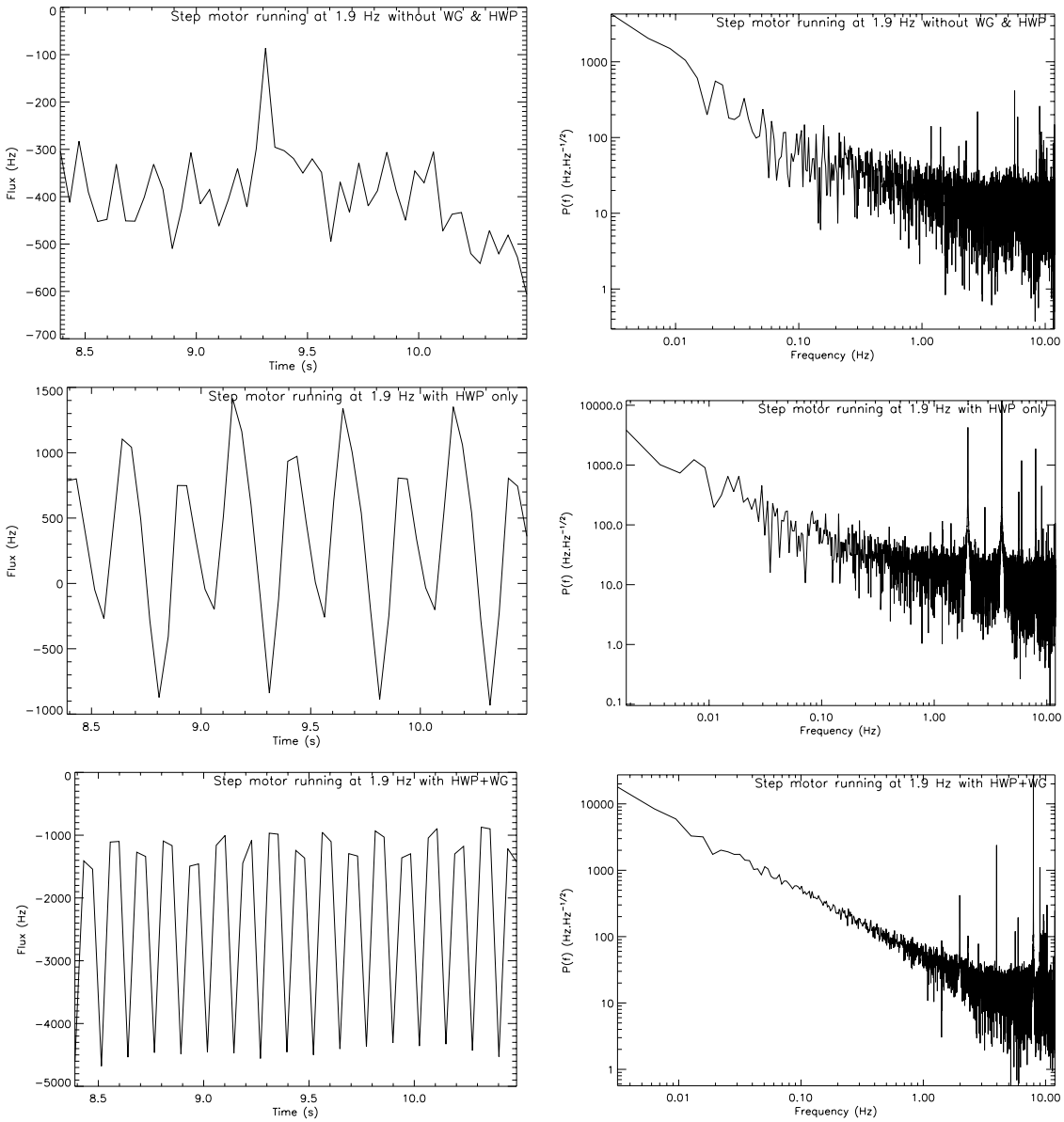

Figure 4.11: *Chunk of data (left) for a KID of the 1.15 mm array and corresponding power spectrum (right). From top to bottom the data represent the three configurations (a), (b) and (c) as explained in the text are represented.*

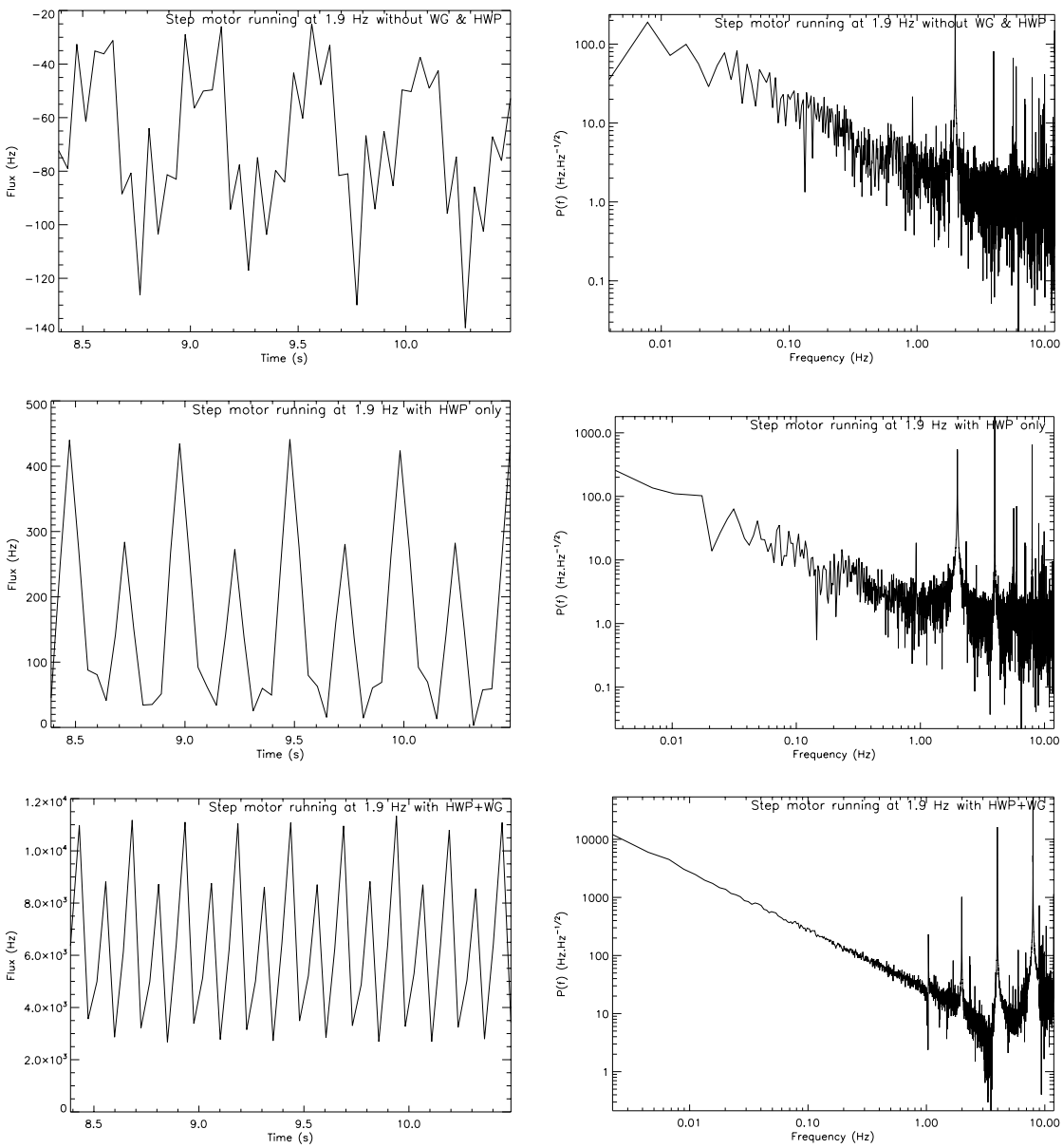

Figure 4.12: *Chunk of data (left) for a KID of the 2.05 mm array and corresponding power spectrum (right). From top to bottom the data represent the three configurations (a), (b) and (c) as explained in the text are represented.*

4.2.4 Characterisation of the *NIKA* final HWP

As shown in the previous section a single plate sapphire HWP shows a high level of instrumental polarisation due to its non-idealities. In addition, since the HWP is optimised to work in the 1.15 mm and the characterisation shows a loss of 25% of the incoming polarised signal in the 2.05 mm channel. For these reasons, we decided to use a more sophisticated HWP and we chose the metal mesh solution. This HWP, made also at Cardiff University, has been used during the last two polarisation runs of *NIKA*. The observations performed with this optical system on point and extended polarised sources are reported in Chap. 7.

As for the previous configuration we wanted to characterise this new HWP in the whole

optical *NIKA* chain. The final HWP was designed to allow an approximately constant phase shift of the transmitted radiation over a broad spectral band including the two *NIKA* bands. A two-layer broadband anti-reflection coating was added to the HWP to maximise the transmission across the band. In particular the HWP phase shift angle ϕ optimised over the full bandwidth from 100 to 350 GHz during the fabrication is shown on Fig. 4.13 and it will be used in the analytical model to fit the power spectra measured.

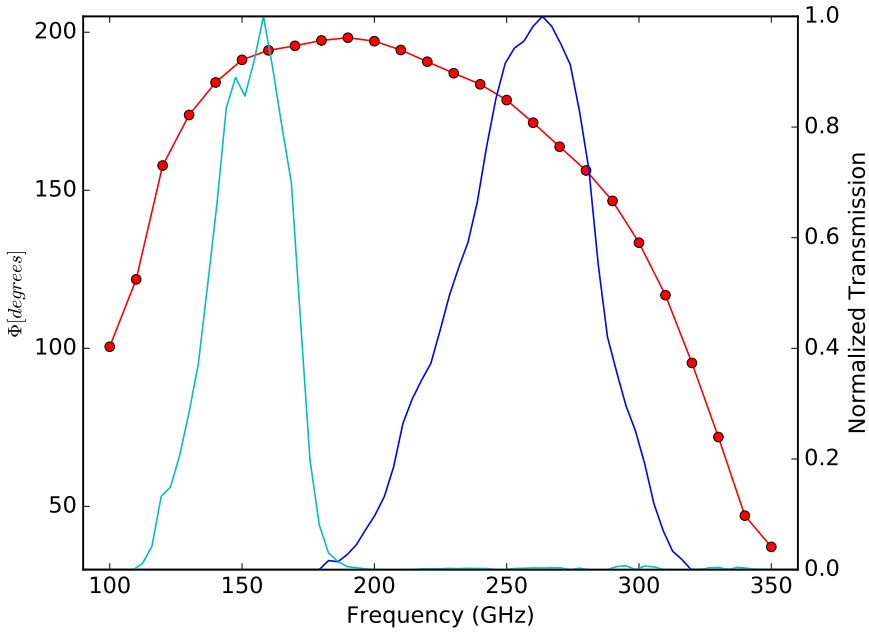

Figure 4.13: *Phase shift angle as a function of the frequency for the NIKA HWP (red). NIKA band pass in cyan (2.05 mm) and blue (1.15 mm).*

The power spectra measured for different HWP angles are shown on Fig. 4.14 where it is represented the measured transmission as a function of the frequency for four HWP positions (dashed solid line), going from the maximum (black solid line) to the minimum of transmission. The angle between the maximum and the minimum is $46.8 \pm 1.8°$, which agrees the expected 45 degrees from Eq. (2.30). An uncertainty of 1.8° has to be considered because the mechanical modulator completes 100 steps per tour of the HWP. Therefore, this uncertainty will represent the precision associated to the determination of the HWP zero, corresponding to its optical axis in the reference frame of the telescope cabin.
We have performed a total of ten independent measurements varying the angle of the *NIKA* HWP axis with respect to the optical axis. The maximum of the spectra measured are reported on bottom of Fig. 4.14 as a function of the HWP angle. The dots show an attenuation of the signal with a maximum corresponding to an angle of 46.8°. In the top panel of the figure we report the power spectra obtained for these different HWP angles measurements showing an attenuation of the signal as expected. In this case we do not observe a distortion of the spectrum, this indicates a better transmission of the polarised signal in the full *NIKA* bandwidth.

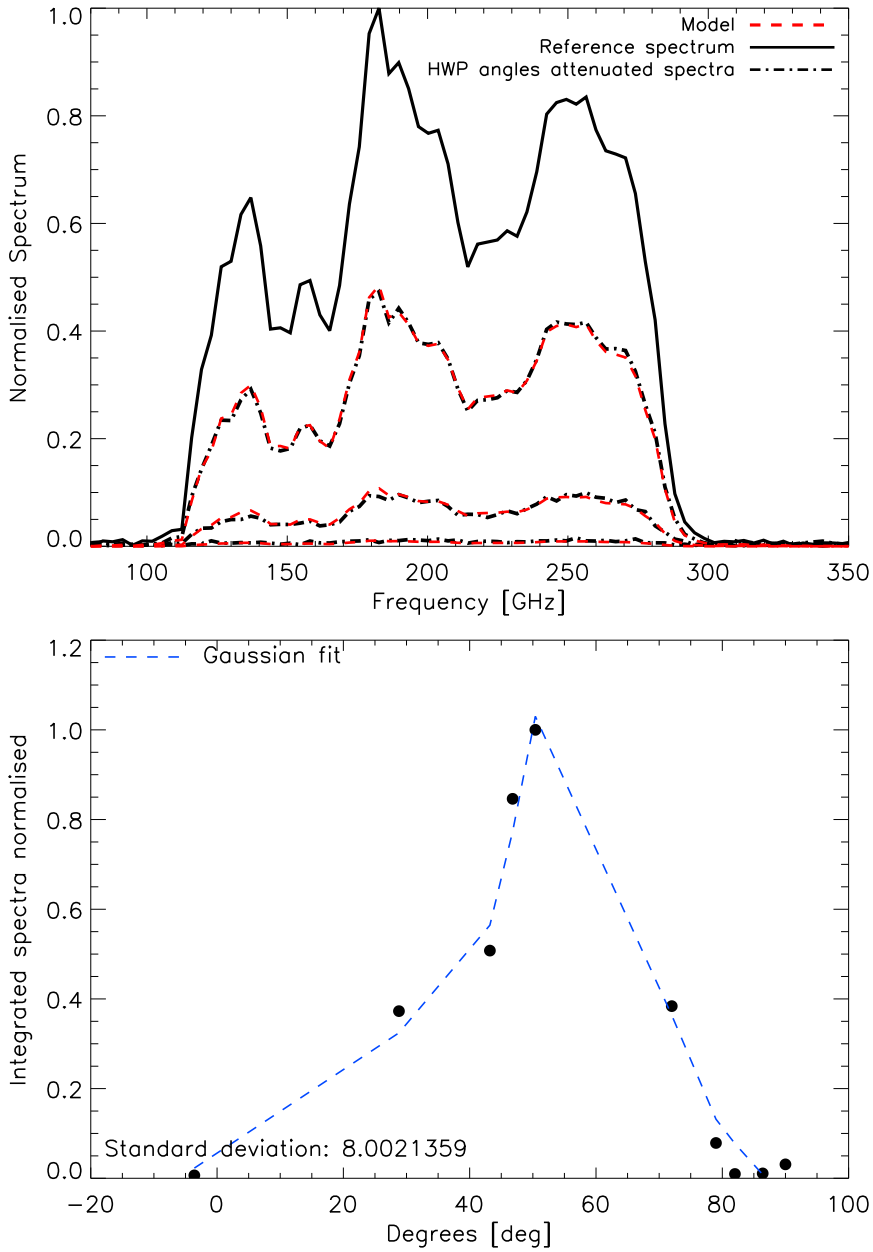

Figure 4.14: **Top** *Spectral transmission of the NIKA HWP at different angles with respect to the optical axis. The red curves corresponds to the best-fit model for the different power spectra.* **Bottom** *The plot shows the maximum of the power spectra measured for each HWP angle measured as a function of the angle.*

The model shown in red dotted line on Fig. 4.14 is equivalent to the previous characterisation. The transmission coefficient estimated for this new HWP is also reported in Tab. 4.1. The best fit models obtained for each position of the HWP are plotted in red in Fig. 4.14. Using the Eq. 4.16 we can estimate the polarisation efficiency of the system, ρ_{pol}. The value measured together with the effective phase-shift estimated in the *NIKA* bandpass are reported in Tab. 4.1. Comparing the values found for the metal mesh HWP with respect to the single layer HWP, we see a notable improvement in terms of total polarised light transmitted across the *NIKA*

bandwidth with a performance loss less than 0.6 % in both *NIKA* millimetre channels.

By multiplying ρ_{pol} by the intensity spectral bandpass we obtain the polarisation spectral bandpass shown on Fig. 4.15. The figure shows the good performance of this system in transmitting the polarised light in the full bandwidth of *NIKA*. In *NIKA2* we used the same technology but optimised only in the 1.15 mm channel.

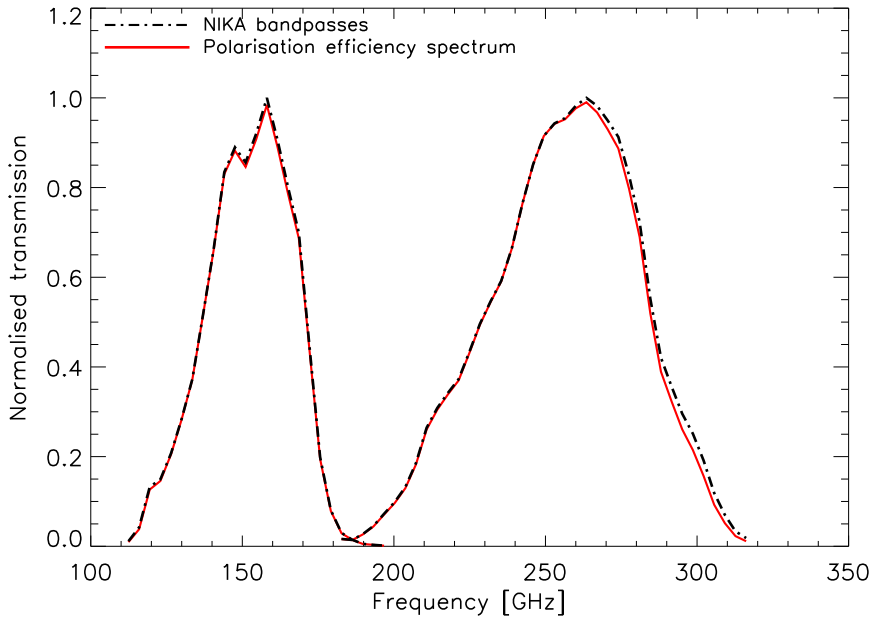

Figure 4.15: *Renormalised polarisation efficiency across the NIKA bandwidth.*

4.2.5 Propagating uncertainties on the HWP parameters to the output polarised signal

The aim of this section is the estimation of the HWP Mueller matrix uncertainty. Let's generalise Eq. 2.30 including the transmission coefficient uncertainties $\delta\beta$ and $\delta\alpha$ in the Mueller matrix. The Jones matrix 2.11 is then modified as follows:

$$J + \Delta J = \begin{pmatrix} \alpha + \delta\alpha & 0 \\ 0 & (\beta + \delta\beta)e^{\phi+\delta\phi} \end{pmatrix} \tag{4.17}$$

The corresponding Mueller matrix in the Eq.2.30 becomes:

$$M = \widetilde{M} + \Delta M \tag{4.18}$$

Let's assume the Eq. 2.30 for $\widetilde{M}$ and derivate ΔM:

$$\Delta M = \begin{pmatrix} \alpha^2 + \delta\alpha^2 + 2\alpha\delta\alpha + \beta^2 + \delta\beta^2 + 2\beta\delta\beta & (\alpha^2 + \delta\alpha^2 + 2\alpha\delta\alpha - \beta^2 - \delta\beta^2 - 2\beta\delta\beta)\cos 2\theta & (\alpha^2 + \delta\alpha^2 + 2\alpha\delta\alpha - \beta^2 - \delta\beta^2 - 2\beta\delta\beta)\sin 2\theta \\ (\alpha^2 + \delta\alpha^2 + 2\alpha\delta\alpha - \beta^2 - \delta\beta^2 - 2\beta\delta\beta)\cos 2\theta & (\alpha^2 + \delta\alpha^2 + 2\alpha\delta\alpha + \beta^2 + \delta\beta^2 + 2\beta\delta\beta)\cos^2 2\theta + B & C \\ 0 & C & D \end{pmatrix} \tag{4.19}$$

where:

1. $B = 2(\alpha\beta + \alpha\delta\beta + \beta\delta\alpha + \delta\alpha\delta\beta)\sin^2 2\theta(\cos\phi - \sin\phi\delta\phi)$
2. $C = [\alpha^2 + \delta\alpha^2 + \beta^2 + \delta\beta^2 + 2\beta\delta\beta - (2\alpha\beta + 2\beta\delta\alpha + 2\delta\beta\delta\alpha + 2\alpha\delta\beta)(\cos\phi - \sin\phi\delta\phi)]\sin 2\theta\cos 2\theta$
3. $D = (\alpha^2 + \delta\alpha^2 + 2\alpha\delta\alpha + \beta^2 + \delta\beta^2 + 2\beta\delta\beta)\sin^2 2\theta + 2(\alpha\beta + \alpha\delta\beta + \beta\delta\alpha)\cos^2 2\theta(\cos\phi - \sin\phi\delta\phi)$

Let's consider the first order approximation:

$$\Delta M = \begin{pmatrix} 2\alpha\delta\alpha + 2\beta\delta\beta & (2\alpha\delta\alpha - 2\beta\delta\beta)\cos 2\theta & (2\alpha\delta\alpha - 2\beta\delta\beta)\sin 2\theta \\ (2\alpha\delta\alpha - 2\beta\delta\beta)\cos 2\theta & 2(\alpha\delta\alpha + \beta\delta\beta)\cos^2 2\theta + 2(\alpha\delta\beta + \beta\delta\alpha)\sin^2 2\theta\cos\phi - 2\alpha\beta\sin^2 2\theta\sin\phi\delta\phi & C \\ 0 & C & D \end{pmatrix} \tag{4.20}$$

where:

1. $C = [2(\alpha\delta\alpha + \beta\delta\beta) - (2\alpha\delta\beta + 2\beta\delta\alpha)\cos\phi + 2\alpha\beta\sin\phi\delta\phi]\sin 2\theta\cos 2\theta$
2. $D = (2\alpha\delta\alpha + 2\beta\delta\beta)\sin^2 2\theta + [2(\alpha\delta\beta + \beta\delta\alpha)\cos\phi - 2\alpha\beta\sin\phi\delta\phi]\cos^2 2\theta$

Let's derive the uncertainties associated to a measurement of I, Q, U Stokes parameters:

$$\Delta \begin{pmatrix} I \\ Q \\ U \end{pmatrix} \equiv \Delta M \begin{pmatrix} I \\ Q \\ U \end{pmatrix} \tag{4.21}$$

The resulting matrix becomes:

$$\Delta M \begin{pmatrix} I \\ Q \\ U \end{pmatrix} \equiv \begin{pmatrix} 2(\alpha\delta\alpha + \beta\delta\beta)I + 2(\alpha\delta\alpha - \beta\delta\beta)\cos 2\theta Q + 2(\alpha\delta\alpha - \beta\delta\beta)\sin 2\theta U \\ 2(\alpha\delta\alpha - \beta\delta\beta)\cos 2\theta I + E \cdot Q + F \cdot U \\ E \cdot I + F \cdot Q + \{2(\alpha\delta\alpha + \beta\delta\beta)\sin^2 2\theta + [2\alpha\delta + \beta\delta\alpha]\cos\phi - 2\alpha\beta\sin\phi\delta\phi]\cos^2 2\theta\} \cdot U \end{pmatrix} \tag{4.22}$$

where:

1. $E = 2(\alpha\delta\alpha + \beta\delta\beta) + 2(\alpha\delta\beta + \beta\delta\alpha)\sin^2 2\theta\cos\phi - 2\alpha\beta\sin^2 2\theta\sin\phi\delta\phi$
2. $F = [2(\alpha\delta\alpha + \beta\delta\beta) - 2(\alpha\beta + \beta\delta\alpha)\cos\phi + 2\alpha\beta\sin\phi\delta\phi]\cos 2\theta\sin 2\theta$

Since the uncertainty on the coefficient transmissions equals to $5 \cdot 10^{-3}$ the standard error on the Stokes parameters I, Q, U are then approximated to:

$$\frac{\Delta Q}{I} \simeq \frac{\Delta U}{I} \leq \frac{\Delta I}{I} \propto \sqrt{(10^{-3})^2 + (10^{-3})^2} \leq 0.002 \tag{4.23}$$

The HWP transmission coefficients uncertainties generate a very low error, at a level of 0.2%, on the estimation of the Stokes parameters. It will be therefore neglected in the estimation of the polarisation of the sky.

4.3 Conclusions

In this chapter I have presented the polarisation efficiency of *NIKA*, characterised in laboratory at Néel Institute before the installation at the IRAM 30 m telescope. During the three polarisation runs of *NIKA* at the telescope two different configurations of HWP have been adopted: the first consisted of a single sapphire plate and the second of a metal mesh HWP. The single sapphire plate showed a high level of instrumental polarisation, especially in the 2.05 mm band. The metal mesh HWP has been further adopted in order to maximise the transmission of the incoming polarised signal over the *NIKA* band and to reduce the instrumental effects due to a non ideal behaviour of the single layer HWP.

The characterisation of this polarisation system showed a quasi-totally transmission of the polarised light in the full *NIKA* bandwidth. For *NIKA2* a similar polarisation system has been conceived and installed at the telescope during the commissioning campaign in October 2015. The commissioning of its polarisation capability is foreseen for the winter 2017.

Part III

The NIKA polarimeter on the sky

5

Observations at the IRAM 30-meter telescope

Contents

5.1 Observational strategies **85**

5.2 Opacity determination and calibration **86**

5.2.1 Skydip 87

5.2.2 Polarised Skydip 88

5.3 Realtime observations **88**

5.3.1 Focal plane reconstruction 88

5.3.2 Focus determination 90

5.3.3 Pointing correction 93

5.4 Polarisation setup at the telescope **94**

5.5 Conclusions **95**

An observational campaign with *NIKA* is generally preceded by a technical campaign to set up the instrument. At the beginning of the observations we need to determine position of the detectors in the focal plane. Furthermore, during observations we need to account for the variable weather conditions and temperature variations in the telescope cabin. These effects may modify the properties of the optical elements inducing changes in the focus and pointing of the telescope. Thus, these changes need to be monitored and corrected for when needed. This chapter explains the procedure of calibration adopted by *NIKA* to estimate the correction of the atmospheric absorption, the focal plane reconstruction and the procedures of focus and pointing. At the end of the chapter we will be presenting the polarisation setup at the telescope together with the constraints in terms of telescope scanning speed in the observation polarisation mode.

5.1 Observational strategies

In order to recover the astrophysical signal we need to modulate it in time throughout a scan on the sky. The scanning strategies adopted by *NIKA* are:

1. **Cross**: used mainly to check the position of the source on the sky and estimate pointing corrections. The telescope scans the source back and forth in azimuth and elevation as represented on left panel of Fig. 5.1.

2. **OTF (On The Fly)**: it consists of a sequence of subscans as represented on the right panel of the Fig. 5.1. The telescope carries out severall subscans moving linearly in azimuth (right excursion) and elevation (declination). For the reconstruction of the focal plane and in particular to map extended sources we prefer to use this scanning strategy. OTF can be also used in equatorial coordinates, *i. e. Right Ascension* (R.A.) - *Declination* (Dec.).

3. **Lissajous**: the sky is scanned following two sinusoidal lines, this method is useful to map in detail a small region of the sky. During a Lissajous the detectors pass on the source $\sim$ 100 % of the integration time while in an "OTF" map they spend a fraction of the time off-source due to instrumental constraints.[1]

Fig. 5.1 shows the three scanning strategies discussed above, where the cross and lissajous strategies are shown in azimuth-elevation plane and the OTF map in equatorial coordinates.

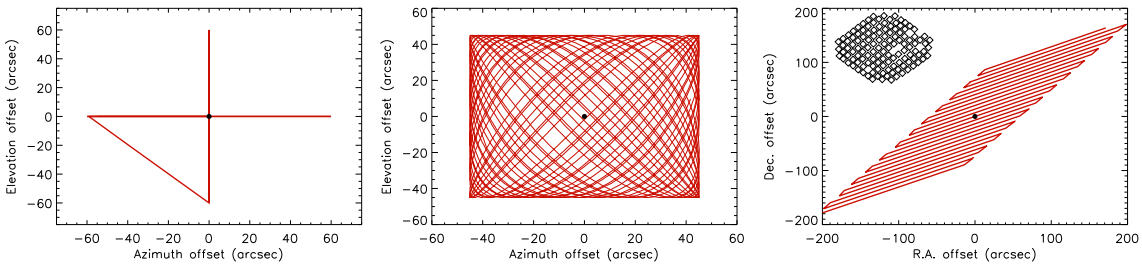

Figure 5.1: *From left to right NIKA observational strategies: the cross (left) and Lissajous (centre) maps are projected in the azimuth-elevation plane and the OTF geometry (right) is oriented in equatorial coordinates (R.A. - Dec.). Credits for the images: [Adam, 2015].*

5.2 Opacity determination and calibration

Observations of the sky in intensity and polarisation can be performed from the ground using specific frequency bands called "atmospheric window", for which the atmosphere is almost transparent to electromagnetic waves. However, atmosphere appears to be the warmest body along the line of sight of ground-based experiments. Water vapour or molecules radiate at radio and millimetre wavelengths. Figure 5.2 shows the *NIKA* spectral transmission and the spectral emissivity of those molecules. These molecules are also involved in turbulent processes, which result in both temporal and spatial correlations between detectors. If treated as an additional noise-like component, atmospheric contamination results in an important additional $1/f$ noise in the time streams of any specific given detector.

The atmosphere emission is circularly polarised light which vanishes in the frequency bands of interest for *NIKA*. Therefore, in the following we will assume the atmosphere unpolarised at the *NIKA* wavelengths. However, it is always possible that it can be transformed into linear polarised radiation due to parasitic instrumental polarisation. Chap. 6 discusses the decorrelation methods

[1]With its 6.5 arcminutes of FoV, *NIKA2* will be immune to that and the Lissajous mode becomes irrelevant.

used in the *NIKA* data analysis software to remove the atmospheric emission contribution from the observations.

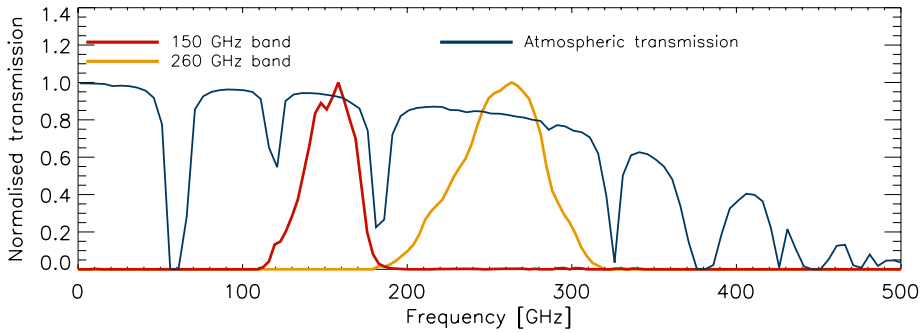

Figure 5.2: *NIKA spectral transmission for the 1.15 mm channel (260 GHz) and for the 2.05 mm channel (150 GHz) are respectively shown in yellow and red. The atmospheric transmission is shown in blue.*

5.2.1 Skydip

It is usual to model the atmosphere emission as a grey body, such that in the Rayleigh-Jeans regime:

$$I_{\rm atm} \propto \nu^2 \cdot T_{\rm atm} \cdot (1-k) \propto \nu^2 \cdot T_{\rm RJ}, \tag{5.1}$$

where $k = e^{-\tau A}$ is the transmission coefficient, τ is the optical depth at the zenith, A the air mass (A $\propto 1/\sin(\delta)$ for δ (elevation) ≥ 30 deg) and $T_{\rm atm}$ the atmospheric temperature. For each KID we can define the resonance frequency in dark condition $(f_0^{\rm ini})_k$ as an absolute resonance frequency defined by the frequency tone. When the strong atmosphere emission is measured by the detectors, their resonance frequency shifts, so that:

$$(f_0)_k = (f_0^{\rm ini})_k + C_k T_{\rm atm}[1 - \exp(-\frac{\tau}{\sin(\delta)})], \tag{5.2}$$

where $(f_0)_k$ is the acquired signal corresponding to the absolute shift in the frequency tone for each pixel. C_k is the optical response of each detector corresponding to the calibration conversion factor measured in Hz/K and T_{atm} in K (Kelvin). The linearity of the KIDs and their short time constants permit to use them as a tau-meter, an instrument that measures the opacity of the atmosphere. We use a procedure called a "Skydip", (see [Dicke *et al.*, 1946]), to scan the sky from 65 to 20 degrees above the horizon in an empty (*i.e.* without strong sources) region of the sky. This permits us to measure the absolute resonance frequency variation on the detectors with respect to the airmass variation.

By performing a fit of the three parameters, $(f_0^{\rm ini})_k$, C_k and τ for all valid detectors at the same wavelengths, we obtain a common sky opacity at the zenith τ. Assuming this common value of τ we can estimate the coefficients $(f_0^{\rm ini})_k$, C_k for each detector. $(f_0^{\rm ini})_k$, C_k are then applied to all the detectors to recover the opacity of any observational scan. This is obtained by inverting Eq. 5.2 as:

$$\tau_{scan} = -sin(\delta)\ln(1 - \frac{(f_0)_k - (f_0^{ini})_k}{C_k T_{atm}}) \tag{5.3}$$

The recovered opacity at both wavelengths permits to correct from atmospheric absorption the observed timelines simply by multiplying by $\exp(\tau_{\rm scan}/\sin(\delta))$. The accuracy of this correction is estimated to be 5% at 260 GHz and 6.5% at 150 GHz [Catalano *et al.*, 2014].

5.2.2 Polarised Skydip

During the observational campaign in polarisation we chose to perform Skydip scans in the polarisation mode configuration. In this way we account for the system (HWP + polariser) transmission efficiency. The Skydip procedure is the same of total intensity observations but in this case the HWP continuously rotates. In Chap. 6 we will see that the presence of a rotating HWP leads to an additional noise due to the modulation of the background signal. In order to correctly estimate the calibration coefficient C_k this latter must be subtracted from the timelines for each sub-scan between different elevation scans. Furthermore, the variation in amplitude of this additional noise with the elevation could indicate the presence of instrumental polarisation varying with the source sky position. In Chap. 7 I will complete the interpretation on the instrumental polarisation effects using polarised Skydip observations.

5.3 Realtime observations

While the skydip is a realtime procedure, the opacity correction (see Sec. 5.2.1) is often applied offline. By contrast the focal plane reconstruction, the focus, and pointing corrections are reduced in realtime, as they are necessary to make observations of quality. The sections below describes each procedure.

5.3.1 Focal plane reconstruction

5.3.1.1 *NIKA*

The natural frequency multiplexing capability of *NIKA* permits us to simultaneously read the detectors through a single transmission feedline but the exact position of each pixel in the focal plane is unknown. Thus, it is necessary to have a specific observation procedure allowing us to reconstruct it. For this purpose we use large OTF maps called "geometries". This permits us to have a map per pixel projected in Nasmyth coordinates (*i.e.* cabin referential frame). The calibration source, typically a planet (*e.g.* Uranus), has a small size compared to our beam and can be considered as a point source. The source is raster-scanned at 60 arcsec/s and each subscan is 420 arcsec long. This scanning speed provides about 10 and 12 points per FWHM at 1.15 mm and 2.05 mm, respectively. Hence it provides an excellent beam sampling. In order to have a clear determination of the beam pattern parameters (position, width and orientation) for each KID, we proceed in two steps:

1. a median filter of approximately 5 × FWHM of width is applied to the detector timelines to subtract most of the atmospheric signal, low-frequency and correlated electronic noise while preserving most of the planet signal (less than 1 % lost at scales smaller than 2.5 × FWHM). These timelines are then projected onto individual maps per detector, and an elliptical Gaussian is fitted on the source. The centroid position provides a first estimation of the pointing parameters of each pixel. The amplitude of the Gaussian gives a calibration in Jy Hz^{-1}, where the shift of the resonant frequency for each detector is reconstructed in Hz units. If the atmospheric absorption is known and accounted for, this becomes a determination of the absolute calibration for each detector. If not, this can still be considered as a cross-calibration of KIDs all at once, and they can be combined to produce a single map of the source. This map provides the position of the source in sky coordinates (*R.A., Dec coordinates*).

2. We then build a template of the low frequency part of the signal (mostly due to sky noise and electronic noise) using all the detectors not detecting the source (typically further

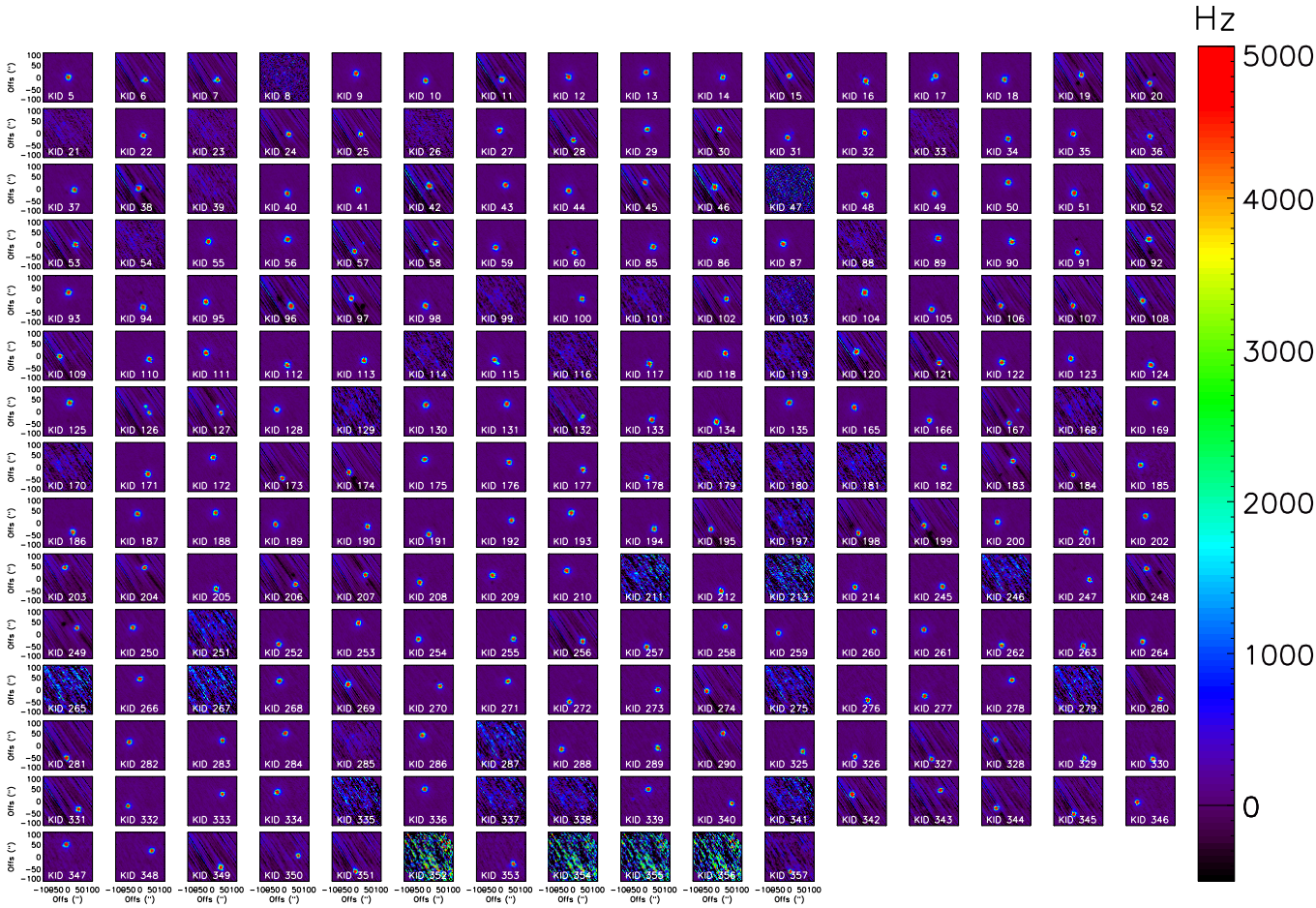

Figure 5.3: *Maps of the planet Uranus per KID used for the reconstruction of the position of the 260 GHz detectors in the focal plane. The maps for which the source is not observed correspond to off-resonance detectors. The pair of detectors 57-58 and 126-127 are excluded from further analysis because they display a double signal due to cross talk.*

than a few beam FWHM, about 30 arcsec). This template is then subtracted from each timeline. This leads to a clean determination of the planet signal, minimising filtering. Timelines are then projected into individual maps per KID, and an elliptical Gaussian fit provides the final pointing parameters and the estimation of the FWHM per frequency band, which is the angular resolution of the instrument.

Assuming that the observed map per KID can be modelled as:

$$M_k(x,y) = (\delta f_0^{max})_k exp(-\frac{(x-x_0)^2+(y-y_0)^2}{2\sigma_k^2}) + n_k \tag{5.4}$$

we determine:

- the position of the detector (x_k, y_k) on the focal plane. This is given with respect to the position of a chosen reference pixel in the centre (x_0, y_0) of the array.
- a measurement of the optical response of the detectors, $(\delta f_0^{max})_k$ in units of Jy Hz^{-1}.
- a first measurement of the beam width σ_k, of each detector and an identification of misbehaving detectors. In particular we search for those affected by cross talk that shows up as double, or triple sources.
- n_k which represents the noise term.

Figure 5.3 shows an example of the maps per pixel obtained for a geometry map of Uranus for the 260 GHz array. From these maps we can identify and discard the misbehaving detectors, which are mainly affected by cross-talk. The reconstructed focal plane for the polarisation *Run* 12 is shown on Fig. 5.4, where on the top left panel it is represented the 260 GHz array and on the top right panel the 150 GHz array. There are 159 and 119 "good pixels" at 260 and 150 GHz, respectively. The distribution of the FWHM obtained by a Gaussian fit on the maps per pixel is shown on bottom of Fig. 5.4. The average FWHM value measured at 260 GHz and 150 GHz is 12.6 ± 0.3 arcsec and 18.5 ± 0.4, respectively. These values are consistent with the expected values of 12 arcsec and 18.2 arcsec.

5.3.1.2 *NIKA2*

The *NIKA2* instrument consists of three arrays of ∼ 1000 detectors each. *NIKA2* was installed at the telescope in October 2015 to enter in its commissioning phase. Figure 5.5 shows the focal plane covered by the three detectors arrays. Only the detectors with high S/N are considered as "good", "bad pixels" with too large noise or elliptical beams are excluded. The number of "good" detectors was measured during the *Run* 15 performed in January 2016 and it results to be 1008, 841 and 907 for the array 1 (first 260 GHz array), array 2 (150 GHz array) and array 3 (second 260 GHz array), respectively. The *NIKA2* camera contains more detectors per array compared to *NIKA*, permitting us to cover a circular FOV of 6.5 arcminutes diameter. Fig. 5.5 shows the reconstructed focal plane of the three arrays at 260 GHz (top), 150 GHz (centre) and 260 GHz (bottom) of *NIKA2* showing more than 80 % of detectors correctly functioning.

5.3.2 Focus determination

In order to optimise the focus of the instrument during the observations at the telescope we use a focus optimisation procedure, consisting of different OTF maps at different positions of the secondary mirror in a given direction. A series of five *Lissajous* OTF maps (see Fig. 5.1)

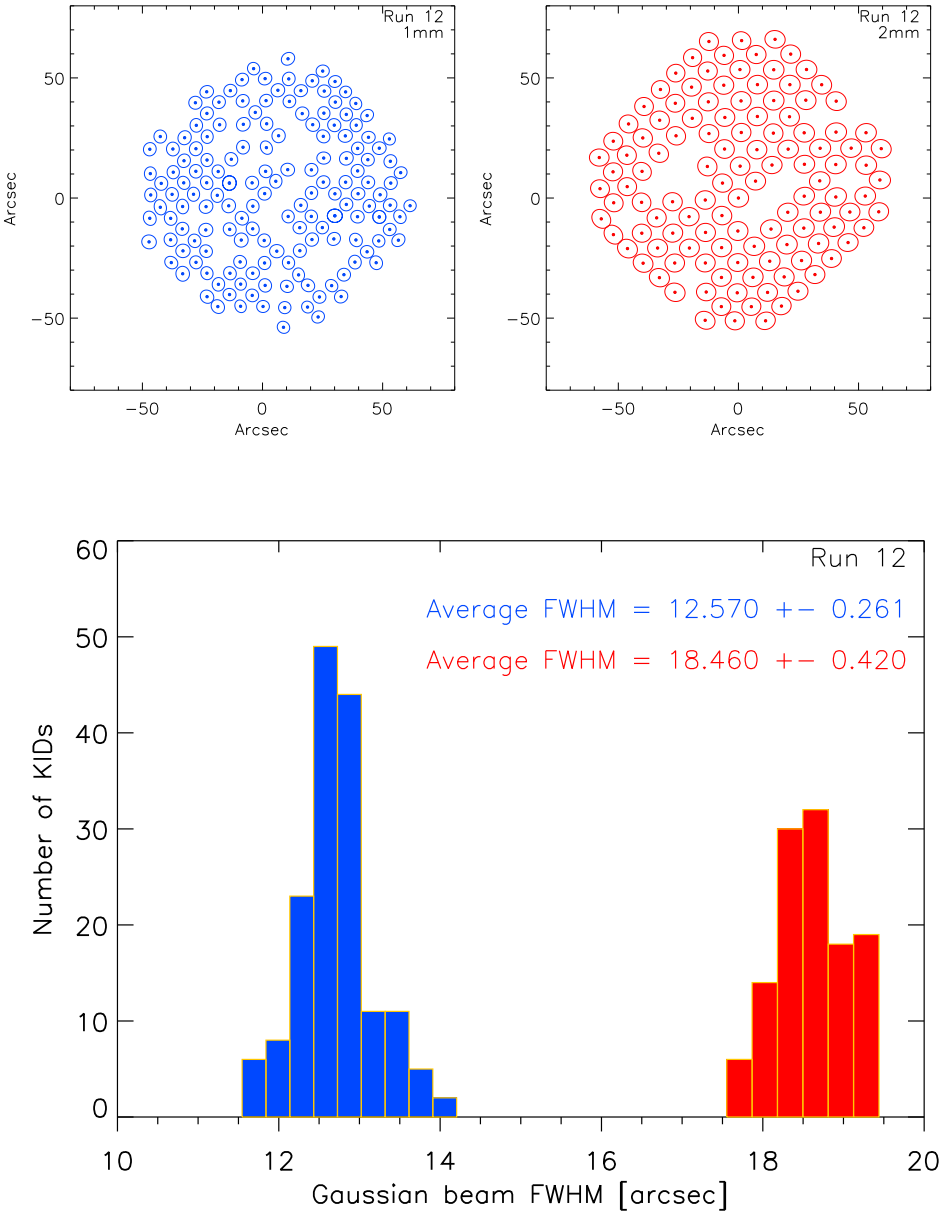

Figure 5.4: **Top**: *NIKA detector position on the focal plane at 260 GHz (left) and 150 GHz (right) for the polarisation Run 12 (February 2015). Beam pattern contours have a diameter of* $1\sigma = FWHM/\sqrt{8\ln 2}$. **Bottom**: *beam FWHM distribution at 260 (blue) and 150 (red) GHz.*

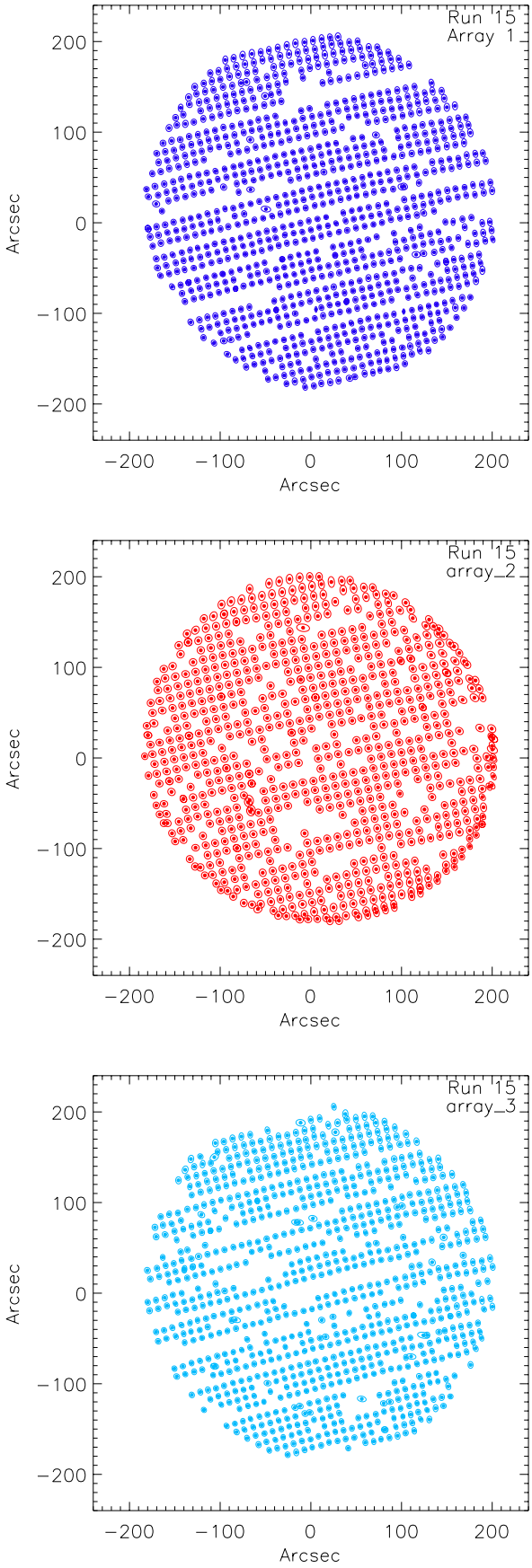

Figure 5.5: *NIKA2 reconstructed focal plane for the 260 GHz array 1 (top), 150 GHz array 2 (centre) and 260 GHz array 3 (bottom). Each circle represents a detector. We excluded from this plot pixels having a too large noise or too elliptic beams. We keep more than 80% of the detectors.*

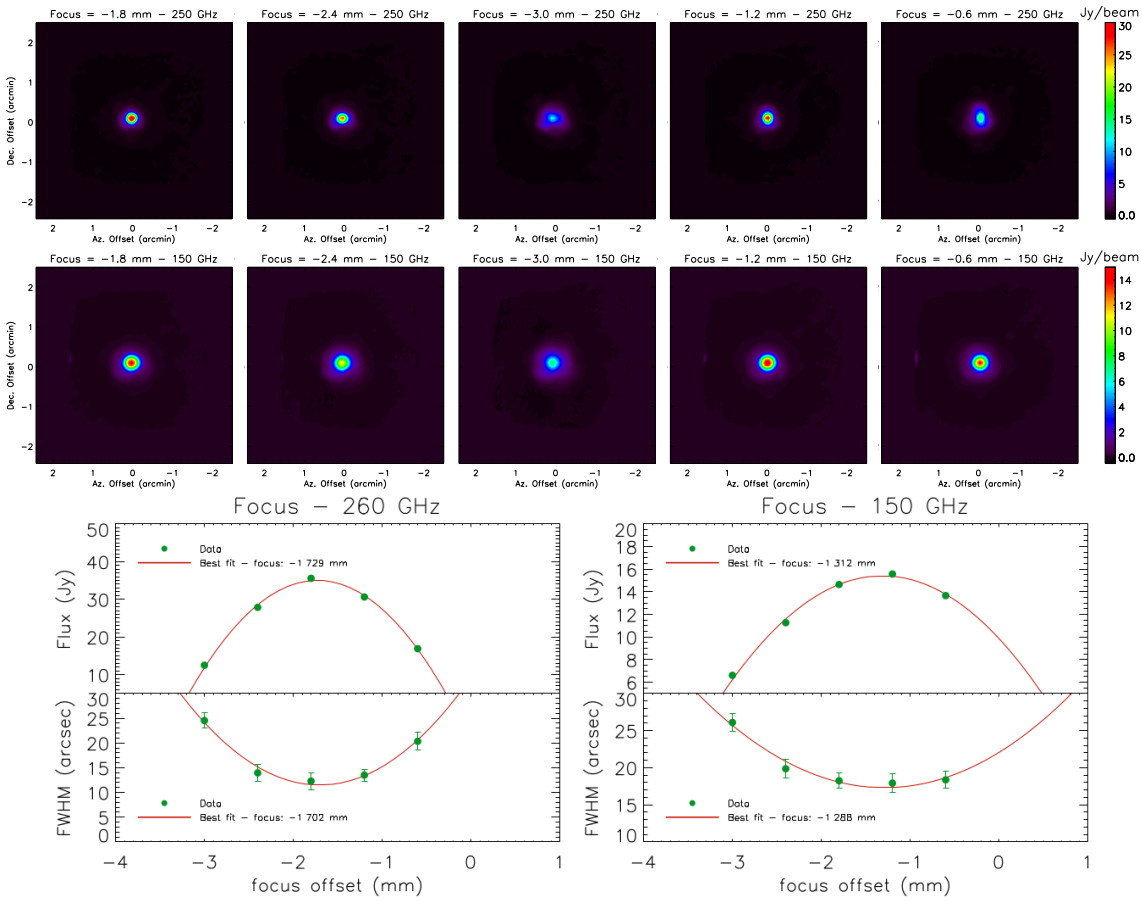

Figure 5.6: **Top**: *Uranus focus maps, at 260 (top) and 150 (bottom) GHz.* **Bottom**: *Measured flux (top) and FWM (bottom) we show in red the best parabolic fit used to determine the optimal focus position at 260 (left) and 150 GHz (right).*

of 1 arcmin × 1 arcmin are performed on a strong source, *e.g.* a planet. Although we are more interested in the determination of the focus with respect to the optical axis, we also test lateral focus in two perpendicular directions. Each scan corresponds to different positions of the secondary mirror in a given direction. For each scan the combined map is fitted to a 2D Gaussian and we compute the FWHM and amplitude of the beam. The best value of the focus corresponds to the minimum of the FWHM or the maximum of the amplitude.

Fig. 5.6 shows the five maps obtained for a focus optimisation procedure performed on the planet Uranus. Finally we fit a parabola to have the best-fit amplitudes and FWHMs in order to determine the best focus position. The focus is repeated every 2-3 hours, specially during the sunset and sunrise because the change of the ambient temperature can deform the telescope mirrors.

5.3.3 Pointing correction

The pointing model of the IRAM 30 m telescope is based on the position of known sources on the sky [Greve *et al.*, 1996]. However, the measured position of sources can vary by few arcsec with respect to the expected one. Thus, we can improve the pointing accuracy by measuring the position offsets from the expected quasar position. In order to calculate the pointing offset

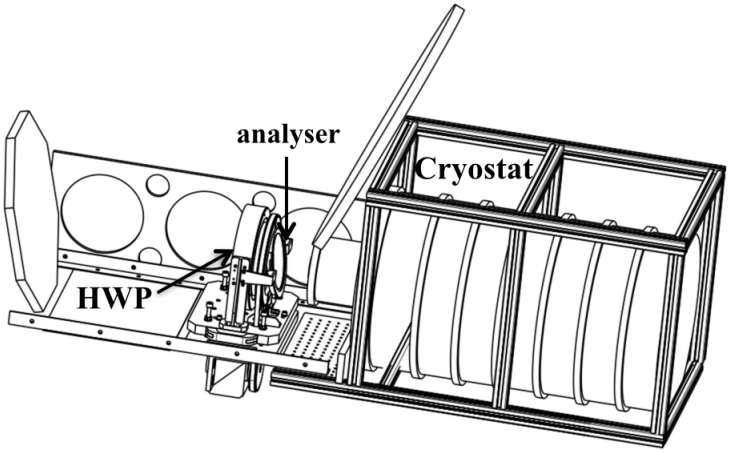

Figure 5.7: *Instrumental setup for polarisation measurements at the telescope. From the left to right the last mirror of the telescope optics, the HWP mounted in a mechanical holder that is actioned actioned by a step motor and analyser tilted by $\sim$ 10 degrees with respect to the HWP and the NIKA cryostat.*

we perform back and forth scans in azimuth and elevation called *cross* (Fig. 5.1). A gaussian fit on the source position gives the shift in azimuth and elevation with respect to the expected position. The offsets are then corrected at the telescope level before observing the target source. Focus, pointing and skydip are the main necessary steps to do observations at the telescope. In total intensity or in polarisation observations these procedures are repeated several times per day to guarantee the best observing conditions.

5.4 Polarisation setup at the telescope

The polarisation setup of *NIKA* has been mounted at the telescope for the first time during a technical campaign in January 2014. Fig. 5.7 shows a schematic representation of the polarisation setup as mounted in the telescope cabin. Polarised light is reflected by the last mirror of the telescope optics and passes through the HWP and the polariser placed in front of the *NIKA* cryostat window. The polariser is tilted by $\sim 10°$ with respect to the optical axis to avoid standing waves with the cold optical filters inside the cryostat. The choice of the HWP rotation speed is constrained by several factors. If the rotation is fast compared to the scanning speed and the angular resolution, all Stokes parameters for a given direction in the sky can be derived quasi-simultaneously, thus rejecting further residual low frequency drifts. Even if the fast rotation places parasitic signals at harmonics of the rotation frequency outside the signal band, we can efficiently correct for this noise, see Sec. 6.3.1. Fast rotation also sets tighter mechanical constraints on the stepper motor and demands a faster data acquisition rate. In order to correctly perform measurements of the polarised signal from the astrophysical sources we have to find a trade-off between the acquisition sampling frequency, the scanning speed of the telescope and the rotation frequency of the HWP. The sky should be sampled with enough samples per beam to satisfy at least the Nyquist/Shannon sampling theorem, usually taken as 3 pixels per FWHM. A correct determination of the three Stokes parameters I, Q, U requires at least 3 samples for a quarter of HWP rotation (n_{points}). The HWP rotational frequency is thus

defined as:

$$\nu_{\mathrm{HWP}} = \frac{f_{\mathrm{sampling}}}{4 \cdot n_{\mathrm{points}}}. \tag{5.5}$$

A single rotation is enough for the determination of Stokes I, Q, U and we can write:

$$T_{\mathrm{pol}} = \frac{1}{4 \cdot \nu_{\mathrm{HWP}}}. \tag{5.6}$$

Considering the most constraining wavelength at 1.15 mm with nominal FWHM = 12 arcsec, we can calculate the maximum scanning speed of the telescope as:

$$v_{scan}^{max} = \frac{FWHM}{T_{\mathrm{pol}} \cdot \mathrm{nyquist}_{\mathrm{points}}}. \tag{5.7}$$

Varying the sampling frequency and points per beam we modify the rotation frequency of the HWP and consequently the scanning speed. For the observations reported in this thesis we used a sampling frequency of 47.68 Hz and we imposed to have 5 samples per beam and 4 samples per quarter of HWP rotation. Consequently we set the HWP rotation frequency at 2.98 Hz and the maximum scanning speed of 26.23 arcsec s^{-1}. These parameters can be modified to increase the scanning speed of the telescope.

5.5 Conclusions

In this chapter I presented the *NIKA* realtime observations. The focal plane determination, the opacity correction, the focus and pointing corrections are the main realtime procedures needed at the IRAM 30 m telescope. In polarisation mode the telescope scanning speed is constrained by the sampling frequency and the HWP rotation frequency. The latter depends on the mechanical characteristics of the mechanical holder. In wide terms, increasing the rotational speed of the HWP we can scan the sky faster. Next chapter presents the dedicated data analysis software for polarisation observations that allows us to recover the polarised signal located at four times the rotational frequency of the HWP and to produce the Stokes parameters I, Q, U maps.

6

A dedicated polarisation data analysis

Contents

6.1 Unpolarised TOI processing 98

6.1.1 Correlated noise 99

6.1.2 Uncorrelated noise: intrinsic detector noise 100

6.1.3 Glitches 100

6.1.4 Noise decorrelation methods 100

6.2 Polarized demodulation map making 101

6.2.1 *NIKA*'s polarised timelines: simulation 101

6.2.2 Demodulation of the polarised signal: the lock-in procedure . . 102

6.2.3 Link with the classical maximum likelihood map making 104

6.2.4 Covariance of the estimated Stokes parameters 107

6.3 Polarised timelines: observations 111

6.3.1 HWP Synchronous Signal correction: HWPSS 112

6.3.2 Map making and demodulation: validation on observed data . . 115

6.3.3 Decorrelation methods applied to an extended polarised source 117

6.3.4 Noise correlation in the decorrelated maps 119

6.4 Instrumental polarisation IP 124

6.4.1 Intensity to polarisation leakage correction 125

6.4.2 Leakage correction on point and extended sources 130

6.5 Conclusions 131

The data analysis software developed for *NIKA* polarisation observations will be now presented. The first stage of this work, described in this chapter, is the construction of a pipeline able to

produce the maps of Stokes I, Q and U. Next chapter we will present how this pipeline was used for both calibration and science purposes.

This polarisation pipeline was built on existing modules developed for total power observations and successfully used in [Adam *et al.*, 2014b; Adam *et al.*, 2015; Catalano *et al.*, 2014]. These modules were developed in particular to subtract atmospheric emission and electronic noise. They are briefly reviewed in Sec. 6.1. The development of specific map making tools for polarisation will be presented relating them to the classical maximum likelihood map making in Sec. 6.2. Before validating its underlying assumptions in Sec. 6.3.2, I will introduce the largest systematic effect that we had to deal with, namely the "Half Wave Plate Synchronous Signal" (HWPSS) (Sec. 6.3). Finally I will show how our first maps of an unpolarised source (Uranus) revealed a non trivial instrumental polarisation effect and how we dealt with (Sect. 6.4.1).

6.1 Unpolarised TOI processing

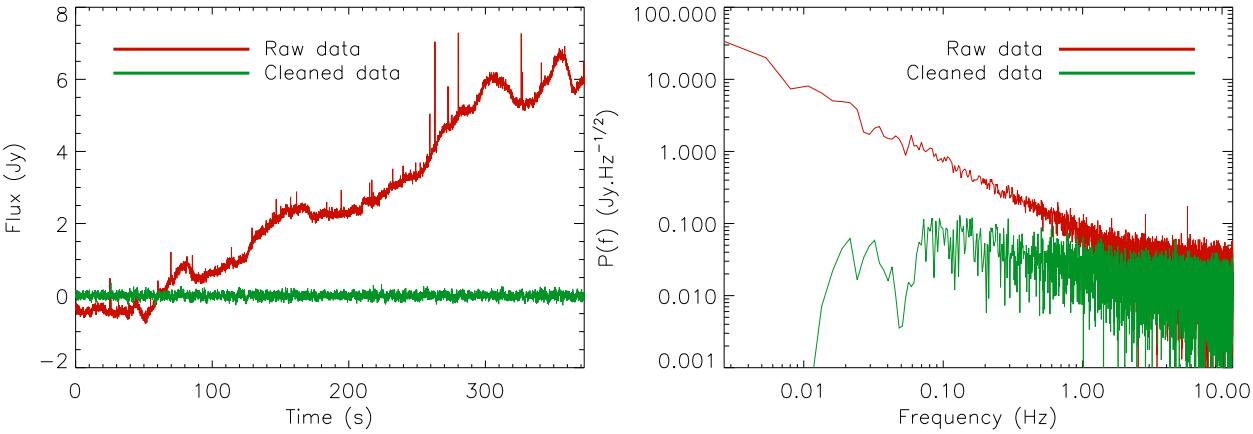

Figure 6.1: *TOIs before (red) and after (green) decorrelation (left panel) and their power spectra (right panel) for a given NIKA detector. Figure borrowed from [Adam et al., 2014b].*

The *NIKA* instrument provided observations in total intensity and in polarisation in the two frequency bands at 150 and 260 GHz. In total intensity a data analysis pipeline was developed to process time ordered information (TOI) [Catalano *et al.*, 2014; Adam *et al.*, 2014b]. In this first section I will briefly introduce the main steps of this data analysis.

The left and right panels of Fig. 6.1 show in red the timeline and the power spectrum of a total intensity observation for a given detector. Before decorrelation the TOI signal appears dominated by the atmospheric emission, which is responsible for the low frequency drifts in the red TOI and the obvious rise at frequency below 1 Hz in the red power spectrum. Cosmic rays hitting the instrument can be seen as spikes in the TOI but they have been removed before computing the power spectra. Pulse tube frequency lines appear at high frequency (> 1 Hz) in the power spectrum and are filtered out in the green line spectrum. The electronic noise dominates at low frequencies between 1-5 Hz in the power spectrum before decorrelation. We can then model the observed signal by a KID k as:

$$\begin{aligned} d_k(t)(f_b,t) &= \mathbf{A}_{t,p} \times S(f_b,x,y) \times \alpha_k \times \gamma^{\rm atm}(\tau^{\rm atm}) \\ &+ \alpha_k^{\rm atm} A_k(f_b,t) + n_k(t) + G_k(t) + \epsilon_k E_k(f_b,t) + C_k(t) \end{aligned} \tag{6.1}$$

where f_b indicates the frequency band considered, 150 and 260 GHz.

- $S(f_b, x, y)$ corresponds to the sky signal at the sky position (x, y). $\gamma^{\rm atm}(\tau^{\rm atm})$ represents the atmospheric absorption, which depends on the atmospheric opacity $\tau^{\rm atm}$. $\mathbf{A}_{t,p}$ is the pointing matrix provided by the telescope pointing data. It is worth 1 if the pixel p correspond to the observed sky position and zero otherwise;
- $A_k(f_b, t)$ represents the atmospheric emission and $\alpha_k^{\rm atm}$ a calibration factor;
- $n_k(t)$ is the detector intrinsic noise;
- additional contributions can be due to spurious signals corresponding to cosmic ray hits in the detectors, called glitches $G_k(t)$;
- $E_k(f_b, t)$ is the electronic noise and ϵ_k the noise electronic response;
- $C_k(t)$ takes into account for any additional noise induced by the cryogenic machines.

The main steps for processing total intensity TOIs are: loading raw data including telescope parameters and pointing; calibrating TOI including atmospheric absorption correction using skydip scans to deduce the opacity (see Sec. 5.2.1); flagging misbehaving detectors; flagging cosmic ray hits; decorrelating atmospheric and electronic noise and map making using inverse variance weighting. Next sections describe the main noise decorrelation methods used in the pipeline. The map making is discussed in Sec. 6.2 in the case of polarisation observations.

6.1.1 Correlated noise

Atmospheric emission The IRAM 30 m telescope observes in specific frequency bands called "windows", for which the atmosphere is almost transparent to mm waves. However, the atmosphere is the warmest body along the line of sight for ground-based experiments; it is expected to be correlated between detectors and can be considered one of the most insidious sources of systematic effects. Moreover, despite the atmospheric signal is expected to be largely unpolarised, optical systematics, such as instrumental polarisation or imperfect half-wave plates, can turn it into polarised signals.

Electronic noise Detectors having the same feedline present the same correlated electronic noise, which contributes both at short and long time scales. As the electronic readout board is made of the superposition of 5 frequency bands, we observe fine structures in the correlation between detectors (see [Adam, 2015] for more details). The electronic noise mixed up with the atmospheric noise complicates the decorrelation procedures. Anyway, the noise power spectrum of this component results in $1/f^{\beta}$ like noise with $\beta \simeq -0.6$. It is possible to subtract this electronic noise component combining detectors of the same electronic band in order to produce a common mode template.

Pulse tube harmonics During the first observational campaigns of *NIKA* the pulse tube used in the cryogenic system produced high frequency ($>$ 1 Hz) mechanical vibrations. These vibrations produced a synchronous signal in the data at the pulsation frequency and its harmonics. Fig. 6.1 on right shows the power spectrum of a TOI after glitch subtraction. The small narrow peaks observed in the power spectrum at high frequency correspond to the signal produced by the pulse tube. To subtract this additional noise the peaks are identified in the power spectrum and fixed to zero in the Fourier space. This effect was significantly reduced in 2013 and for the subsequent observational campaigns.

6.1.2 Uncorrelated noise: intrinsic detector noise

While the atmospheric and electronic noise are correlated between detectors, the KIDs are affected by a decorrelated photon and electronic noise depending on the detectors. This intrinsic detector noise is generally approximatively white after the decorrelation as shown on Fig. 6.1 (green line).

6.1.3 Glitches

Cosmic rays hitting the detectors induce glitches in the data. The time response of KIDs (below 1 ms) is negligible compared to the sampling frequency $F_s = 23.842$ Hz in total intensity observations, such that cosmic ray impacts show up as peaks in the TOI. In order to detect these events, flag and clean them, we use a polynomial fit $p(t)$ in a time $t_1 < t < t_2$ and we estimate the standard deviation of the difference between the data and the polynomial fit. The samples above a threshold detection $n_\sigma = 5\ \sigma$ are interpreted as glitches and removed, satisfying the following condition:

$$n_\sigma \times \sqrt{V[m_k(t) - p(t)]} < |m_k(t) - p(t)|. \tag{6.2}$$

Finally, TOI is linearly interpolated in the glitches affected samples to avoid perturbing in the decorrelation methods. Flagged samples are not projected onto maps. Detectors too noisy or affected by a high level of cross talk, *i.e.* double signal detected, are also flagged.

6.1.4 Noise decorrelation methods

Decorrelation methods are based on the construction of a template, of the correlated signal, named common mode, which is then subtracted from the raw data. Experiments with several hundred detectors permit us to use the detectors that do not see the source (*Off source* hereafter) to calculate a common mode template. This is a great advantage, as filtering effects are significantly reduced in the final maps. In the case of a point source the decorrelation is trivial because we can easily mask the source and use the detectors *Off source* for the common mode model. For extended sources the decorrelation is complicated by the presence of diffuse emission at large angular scales. In the following sections I will describe the decorrelation methods adopted in the *NIKA* pipeline to correct the observations from atmospheric noise, which is always dominant even in good weather conditions. The electronic (correlated) noise is intrinsically subtracted because it is included in the common mode template.

Median common mode Since the atmospheric term $A_k(\nu_b, t)$ has a dominant contribution to the signal, a simple common mode decorrelation method can be used. For example, a median calculated using the TOIs of each sample. We first inter-calibrate the detectors such that:

$$d_k(t) = g_k \times \mathrm{median}_{k'}[d_{k'}(t)]. \tag{6.3}$$

The common mode $C(t)$ is then given by computing the gain g_k:

$$C(t) = \frac{1}{N_{\mathrm{KIDs}}} \sum_{k=1}^{N_{\mathrm{KIDs}}} \frac{1}{g_k} \times d_k(t). \tag{6.4}$$

We therefore subtract the calculated common mode $C(t)$ by linear fitting the coefficients g'_k and a constant term. The decorrelated TOIs are given by:

$$d'_k(t) = d_k(t) - g'_k \times C(t) + \mathrm{constant}. \tag{6.5}$$

The coefficients g_k and g'_k are generally calculated per subscan to account for temporal variations in $\alpha_k^{\rm atm}$. The main disadvantage of this method is that the signal is not accounted for, leading to bias and filtering effects.

Common mode masking the source The main objective of this method is to reduce to a minimum the contribution of the signal in the reconstructed common mode. For this, we can take advantage of the detectors observing the sky outside the source, to build a common mode template to be subtracted from the TOIs. This method is named *"common mode kids out"* in the *NIKA* pipeline. For point source observations a simple circular mask centred on the source can be used. The KIDs outside this mask are used for the common mode template reconstruction. Using this mask and the knowledge of the detector position on the sky at each time t permits us to define the weight function $w_k(t)$ given by:

$$w_k(t) = \begin{cases} 0 & \text{for the KID on source} \\ 1 & \text{for the KID off source.} \end{cases} \tag{6.6}$$

In the case of extended source observation the estimation of the mask is complicated by the diffuse emission at large radii. Therefore, we can apply a basic common mode decorrelation (without mask) for a first iteration and estimate a signal-to-noise S/N map. On this map a significant region of the source (S/N $> 3\ \sigma$) is selected to define the function $w_k(t)$. Although this method reduces the bias of the signal in the common mode template, it is counterbalanced by an increase of the noise where the number of detectors is smaller. If the mask considered is too large the number of detectors decreases to become ~ 1 near the source and consequently the noise increases significantly. A well-defined mask makes this method adapted to extended source observations. In Sec. 6.3.3 we will see how this method is efficient to subtract the correlated noise on an extended source observation. This method is the most commonly used in the *NIKA* data analysis pipeline. By contrast, we will see that for polarisation data the noise decorrelation is not necessary because the polarised signal is extracted at four times the HWP rotation frequency, far from the knee frequency of the atmospheric noise.

6.2 Polarized demodulation map making

In this section, I present the broad lines of the *NIKA* polarisation map making. It fully exploits *NIKA*'s specific polarisation modulation with a continuous and fast rotating HWP. Based on educated simulations, I first introduce the temporal and spectral content of the TOIs during polarised observations. This will be the basis of the "demodulation" and posterior projection of the TOIs onto maps. I then show how this method relates to the classical maximum likelihood map making.

6.2.1 *NIKA*'s polarised timelines: simulation

Adopting the Stokes formalism and assuming that no circular (V) polarisation is present, according to Eq. 2.12, at time t when the telescope is pointing in the direction p, after the HWP and the polariser, a KID, k, measures a combination of the three Stokes parameters:

$$d_k(t) = \frac{1}{2}\{I_p + \rho_{\rm pol}[Q_p \cos(4\omega t + 2\psi(t)) + U_p \sin(4\omega t + 2\psi(t))] + n_k(t)\}. \tag{6.7}$$

Notice that we assume perfect calibration. The noise term $n_k(t)$ accounts for atmospheric and electronic noise. The $4\omega t$ term corresponds to the angle displacement of the HWP with respect

to the polarisation reference frame. We keep calling ωt the position angle of the HWP w.r.t the transmission axis of the polariser, and $\psi(t)$ is the angle between this transmission axis and the local sky meridian is defined from north to east in the equatorial system as:

$$\psi(t) = \tau - \epsilon(t) - \eta(t) \tag{6.8}$$

where $\tau = 45.54°$ is the tilt of the switch mirror of the Nasmyth system, defined in the cabin reference frame, along the elevation axis. $\epsilon(t)$ represents the elevation and $\eta(t)$ the parallactic angle.

As a working example, let us assume that we raster scan a polarised point source with a series of subscans in azimuth (α) at constant increasing elevation (δ) and at constant speed $\dot{\alpha}$. This scanning strategy is pseudo periodic, so the signal content of the timeline will also be pseudo-periodic, showing peaks at harmonics of the subscan frequency. The power spectrum of such a simulated timeline is presented on Fig. 6.2, with a subscan period of few seconds. In addition to these peaks, two important features show up. First, the beam acts like a lowpass. Indeed, assuming a perfect Gaussian beam of width $FWHM = 12$ arcsecond (like we expect at 1.15 mm in *NIKA*), the cut off at high spatial resolution turns into a high temporal frequencies cutoff with typical gaussian width $FWHM_\nu = \dot{\alpha}/2\pi FWHM$. This beam cutoff defines the signal band. Second, the fast modulation by the HWP shifts the polarised content of the signal to higher frequencies and it centres the polarised signal band around the fourth harmonic of the mechanical rotation of the HWP. We observe a broad pattern on Fig. 6.2 around 12 Hz, which also consists in a series of peaks at harmonics of the subscan frequency (like for intensity), damped by the beam like for intensity.

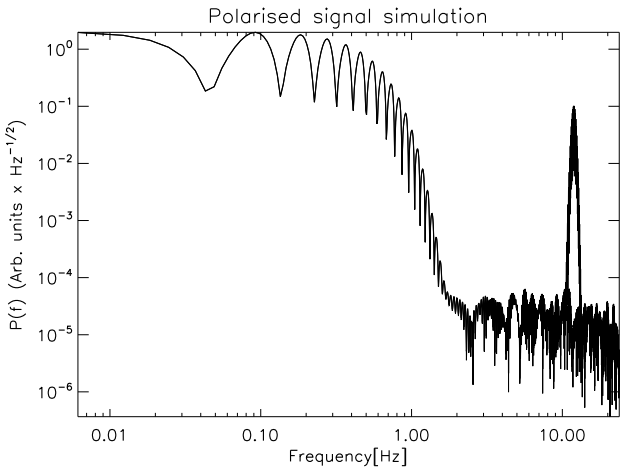

Figure 6.2: *Power spectrum of a simulated TOI for a polarised high signal-to-noise point source observed under a raster scan. The modulation of the HWP in front of a polariser shifts the polarised signal at four times the rotational frequency of 2.98 Hz.*

6.2.2 Demodulation of the polarised signal: the lock-in procedure

We saw in the previous section that when the HWP rotation is fast compared to the scanning speed, the intensity signal band is at low frequencies and the polarisation signal band is well separated and at higher frequencies. It is thus trivial to think that a simple lowpass, above the beam cutoff and below the low tail of the polarised band would produce a timeline with only total intensity and noise. The idea is now to do something equivalent to isolate polarisation

from intensity. The solution is to lock-in the timeline with a reference cosine or sine signal:

$$r_k^Q(t) \equiv \begin{pmatrix} \cos(4\omega t_1 + 2\psi_1(t)) \\ \vdots \\ \cos(4\omega t_k + 2\psi_k(t)) \\ \vdots \\ \cos(4\omega t_N + 2\psi_N(t)) \end{pmatrix}, \quad r_k^U(t) \equiv \begin{pmatrix} \sin(4\omega t_1 + 2\psi_1(t)) \\ \vdots \\ \sin(4\omega t_k + 2\psi_k(t)) \\ \vdots \\ \sin(4\omega t_N + 2\psi_N(t)) \end{pmatrix} \tag{6.9}$$

to extract the Q and U signal, respectively. The basis of this lock-in or "demodulation" map making is therefore to produce three timelines per KID from the raw recorded data: one that is simply low-passed that has no polarisation signal *i.e.* a "pure-I" timeline, one that is a "pure-Q" timeline (locked-in with the cosine reference and low-passed) and a "pure-U" timeline, locked-in with the sine reference and low-passed to remove high frequency noise. The Stokes I, Q and U for a KID k are therefore obtained by:

$$\begin{aligned} d_k(t) \times r_k^Q(t) &= \frac{1}{2}\{I_p \cos(4\omega t_k + 2\psi_k(t)) + \rho_{\rm pol}[Q_p \cos^2(4\omega t_k + 2\psi_k(t)) \\ &+ U_p \sin(4\omega t_k + 2\psi_k(t)) \cos(4\omega t_k + 2\psi_k(t))]\} \\ &+ n_k(t) \cos(4\omega t_k + 2\psi_k(t)), \end{aligned} \tag{6.10}$$

$$\begin{aligned} d_k(t) \times r_k^U(t) &= \frac{1}{2}\{I_p \sin(4\omega t_k + 2\psi_k(t)) + \rho_{\rm pol}[U_p \sin^2(4\omega t_k + 2\psi_k(t)) \\ &+ Q_p \sin(4\omega t_k + 2\psi_k(t)) \cos(4\omega t_k + 2\psi_k(t))]\} \\ &+ n_k(t) \sin(4\omega t_k + 2\psi_k(t)). \end{aligned} \tag{6.11}$$

Using trigonometric relations:

$$\begin{aligned} d_k^Q(t) &= 2 \times d_k(t) \times r_k^Q(t) = 2 \times \{\frac{1}{2}\{\rho_{\rm pol}[Q_p + Q_p \cos(8\omega t_k + 4\psi_k(t)) \\ &+ U_p \sin(8\omega t_k + 4\psi_k(t))] + 2I_p \cos(4\omega t_k + 2\psi_k(t))\} \\ &+ n_k(t) \cos(4\omega t_k + 2\psi_k(t))\}, \end{aligned} \tag{6.12}$$

$$\begin{aligned} d_k^U(t) &= 2 \times d_k(t) \times r_k^U(t) = 2 \times \{\frac{1}{2}\{\rho_{\rm pol}[U_p - U_p \cos(8\omega t_k + 4\psi_k(t)) \\ &+ Q_p \sin(8\omega t_k + 4\psi_k(t))] + 2I_p \sin(4\omega t_k + 2\psi_k(t))\} \\ &+ n_k(t) \sin(4\omega t_k + 2\psi_k(t))\}. \end{aligned} \tag{6.13}$$

The factor "2" accounts for the polarisation loss by using a polariser. After low passing in the Fourier domain we obtain three "pure" timelines I, Q, U. Notice that the polarisation efficiency was estimated to be ~ 1, see Sec. 4. Fig. 6.3 shows the data before and after demodulation. Top panel shows the power spectrum of a simulated timeline for a polarised point source observed under a raster scan with polarisation modulated at four ωt. The bottom panel shows the Stokes Q content after the lock-in, the polarised signal is now isolated by the Stokes I and put at low frequency.

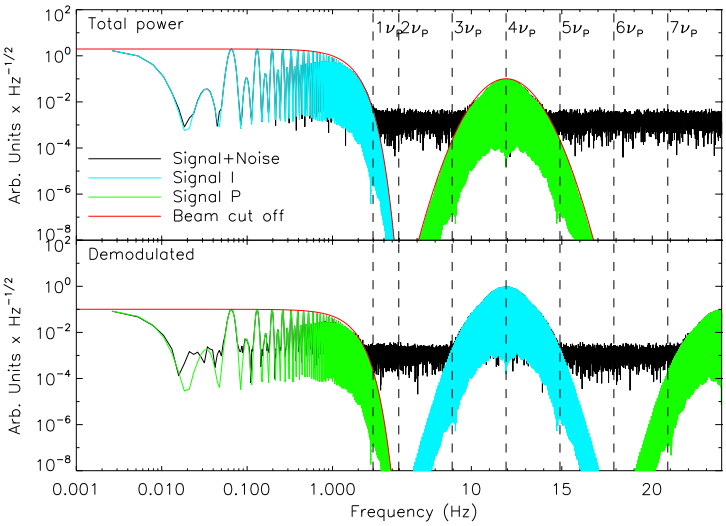

Figure 6.3: *The top panel shows the power spectrum of a simulated detector observed TOI for a polarised point source observed under a raster scan, and polarisation modulation by a continuously rotating HWP facing a polariser. The raw signal plus noise TOI (black) has its total intensity content highlighted in cyan and the polarised content in green. The polarisation signal band is centred on the fourth HWP harmonics while the intensity signal band lays at lower frequencies. On the bottom plot, we present the TOI for "Q" after demodulation (see 6.2.2). We observe that half of its Stokes Q content has been put at low frequency while the Stokes I content and the remaining polarised contents are shifted at frequencies higher than the signal band.*

The "pure" Stokes I, Q, U timelines can then be simply projected onto maps with a simple inverse noise variance weighting.

6.2.3 Link with the classical maximum likelihood map making

Gathering all KID measurements in a single vector and all sky Stokes parameters in a single vector as well, we can generalize Eq. (6.7) to

$$D_t = \mathbf{A}_{tp} S_p + N_t, \tag{6.14}$$

where

$$\mathbf{A}_{t,p} = \frac{1}{2} \begin{pmatrix} A^1_{t,p} & A^1_{t,p}\cos(4\omega t_1 + 2\psi_1(t)) & A^1_{t,p}\sin(4\omega t_1 + 2\psi_1(t)) \\ \vdots & \vdots & \vdots \\ A^k_{t,p} & A^k_{t,p}\cos(4\omega t_k + 2\psi_k(t)) & A^k_{t,p}\sin(4\omega t_k + 2\psi_k(t)) \\ \vdots & \vdots & \vdots \\ A^N_{t,p} & A^N_{t,p}\cos(4\omega t_N + 2\psi_N(t)) & A^N_{t,p}\sin(4\omega t_N + 2\psi_N(t)) \end{pmatrix}, \tag{6.15}$$

$$S_p \equiv \begin{pmatrix} I_p \\ Q_p \\ U_p \end{pmatrix}, \quad D_t \equiv \begin{pmatrix} d_1(t) \\ \vdots \\ d_k(t) \\ \vdots \\ d_N(t) \end{pmatrix}, \quad N_t \equiv \begin{pmatrix} n_1(t) \\ \vdots \\ n_k(t) \\ \vdots \\ n_N(t) \end{pmatrix}. \tag{6.16}$$

Under the assumption that the noise is Gaussian and stationary, the maximum likelihood estimator of S_p is

$$\tilde{S} = (\mathbf{A}^T\mathbf{N}^{-1}\mathbf{A})^{-1}\mathbf{A}^T\mathbf{N}^{-1}D_t \tag{6.17}$$

where $\mathbf{N} \equiv \langle NN^T \rangle$ is the covariance matrix of the noise. This equation involves the computation and the inversion of large matrices: $\mathbf{N}$ typically has $(N_{det} \times N_{samples})^2$ elements. While optimal map making algorithms have been developped in the context of other projects [Cantalupo *et al.*, 2010], they remain computationally expensive. However, if detector noise is white and uncorrelated between detectors, $\mathbf{N}$ becomes diagonal, hence trivial to invert, and Eq. 6.17 can even be solved pixel by pixel. Let us thus assume that we have cleaned the TOI's of atmospheric and electronic noise using the tools presented in Sec. 6.1.4 and that we approximate $\mathbf{N}^{-1}$ by its diagonal $1/\sigma^2_{det}$:

$$\begin{aligned} [\mathbf{A}^T\mathbf{N}^{-1}\mathbf{A}]_{ij} &\simeq \left[\mathbf{A}^T\Delta\mathbf{A}\right]_{ij} \\ &= \mathbf{A}_{li}\Delta_{lk}\mathbf{A}_{kj} \end{aligned}$$

Because of the density of KIDs on the focal plane that ensures high redundancy, thanks to the rotation of the HWP at several Hz and the associated sampling rate at 16 samples per full rotation, the product of cosines and/or sines $\mathbf{A}_{li}\mathbf{A}_{kj}$ becomes vanishingly small and so:

$$\begin{aligned} \mathbf{A}^T\mathbf{N}^{-1}\mathbf{A} &\simeq \begin{pmatrix} \sum_i 1/\sigma_i^2 & 0 & 0 \\ 0 & \sum_i \cos^2(4\omega t_i + 2\psi_i(t))/\sigma_i^2 & 0 \\ 0 & 0 & \sum_i \sin^2(4\omega t_i + 2\psi_i(t))/\sigma_i^2 \end{pmatrix} \\ &\simeq \begin{pmatrix} \sum_i 1/\sigma_i^2 & 0 & 0 \\ 0 & \sum_i 1/2\sigma_i^2 & 0 \\ 0 & 0 & \sum_i 1/2\sigma_i^2 \end{pmatrix} \end{aligned} \tag{6.18}$$

Let us now look at the other term of Eq. (6.17): $\mathbf{A}^T\mathbf{N}^{-1}D$. Now that we replace $\mathbf{N}^{-1}$ by Δ, we are left with computing quantities, such as $\sum_i d_i/\sigma_i^2$, $\sum \cos(4\omega t_i + 2\psi_i(t))d_i/\sigma_i^2$ and $\sum \sin(4\omega t_i + 2\psi_i(t))d_i/\sigma_i^2$, where the i index runs on each sample (regardless of its associated detector) that falls into a given I, Q or U map pixel.

We represent hereafter the term ωt_i with ω_i and the term $\psi_i(t)$ with ψ_i for the sake of simplicity.

Droping the noise term temporarily for clarity:

$$
\begin{aligned}
\sum_i d_i/\sigma_i^2 &= \sum_i (I_p + Q_p\cos(4\omega_i + 2\psi_i) + U_p\sin(4\omega_i + 2\psi_i))/\sigma_i^2 \\
\sum_i \cos(4\omega_i + 2\psi_i) d_i/\sigma_i^2 &= I_p \sum_i \cos(4\omega_i + 2\psi_i)/\sigma_i^2 + Q_p \sum_i \cos^2(4\omega_i + 2\psi_i)/\sigma_i^2 \\
&\quad + U_p \sum_i \cos(4\omega_i + 2\psi_i)\sin(4\omega_i + 2\psi_i)/\sigma_i^2, \\
&= \frac{Q_p}{2}\sum_i \frac{1}{\sigma_i^2} + I_p \sum_i \cos(4\omega_i + 2\psi_i)/\sigma_i^2 + \frac{Q_p}{2}\sum_i \cos(8\omega_i + 4\psi_i)/\sigma_i^2 \\
&\quad + \frac{U_p}{2}\sum_i \sin(8\omega_i + 4\psi_i)/\sigma_i^2 \qquad (6.19) \\
\sum_i \sin(4\omega_i + 2\psi_i) d_i/\sigma_i^2 &= I_p \sum_i \sin(4\omega_i + 2\psi_i)/\sigma_i^2 + Q_p \sum_i \cos(4\omega_i + 2\psi_i)\sin(4\omega_i + 2\psi_i)/\sigma_i^2 \\
&\quad + U_p \sum_i \sin^2(4\omega_i + 2\psi_i)/\sigma_i^2, \\
&= \frac{U_p}{2}\sum_i \frac{1}{\sigma_i^2} + I_p \sum_i \sin(4\omega_i + 2\psi_i)/\sigma_i^2 - \frac{U_p}{2}\sum_i \cos(8\omega_i + 4\psi_i)/\sigma_i^2 \\
&\quad + \frac{Q_p}{2}\sum_i \sin(8\omega_i + 4\psi_i)/\sigma_i^2. \qquad (6.20)
\end{aligned}
$$

Here again, the fast rotation of the HWP and our associated sampling rate make the sums of cosines and sines become negligible compared to the noise weighted averages $\sum_i (I_p/\sigma_i^2)/\sum_i \sigma_i^2$, $\sum_i (Q_p/2\sigma_i^2)/\sum_i \sigma_i^2$ and $\sum_i (U_p/\sigma_i^2)/\sum_i \sigma_i^2$. So, to summarise:

- provided the TOI's have been processed in a way that leaves a residual noise that is close enough to white, $\mathbf{N}^{-1}$ can be approximated by the diagonal matrix of individual detectors inverse variance.

- The fast rotation of the HWP and the high sampling rate leaves negligible off-diagonal terms in $\mathbf{A}^T\mathbf{N}^{-1}\mathbf{A}$ and the diagonal terms reduce to a noise weighted average.

- $\mathbf{A}^T\mathbf{N}^{-1}D$ requires to sum and multiply the data samples by cosines and sines of the polarisation measurement angle, exactly like in the demodulation introduced in Sec. 6.2.2. This "extracts" I, Q and U as constant offsets while averaging out the other components.

In the case of *NIKA*, with its filled array, fast HWP rotation and high sampling rate, if the TOI's are pre-whitened from atmospheric and electronic noise, the maximum likelihood estimator of the Stokes maps reduces to the demodulation estimator, which further justifies our choice.

6.2.4 Covariance of the estimated Stokes parameters

In addition to the projection of I, Q and U maps, we must also estimate their associated uncertainties and covariances. Error propagation in the simple inverse noise weighted coaddition of Sec. 6.2.2 is straightforward and provides the variances on I, Q and U. Let us now estimate the "cross" covariance terms between different Stokes parameters. Although we project the pure-I, Q and U timelines separately neglecting the off-diagonal covariance terms in Eq. 6.18, they are obtained from the same initial detector timelines and can therefore have a non zero correlation. Beside, detectors themselves are partially correlated (see Sec. 6.1.2), and this correlation has to be accounted for as well. Let's compute the covariance between Stokes parameters estimates in a pixel p. The covariance matrix is given by:

$$C_{pp} = \langle \begin{pmatrix} \hat{I}_p\hat{I}_p & \hat{I}_p\hat{Q}_p & \hat{I}_p\hat{U}_p \\ \hat{Q}_p\hat{I}_p & \hat{Q}_p\hat{Q}_p & \hat{Q}_p\hat{U}_p \\ \hat{U}_p\hat{I}_p & \hat{U}_p\hat{Q}_p & \hat{U}_p\hat{U}_p \end{pmatrix} \rangle \tag{6.21}$$

Let's denote by i, j indices that run on detectors and time and that address each sample that falls into pixel p:

$$\langle \hat{I}_p\hat{I}_p \rangle = \frac{1}{\left(\sum_i 1/\sigma_{Ii}^2\right)^2} \sum_{ij} \frac{1}{\sigma_{Ii}^2\sigma_{Ij}^2} \langle n_{Ii} n_{Ij} \rangle \tag{6.22}$$

$$\langle \hat{Q}_p\hat{Q}_p \rangle = \frac{1}{\left(\sum_i 1/\sigma_{Qi}^2\right)^2} \sum_{ij} \frac{1}{\sigma_{Qi}^2\sigma_{Qj}^2} \langle n_{Qi} n_{Qj} \rangle \tag{6.23}$$

$$\langle \hat{U}_p\hat{U}_p \rangle = \frac{1}{\left(\sum_i 1/\sigma_{Ui}^2\right)^2} \sum_{ij} \frac{1}{\sigma_{Ui}^2\sigma_{Uj}^2} \langle n_{Ui} n_{Uj} \rangle \tag{6.24}$$

$$\langle \hat{I}_p\hat{Q}_p \rangle = \frac{1}{\sum_i 1/\sigma_{Ii}^2} \frac{1}{\sum_j 1/\sigma_{Qj}^2} \sum_{ij} \frac{1}{\sigma_{Ii}^2\sigma_{Qj}^2} \langle n_{Ii} n_{Qj} \rangle \tag{6.25}$$

$$\langle \hat{I}_p\hat{U}_p \rangle = \frac{1}{\sum_i 1/\sigma_{Ii}^2} \frac{1}{\sum_j 1/\sigma_{Uj}^2} \sum_{ij} \frac{1}{\sigma_{Ii}^2\sigma_{Uj}^2} \langle n_{Ii} n_{Uj} \rangle \tag{6.26}$$

$$\langle \hat{Q}_p\hat{U}_p \rangle = \frac{1}{\sum_i 1/\sigma_{Qi}^2} \frac{1}{\sum_j 1/\sigma_{Uj}^2} \sum_{ij} \frac{1}{\sigma_{Qi}^2\sigma_{Uj}^2} \langle n_{Qi} n_{Uj} \rangle \tag{6.27}$$

In which n_Q and n_U are the noise terms of the pure-Q and U timelines. In the most general situation, the cross-correlation term $\langle n_{Qi} n_{Uj} \rangle$ is not straightforward to compute. It involves different detectors and samples taken at different times and requires in principle the estimation of the cross-correlation function between different KIDs and at different times. We will proceed in three steps. First, we will discuss the ideal case where noise is white and without KID to KID correlation. Second, we will take the other extreme case where noise has a strong $1/f$ like component and all KIDs are correlated to illustrate the decorrelating power of the rotating HWP. Third, we will show that *NIKA* data are actually close to the ideal case. For the rest of this discussion, we note that the lowpass done at the end of the demodulation to reject high frequency modulated intensity and polarisation left overs does not add noise to the timelines. We can then simplify our math while deriving an *upper limit* to the noise by ignoring the lowpass here and writing:

$$n_{Qi} = n_i \times \cos(4\omega_i + 2\psi_i)$$
$$n_{Uj} = n_j \times \sin(4\omega_j + 2\psi_j)$$

where n is simply the raw detector noise, thus we will consider:

$$\langle \hat{I}_p \hat{I}_p \rangle = \frac{1}{\left(\sum_i 1/\sigma_{Ii}^2\right)^2} \sum_{ij} \frac{1}{\sigma_{Ii}^2 \sigma_{Ij}^2} \langle n_i n_j \rangle \tag{6.28}$$

$$\langle \hat{Q}_p \hat{Q}_p \rangle = 4 \times \frac{1}{\left(\sum_i 1/\sigma_{Qi}^2\right)^2} \sum_{ij} \frac{1}{\sigma_{Qi}^2 \sigma_{Qj}^2} \cos(4\omega_i + 2\psi_i) \cos(4\omega_j + 2\psi_j) \langle n_i n_j \rangle \tag{6.29}$$

$$\langle \hat{U}_p \hat{U}_p \rangle = 4 \times \frac{1}{\left(\sum_i 1/\sigma_{Ui}^2\right)^2} \sum_{ij} \frac{1}{\sigma_{Ui}^2 \sigma_{Uj}^2} \sin(4\omega_i + 2\psi_i) \sin(4\omega_j + 2\psi_j) \langle n_i n_j \rangle \tag{6.30}$$

$$\langle \hat{I}_p \hat{Q}_p \rangle = 2 \times \frac{1}{\sum_i 1/\sigma_{Ii}^2} \frac{1}{\sum_j 1/\sigma_{Qj}^2} \sum_{ij} \frac{1}{\sigma_{Ii}^2 \sigma_{Qj}^2} \cos(4\omega_j + 2\psi_j) \langle n_i n_j \rangle \tag{6.31}$$

$$\langle \hat{I}_p \hat{U}_p \rangle = 2 \times \frac{1}{\sum_i 1/\sigma_{Ii}^2} \frac{1}{\sum_j 1/\sigma_{Uj}^2} \sum_{ij} \frac{1}{\sigma_{Ii}^2 \sigma_{Uj}^2} \sin(4\omega_j + 2\psi_j) \langle n_i n_j \rangle \tag{6.32}$$

$$\langle \hat{Q}_p \hat{U}_p \rangle = 4 \times \frac{1}{\sum_i 1/\sigma_{Qi}^2} \frac{1}{\sum_j 1/\sigma_{Uj}^2} \sum_{ij} \frac{1}{\sigma_{Qi}^2 \sigma_{Uj}^2} \cos(4\omega_i + 2\psi_i) \sin(4\omega_j + 2\psi_j) \langle n_i n_j \rangle \tag{6.33}$$

Ideal case: white noise In this case, $\langle n_i n_j \rangle = \sigma_i^2 \delta_{ij}$. In *NIKA*'s case with high redundancy per pixel and uniform angular coverage, all cross terms in Eqs. (6.28-6.33) vanish but those in $\cos^2$ and $\sin^2$ average to $1/2$. The covariance terms are exactly those derived from the inverse noise weighting coaddition for I, Q and U and covariances IQ, IU and QU are zero.

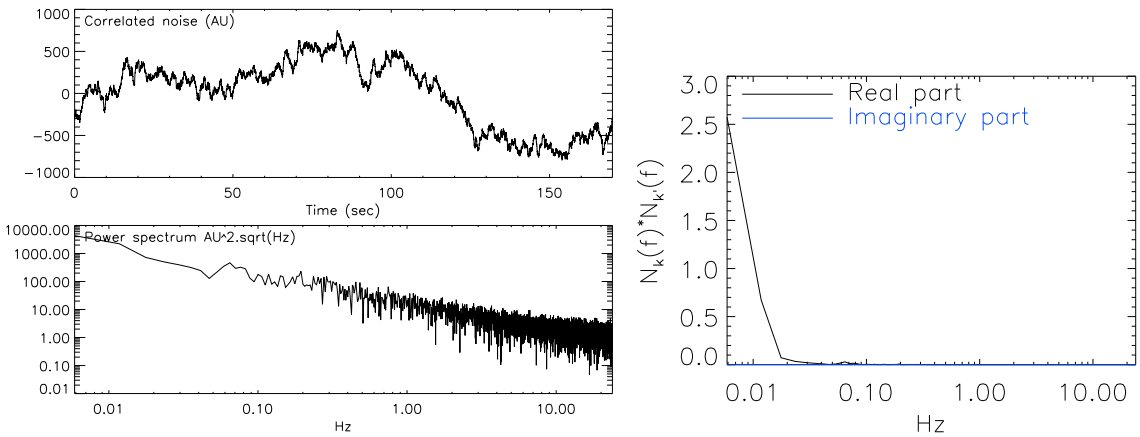

Figure 6.4: **Left**: *$1/f$ timeline with a knee frequency larger than the polarisation modulation frequency to study the propagation of correlated noise up to covariances of Stokes parameters on final maps. Bottom-left: power spectrum of this timeline.* **Right**: *cross-spectrum of two different KIDs. The high rise at low frequency is typical of the simulated correlated noise.*

Worst case: strong noise correlation In order to show how much *NIKA*'s redundancy - both in terms of angles and focal plane occupation - helps producing clean Stokes maps, we here perform a simulation of a worst case scenario, where a strong correlated component between detectors (atmosphere, electronics...) remains in the data and invalidates the white

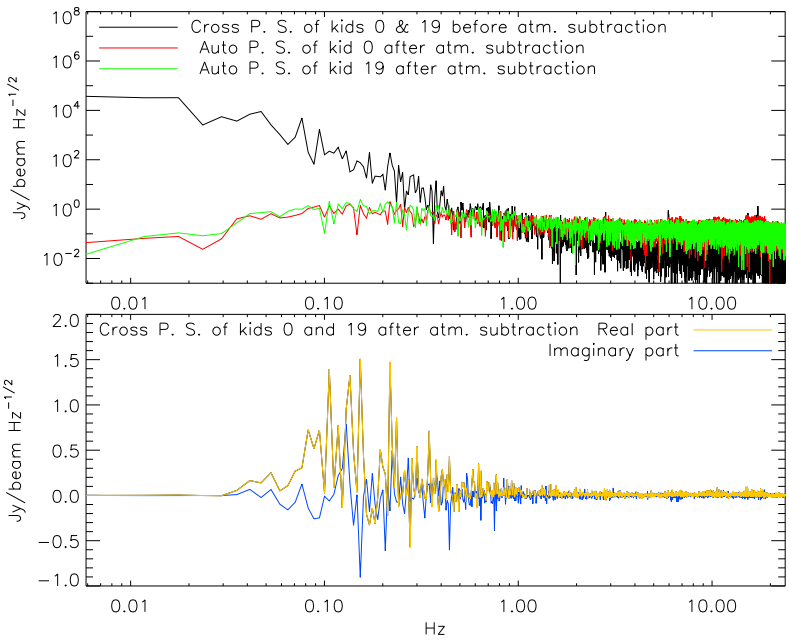

Figure 6.5: **Top**: *The cross-power spectrum of two KIDs before atmosphere subtraction in black shows their high initial correlation. On the same plot, we show the auto-power spectra of the same KIDs after atmosphere subtraction to illustrate how much this correlated component contributes to the signal.* **Bottom**: *Cross-power spectrum of the two KIDs after atmosphere subtraction. The real and imaginary parts of the cross-spectrum are zero on average. They are not strictly zero on this particular realisation, but in any case closer to the white noise case and much smaller than the initial cross-correlation displayed in black on the top plot.*

noise hypothesis. We simulate a $1/f$ noise component with a knee frequency at 15 Hz, well above *NIKA*'s modulation frequency. Each KID timeline is a combination of this noise, with a cross-correlation coefficient set to 1, and we add independent white noise per KID. Such a timeline and its associated power spectrum are presented on Fig. 6.4. These timelines are associated with a true observation scan (of 3C286), hence with an exact observational coverage. We pass these timelines through the pipeline to project Stokes maps, without performing any decorrelation or lowpass. We perform 100 such simulations and derive the final covariances on Stokes parameters (II, IQ, IU, QQ, QU, UU) per pixel from the obtained maps. The result is shown on Fig. 6.6. The intensity variance map sets the scale for how timeline correlation propagates to maps. Clearly, the other covariance terms are much smaller and can be simply ignored. These results can be generalised to the cross pixel covariances as in this case, samples are necessarily taken at different time and so the cross products of cosines and sines vanish.

***NIKA*'s noise correlation** The worst case scenario presented above could be enough to convince ourselves to ignore Stokes parameter cross terms in the covariance matrix. However, it is interesting to note that real *NIKA* data are actually closer to the ideal white noise case. Indeed, the knee frequency of the atmospheric and electronic noise is below 1 Hz while the polarisation band goes from 9 to 15 Hz. Atmospheric and electronic residuals may remain, even after the lock-in and lowpass in the pure-I timeline, but in any case, nowhere near a correlated component like the one simulated in the above paragraph. And indeed, Fig. 6.5 shows the

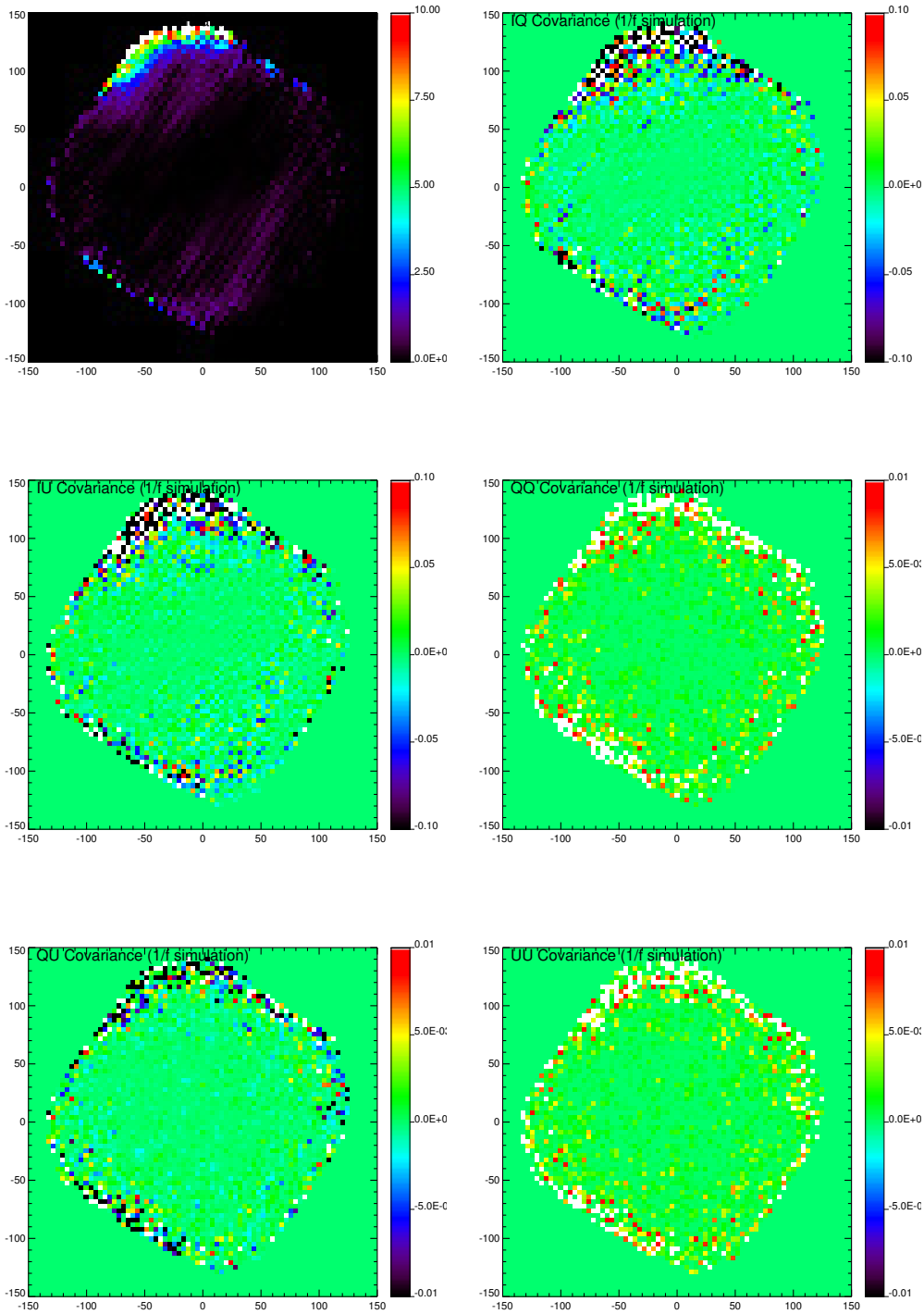

Figure 6.6: *From left to right: Stokes parameters covariances maps II, IQ, IU, QQ, QU, UU derived from 100 simulations of correlated $1/f$ noise like that presented on Fig. 6.4. The diagonal terms II, QQ, UU maps show what is the level of correlated noise propagated to the maps using coaddition. The cross terms IQ, IU and QU maps show how the modulating* cos *and* sin *terms in Eqs. (6.28-6.33) damp the timeline noise correlation by two to three orders of magnitude smaller.*

cross-power spectrum of two typical KIDs on real *NIKA* timelines before and after atmosphere subtraction, that shows small residual cross-correlation compared to Fig. 6.4. On bottom of the figure it is shown the cross-power spectrum of the two KIDs after atmosphere subtraction. The real and imaginary parts result zero on average. Furthermore, in real data we apply the lowpass that rejects any residual of intensity that would be modulated at high frequency in the pure-Q and pure-U timelines. To conclude this section, the fast modulation of the polarisation by the HWP makes covariance cross between different Stokes parameters negligible compared to the standard variances of I, Q and U obtained during the demodulation projection.

6.3 Polarised timelines: observations

In the previous sections we have seen that a continuous modulation of a HWP facing a polariser produces a signal that is a combination of total intensity and polarisation. The polarisation located at four times the rotational frequency ω as explained by the Eq. 3.11 is then obtained by "demodulating" the raw data as explained in the previous section (Sec. 6.2.2) to obtain Stokes I, Q, U timelines. The observations presented in this section and along all the thesis have been obtained with a HWP rotational frequency of 2.98 Hz. Rotating the HWP at this frequency places the polarisation signal well above 2 Hz and permits a natural rejection of the two major low frequency noise components, atmospheric and electronic noise. A raw observed timeline TOI and the corresponding power spectrum are shown on Fig. 6.7. Like in the case of total intensity measurements (see Fig. 6.1) a strong contribution of the atmospheric signal appears with a $1/f$ like spectrum (right panel). Furthermore, an additional noise component appears peaked at harmonics of the HWP rotation frequency ω in the power spectrum (right panel Fig. 6.7).

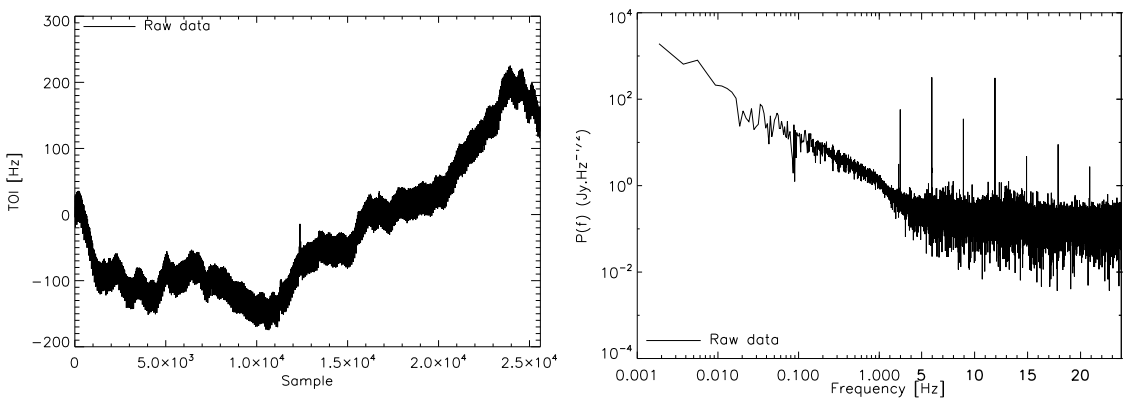

Figure 6.7: **Left** *Time ordered informations (TOI).* **Right** *power spectrum a one detector KID.*

Therefore, Eq. 6.1 describing a KID measurement has to include this additional noise contribution and the signal $S(f_b, x, y)$ includes a modulated polarised signal. We can therefore extend the formalism of Eq. 6.1 to polarisation observations as:

$$\begin{aligned} d_k(t)(f_b,t) &= \frac{1}{2}\mathbf{A}_{t,p}\{I_p + \rho_{\rm pol}[Q_p\cos(4\omega t + 2\psi_k(t)) + U_p\sin(4\omega t + 2\psi_k(t))]\} \times \alpha_k \times \gamma^{\rm atm}(\tau^{\rm atm}) \\ &+ HWPSS(\omega) + \alpha_k^{\rm atm} A_k(f_b,t) + n_k(t) \\ &+ G_k(t) + \epsilon_k(t)E_k(f_b,t) + C_k(t) + \mathcal{IP} \end{aligned} \tag{6.34}$$

The atmospheric $A_k(f_b, t)$, electronic $E_k(f_b, t)$, glitches $G_k(t)$, pulse tube spectral lines $C_k(t)$ terms have been already discussed in Sec. 6.1 for total intensity observations. The additional parasitic signal HWPSS (HWP Synchronous Signal) was expected as it had been already known from experiments like MAXIMA [Johnson *et al.*, 2007] and EBEX [Chapman *et al.*, 2014]. In Sec. 6.3.1 we will see how we model this signal to subtract it from the observations.

Further, a polarisation experiment can present instrumental polarisation $\mathcal{IP}$. In the case of *NIKA*, the $\mathcal{IP}$ is observed to be consistent with an intensity to polarisation leakage. This effect will be discussed in Sec. 6.4.1.

The main steps of the polarisation data reduction pipeline are summarised here (see Fig. 6.8) and discussed in details in the following. Fig. 6.8 shows the scheme of the polarised map making. The raw data as read by the detectors are calibrated and corrected for atmospheric absorption. A deglitching procedure is applied on the observed raw data to avoid the contamination of cosmic rays hits (expected to be 1 per minute). Then, the HWPSS is subtracted at the timelines level. After that, the I, Q, U timelines are obtained by the lock-in procedure. A noise decorrelation, mainly to clean the Stokes I timelines is applied. A deglitching procedure is applied to Stokes I, Q, U timelines to be safe. Finally, the intensity to polarisation leakage correction (detailed in Sec. 6.4.1) permits us to obtain cleaned timelines to be projected onto maps.

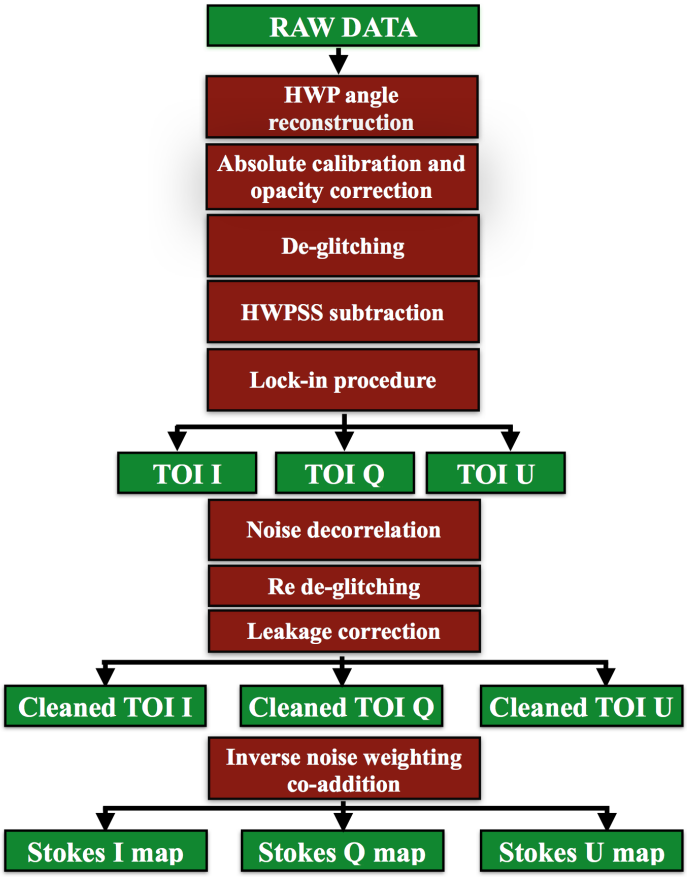

Figure 6.8: *Main steps of the polarisation data reduction pipeline.*

6.3.1 HWP Synchronous Signal correction: HWPSS

This signal, already observed and modelled by Maxima [Johnson *et al.*, 2007] and EBEX [Chapman *et al.*, 2014] shows up as the strongest noise contribution during polarisation observations.

Although the exact origin of this noise is not yet known, it can be explained by a modulation of the background signal due to imperfections of the HWP that lead to a strong additional parasitic signal. During laboratory tests this signal already showed up in the timeline, see Chap. 4. Like Maxima and EBEX, we find that the signal is well fitted by a sum of harmonics of the HWP rotation frequency, ν_P with amplitudes slowly and linearly drifting with time. We can model the HWPSS as a sum of $n = 8$ harmonics of the HWP rotation frequency with amplitudes A_n and B_n:

$$HWPSS(t) = \sum_{n=1}^{8} A_n \cos n\omega t + B_n \sin n\omega t \tag{6.35}$$

where

$$\begin{aligned} A_n &= A_n^0 + \epsilon_{A_n} t \\ B_n &= B_n^0 + \epsilon_{B_n} t \end{aligned} \tag{6.36}$$

and $\omega = 2\pi\nu_P$. We consider up to 8 harmonics of ν_P and explicitly include a linear variation of the amplitude coefficients both for the sine and cosine components when we fit this model to the data.

HWP harmonics amplitudes stability Eq. 6.35 assumes a linear and weak drift in time of the HWPSS coefficients. We have verified this assumption in the data. In order to do that we used a simplified model of Eq. (6.35) to fit the amplitudes A_n and B_n over a portion of 30 seconds of the data. Each point of Fig. 6.9, for an observation scan of Uranus, represents the amplitude fitted for the four main harmonics of HWPSS as a function of time. The cosine A_n (red) and sine B_n (blue) amplitudes show a slow and linear drift in time. We observe that the relative amplitude variation is at most $2 \cdot 10^{-3}$ Jy/s. The assumption done for our model of the HWPSS is therefore validated.

HWPSS vs atmospheric variations Polarisation data appears dominated by HWPSS. This signal may come from thermal emission of the HWP mechanical motor and/or differential transmittance from the HWP and modulated instrumental polarisation. Eq. 3.11 shows that differential transmittance contributes primarily at 2 ω, and polarised signals generated by instrumental polarisation dominate at 4 ω. In order to characterise the variation of this parasitic signal it is interesting to study the amplitudes variation as a function of the atmospheric emission. To do that we take different days of observation of the quasar 3C 286 [1]. Fig. 6.10 reports the total power amplitude $A_n^2 + B_n^2$ for the four main HWP harmonics defined as a function of the atmospheric opacity. We observe a strong correlation with atmosphere variation. The correlation is stronger at 1.15 mm than at 2.05 mm. This can be explained by the fact that the 1.15 mm channel is more sensitive to atmosphere variations because of the water vapor emission [Pardo *et al.*, 2002] (water vapor secondary line at 183 GHz). By contrast, the 2.05 channel is only slightly sensitive to the roto-vibrational emission line of dioxygen (at 119 GHz). As a consequence the correlation between atmospheric variations and the HWPSS amplitudes at 1.15 mm suggests a modulation of the atmospheric signal due to some reflections in the telescope cabin. Anyway, the model described above is able to fit the parasitic signal independently on the atmospheric conditions. For example, the left panel of Fig. 6.11 shows in green the data of Fig. 6.7 obtained after subtraction of the HWPSS using the template technique presented above. The right panel of Fig. 6.11 shows the associated power spectrum (green line). We observe that the parasitic HWPSS is efficiently removed.

[1] Its polarisation properties will be discussed in Chap. 7.

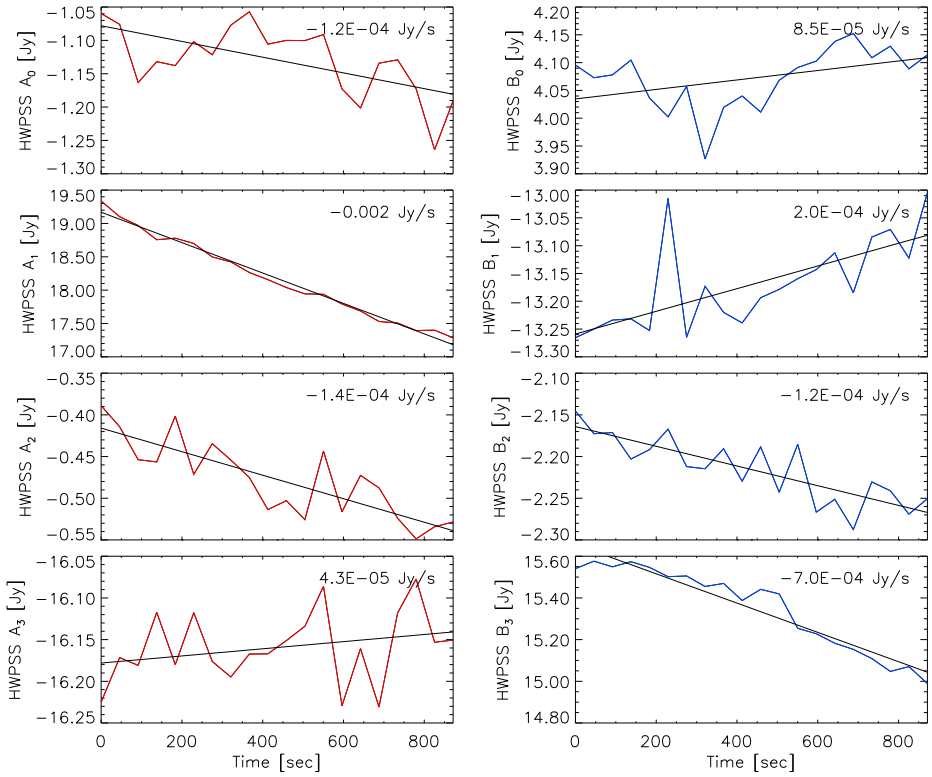

Figure 6.9: *Absolute amplitudes of the four main harmonics of the HWPSS as a function of time. The cosine amplitudes are represented in red and sine amplitudes in blue. Each point is a measure of these amplitudes on a chunk of about 30 seconds of data. The amplitudes show a slow and linear drift in time.*

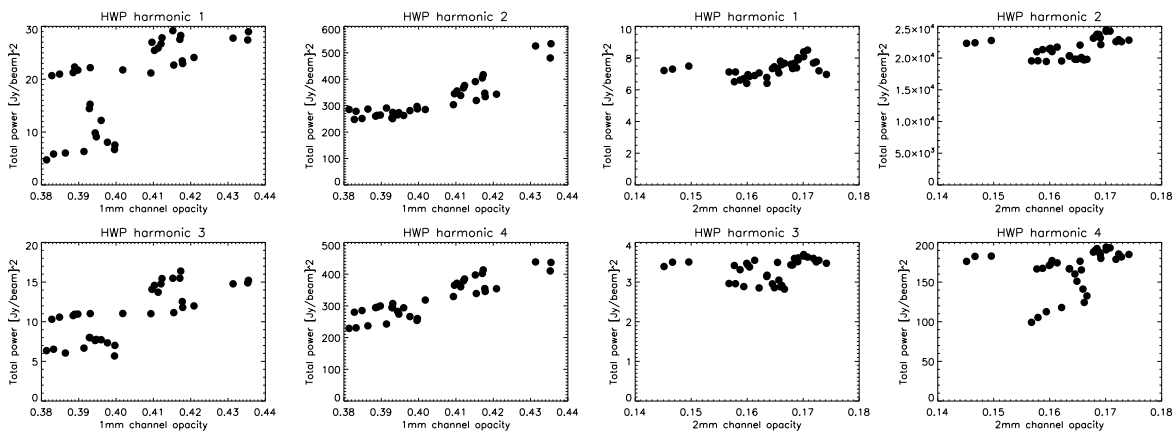

Figure 6.10: *Total power content for the four main harmonics of the HWP. Amplitudes of HWP template harmonics at 1.25 mm (***Left***) and 2.05 mm (***Right***) are represented vs the opacity measured during three days of observation of a quasar.*

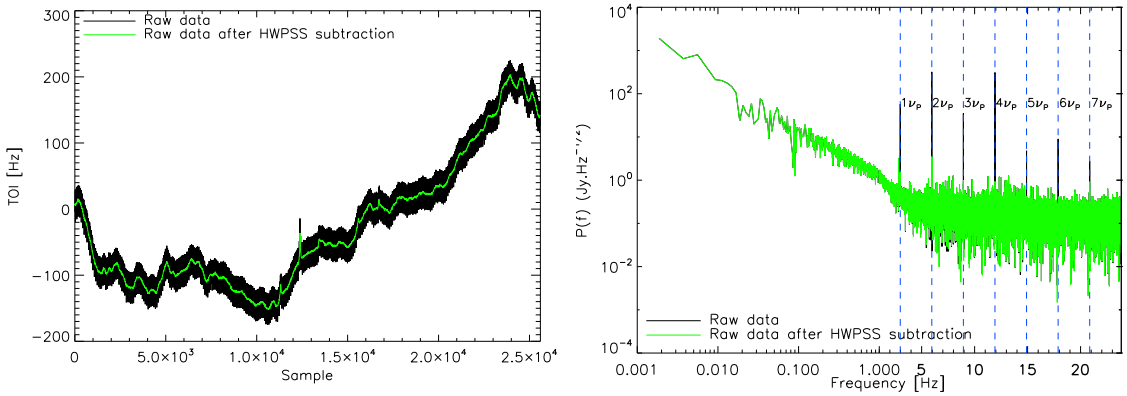

Figure 6.11: **Left** *Time ordered informations (TOI) for one KID before (black) after (green) subtraction of the HWPSS noise.* **Right** *Corresponding power spectrum.*

6.3.2 Map making and demodulation: validation on observed data

Once the most annoying noise is subtracted we can apply the lock-in procedure (explained in Sec. 6.2) to obtain the three Stokes timelines I, Q, U. The lock-in procedure is shown here applied to the timeline presented on Fig. 6.11. The left panel of Fig. 6.12 shows the three timelines I, Q, U obtained after the lock-in procedure and their power spectra are reported on the right panel. The "pure" Stokes I timeline on the top left of the figure corresponds to the intensity signal dominated by the low frequency noise. The central and bottom panels of Fig. 6.12 show the "pure" Stokes Q and U timelines (left) and their spectra (right). For illustration, we also present in red the best-fit $1/f$ like noise spectrum with knee frequency of 1.3 Hz in the Stokes I.

A low pass filter is also applied to the pure Stokes I, Q and U TOIs to reject high frequency noise. The frequency cutoff is set slightly below the HWP rotation frequency. This leads to a significant reduction of the $1/f$ like noise in the pure Stokes I TOI power spectrum and of the residual low frequency tail on the pure Stokes Q and U TOIs.

For illustration, the left panel of Fig. 6.13 shows raw data (black) and HWPSS subtracted data (red) TOIs for a randomly selected set of detectors. The accuracy of the HWPSS subtraction is also confirmed by representing data as observed by different detectors. On the right panel of Fig. 6.13 it is represented in red the HWPSS subtracted Stokes I timeline and the Stokes Q timeline obtained after the lock-in procedure. We confirm that the noise in the "pure" Q and U TOIs is white.

After the lock-in procedure the data analysis pipeline provides to clean data from the low frequency noise. In particular, as discussed above, for the Stokes intensity parameter I. The subtraction of this noise contribution is achieved by using the decorrelation methods developed for total intensity observation and presented in Sec. 6.1.4. In order to compare the efficiency of total intensity decorrelation methods to clean intensity Stokes I in polarisation observations we will use the observations of an extended polarised source, Orion Molecular Cloud (OMC-1). In the next section we will be presenting the resulting Stokes I and Q[2] maps by using the different decorrelation methods.

[2]We report only the Q map but similar results are obtained on U map.

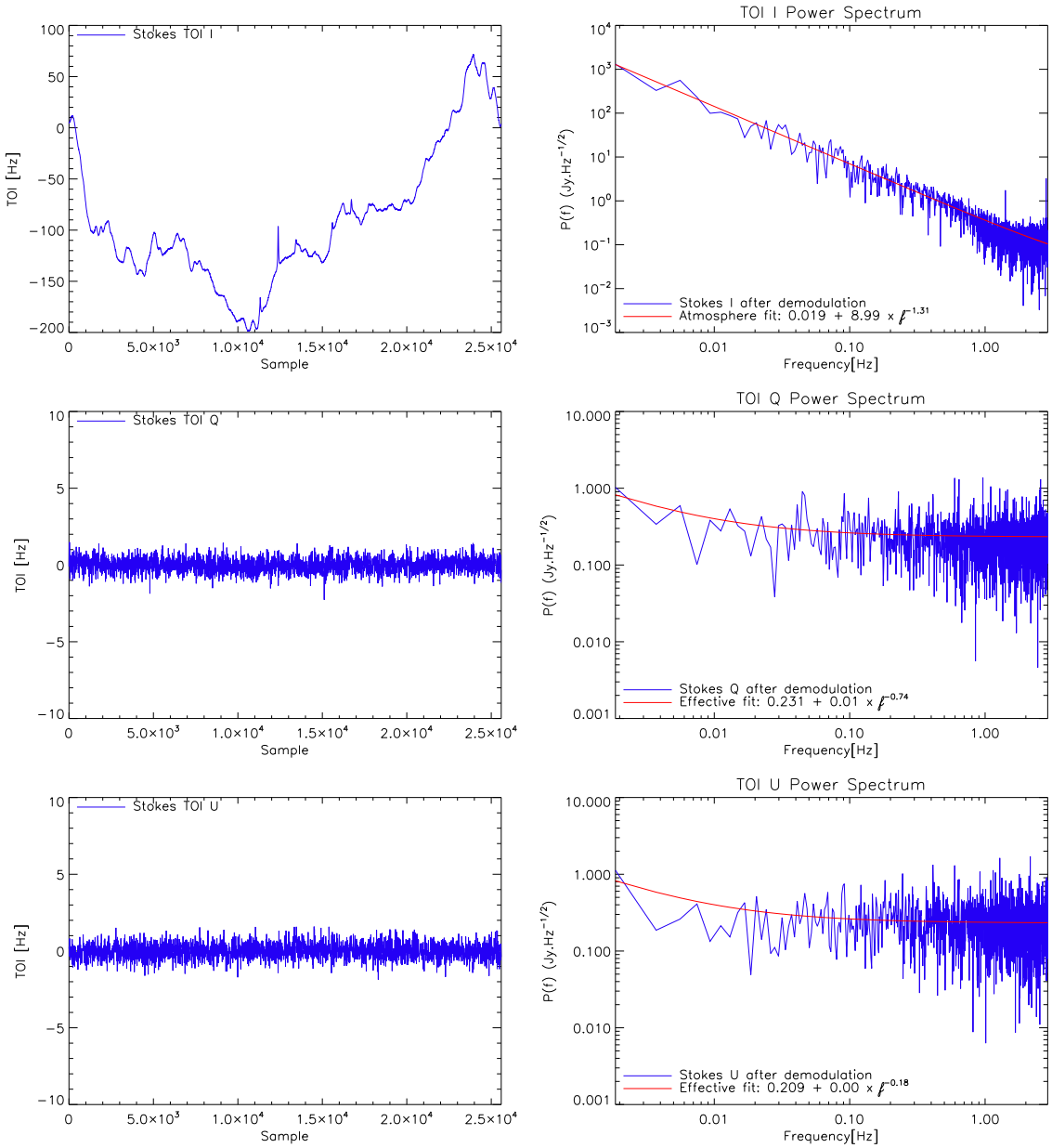

Figure 6.12: *From top to bottom "pure" Stokes TOI I, Q, U obtained after the demodulation procedure (left) and corresponding spectrum (right) for a KID of one observation. A bandpass filter ($[0.01, 2.9]$ Hz) is applied to reject any high frequency noise.*

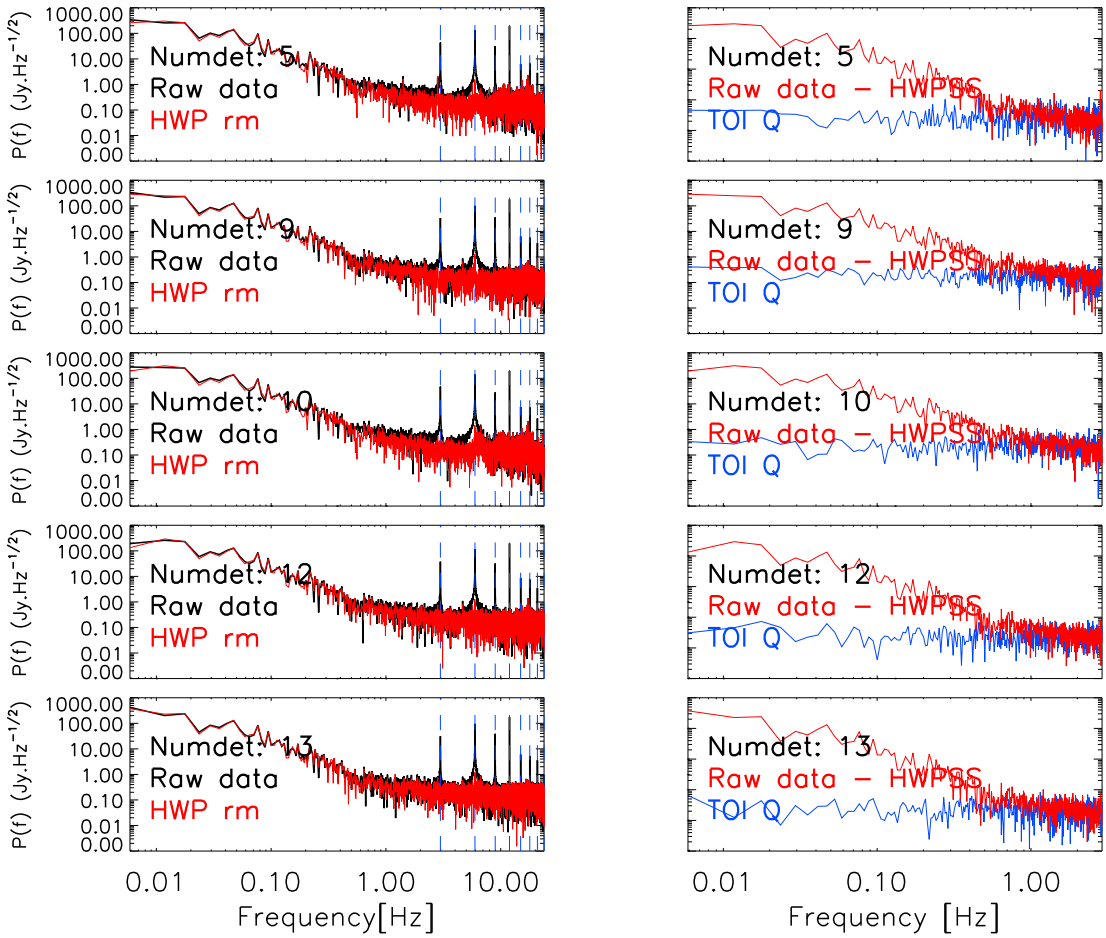

Figure 6.13: **Left**: *power spectrum for five pixels of the raw data (black) and the subtracted data (red) for the HWPSS template.* **Right**: *power spectrum for the same pixels of subtracted Stokes TOI_I obtained after demodulation procedure (red) and of the Stokes TOI_Q (blue).*

6.3.3 Decorrelation methods applied to an extended polarised source

As already introduced for polarisation observations we use the decorrelation methods developed for total intensity observations (see Sec. 6.1.4). For point source observations a simple common mode decorrelation can be applied to clean maps, whereas extended source observations can be biased by the diffuse emission at large angular scales. The method commonly used in the *NIKA* data analysis pipeline is the common mode decorrelation masking the source. To validate this method we use here observations of Orion Molecular Cloud (OMC-1). This strong source at 260 GHz ($\sim$ 48 Jy at the peak) presents a diffuse dust emission.

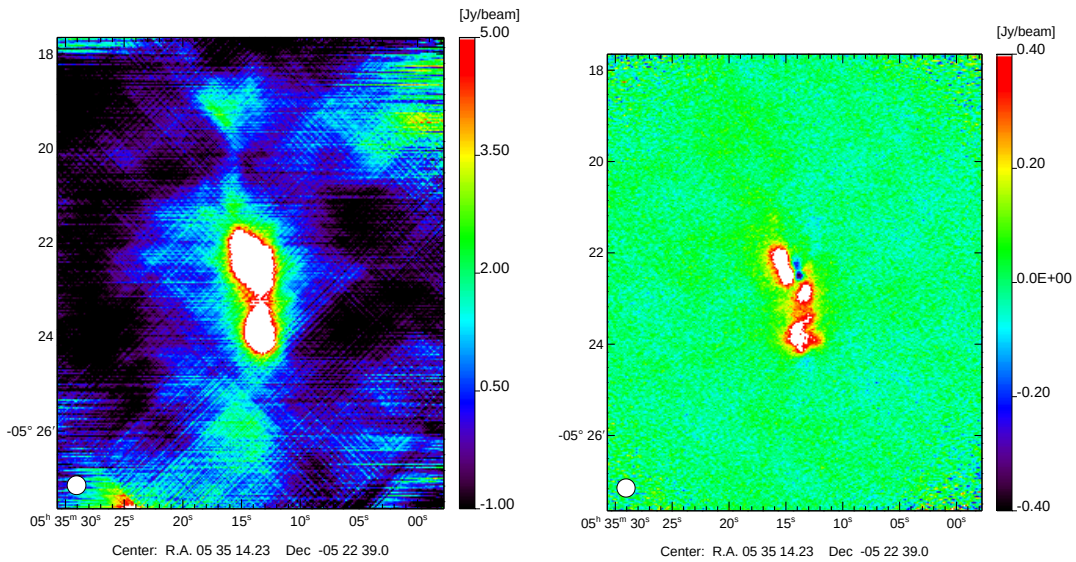

Figure 6.14: *260 GHz Orion Stokes I (left) and Q (right) maps obtained without applying decorrelation techniques. These maps are a combination of 18 OTF scans for a total integration time of $\sim$ 5 hours. In intensity as OMC-1 is a particularly bright source we can clearly distinguish the source in the map. However we observe a strong contribution from low frequency noise. In polarisation, even if the signal is weaker, it can be clearly identified and the noise seems to be uncorrelated pixel-to-pixel.*

Fig. 6.14 shows the map obtained by the combination of 18 OTF scans for a total integration time of $\sim$ 5 hours. As already observed in the Stokes I, Q, U timelines shown on Fig. 6.12, we expect the final maps dominated by a high low frequency noise in intensity I and a residual noise consistent with a white noise on polarised maps Q, U. Indeed, it is what we observe on Fig. 6.14 where the combined Stokes I, Q maps of OMC-1 are obtained without applying decorrelation techniques. Low frequencies noise can be easily identified on large angular scale of the Stokes I map, whereas the noise in Q map (right panel of the figure) does not show evidence of pixel-pixel correlations. The decorrelation does not have effect on polarisation data that are already cleaned by low frequency noise thanks to the detection strategy chosen. However, let us continue the comparison with the other decorrelation methods presented in Sec. 6.1.4.

Median common mode applied to OMC-1 The simple common mode calculated on all detectors reduces the atmospheric signal but it can blend noise and signal. This can produce a subtraction also of the signal. The maps obtained applying this decorrelation method are shown on Fig. 6.15. The Stokes Q map remains are unchanged as expected. Although the Stokes I map is cleaned by the nosiest component, the extension of the diffuse emission is rather vague at large angular scales of the source. At small angular scales the signal appears filtered comparing to the Fig. 6.14.

Common mode decorrelation applied to OMC-1 A common mode decorrelation masking the source could improve the reconstruction of the diffuse signal of the source. A first iteration is done combining all the observational scans of the source to have the best S/N map. In this case the common mode template is calculated using all the detectors. Fig. 6.16 presents the intensity I and polarisation Q maps obtained at the end of this first iteration. Without

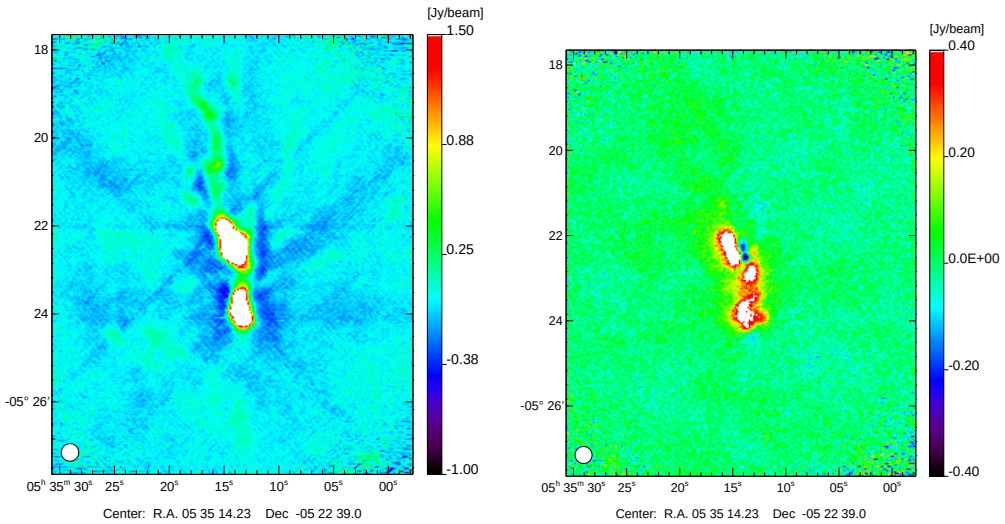

Figure 6.15: *Orion Stokes I map (left) and Q map (right) observed at 260 GHz obtained using a median common mode method to decorrelate the atmospheric noise. The diffuse emission is not yet well defined on large scales of the source in the Stokes I map. The emission in the Q map results unchanged with respect to the Q map shown on Fig. 6.14.*

masking the source the common mode template subtraction shows filtering effect on the edges of the source and the diffuse emission at large angular scales is completely subtracted. However this map can be used to estimate the S/N map and to calculate the mask where S/N $> 3\ \sigma$. For illustration, the Q map is always shown but it is not modified by the decorrelation.

Common mode decorrelation masking the source Finally, a mask on the source allows the determination of the common mode template only using the detectors observing the regions outside the source. Applying this decorrelation method we obtain the maps illustrated on Fig. 6.17. The left panel of the figure shows the intensity map I. In this case the filtering effects around the source are limited because the detectors in this region are not used for the decorrelation. The diffuse signal observed in the north region of the source emission is now recovered together with the emission coming from Orion bar (extended signal at south of the source).

Orion OMC-1 observations confirm that a common mode decorrelation masking the source is well adapted to recover the diffuse emission on extended sources, reducing filtering effects on the edges of the source. For illustration, the timelines in Stokes I, Q, U obtained using this decorrelation method are reported on Fig. 6.18. We clearly note the good subtraction of the low frequency noise in Stokes I, reducing the noise at the zero level. In Q and U we observe a small atmospheric residual emission probably due to a coupling of the atmosphere with the intensity to polarisation leakage, see Sec. 6.4.1.

6.3.4 Noise correlation in the decorrelated maps

Previous sections discussed the most important contributions to the correlated noise. These consist of electronic noise, HWPSS parasitic signal and atmospheric emission. The HWPSS subtraction is done at the beginning of the pipeline process on raw data before the lock-in procedure to obtain "pure" Stokes I, Q, U timelines. Accordingly to this procedure we have

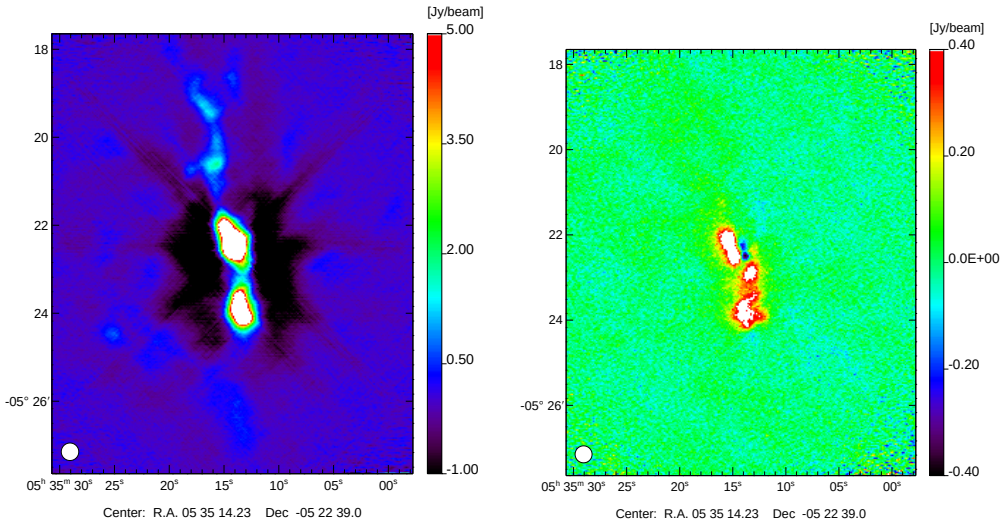

Figure 6.16: *Orion Stokes I map (left) and Q map (right) obtained after the first iteration of the common mode decorrelation without masking the source. In the I map the zero level is not well defined and the subtraction causes filtering effects on the edges of the source. The polarised map is identical to the not decorrelated one.*

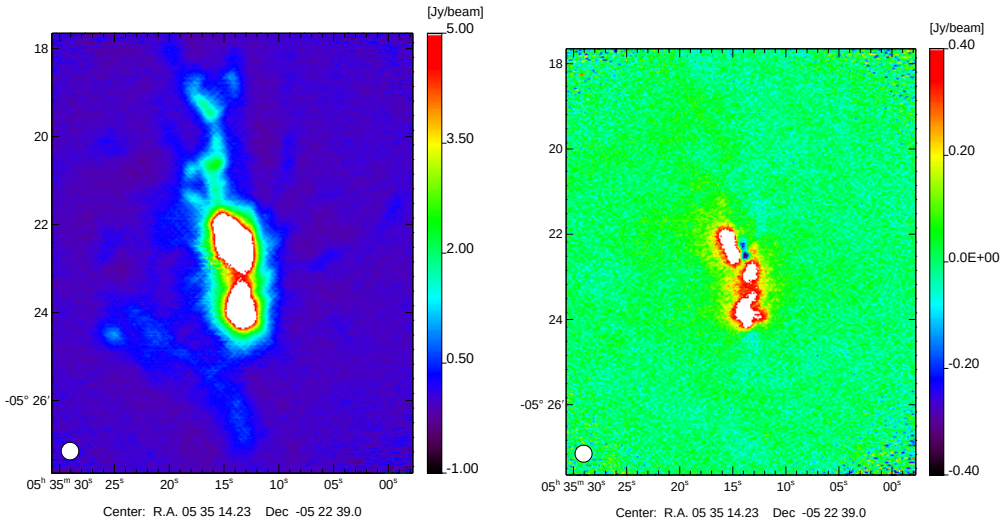

Figure 6.17: *Orion Stokes I map (left) and Q map (right) after the common mode decorrelation masking the source. In this case the common mode template is reconstructed with the detectors off source and the signal on the source is preserved. The polarised Q map is identical to the undecorrelated one. U map not illustrated here presents the same feature.*

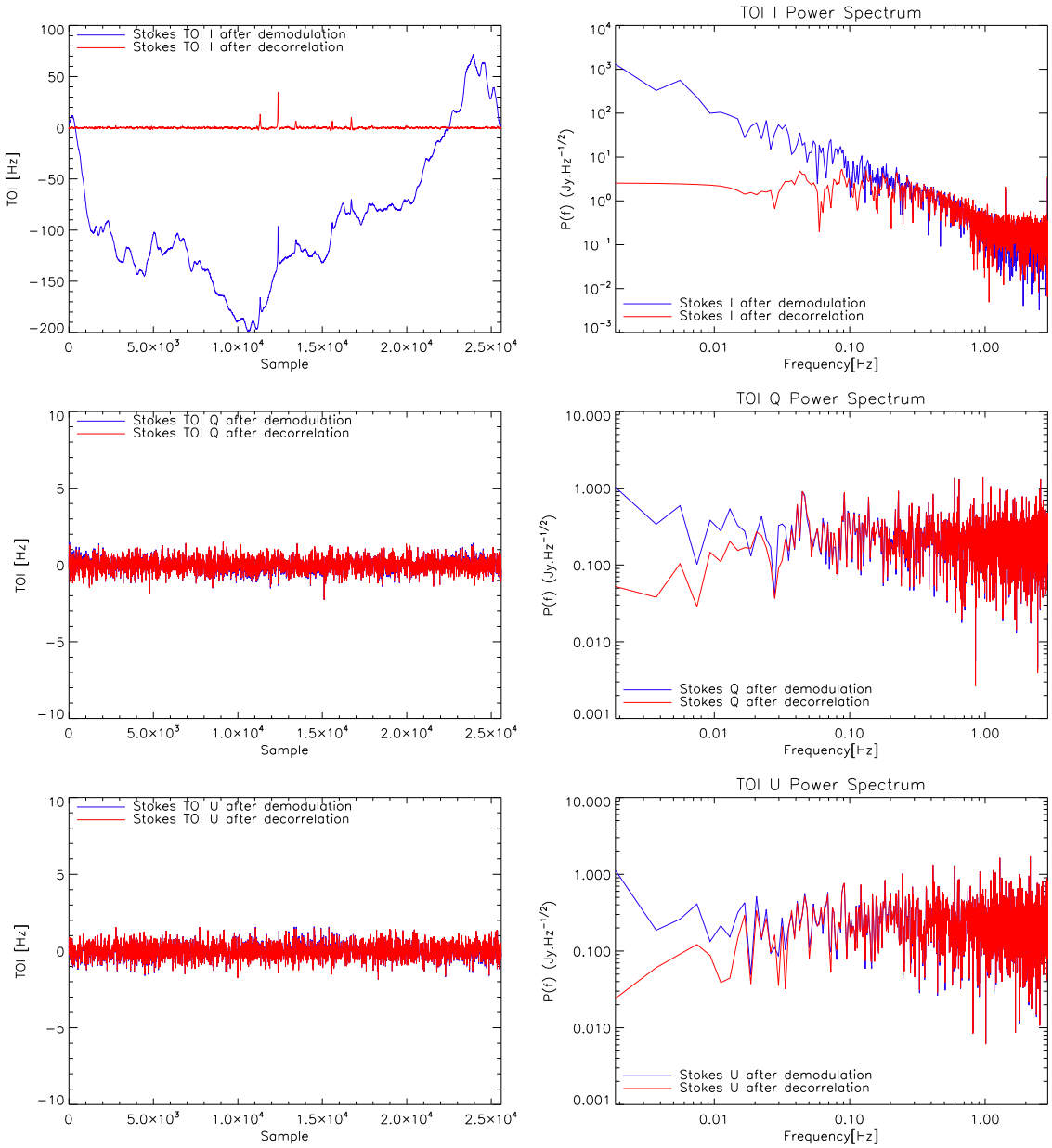

Figure 6.18: *From top to bottom "pure" Stokes TOI I, Q, U (left) obtained after the demodulation procedure in blue and after common mode decorrelation masking the source in red and corresponding power spectrum (right) for a single KID.*

Stokes I timelines showing low frequency correlated noise and white noise in Stokes Q and U timelines. Finally taking advantage of the detectors *off source* we clean the Stokes I TOI subtracting a "common mode template", see Sec. 6.1.4 for details. After decorrelation the Stokes parameters timelines are supposed to be uncorrelated. The aim of this section is to verify this condition. We will validate the assumption done using polarised timeline simulation in Sec. 6.2.4 on real observations. We will discuss here the auto and cross correlation spectra between Stokes parameters timelines: II, IQ, IU, QQ, QU and UU. Under Wiener theorem definition, the Fourier transform of a generic correlation function $R_{xy}(t)$ is equals to the power spectrum $S_{xy}(j\omega)$, which is a complex function of ω. This shows the correlation between two signal $x(t)$ and $y(t)$ in terms of spectrum. For each frequency ω the real part of the power spectrum $S_{xy}(\omega)$ will be:

$$|S_{xy}(\omega)|^2 \leq S_{xx}(\omega)S_{yy}(\omega) \tag{6.37}$$

We can therefore define the correlation coefficients as:

$$\rho^S_{QU} \equiv \frac{S_{QU}}{\sqrt{S_{QQ}S_{UU}}} \quad \rho^S_{IQ} \equiv \frac{S_{IQ}}{\sqrt{S_{II}S_{QQ}}} \quad \rho^S_{IU} \equiv \frac{S_{IU}}{\sqrt{S_{II}S_{UU}}} \tag{6.38}$$

The equality in Eq. 6.37 corresponds to the maximum spectral correlation between the two signals $x(t)$ and $y(t)$. This property permits us to write the covariance terms in Eq. 6.22 as their power spectrum. In the case of uncorrelated noise between samples in I, Q and U the power spectra S_{II}, S_{QQ} and S_{UU} should be consistent with zero. Furthermore, if there is no correlation between Stokes parameters the covariance matrix reduces to a block diagonal and the diagonal elements are directly the simple variance σ_i^2 for each detectors as shown by the matrix in Eq. 6.19. Fig. 6.19 shows correlation coefficients ρ_{IQ}, ρ_{IU} and ρ_{QU} calculated for a single KID for the observation of a quasar 3C 286. We note that the average corresponds to zero in the spectra. In addition auto spectra S_{QQ} and S_{UU} are consistent with a white noise like spectra. This validates the assumption of an uncorrelated noise in QQ, UU, IQ, IU, QU for each KID. Let us now verify the correlation between Stokes parameters in the final maps.

In order to check the contribution of any residual correlation on the final maps, we take a single observational scan of a very weak quasar (3C286) in order to have very low S/N. Then, we estimate the auto and cross correlation spectra on maps: $S_{II}, S_{QQ}, S_{UU}, S_{IQ}, S_{IU}, S_{QU}$. The spectra obtained are shown on Fig. 6.20. We observe an offset value between the power spectrum II and QQ, UU probably due to the detection of a weak signal due to the source on Stokes I map, which is not detected on Q and U maps. Since the dots on Fig. 6.20 represent the negative values of the spectrum we can conclude that the cross correlation between Stokes parameters is consistent with zero. We validate here the assumption of Stokes parameters I, Q, U not correlated to each other on a measured observation map. In this way we can neglect the off diagonal terms in the noise covariance matrices "per pixel", see 6.2.4.

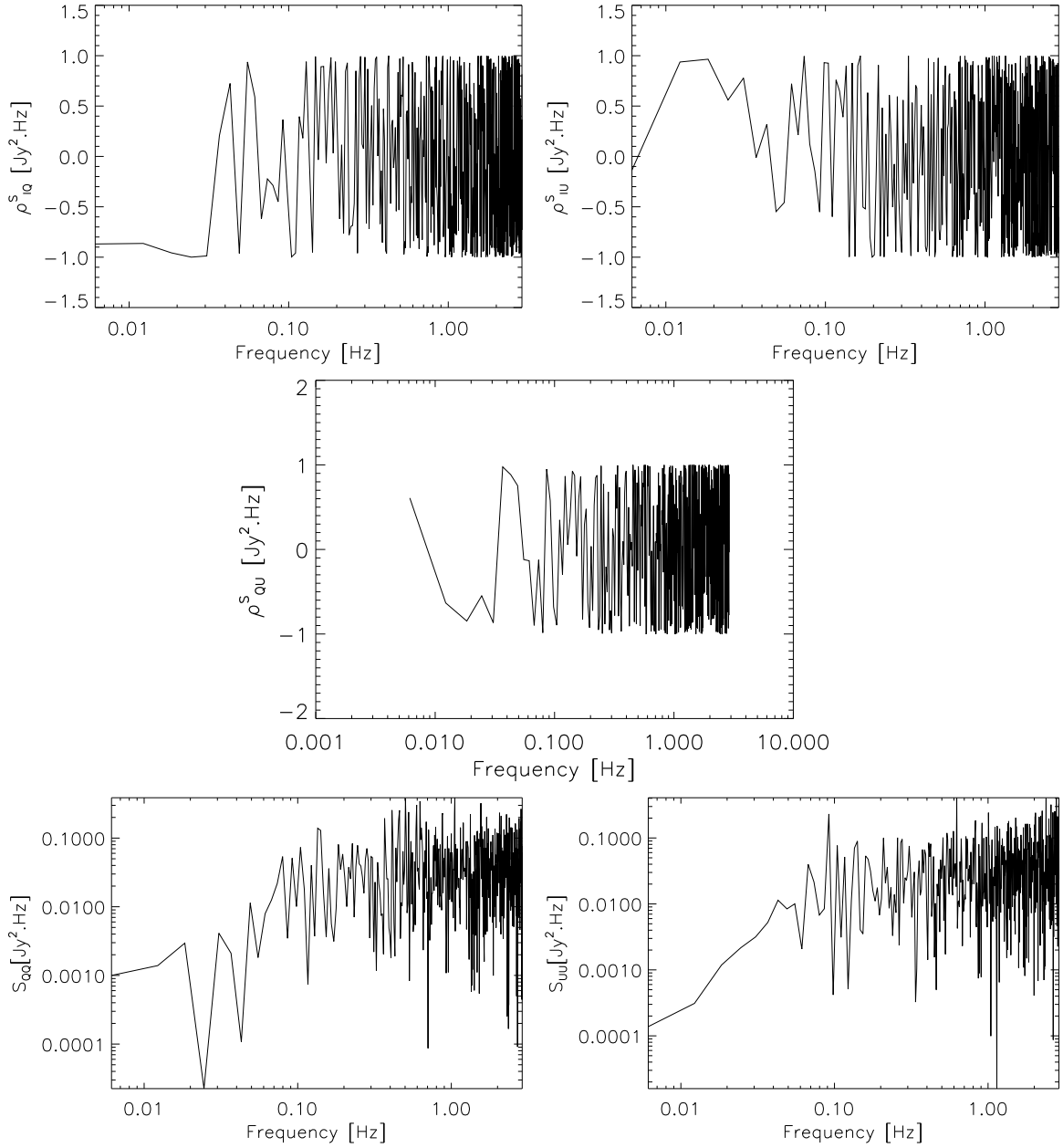

Figure 6.19: **Top**: *correlation coefficients* ρ^S_{IQ}, ρ^S_{IU} *and* ρ^S_{QU}. *Their average is consistent with zero.* **Bottom**: *auto spectra QQ (left) and UU (right). The spectra are consistent with a white noise like spectrum.*

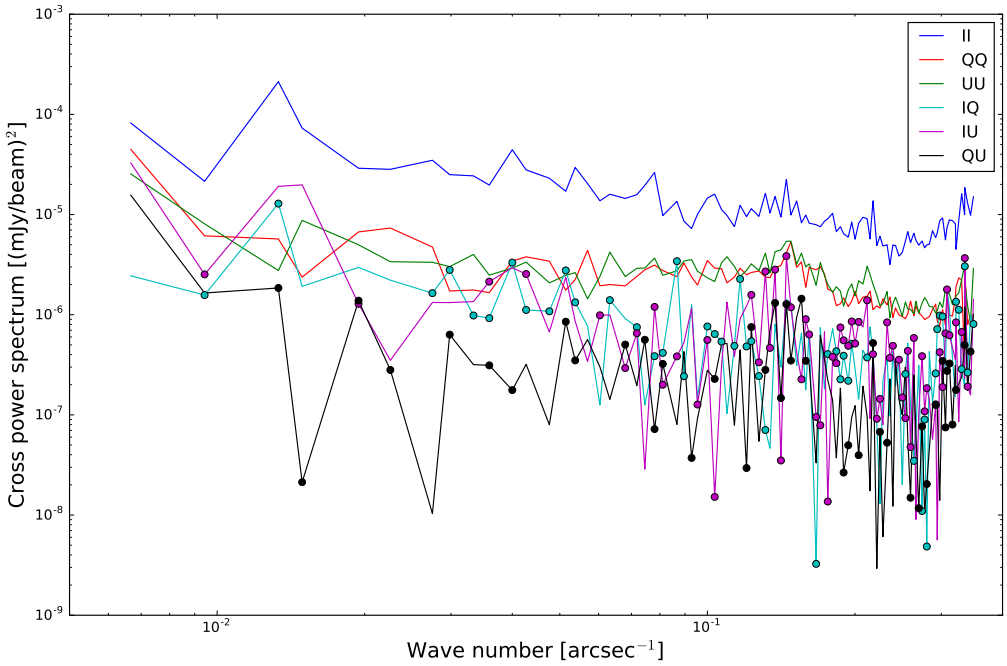

Figure 6.20: *Auto and cross spectra between Stokes parameters maps I, Q, U. The dots represent negative values.*

6.4 Instrumental polarisation IP

In polarisation experiments several instrumental effects may lead to high instrumental polarisation. In this thesis we will call instrumental polarisation any instrumental systematic effect leading to the observation of fake polarisation for an input unpolarised source. In order to estimate the level of such instrumental polarisation at the telescope we have repeatedly observed Uranus, which is expected to be unpolarised [Wiesemeyer *et al.*, 2014] and bright (47.2 Jy at 1.15 mm, 16.4 Jy at 2.05 mm). At the time of observations it had an apparent diameter of 3 arcseconds and can then be considered as a point source compared to *NIKA* beams.

The polarisation observations on Uranus have shown a bipolar pattern (see Fig. 6.21), which consists of a negative and positive signal in Q and U maps. It is partially consistent between the two bands, with a peak to peak amplitude at the level of 3% of the total intensity. Such an effect has already been observed on other experiments, (e. g. XPOL [Thum *et al.*, 2008], BICEP2 [BICEP2 and Keck Array Collaborations *et al.*, 2015], QUAD [Hinderks *et al.*, 2009]). We have performed several observations of Uranus in order to better understand this effect, *e.g.* if it changed with the elevation due to reflections between mirrors in the cabin. Fig. 6.21 shows the Stokes Q, U maps projected in equatorial coordinates (R.A., Dec.) obtained at 150 (top) and 260 (bottom) GHz for two scans of Uranus, respectively. The maps have been performed in two different days. This comparison shows that the bipolar pattern rotates when the source moves on the sky.

Let us verify if this systematic effect is fix in the Nasmyth cabin reference frame. The Uranus maps projected in Nasmyth coordinates are shown on Fig. 6.22. The comparison between the two scans performed at different elevation of the source shows a bipolar pattern with fixed

orientation. Although the origin of this systematic effect is not completely understood, it is probably related to the optics mounted in the telescope cabin. We conclude that this systematic effect does not depend on the position of the source on the sky and it remains constant in terms of its orientation in Nasmyth coordinates.

Furthermore, we observe a difference in terms of flux between the two scans. This could suggest a change in the amplitude of this systematic effect depending on the source position on the sky. This difference can be explained with a variation of the detected flux on the I maps, which can be affected by different atmospheric conditions and as a consequence different atmospheric absorptions. Indeed, comparing the two Q maps we observe a difference of $\sim 15\%$, which corresponds to the calibration error.

We can therefore, at the first order approximation, use the observation of Uranus in Nasmyth coordinates to build a template of the leakage effect to be subtracted to other observations.

6.4.1 Intensity to polarisation leakage correction

Although we still lack a convincing physical interpretation of the observed instrumental polarisation signal, we can model it as leakage from total intensity I into Q and U, and write the observed Stokes parameters in Nasmyth coordinates as:

$$\begin{aligned} \hat{I}_N &= B_I * I_N + \mathcal{N}_I, \\ \hat{Q}_N &= B_I * Q_N + \mathcal{L}_N^{IQ} * I_N + \mathcal{N}_Q, \\ \hat{U}_N &= B_I * U_N + \mathcal{L}_N^{IU} * I_N + \mathcal{N}_U, \end{aligned} \tag{6.39}$$

where I_N, Q_N and U_N are the original sky Stokes parameters in Nasmyth coordinates. B_I represents the *NIKA* beam pattern and $*$ denotes spatial convolution. The different noise contributions discussed above are accounted for in $\mathcal{N}_{I,Q,U}$. Finally, we model the leakage term as the convolution of the original intensity map with beam pattern like kernels $\mathcal{L}_N^{IQ}$ and $\mathcal{L}_N^{IU}$ for Q and U, respectively. These two kernels are directly estimated from the Q_N and U_N maps of Uranus for the observational beam map done on February, 13th and already presented on Fig. 6.22 and 6.21. Note that we do the assumption that there is no modification of the intensity signal and account for any loss of power at the calibration stage.
Let's summarise the algorithm developed to correct for this leakage effect and based on the above model [Ritacco *et al.*, 2016b].

1. With the demodulation and projection techniques presented in Sec. 6.2, we build maps of Stokes I, Q and U of the observed signal in equatorial coordinates. These maps can be the result of multiple observation scans to obtain the best possible signal to noise. We only need the I map in the following to derive the leakage signal that we want to subtract.

2. Rotate the I map into Nasmyth coordinates to obtain $\hat{I}_N$ for a given scan. The needed rotation angle, which is the combination of the elevation and the parallactic angles, varies along the scan. However, we find that not accounting for this variation leads to negligible differences.

3. Build Fourier space convolution/deconvolution kernels of the form $\tilde{\mathcal{L}}_{IQ}/\tilde{B}_I$ and $\tilde{\mathcal{L}}_{IU}/\tilde{B}_I$ from observations of the planet Uranus.

4. Multiply the Fourier transform of I^N by the above kernels and transform the result back into real space to build maps of leakage from I into Q and U.

Figure 6.21: *Uranus 150 GHz (a) and 260 GHz (b) Stokes Q and U maps for the scan 219 (top row) and for the scan 158 (bottom row) projected in equatorial coordinates. The two observational scans shown have been performed at different elevation of the source. The projection in equatorial coordinates shows the rotation of the bipolar pattern.*

(a)

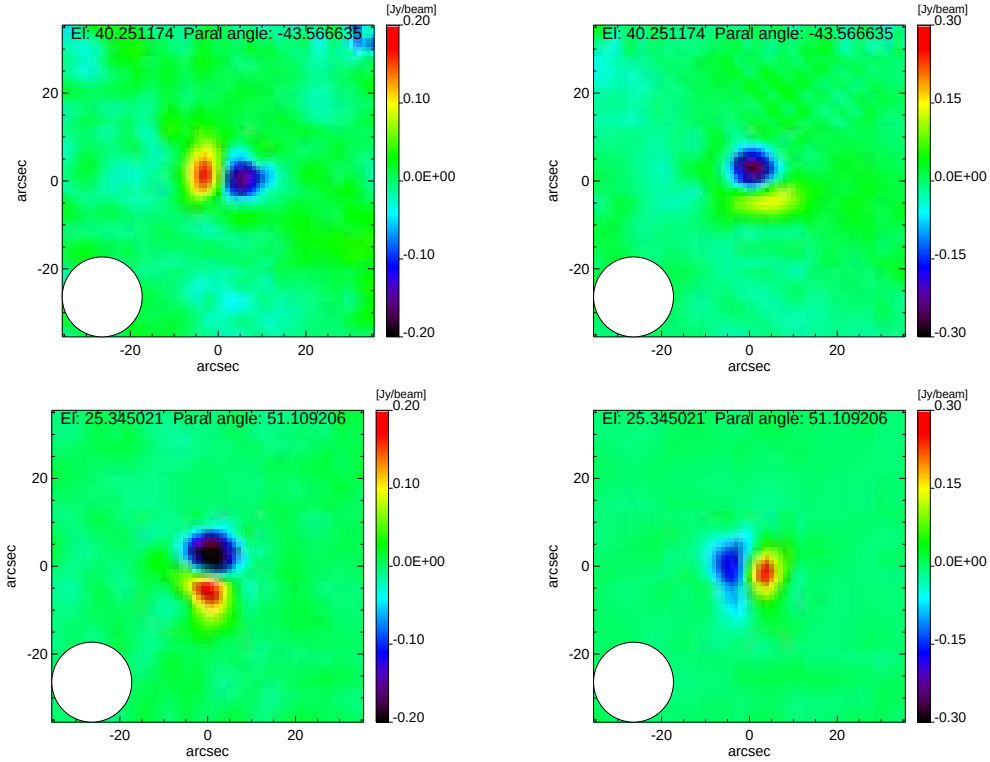

(b)

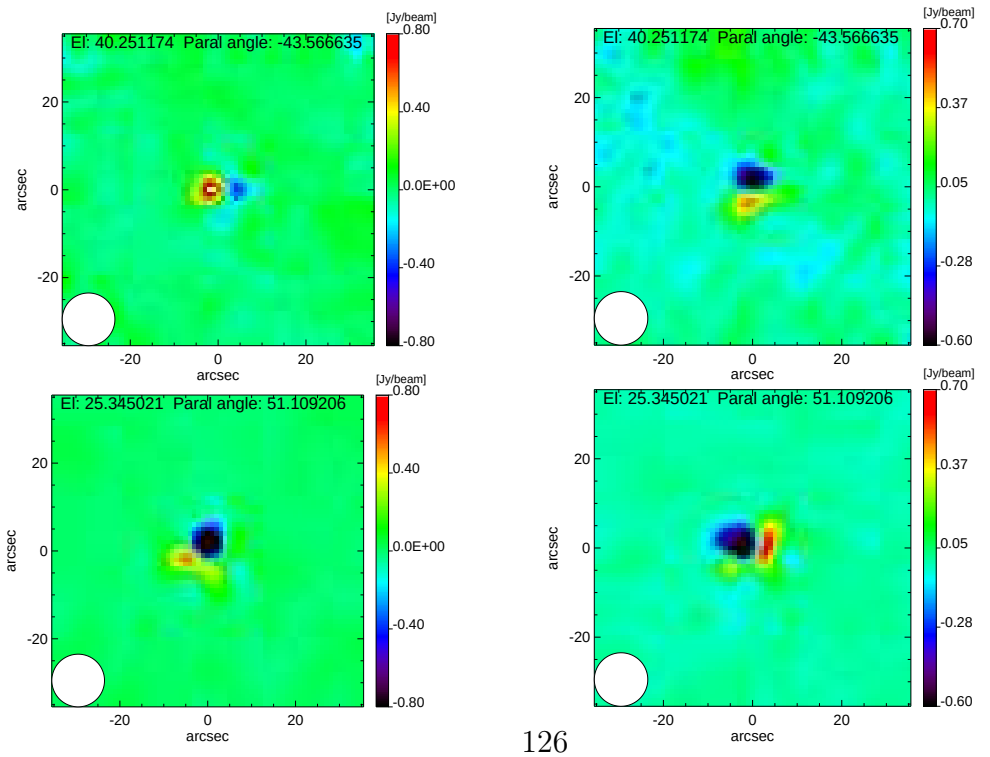

Figure 6.22: *Uranus 150 GHz (a) and 260 GHz (b) Stokes Q and U maps for the scan 219 (top row) and for the scan 158 (bottom row) projected in NASMYTH coordinates. The bipolar pattern appears fixed in this coordinates reference frame.*

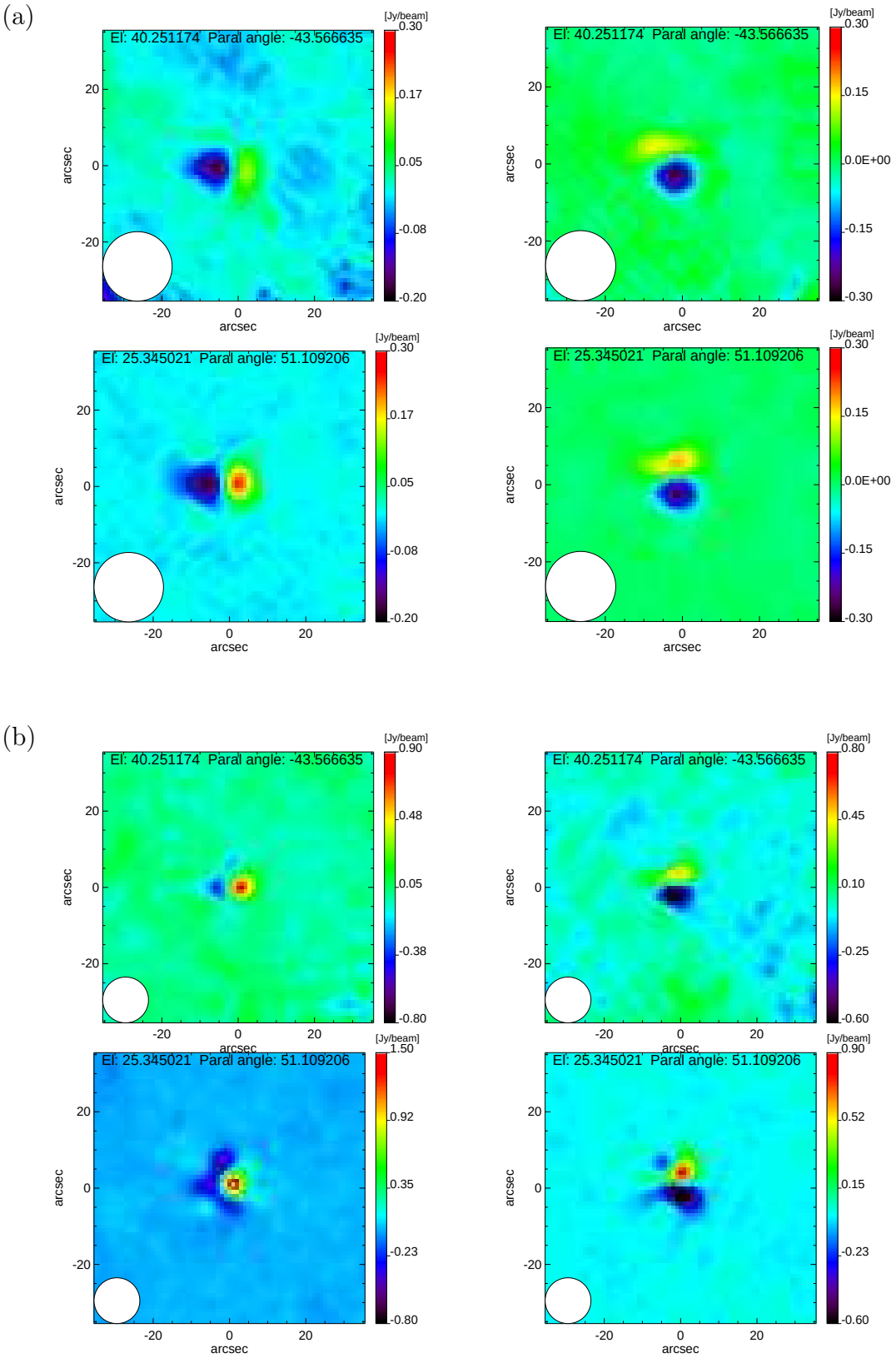

5. Deproject the obtained maps with the actual scanning strategy to produce Q and U TOIs that are then subtracted from the decorrelated pure Stokes Q and U TOIs presented in Sec. 6.2.

6. Project these corrected TOIs onto final maps following the same map making procedure as in Sec. 6.2.

In order to give an example of this correction we report on Fig. 6.23 the Uranus Stokes I, Q and U maps projected in Nasmyth coordinates for an observational scan obtained before (top) and after (bottom) leakage correction. Note that to compute the leakage kernels we use a set of independent Uranus observations to cross check the efficiency of the procedure. We observe that after leakage correction the residual leakage in the Q and U maps of Uranus drops below 1 %. This residual can be interpreted as "straightforward" instrumental polarisation, *i.e.* an induced polarisation directly proportional to I and most probably dependent from the source position on the sky. This instrumental polarisation is below 1% for both Q and U, and can be corrected by subtracting the relative fraction of the total intensity map from our polarisation maps.

Atmospheric contribution to the leakage effect

In order to investigate the possibility of a residual atmospheric noise coupled with the intensity to polarisation leakage we use a very weak quasar observation and we project the quasar data into maps without applying any decorrelation procedure. The intensity map is thus representative of the atmosphere emission. Then, to "simulate" the expected timelines due to an atmospheric to polarisation leakage we convolve the Stokes I map with Q and U Uranus maps. Finally we reconstruct "pure" Q and U timelines starting from these convolved maps. Fig. 6.24 shows the power spectra of these "simulated" leakage timelines. The small residual $1/f$ like component noise indicates a small contribution of the atmosphere to the leakage effect.

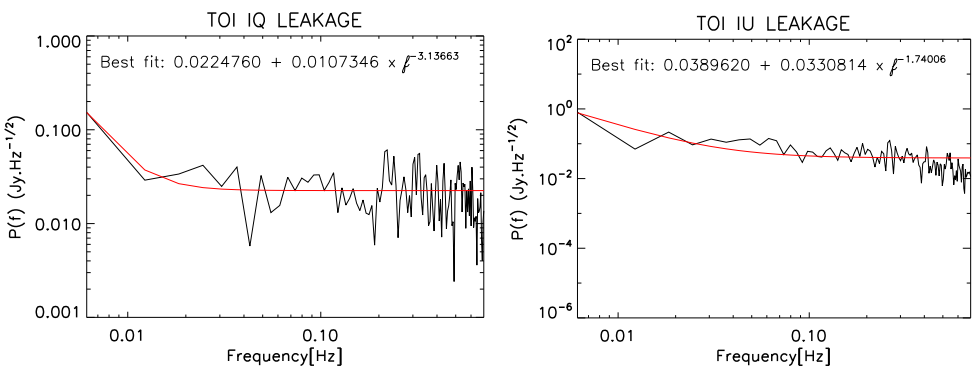

Figure 6.24: *Power spectra of the simulated Q and U atmospheric timelines produced by the intensity to polarisation leakage.*

Noise properties after leakage correction

Fig. 6.25 shows the power cross spectra between Stokes parameters maps obtained after correction for the intensity to polarisation leakage effect. The noise in Q and U is slightly higher after the correction for the leakage effect, as one would expect. Fig. 6.26 shows the difference between Stokes Q and U maps obtained before and after leakage effect correction. Let's note the presence of a bipolar pattern at a level of 10^{-3}, whereas in terms of noise we do not observe

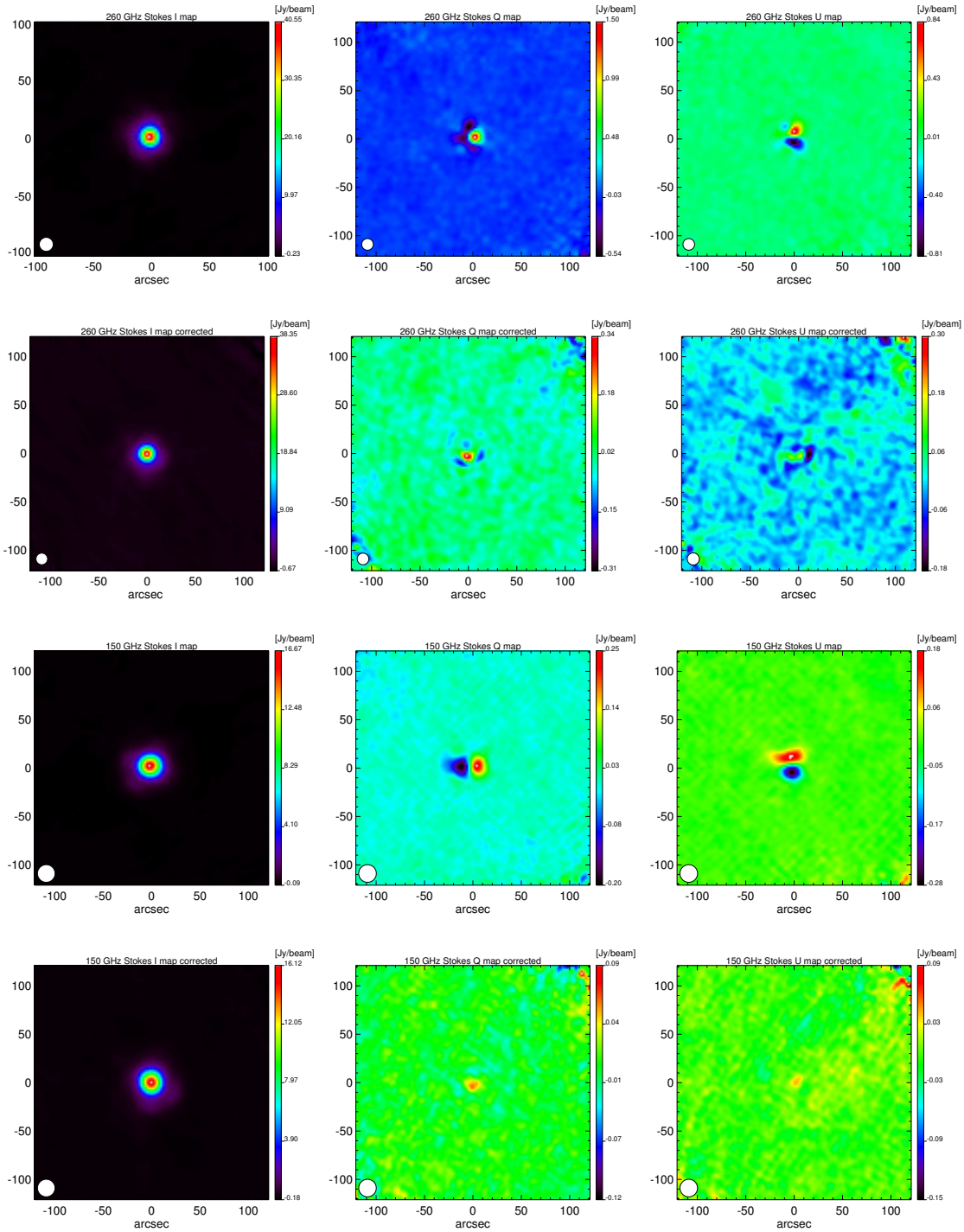

Figure 6.23: *From top to bottom Uranus Stokes I, Q and U maps in Nasmyth coordinates before and after leakage correction at 260 GHz and 150 GHz, respectively. After the leakage correction, we are left with a residual instrumental polarisation below 1% that can be taken into account.*

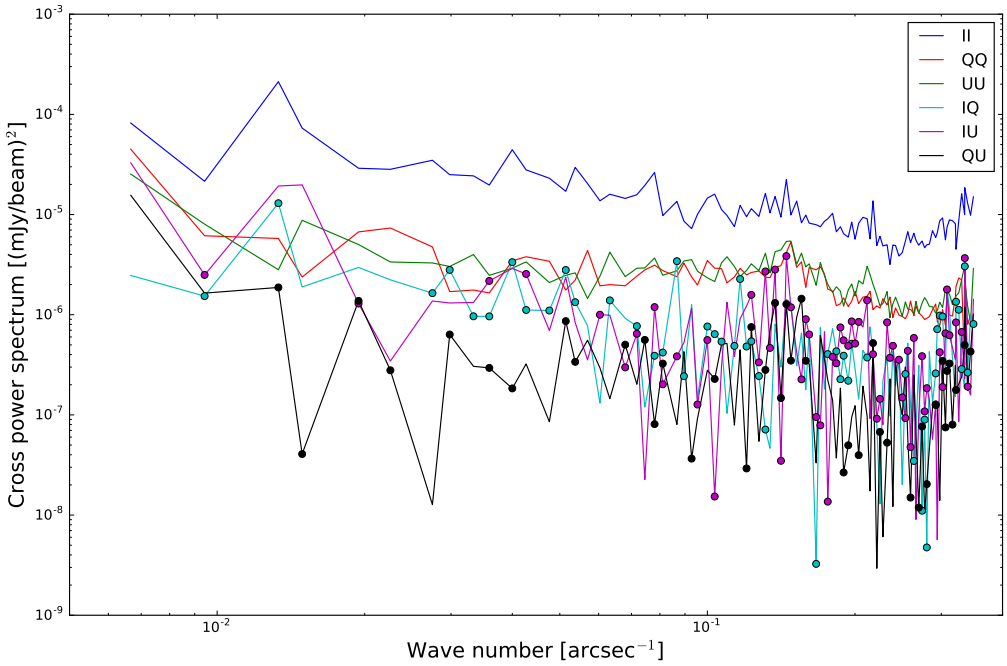

Figure 6.25: *Auto and cross spectra between Stokes parameters maps I, Q, U after correction for the leakage effect. The dots represent negative values.*

a significant variation. We can then conclude that the correction for the leakage effect does not add a significant level of noise.

6.4.2 Leakage correction on point and extended sources

For further validation of the model developed to correct the intensity to polarisation leakage observed on an unpolarised source we applied the intensity to polarisation leakage correction to a known polarised source.

Point source The top row panel of Fig. 6.27 shows Stokes I, Q and U maps obtained at 260 GHz before correction for the intensity to leakage effect and the bottom row panels shows the Stokes maps after correction. In the same way Fig. 6.28 shows the Stokes maps obtained at 150 GHz before and after correction for the leakage effect. We clearly see in the Q and U maps a bipolar structure similar to the one observed on the Uranus maps. The bottom row of the figure presents the leakage corrected maps, which show no residual bipolar structure but slightly increased noise contribution. Indeed, the division by $\tilde{B}_I$ boosts the signal on small angular scales and therefore noise, but the damping by $\mathcal{L}_{IQ}$ compensates and ensures regularisation.

For a single observation with fixed scanning direction, we observe on Fig. 6.28 a small increase of the low frequency noise (striping). This is then compensated by the combination of multiple scans in different orientations. This noise boost could be avoided at the expense of angular resolution if we do not deconvolve by the intensity beam and directly produce a template by convolving the observed intensity map by $\mathcal{L}_{IQ}$ and $\mathcal{L}_{IU}$. The resulting leakage corrections would be convolved twice by the intensity (instrumental) beam and could be subtracted from the Q

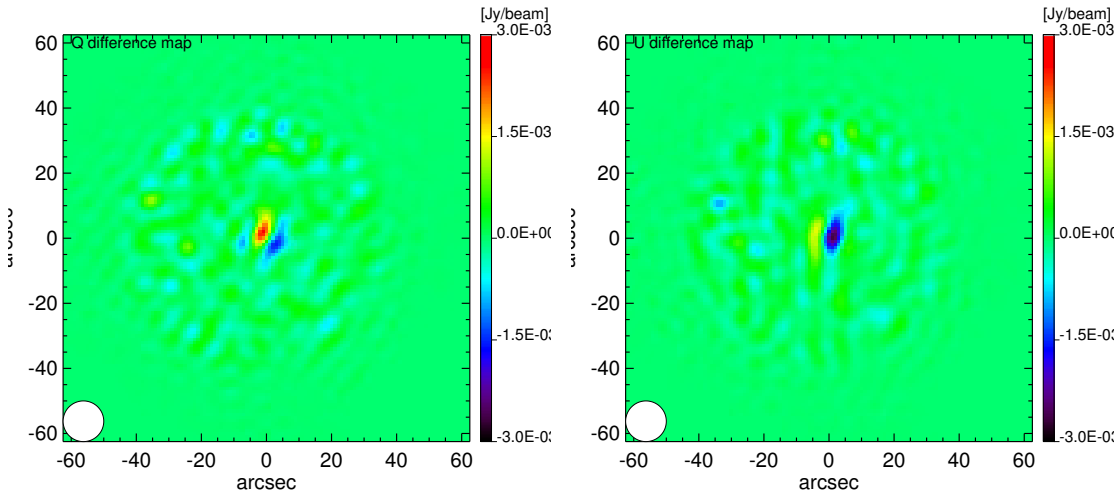

Figure 6.26: *Difference maps between the maps in Q (left) and U (right) used for the cross power spectra represented in Fig. 6.20 and 6.25.*

and U maps convolved by an extra gaussian kernel equivalent to the intensity beam. The final resolution would then be 17 and 25.5 arcsec at 1.25 and 2.05 mm, respectively. Another option for point source observation, is to generate a simulated point source with the appropriate flux, and convolve it directly by $\mathcal{L}_{IQ}$ and $\mathcal{L}_{IU}$ to derive the leakage corrections. The latter method cannot be applied to a diffuse source of a priori unknown structure.

Extended sources The algorithm explained in Sec. 6.4.1 has been adopted for the leakage correction of extended sources as well. In order to give an example of this effect on a diffuse source we report on Fig. 6.29 the leakage maps IQ and IU of the Crab nebula, (Stokes I map represented on Fig. 8.1). These leakage maps show a low level of the intensity to polarisation leakage, about 0.5 %. The level of spurious polarisation is well below to that one observed on a point source. This is probably due to a compensation of the negative and positive signal between adjacent pixels. Although the leakage effect is very weak on a diffuse source the correction is still applied to all the extended sources observations presented in this thesis and reported in the next chapter.

6.5 Conclusions

In this chapter I have discussed the entire pipeline specifically developed for polarisation observations. The continuous rotating HWP detection strategy adds an additional parasitic noise. This is well represented by a sum of harmonics of the HWP rotation frequency and efficiently subtracted. The demodulation technique (also called lock-in procedure) allows us to determine Stokes I, Q, U timelines. While the polarised timelines Q, U show a white noise like spectrum, the Stokes I timeline presents residual correlated noise due to the atmospheric and electronic noise. I also presented Orion Molecular Cloud (OMC-1) observations to discuss the different decorrelation methods presented and previously developed for total intensity observations of *NIKA*. Stokes I map of this extended source is well reconstructed using a common mode decorrelation masking the source. Stokes Q and U maps are unchanged before and after decorrelation

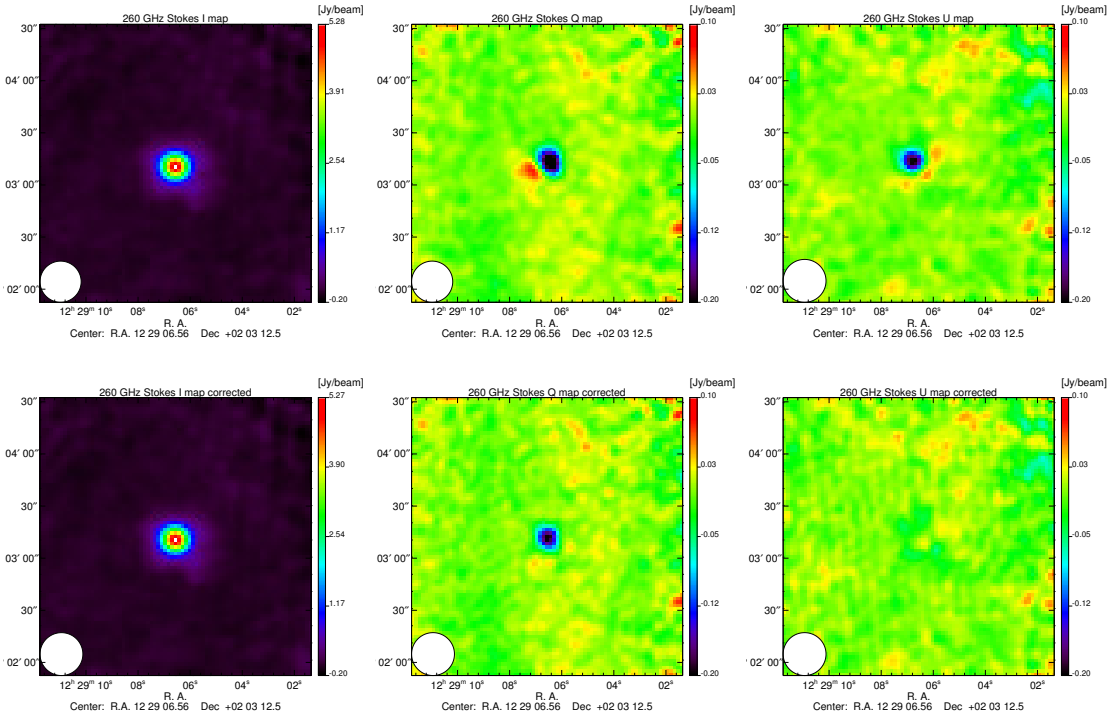

Figure 6.27: **Top**: *Stokes I, Q, U maps of the quasar 3C 273 observed at 260 GHz before correction for the leakage effect.* **Bottom**: *I, Q, U maps after correction. The polarisation angle and degree are reported in the Chap. 7.*

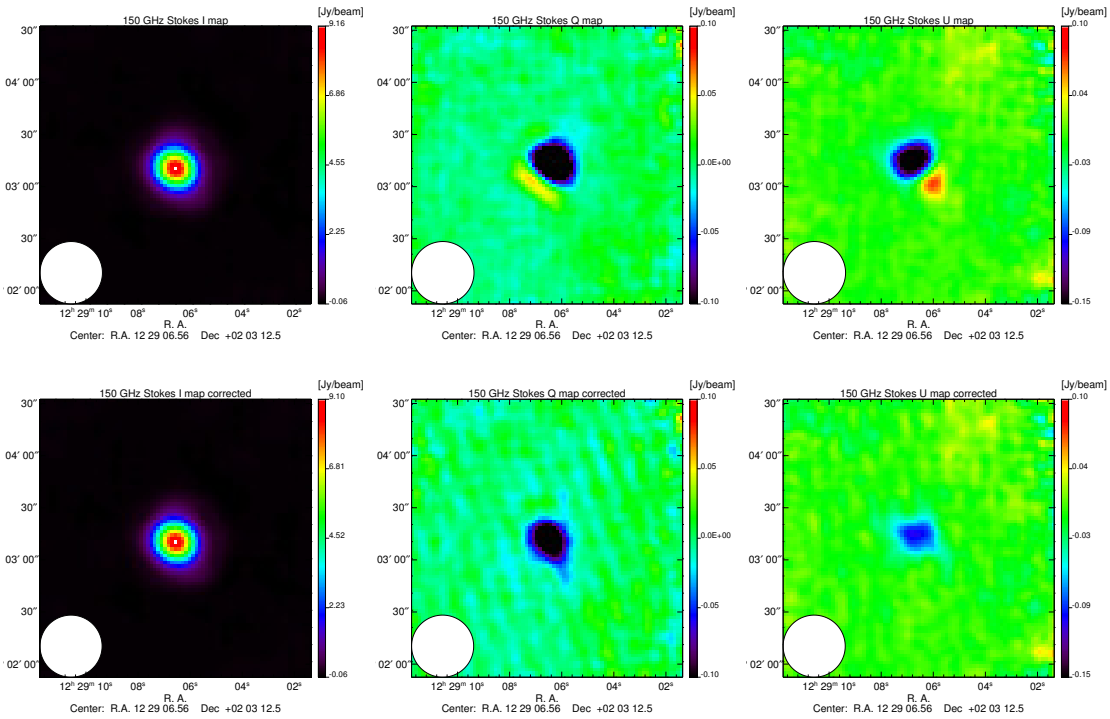

Figure 6.28: **Top**: *Stokes I, Q, U maps of the quasar 3C 273 observed at 150 GHz before correction for the leakage effect.* **Bottom**: *I, Q, U maps after correction.*

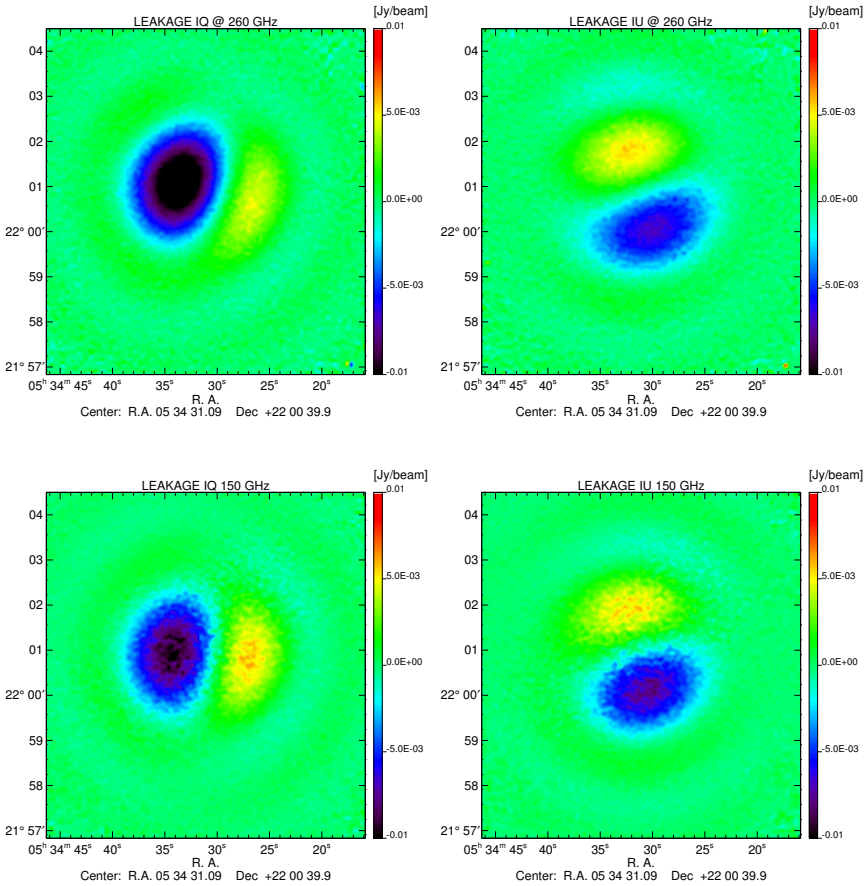

Figure 6.29: *Final leakage maps of the Crab nebula obtained by the subtraction of the final maps before and after leakage correction.*

showing up the potentiality of the detection strategy chosen to reject low frequency noise.

Observations of Uranus, which is expected to be unpolarised, have shown a bipolar pattern consistent of a negative and positive signal on Stokes Q, U maps at a level of $\sim 3\%$ peak-to-peak at both wavelength channels. Although the physical origin of this effect is still unknown an algorithm to subtract this effect has been developed. According to the literature this effect can be interpreted as an intensity to polarisation leakage. An intensity to polarisation leakage subtraction algorithm has been developed and presented in this chapter. This is applied to all the polarised observations presented in this work.

7

Polarisation observations of the NIKA instrument

Contents

7.1 *NIKA* intensity calibration procedure 136

7.2 Polarised observations 140

7.2.1 Polarisation reconstruction accuracy 144

7.2.2 Validation of the polarisation reconstruction on QUASARS . . 147

7.2.3 Estimation of the *NIKA* sensitivity in polarisation observations 151

7.3 Observations of compact and extended sources 153

7.3.1 M87 153

7.3.2 Cygnus-A 157

7.3.3 Orion OMC-1 molecular cloud 159

7.3.4 Spectral index maps 167

7.4 Summary and conclusions 167

In order to characterise the performance of the *NIKA* polarimeter on the sky we did three observational campaigns at the telescope. During the first one, carried out on January, 2014 (*Run 7*), we have used the HWP consisting of a single sapphire plate. This campaign helped us on getting ready for facing problems related to telescope polarisation observations. The second campaign at the telescope was performed on October, 2014 (*Run 9*), during which we adopted the final *NIKA* HWP consisting of multi-mesh HWP. Unfortunately, during this campaign the step motor broke and furthermore several problems occurred in the acquisition system. During the third and last campaign of the *NIKA* instrument in February, 2015 (*Run 12*) the instrumental setup worked as expected and allowed for several polarised source observations. These observations are reported in this chapter. At the end of the campaign *NIKA* was dismounted to leave place to *NIKA2*. In the first part of the chapter we will be presenting the *NIKA* absolute calibration and in the second part the polarisation angle and degree reconstruction accuracy.

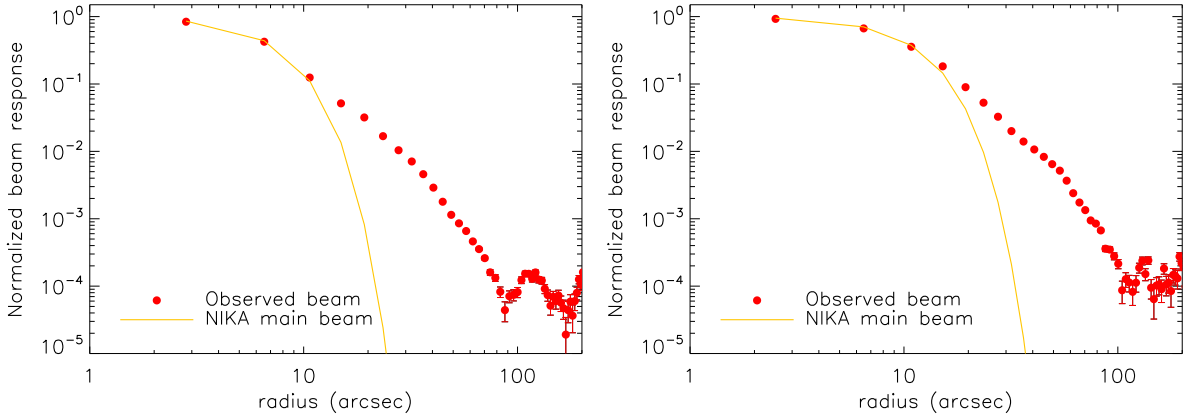

Figure 7.1: **Top panel**: *Uranus radial profile showing the combined NIKA beam pattern (red dots) and the secondary beam contribution for the 1.15 mm channel (left) and 2.05 mm channel (right). In yellow it is shown the 2D Gaussian best-fit to the data.*

7.1 *NIKA* intensity calibration procedure

The *NIKA* detectors measure the incoming optical power integrated over the frequency band, on the effective collecting surface and within the beam extension. In order to calibrate the KIDs response we use known point sources, *e.g.* planets. The *NIKA* primary calibrator is Uranus, which is a very well known source with a strong emission at the *NIKA* wavelengths. Uranus is also used to characterise the angular response of the instrument.

Assuming at the first order a circular form for the instrument beam, we can characterise the beam extension by the FWHM of the best-fitting 2D Gaussian. The expected values of the beam width at 150 GHz and 260 GHz for the *NIKA* instrument are 18.2 and 12 arcsecond, respectively. The FWHM average value measured at 260 GHz and 150 GHz for the *Run*12 in polarisation is 12.5 arcsec and 18.5, respectively, see Fig. 5.4. However, in the radial profile of Uranus presented on Fig. 7.1 emerges a secondary beam contribution. The best fit, assuming a Gaussian model, is represented in yellow and the measured signal is indicated by dots. The presence of a secondary beam at the IRAM 30 m telescope is a known effect, see [Kramer *et al.*, 2013]. We can also characterise the beam per detector using large OTF maps observations of Uranus, as those used for the reconstruction of the position of the detector, see Sec. 5.3.1. This permits to spend more time per pixel on the source. An example of the maps per pixels obtained are represented on Fig. 5.3. These maps permit the characterisation of the angular response of each pixel and discard those that deviate significantly from the expected values.

For a received intensity $I_\nu(\Omega)$ the optical power measured by a detector on the pixel surface dS, in the frequency range ν and $\nu + d\nu$ and in the solid angle $d\Omega$ can be defined as:

$$dP = I_\nu(\Omega)\ dS\ d\Omega\ d\nu. \tag{7.1}$$

The flux of Uranus is given by its brightness temperature, $T_c(\nu)$, such that the SED (*Spectral energy distribution*) is $S_c(\nu) = \frac{2h\nu^3}{c^2}[\exp(\frac{h\nu}{k_B T_c(\nu)}) - 1]^{-1}$.

The flux measured by the detectors is then obtained by integration across the *NIKA* fre-

quency bands and the beam extension:

$$F_{c,f_b} = \frac{\int \pi\theta_c^2 \times \frac{2h\nu^3}{c^2}\left[\exp\left(\frac{h\nu}{k_{\rm B}T_c(\nu)}\right)-1\right]^{-1} \times \frac{Tr(\nu)}{\nu^2}d\nu}{\int \frac{Tr(\nu)}{\nu^2}d\nu} \qquad \left[\mathrm{Wm^{-2}Hz^{-1}}\right], \tag{7.2}$$

where θ_c is the angular size of the planet as measured during the period of the observations, generally the value of the diameter is $2\theta_c \simeq 3.5''$. To estimate the brightness temperature of Uranus we use the model of [Moreno, 2010] and [Planck Collaboration *et al.*, 2015b], which use a frequency-dependent model with absolute calibration accuracy of 5%. The spectral transmission $Tr(\nu)$ is given by:

$$Tr(\nu) = Tr_{BP}(\nu) \times Tr_{atm}(\nu). \tag{7.3}$$

The spectral transmission of the *NIKA* instrument, $Tr_{BP}(\nu)$ has been measured in the laboratory using a Martin-Puplett Interferometer and a reference bolometer. The atmospheric transmission is obtained from the ATM model [Pardo *et al.*, 2002]. The model used gives an estimation of the Uranus brightness temperatures of $T_c(150\ \mathrm{GHz}) \simeq 111$ K and $T_c(260\ \mathrm{GHz}) \simeq 91$ K [Catalano *et al.*, 2014]. The accuracy of this model is estimated at the level of 5%. The *NIKA* calibration procedure consists in:

- fitting the amplitude of a Gaussian function of fixed angular size on the Uranus maps;
- correcting for atmospheric absorption using the opacity coefficients derived from skydip scans, see Sec. 5.2.1.

The opacity correction is performed by multiplying the data by $\exp(\tau_{f_b}/\sin(el))$, where el is the elevation of the source and τ_{f_b} is the atmospheric opacity estimated for each frequency band f_b.

In order to estimate the overall calibration error we check all the observations of Uranus during the campaign. The variation of the flux measured on Uranus along the observational campaign performed in February, 2015 is reported on Fig. 7.2. In this figure it is shown the measured flux at 260 GHz (top) and at 150 GHz (bottom). We observe that the measured flux is relatively constant except for the first and the last observation scan. Fig. 7.3 represents the atmospheric condition variation in terms of atmospheric opacity τ. The atmosphere is more opaque at 1.15 mm than at 2.05 mm but their ratio remains constant (bottom of the figure). The dispersion calculated by using all the scans of Uranus of this campaign corresponds to 14% at 260 GHz and 5% at 150 GHz, see Fig. 7.2.

Beam spectral dependence The main beam is measured at the effective frequency:

$$\nu_{\rm eff}^{\rm beam} = \frac{\int S_c(\nu)Tr(\nu) \times \nu\ d\nu}{\int S_c(\nu)Tr(\nu)\ d\nu}, \tag{7.4}$$

where the function $Tr(\nu)$ is the *NIKA* the spectral transmission and $S_c(\nu)$ the SED of the

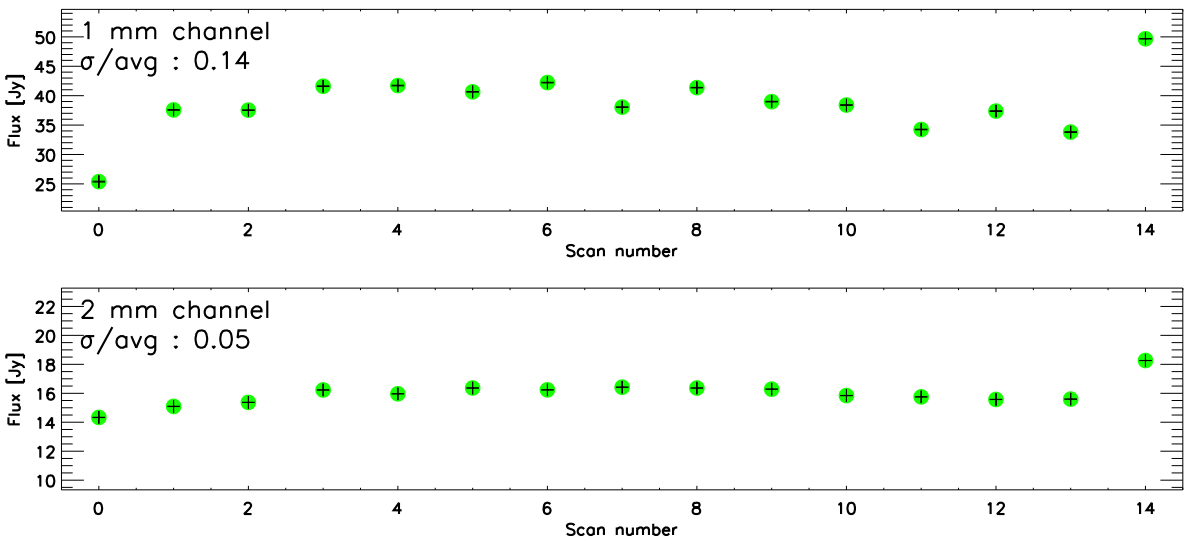

Figure 7.2: *Measured Uranus fluxes and uncertainties for all observations performed during the Run 12 in polarisation in February 2015, for the 1.15 mm channel (***top***) and 2.05 mm channel (***bottom***).*

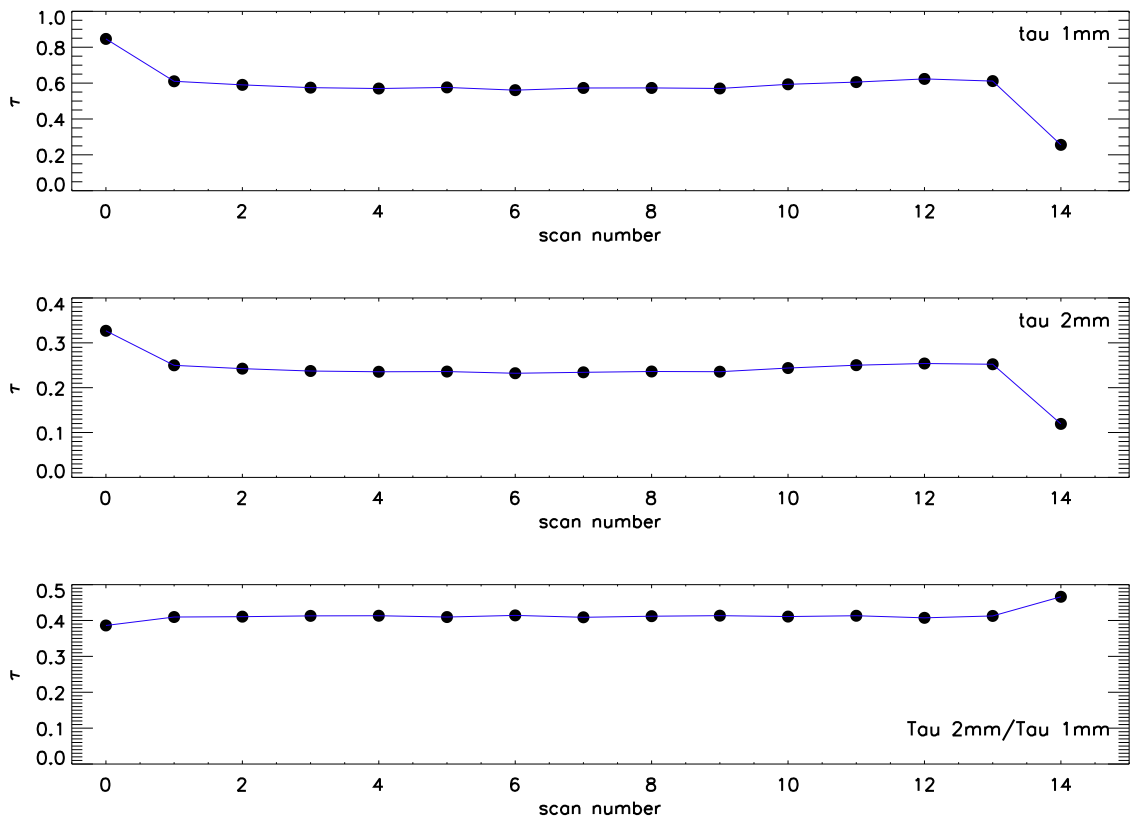

Figure 7.3: *Atmospheric opacity measured at 1.15 mm (top), 2.05 mm (centre) and their ratio (bottom) for the same observations of those presented on Fig. 7.2.*

calibration source. The variation of the angular size of the beam is proportional to $1/\nu$. The measured effective frequencies are equivalent to $\nu_{eff}^{beam} = 156$ and 259. Following [Adam *et al.*, 2014b] we can formalise the beam spectral dependence as:

$$\begin{cases} B(\theta, \phi, \nu) & = B\left(\theta \times \frac{\nu}{\nu_{\rm eff}^{\rm beam}}, \phi, \nu_{\rm eff}^{\rm beam}\right) \\ \Omega_{\rm beam}(\nu) & = \Omega_{\rm beam}\left(\nu_{\rm eff}^{\rm beam}\right) \times \left(\frac{\nu_{\rm eff}^{\rm beam}}{\nu}\right)^2 . \end{cases} \tag{7.5}$$

Point source photometry

For a point source we can compute the total flux of the source by fitting a 2D Gaussian on the observed map calibrated in units of Jy/beam. We use the following model of the data:

$$M_{\rm tot}(x, y) = A_{\rm ps} \exp\left(-\frac{(x - x_0)^2 + (y - y_0)^2}{2\sigma_{\rm beam}^2}\right) + Z_0 + n_k, \tag{7.6}$$

where $A_{\rm ps}$ is the amplitude of the Gaussian, $\sigma_{\rm beam}$ is the standard deviation of the Gaussian main beam and (x_0, y_0) is the position of the source, and Z_0 is the zero level of the map. The fit provides the values of the flux amplitude $A_{\rm ps}$ and the associated error, $\Delta A_{\rm ps}$. We have seen in Chap. 6 that the noise observed on maps can be represented by a correlated Gaussian noise. For a realistic representation of the uncertainties in the flux measurements we repeat the 2D Gaussian fit on different positions on the map outside the point source. The standard deviation of the recovered fluxes on these positions constitutes a good estimate of the uncertainties on the flux measurement.

Since the flux is integrated in the frequency band, in order to compare it with other experiment results we need to specify a reference frequency and give the SED. Therefore, we define the reference flux at the frequency ν_0 as:

$$F_{c,\nu_0} = \pi\theta_c^2 \times \frac{2h\nu_0^3}{c^2}\left[\exp\left(\frac{h\nu_0}{k_{\rm B}T_c(\nu_0)}\right) - 1\right]^{-1}, \tag{7.7}$$

where ν_0 is the central frequency of the *NIKA* bands at 260 GHz and 150 GHz, respectively. Since point sources have a different SED with respect to Uranus, we cannot use the same calibration factor estimated on Uranus and we have to consider a color correction to recover the real observed spectra. In this way we estimate the real flux observed F_{c,f_b}. The flux measured on a point source can be expressed as:

$$F_{{\rm ps},\nu_0} = A_{\rm ps} \times \frac{F_{c,\nu_0}}{A_c} \times \left(\frac{\nu_{\rm eff}^{\rm beam}}{\nu_{\rm ps}^{\rm beam}}\right)^2 \times C_{\rm col}, \tag{7.8}$$

where $A_{\rm ps}$ and A_c are the amplitudes of the Gaussian fit on the point source and the calibration source (*i.e.* Uranus) and $C_{\rm col}$ is the color correction, which is discussed below. $\nu_{\rm ps}^{\rm beam}$ is obtained by the Eq. 7.4. The ratio $\nu_{eff}^{beam}/\nu_{\rm ps}^{beam}$ accounts for the beam spectral dependence. After calibration the data are given in units of Jy/beam where the beam identifies the extension of main lobe of Uranus (2D Gaussian best-fit).

Color corrections To estimate the observed "real" flux at the reference frequency we have to estimate the color correction $C_{\rm col}$ such that:

$$F_s(\nu_0) = C_{\rm col} \times \hat{F}_s \tag{7.9}$$

where $\hat{F}_s$ is the flux obtained from a Gaussian fit on the map. The color correction coefficient can be written as:

$$C_{\rm col} = \frac{F_c(f_b)}{F_c(\nu_0)} \times \frac{F_s(\nu_0)}{F_s(f_b)} = \frac{F_c(f_b)}{F_c(\nu_0)} \times F_s(\nu_0) \times \frac{\int \frac{Tr(\nu)}{\nu^\beta} \times d\nu}{\int F_s(\nu_0) f(\nu/\nu_0) \times \frac{Tr(\nu)}{\nu^\beta} d\nu}, \tag{7.10}$$

where $F_c(f_b)$ and $F_s(f_b)$ are the measured fluxes integrated in the band of the calibrator and of the source observed; $F_c(\nu_0)$ and $F_s(\nu_0)$ are the corresponding fluxes measured at the reference frequency ν_0. The coefficient β describes the type of source considered, 2 for point sources and 0 for extended sources.

Conversion coefficients Since the units of Jy/beam depends on the *NIKA* beam, we need to convert this quantity in the standard brightness units Jy/Sr (Jansky per steradian). In this way we can compare our results with other experiments. Once the main lobe of Uranus Ω_{beam} is measured and it is expressed in steradians we can calculate the real flux of the source observed at an effective frequency using aperture photometry. From Eq. 7.5 and 7.8 we can write the observed flux of the point source at the reference frequency as:

$$F_{{\rm ps},\nu_0} = \int_{-\infty}^{+\infty}\int_{-\infty}^{+\infty} \frac{A_{\rm ps}\ B(\theta,\phi,\nu_{\rm ps}^{\rm beam})}{\Omega_{\rm beam}(\nu_{\rm eff}^{\rm beam})\ C_{\rm col}}\ dx\ dy \tag{7.11}$$

The value in MJy/sr is estimated by the ratio between the spectrum of the source observed $S_c(\nu)$ and the reference spectrum of the calibration source $S_c(\nu_0)$:

$$F_{\rm MJy/sr} = \frac{S_c(\nu)}{S_c(\nu_0)}. \tag{7.12}$$

7.2 Polarised observations

In this section we will be presenting the observations on point and extended sources performed during the *Run*12 (February 2015). The validation of the detection strategy has been performed first using observations of known quasars and then on known diffuse sources. Moreover, we used a skydip observation in order to check the variation of the background signal modulated by the HWP (see Sec. 6.3.1). Next section reports the results obtained by the analysis of a "polarised" skydip observation.

Analysis of a polarised skydip

The skydip procedure, presented in Sec. 5.2.1, is used to determine the coupling coefficients to the air mass of each KID that will then allow to compute the opacity at any time. In polarisation runs we chose to keep the HWP in rotation during skydip observations to account for any performance loss in the estimation of the opacity correction coefficients. Despite the

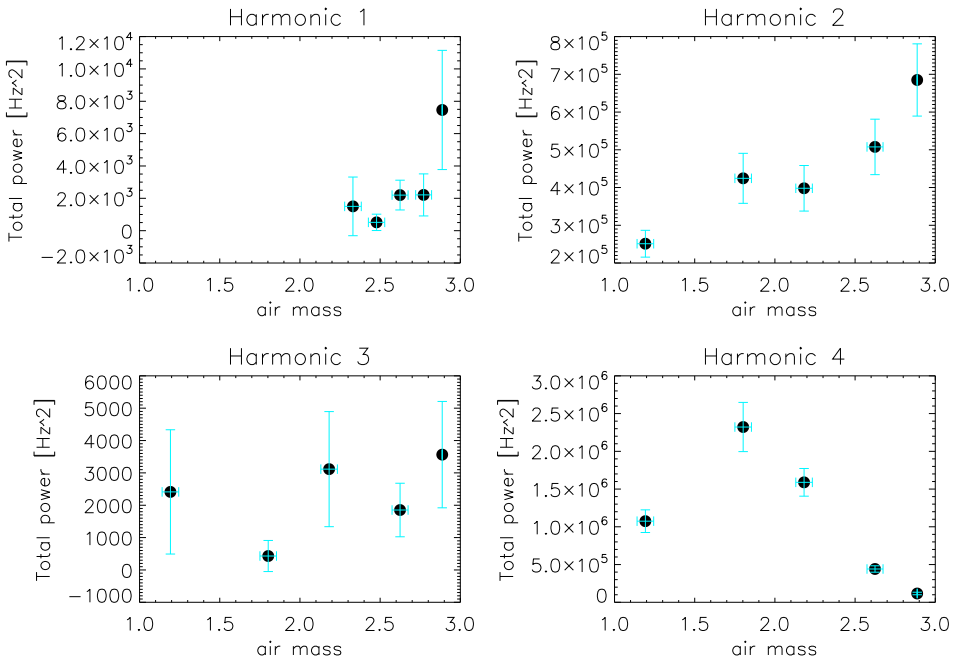

Figure 7.4: *Observed signal for the first four harmonics of the HWP rotation frequency. The total content amplitudes $A_n^2 + B_n^2$ of the cosine and sine terms in Sec.6.3 measured at 260 GHz are reported for a skydip observation of Run 12.*

atmosphere is completely unpolarised at *NIKA* frequencies, we observe on Fig. 6.7 a parasitic signal due to the modulation of the background signal present in the telescope cabin. This HWP synchronous signal (HWPSS), peaked at harmonics of the HWP rotation frequency ω discussed in Sec. 6.3.1, needs to be subtracted from the data to estimate the opacity correction coefficients.

The aim of this section is to use the HWPSS amplitudes A_n and B_n (see 6.3) fitted in the data at each elevation during a skydip observation, to check their variation as function of the air mass amount. Theoretically, since the atmosphere is more opaque towards the horizon (air mass $\propto 1/\sin(el)$), we expect a contribution of such a background signal decreasing with elevation. Fig. 7.4 and 7.5 report the observed signal for the first four harmonics 1ω, 2ω, 3ω, 4ω of the HWPSS as a function of the air mass at 260 and 150 GHz, respectively. Harmonics 1ω, 2ω, 3ω are found to have an opposite trend at 150 GHz and 260 GHz, while the fourth harmonic, 4ω, shows the same behaviour at both *NIKA* frequencies, decreasing with air mass. This trend can be explained considering the contribution of two thermal sources, the background signal in the telescope cabin (black body at $\simeq$ 300 K) and the sky (black body at $\simeq$ 40 K). The thermal difference between these two black bodies increases with the elevation explaining the increase of the HWPSS amplitudes. The different effect observed in the 1ω, 2ω, 3ω harmonic amplitudes between the two *NIKA* frequencies is explained by a more important contribution of the atmosphere fluctuations at 260 GHz than at 150 GHz. The atmosphere signal could be stronger at 260 GHz with respect to the thermal difference between the cabin and the sky. It could be interesting to investigate this effect with further *NIKA2* observations. In any case the HWPSS is well subtracted from the data at any elevation of the observed source, allowing the good reconstruction of its polarisation.

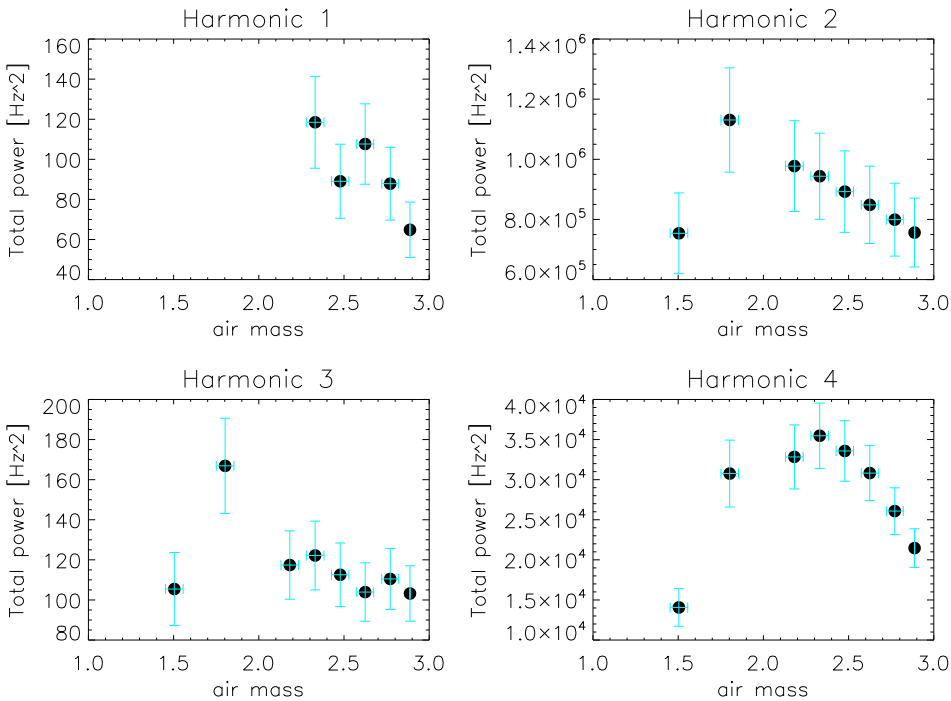

Figure 7.5: *Observed signal for the first four harmonics of the HWP rotation frequency. The total content amplitudes $A_n^2 + B_n^2$ of the cosine and sine terms in Sec.6.3 measured at 150 GHz are reported for a polarised skydip observation of Run 12.*

Photometric accuracy on polarised sources

The photometric calibration described in Sec. 7.1 allows us to obtain calibrated observations. The accuracy of the calibration can be checked on well known point source. For the *NIKA* polarisation *Run* 12 we have chosen to use two quasars, which are indicated as calibrators in literature: 3C 286 and 3C 273. The quasar 3C 286 is indicated as a primary calibrator for polarisation measurements [Agudo *et al.*, 2012].

The Spectral Energy Density of these two quasars reported on Fig. 7.6 has been obtained using observations of *XPOL* [Thum *et al.*, 2008], *Planck* [Planck Collaboration, 2013], ALMA [Fomalont *et al.*, 2014] and *NIKA*. The *NIKA* intensity flux and uncertainties at 1.15 and 2.05 mm are represented in blue. We observe that the *NIKA* data are consistent within error bars with the other experiment results. We also note that the 3C286 data are consistent with a synchrotron spectrum in the form of a power law, $\propto \nu^{\beta}$, with spectral index $\beta \simeq$ -1.007 $\pm$ 0.033 (dashed red line). To explain the 3C273 data we considered two power laws with spectral indices $\beta_1 \simeq$ -0.29$\pm$0.05 and $\beta_2 \simeq$ -0.85$\pm$0.06 (dashed red line).

Pointing accuracy on an extended source In order to check the pointing corrections provided during this observational campaign (*Run* 12) we compare two observations of Orion Molecular Cloud (presented in Sec. 7.3.3). Fig. 7.7 reports the *NIKA* map obtained at 1.15 mm with the over-plotted contours of the SCUPOL intensity map [Matthews *et al.*, 2009]. A shift of about 10 arcsec is applied to the *NIKA* map to match the SCUPOL map. This shift could have been minimised to a few arcsec, which is the pointing accuracy of the IRAM telescope, by performing more often the pointing corrections.

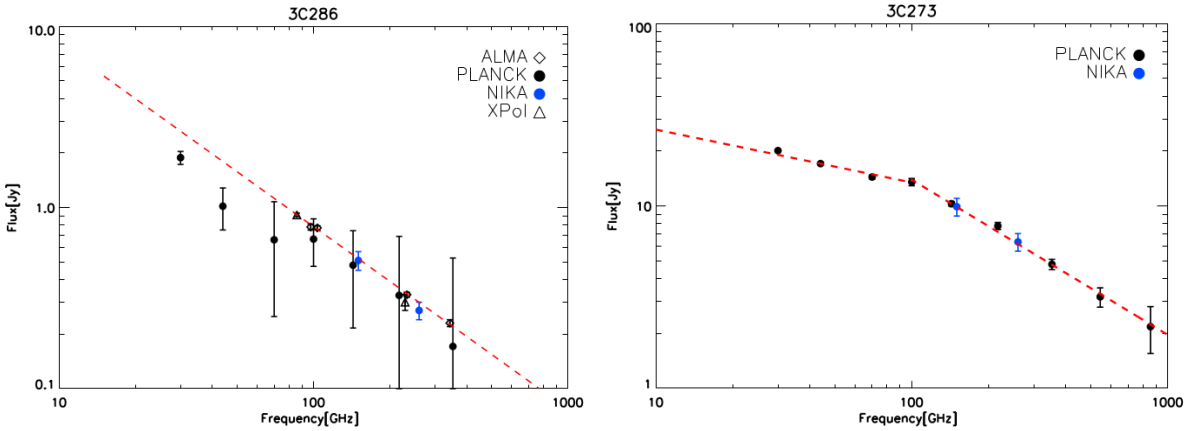

Figure 7.6: *Spectral energy density (SED) in intensity for the quasars 3C286 (left) and 3C273 (right). We consider data from Planck [Planck Collaboration, 2013] (black dot); ALMA [Fomalont* et al.*, 2014](black diamond); XPOL [Agudo* et al.*, 2012](black triangle) and NIKA (blue dots).*

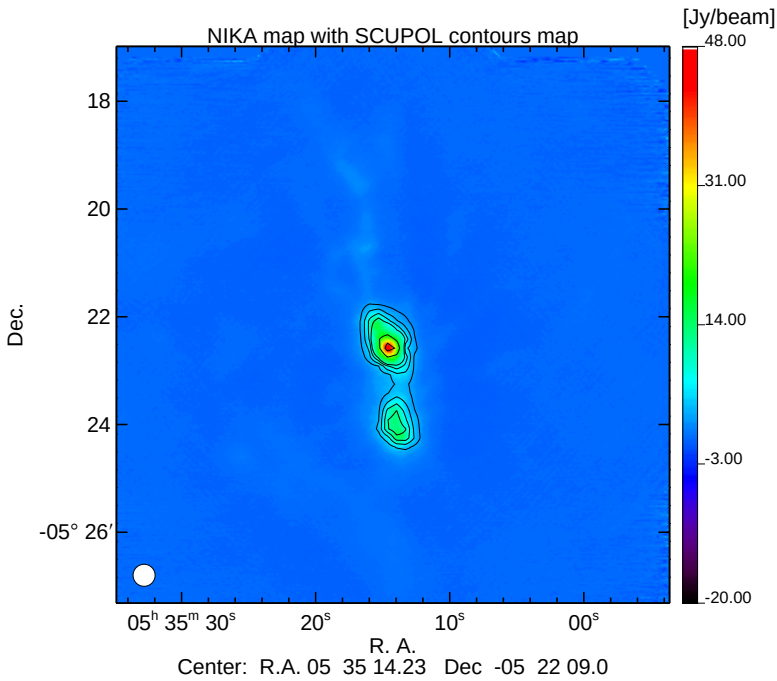

Figure 7.7: *NIKA Stokes I at 260 GHz with SCUPOL map contours observed at 850 μm [Matthews* et al.*, 2009]. The NIKA map is shifted by ∼ 10 arcsec to match the SCUPOL map.*

7.2.1 Polarisation reconstruction accuracy

In observations of linear polarisation it is common to represent the polarised signal in terms of polarisation degree, p, and angle, ψ:

$$p = \frac{\sqrt{Q^2+U^2}}{I}, \tag{7.13}$$

$$\psi = \frac{1}{2}\arctan\frac{U}{Q}. \tag{7.14}$$

These definitions are not linear in I, Q and U and they are biased by the noise. A non Gaussian behaviour is expected for p and ψ leading to both biases and wrong estimates of the uncertainties of p and ψ. In particular regions of low polarised signal-to-noise ratio, when $Q \simeq U \simeq 0$ the noise measured on Q and U maps will yield a non-zero degree of polarisation estimation. Indeed, Fig. 7.8 shows the distribution of the polarisation degree in the case of low and high S/N (polarised signal) as obtained by Eq. 7.13. On the top left panel it is represented the distribution of the simulated polarisation intensity signal P for P $= 1\ \sigma_P$, with:

$$P = \sqrt{Q^2+U^2} \quad \text{and} \quad \sigma_P = \frac{Q+U}{\sqrt{Q^2+U^2}}. \tag{7.15}$$

The distribution on Fig. 7.8 appears not normal, as expected, and the estimation of P results then strongly biased. Ways to correct for this bias have been proposed by [Simmons *et al.*, 1980] and more recently by [Simmons et Stewart, 1985] and [Montier *et al.*, 2015] to whom I refer here. The probability density function (PDF) for an observed polarisation intensity P with true polarisation P_c can be approximated by the Rice distribution [Rice, 1945]:

$$PDF(P|P_c,\sigma_P) = \frac{P}{\sigma_P^2} I_0\left(\frac{PP_c}{\sigma_P^2}\right)\exp[-(P^2+P_c^2)/2\sigma_P^2], \tag{7.16}$$

where I_0 is the zero-order modified Bessel function. The asymmetry of this distribution with respect to P and P_c results in a positive bias of the measured polarisation in the low polarised S/N regime. For high polarised S/N, the Rice distribution is nearly normal with a mean approaching to P_c and a standard deviation σ_P [Rice, 1945]. In order to calculate an unbiased estimate of the true polarisation intensity P_c one needs to compute: $PDF(P_c|P,\sigma_P)$. This posterior probability is given by the product of a likelihood function $L(P_c)$ and a prior [Eadie *et al.*, 1971]. Assuming an uniform prior in P_c and using the Bayes's theorem:

$$PDF(P_c|P,\sigma_P)dP_c = L(P_c)dP_c = \frac{1}{N_L}PDF(P|P_c,\sigma_P)dP_c, \tag{7.17}$$

where the normalisation constant is:

$$N_L = \int_0^\infty PDF(P|P_c,\sigma_P)dP_c. \tag{7.18}$$

The maximum likelihood estimate $\hat{P}$ of the degree of polarisation is the value of P that cancels the derivative of Eq. 7.16:

$$\left|\frac{dL}{dP_c}\right|_{\hat{P}=P_c} = 0 \quad \Longrightarrow \quad PI_1\left(\frac{P\hat{P}}{\sigma^2}\right) - \hat{P}I_0\left(\frac{P\hat{P}}{\sigma^2}\right) = 0, \tag{7.19}$$

where I_1 is the first order modified Bessel function and $\hat{P}$ is the maximum likelihood estimate

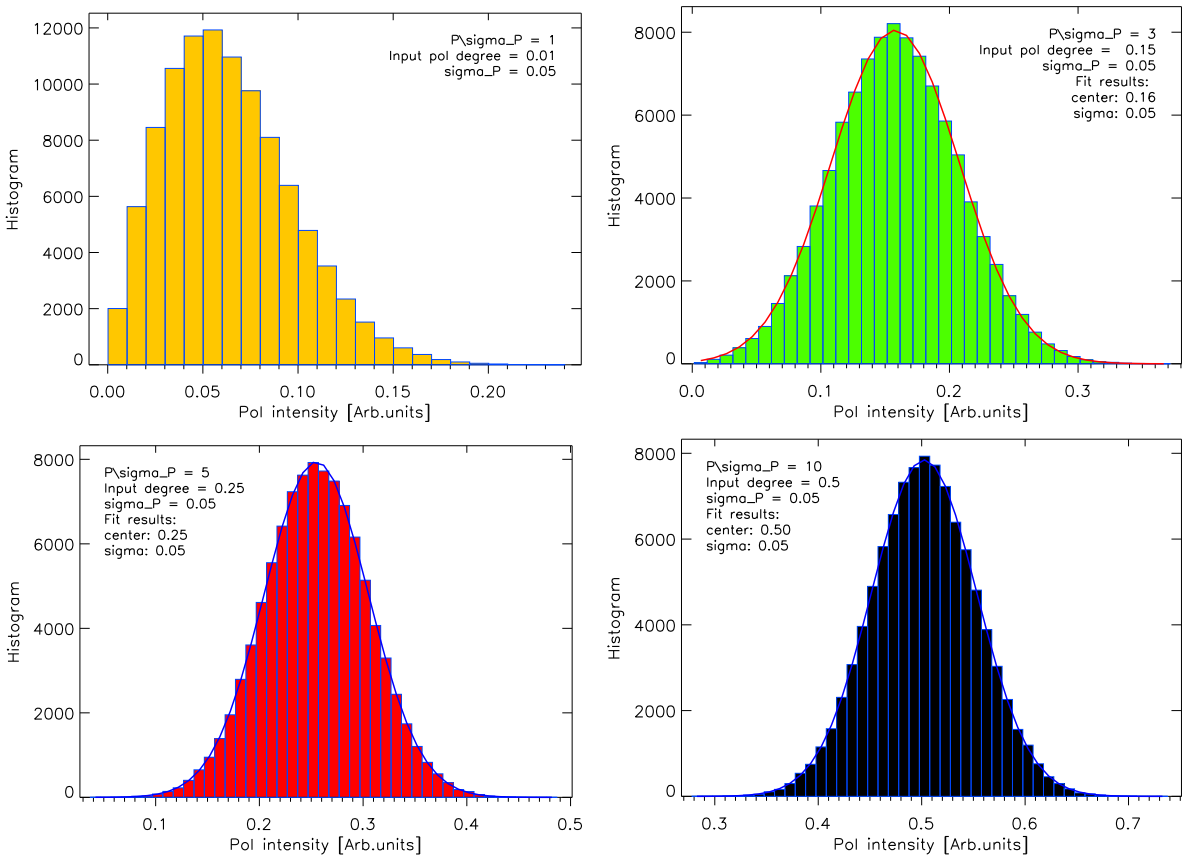

Figure 7.8: *Distribution of polarisation intensity P. On the top left panel it is shown the case of polarisation intensity with S/N* $\sim$ *1* σ_P*, the distribution does not have a Gaussian shape. In this case we need to use more sophisticated methods to estimate the value of the polarisation intensity and its uncertainty. When the S/N increases up to* $\sim$ *3 (top right), 5 (bottom left), 10 (bottom right)* σ_P*, the distribution becomes normal and we can use the high S/N approximation to estimate P and its uncertainty* σ_P*.*

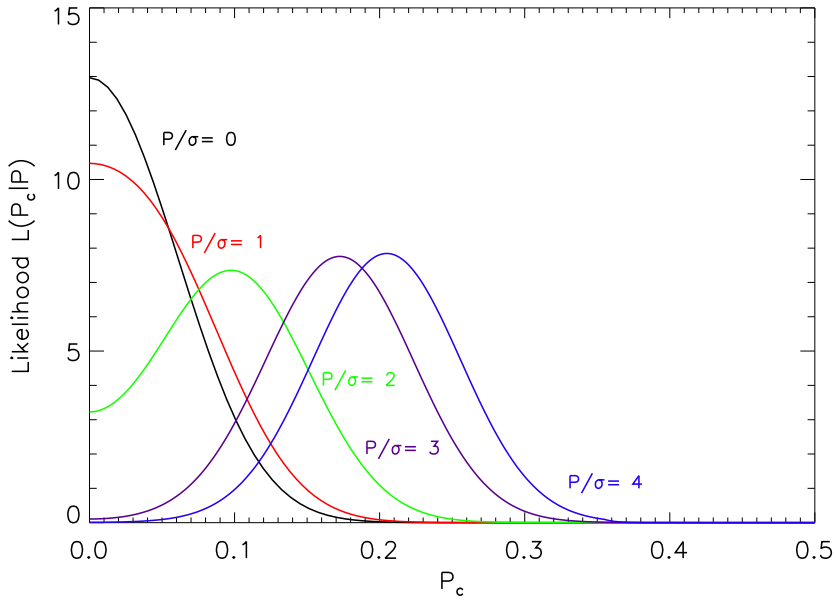

Figure 7.9: *Likelihood function given by Eq. 7.17. The distributions are shown for different values of the measured polarisation P/σ_P.*

of P_c. Eq. 7.19 is solved numerically. The full likelihood is used to determine the uncertainty contours around $\hat{P}$. Fig. 7.9 shows the likelihood function $L(P_c)$ for simulations as function of P/σ_P. At the limits of low and high S/N the estimation of the true polarisation is:

$$\hat{P} = 0 \quad \text{for} \quad P/\sigma_P < 2, \tag{7.20}$$

and

$$\hat{P} \simeq \sqrt{P^2 - \sigma_P^2} \quad P/\sigma_P > 3. \tag{7.21}$$

As discussed above, for very significant polarisation detections ($P \geq 3\sigma_P$) the distribution of the polarised intensity has a Gaussian distribution form. In this case of high S/N the estimation of the polarisation degree can be approximated by:

$$p_c \simeq \sqrt{Q^2 + U^2 - \sigma_Q^2 - \sigma_u^2}/I, \tag{7.22}$$

notice that we assume here high S/N in I. Assuming here a Gaussian distribution of p_c the uncertainty on p_c will be:

$$\sigma_{p_c} = \frac{\sqrt{Q^2\sigma_Q^2 + U^2\sigma_U^2 + p_c^4 I^2 \sigma_I^2}}{p_c I^2}. \tag{7.23}$$

Fig. 7.10 shows simulation of the polarisation angle at low and high S/N. The position angle distribution, although not normal, is symmetric about the measured angle so that estimates and uncertainties on its value are simpler. In the case of very low S/N the distribution becomes asymmetric as shown on the top left panel of the Fig. 7.10. In this case it is not possible to give an estimate of the angle. [Naghizadeh-Khouei et Clarke, 1993] and [Montier *et al.*, 2015] studied in detail this case and proposed an estimator. In Sec. 7.2.2, where we present the results of our observations in the context of *NIKA* prototype data on bright sources, we will restrict to high

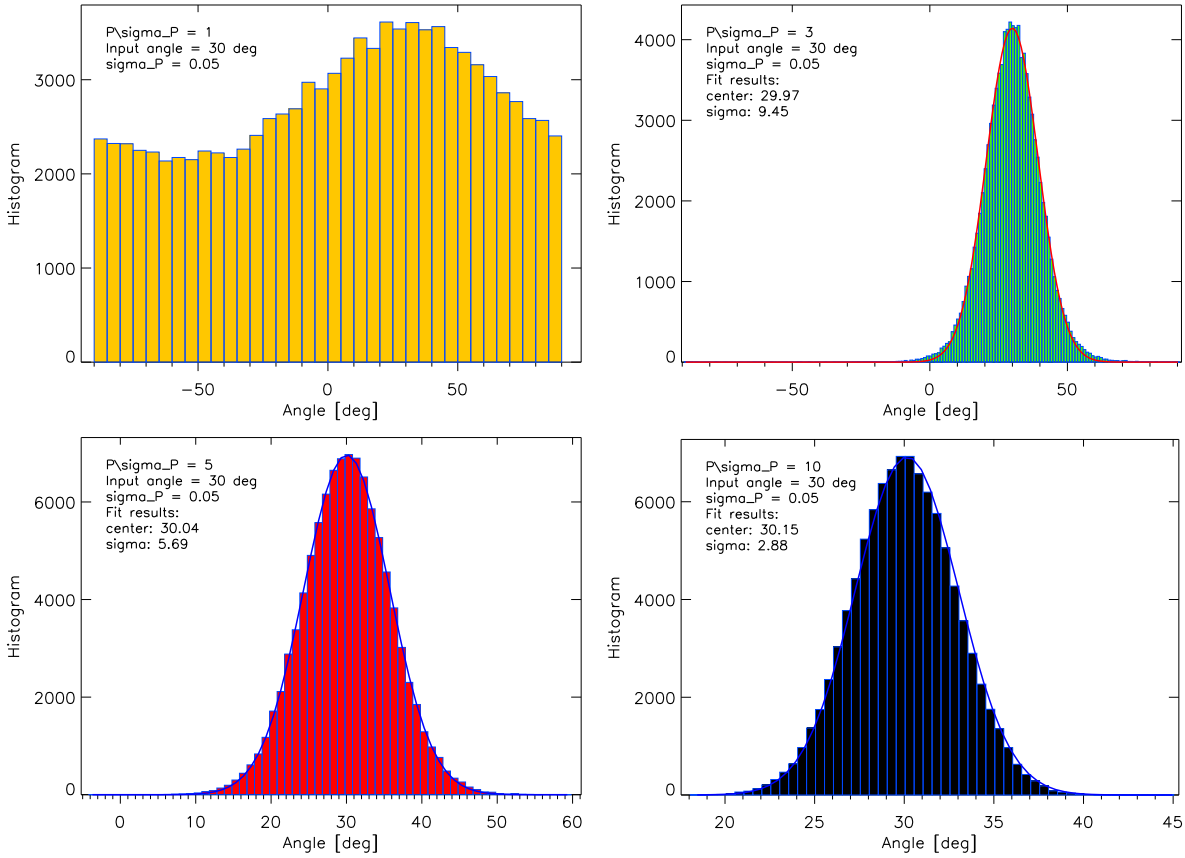

Figure 7.10: *Distribution of polarisation angle in the case of low and high S/N. On the top left panel it is shown the case of polarisation angle for polarisation intensity S/N ∼, the distribution becomes completely asymmetric and it becomes hard to compute an estimate of the central value. Sophisticated statistical methods need to be used to estimate the polarisation angle, see [Naghizadeh-Khouei et Clarke, 1993]. When the S/N increases for* $P = 3\ \sigma_P$ *(top right),* $P = 5\ \sigma_P$ *(bottom left),* $P = 10\ \sigma_P$ *(bottom right) the distribution adopts a Gaussian form and we can use the high S/N approximation (*$> 3\ \sigma_P$*) to estimate the polarisation angle* ψ *and its uncertainty.*

signal-to-noise regions for the sake of robustness. In such case, the angle estimator reduces the classic estimator given by Eq. 7.14 and its associated uncertainty:

$$\sigma_\psi = \frac{\sqrt{Q^2\sigma_Q^2 + U^2\sigma_u^2}}{2P^2}. \tag{7.24}$$

7.2.2 Validation of the polarisation reconstruction on QUASARS

Experiments aiming at measuring the polarisation of astrophysical sources require a precise determination of the instrumental polarisation together with a calibration of the polarisation angle. For the first requirement, observations on a bright and unpolarised source could identify persistent instrumental effects such as leakage effects of the intensity into polarisation (see Sec. 6.4 for the effect observed by *NIKA* on Uranus).

For the second requirement and in order to validate the reconstruction of the angle of polarisation with the *NIKA* camera, we can use known polarised point sources. For this scope during the *Run* 12 (February 2015) we chose to observe stable and highly polarised quasars as known in literature. The quasars selected were: 3C 273, 3C 279, 3C 286, 0923+092. In the following we will briefly discuss the main characteristics of these quasars.

3C 286

3C 286 is a compact steep-spectrum quasar at redshift z = 0.846. Radio images with the Very Large Array[1] at sub-arcsecond resolution have revealed an extended structure composed of three misaligned bright features. Among these, the two brightest ones dominate the linear polarisation emission, and show their electric vector oriented nearly parallel to the axis of the jet like structure between them. The stability of this quasar in terms of intensity and polarisation flux in a large frequency range and the slow flux wavelength dependence make it a primary calibrator for polarisation measurements. The integrated electric vector polarisation angle of the source at all observing wavelengths from 20 cm to 7 mm is $\psi \approx 33°$ [Perley, 1982] , [Perley et Butler, 2013]. At millimetre wavelengths the *XPOL* polarimeter [Thum *et al.*, 2008] has monitored this quasar from 2006 to 2012 [Agudo *et al.*, 2012]. They showed that although this quasar exhibits moderate millimetre flux densities ($F_{3mm} \approx 1$ Jy and $F_{1mm} \approx 0.3$ Jy), its large millimetre polarisation degree ($p_{3mm} \approx 13.5$ % and $p_{3mm} \approx 14.5$ %) and its stability make it a valuable polarisation calibrator for millimetre observations. As presented in Tab. 7.1, *XPOL* observations show that 3C 286 is highly polarised, up to 14%, with PA (polarisation angle) increasing slowly with frequency. These results have been confirmed by observations at 1.3 mm with the CARMA polarimeter [Hull et Plambeck, 2015] in May 2015 (see Tab. 7.1).

NIKA observations on this quasar are reported in Tab. 7.2 and they are in a good agreement with existing data. For illustration we present on Fig. 7.11 the leakage corrected Stokes I, Q and U maps of the quasar 3C 286 at 1.15 (top) and 2.05 mm (bottom) obtained for a total observational time of $\sim$ 1.7 hours. The maps are projected in equatorial coordinates. We observe that even in the case of a faint quasar (particularly at 1.15 mm) the leakage correction, presented in Sec. 6.4.1 can be applied without degrading significantly the signal-to-noise in the final polarisation maps.

3C 279

The blazar 3C 279 is one of the brightest and best monitored flat-spectrum radio quasars (FSRQ) with $z = 0.538$ and was the first object to exhibit apparent superluminal motion. Blazars, a class of active galactic nuclei containing relativistic jets of magnetised plasma pointed close to our line-of-sight, are known to be highly variable in the optical polarisation fraction and electric vector position angle (EVPA) since the early days of polarimetric observations of quasars (e.g. [Kinman, 1967]). Ultra-high resolution observations with the Very Long Baseline Array (VLBA) have demonstrated that EGRET- detected blazars possess the most highly relativistic jets among compact flat spectrum radio sources [Jorstad *et al.*, 2001] and [Kellermann *et al.*, 2004]. This is inferred from the appearance of superluminally moving knots in the jet separating from a bright, compact, stationary "core" in the VLBA images. The source of its strong radio to γ-ray emission is a relativistic jet of material ejected from nearby the black hole in its centre [Wagner *et al.*, 2015]. 3C279 is a variable source but strongly polarised up to 11 %. The results in terms polarisation degree and angle from recent observations of 3C 279 by the SHARP polarimeter

[1] http://www.vla.nrao.edu/

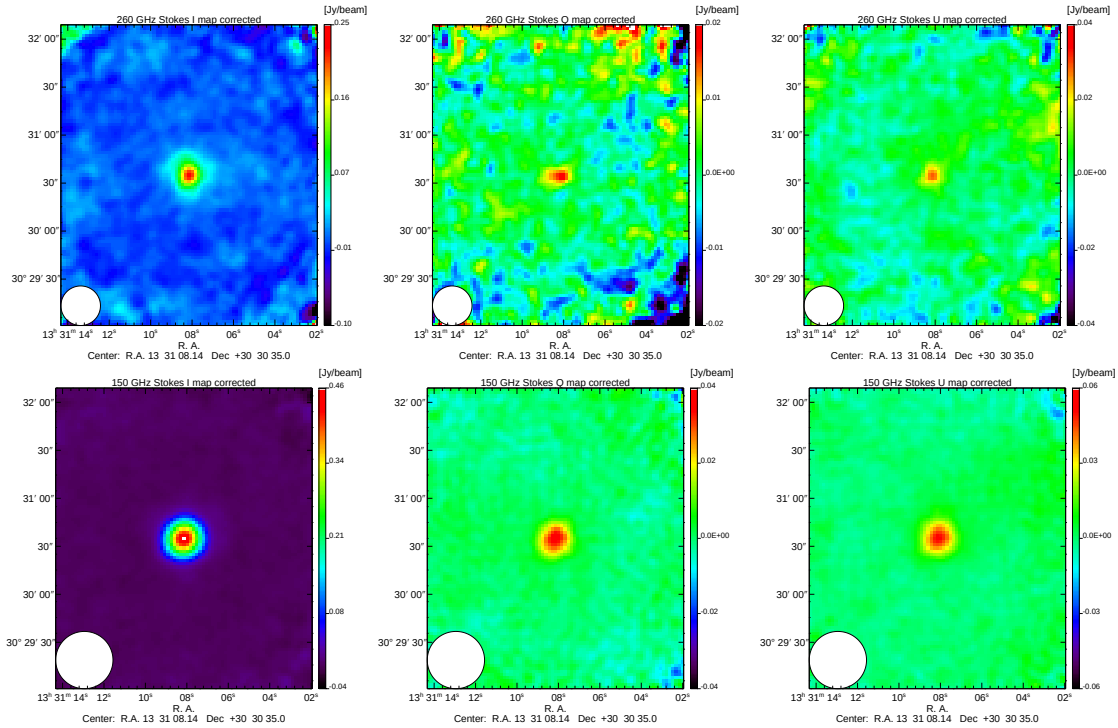

Figure 7.11: *From left to right Stokes I, Q and U maps of the quasar 3C 286 in equatorial coordinates after leakage correction at 260 GHz (top) and 150 GHz (bottom), respectively. The total observation time corresponds to 1.7 hours.*

[Lee *et al.*, 2015] are presented in Tab. 7.1 . These observations were performed in March 2014 at 350 μm, and at 3.5, 7, 13 mm. At *NIKA* wavelengths the core of the 3C 279 appears very bright. The results obtained in terms of Stokes I, Q, U and polarisation degree and angle measured by *NIKA* are reported in Tab. 7.2. Even if this source is not classified as primary calibrator, the results obtained are in agreement with SHARP observations.

3C273 and 0923+092

3C273 This source is located in the constellation of Virgo at a redshift of $z = 0.158$ [Madsen *et al.*, 2015]. It is the first quasar ever to be identified. 3C 273 is the nearest high-luminosity quasar and hence one of the best monitored Active Galactic Nuclei (AGN). From radio to millimetre wavelengths, flares from the relativistic jet dominate the variability of 3C 273 [Abdo *et al.*, 2010]. Even if this source is bright it exhibits low polarisation, at a level of 0.7% [Nartallo *et al.*, 1998]. *NIKA* observations of 3C 273 shows relatively low polarisation, around 3-4 % (see Tab. 7.2), at mm wavelengths. We found good agreement between the results obtained at 1.15 mm with the 1.3 mm results of XPOL, which performed a joint session of observations (see XPOL results in Tab. 7.1). At 3 mm XPOL measured a polarisation angle completely different from its result at 1.3 mm and ours. The polarisation angle is mainly affected by Faraday rotation, which changes the angle as ν^{-2}. It is a weak effect at mm wavelengths, but clearly present in the more active AGNs. There it affects more the 3 mm than the 2 or 1 mm data.

0923+092 Observed at different epochs, the variation in polarisation (and flux) of this quasar is quite weak [Nartallo *et al.*, 1998]. *NIKA* observations (Tab. 7.2) show an angle in agreement with this reference and with XPOL observations performed during a joint session of observation with *NIKA2* (January 2016) (see Tab. 7.1).

To express polarisation angles, we use the IAU convention, which counts East from North in the equatorial coordinate system. Uncertainties in the degree and angle of polarisation of the quasars presented above are computed assuming Gaussian distributed quantities as explained in Sec. 7.2.1. The results obtained by *NIKA* on these quasars in terms of Stokes I, Q, U flux, polarisation degree p and angle ψ are reported in Tab. 7.2. Notice that the uncertainty in Q and U are generally comparable, as expected. A difference between the uncertainties values in Q and U of the quasar 3C 279 can be explained by a residual correlated pixel-to-pixel noise. This residual noise has not been accounted for in the reconstruction of the polarised maps and it can be due to the uncertainty estimation method, which is calculated by 2D Gaussian fit in the regions outside the source. In addition, the absolute calibration uncertainty estimated at a level of 14% at 1.15 mm and 5% at 2.05 mm has to be added. These values come from the intensity flux dispersion measured on all scans of Uranus during an observational campaign (see Sec. 7.1). An additional uncertainty is linked to the HWP zero position determination. Since a step of the motor corresponds to 3.6° the systematic uncertainty on the position of the HWP zero is equivalent to 1.8°.

Tab. 7.1 reports the results obtained from the observations on these quasars by other polarimeters. In particular, during the polarisation *Run* 12 of *NIKA* and the commissioning run of *NIKA2* we had the opportunity to have a joint session of observations with XPOL [Thum *et al.*, 2008]. Fig. 7.12 reports the comparison between *NIKA* observations and XPOL in terms of polarisation degree (top panel) and polarisation angle (bottom) for the quasars described above. Generally we observe good agreement between *NIKA* observations and those from other experiments, both in terms of polarisation degree and angle [Ritacco *et al.*, 2016b].

Table 7.1: *Degree and angle of polarisation of the NIKA observed quasars as measured by external experiments.*

Source	Experiment	Wavelength	p [%]	ψ [°]	Observation date
3C279	SHARP Polarimeter	350 μm, (3.5, 7, 13) mm	10 %-12 %	32-41	2014, March
	XPOL	1.15 mm	11.79 ± 0.29	45.6 ± 0.7	2016, January
3C273	XPOL	1.3 mm	3.6 ±0.2	-76.8±1.6	2015, February
	XPOL	1.15 mm	1.59 ± 0.18	-71.8 ± 3.1	2016, January
	XPOL	3 mm	1.1±0.0	-37.8±0.9	2015, February
3C286	XPOL	1.3 mm	14.4 ± 1.8	33.1 ±5.7	2006-2012
	CARMA	1.3 mm		39.1± 1	2015, May
	XPOL	3 mm	13.5 ±0.3	37.3 ±0.8	2006-2012
0923+392	XPOL	1.15 mm	6.1 ± 2.3	-52.59 ± 10.97	2016, January

Table 7.2: *NIKA measured intensity and polarisation fluxes, polarisation degree and angle at 260 GHz and at 150 GHz for the quasars observed during the February 2015 campaign.*

Source	Frequency [GHz]	I flux [Jy]	Q flux [Jy]	U flux [Jy]	p [%]	ψ [°]
3C279	260	8.52±0.28	0.26±0.01	0.79±0.03	9.8 ±0.4	35.9±0.5(stat)±1.8(syst)
	150	12.21±0.58	0.51±0.02	1.04±0.05	9.5±0.6	31.9±0.7(stat)±1.8(syst)
3C273	260	6.35±0.22	-0.22±0.01	-0.01±0.01	3.4±0.3	-88.7±0.9(stat)±1.8(syst)
	150	9.95±0.48	-0.17±0.01	-0.11±0.01	2.0±0.1	-74.1±1.1(stat)± 1.8(syst)
3C286	260	0.27±0.01	0.021±0.003	0.033±0.004	14.3±1.7	29.6±2.5(stat)±1.8(syst)
	150	0.51±0.03	0.039±0.002	0.056±0.002	13.6±0.8	27.6±0.9(stat)±1.8(syst)
0923+392	260	2.04±0.06	-0.002 ±0.005	-0.066±0.005	3.2±0.3	-46.1±2.4(stat)±1.8(syst)
	150	3.24±0.14	-0.016±0.005	-0.087±0.006	2.7±0.2	-50.4±1.7(stat)±1.8(syst)

7.2.3 Estimation of the *NIKA* sensitivity in polarisation observations

The NEFD (Noise-Equivalent-Flux-Density) (see Sec. 3.4 for the definition) in polarisation mode observation of *NIKA* is estimated on 3C 286, the weaker source we could observe and on which we integrated for 1h40 min.

The measured NEFDs in total intensity are larger than 150 mJy.s$^{1/2}$ at 260 GHz and about 40 mJy.s$^{1/2}$ at 150GHz. These values are not consistent with the observed NEFDs in Q and U, nor with the measured NEFDs when *NIKA* is used in total power mode, without the polarisation module. This is most probably due to residual atmospheric noise in the final maps that we could not reject optimally, especially with only 1h40min of integration. However, since polarisation is not affected by low frequency atmospheric or electronic noise, the measured NEFDs in Q and U (equal to each other) are more reliable and are found to be 120 mJy.s$^{1/2}$ at 260 GHz and 50 mJy.s$^{1/2}$ at 150 GHz. From these values, we can derive the expected NEFDs in I that must be a factor $\sqrt{2}$ lower, that is to say 85 mJy.s$^{1/2}$ at 260 GHz and 35.4 mJy.s$^{1/2}$ at 150 GHz. In order to compare these values to those of *NIKA* in total power mode, we must account for an extra factor 2. Indeed, our absolute calibration is performed on Uranus that is unpolarised and

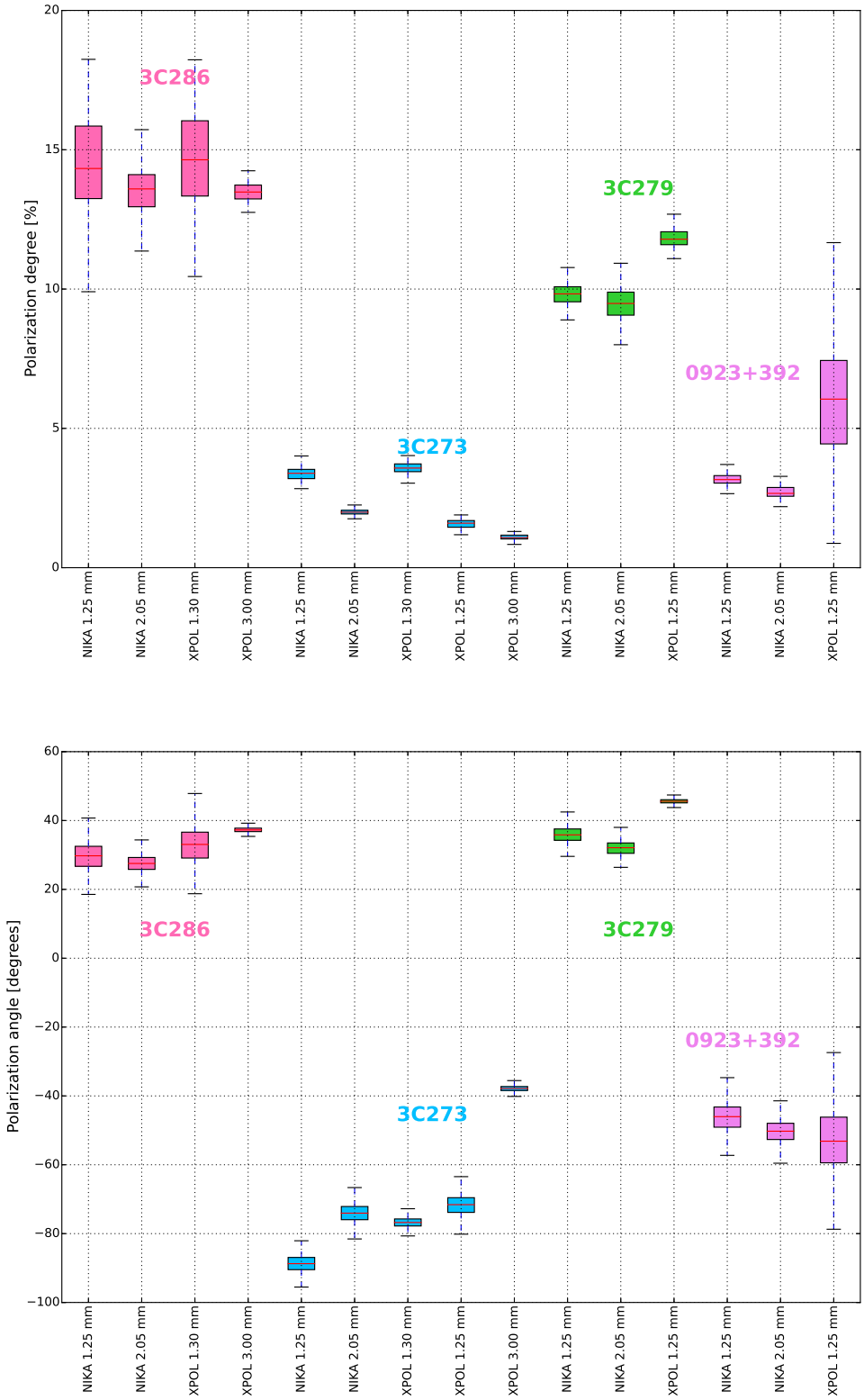

Figure 7.12: *Comparison between the results obtained with the NIKA polarimeter and those obtained XPOL. We show the degree of polarisation (top) and polarisation angle (bottom) for the quasars 3C 286, 3C 273, 3C 279 and 0923+392.*

when the polariser is placed in front of the cryostat, half of the photons are rejected. Thus, accounting for this factor, we end up with 85/2=42.5 and 35.4/2=17.7 mJy.s$^{1/2}$ at 260 and 150GHz respectively, which are very close to the measured values of 48 and 23 on *NIKA* in total power as reported in [Catalano *et al.*, 2014]. To conclude this section Tab. 7.3 reports the summary of the *NIKA* polarimeter performance.

Table 7.3: *Performance of the NIKA polarimeter.*

Array	1.15 mm	2.05 mm
Valid pixels	132	224
Field of View (arcmin)	1.8	1.8
Band-pass (GHz)	190 - 310	110 -180
FWHM (arcsec)	12	18.2
Polarisation capability	yes	yes
Sensitivity (mJy.s$^{1/2}$) in polarisation	120	50
Sensitivity (mJy.s$^{1/2}$) in intensity	42.5	17.7
Instrumental polarisation residual	0.7%	0.6%
Precision in polarisation angle estimation	1.8°	1.8°

7.3 Observations of compact and extended sources

In this section we will be presenting observations of compact and extended polarised sources. These observations allow us to further validate the quality of the reconstruction of the polarised sky signal with the *NIKA* camera. Special care is taken on the verification of the validity of the leakage correction algorithm. During the *Run* 12 we have performed observations of different types of sources: Cygnus A, a radio galaxy with diffuse emission between the two lobes; the Orion molecular cloud OMC-1, a nearby highly polarised galactic cloud; and M87, an external galaxy [Ritacco *et al.*, 2016b]. Observations of the Crab nebula have been performed several times during the *NIKA* polarisation runs. A preliminary report on these observations has been given in [Ritacco *et al.*, 2016a] and a more detailed analysis is presented in Chap. 8.

Next section presents observations of M87, Cygnus A and OMC-1. The Stokes I, Q, U maps have been obtained using the data analysis software described in Sec. 6.

7.3.1 M87

M87, also designated as 3C 274, or NGC 4486, or Virgo A, is a giant elliptical galaxy [de Vaucouleurs *et al.*, 1976] located near the core of the Virgo cluster. Its nucleus is a radio and X-ray source from which emanates an optical jet. M87 is estimated to be about 16 Mpc from Earth [Mould *et al.*, 1980]. The core and the jet can be seen at all wavelengths from radio to X-rays. Fig. 7.13 presents the *NIKA* leakage corrected Stokes I, Q and U maps at 260 (top) and 150 (bottom) GHz. The peak flux of the intensity I map is $\sim$ 0.6 Jy/beam and $\sim$ 1.5 Jy/beam at 260 GHz and 150 GHz, respectively. This confirms the fact that the M87 emission is dominated by synchrotron.

The polarisation vectors are over-plotted on the Stokes intensity I map observed at 150 GHz where the intensity $I > 0$ and the polarisation intensity is detected at S/N $>$ 2 (P $>$ 2 σ_P). They show up well-aligned following the intensity contours. This suggests the existence of a large scale ordered magnetic field in the radio lobes of M87. The size of the vectors represent the polarisation degree and their orientation the angle. We do not observe a significant polarisation

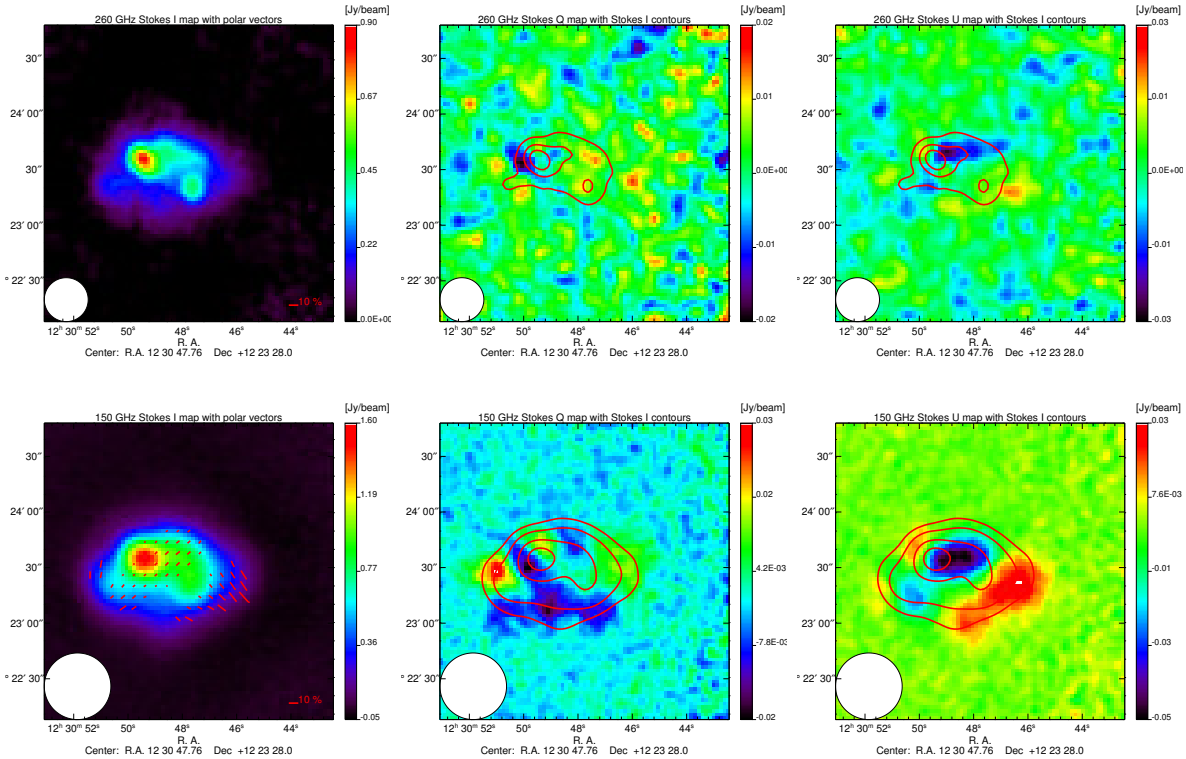

Figure 7.13: *M87 leakage corrected Stokes I, Q and U maps at 260 GHz (top) and 150 GHz (bottom). The contours in Q and U represent the intensity map for each frequency. They start from 0.2 Jy/beam with steps of 0.2 Jy/beam. Polarisation vectors are overplotted in red on the intensity image when $I > 0$ and $P > 2\,\sigma_P$.*

at 260 GHz. This is most probably due to the low S/N. Fig. 7.14 shows the polarisation intensity P maps at both *NIKA* frequencies and Fig. 7.15 shows the polarisation degree and angle observed at 150 GHz, respectively. Only the regions with 2% of polarisation are significant and consistent with the regions where polarisation vectors are over-plotted on the intensity I map. The leakage maps on Fig. 7.16 show up the low level of this systematic effect on extended source observations, peak-to-peak is estimated lower than 1 % of the total intensity at 150 GHz. At 260 GHz the leakage effect is blended to the noise. To our knowledge this is the first detection in polarisation of this source at 150 GHz.

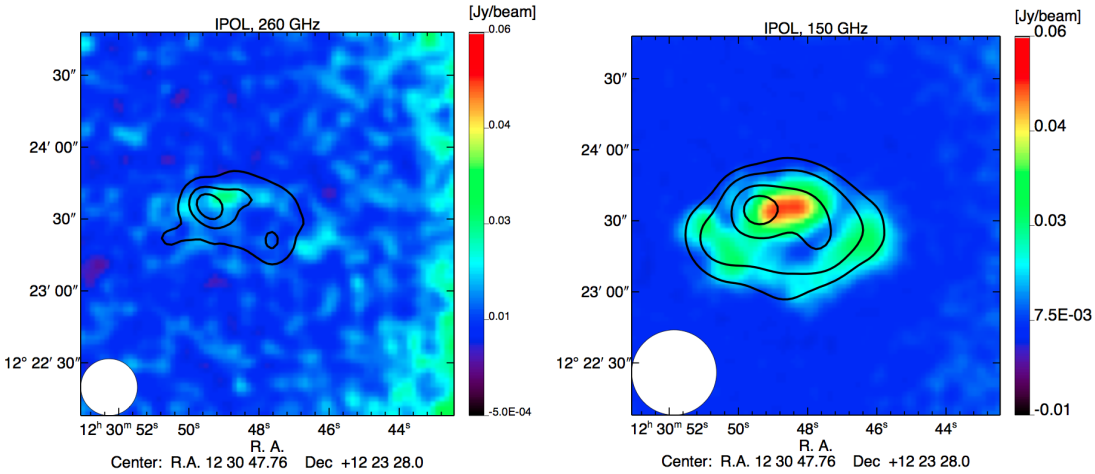

Figure 7.14: *Polarisation intensity at 260 GHz (left) and 150 GHz (right) for the radio galaxy M87 with intensity contours over plotted in red. We observe that the maximum of polarisation intensity is shifted with respect to the maximum in intensity.*

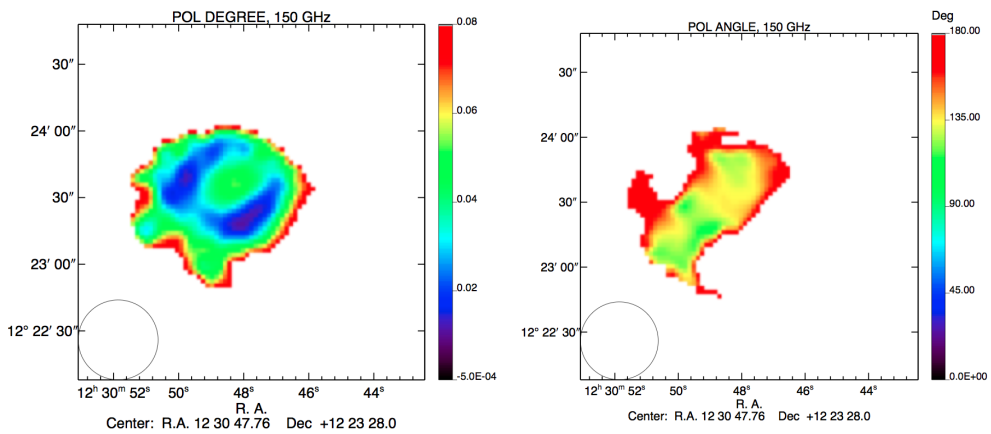

Figure 7.15: *Polarisation degree (left) and angle (right) map of M87 in the region where $P > 2\ \sigma_P$. The most polarised regions of the source reaches a value of the polarisation degree of $\sim$ 2%.*

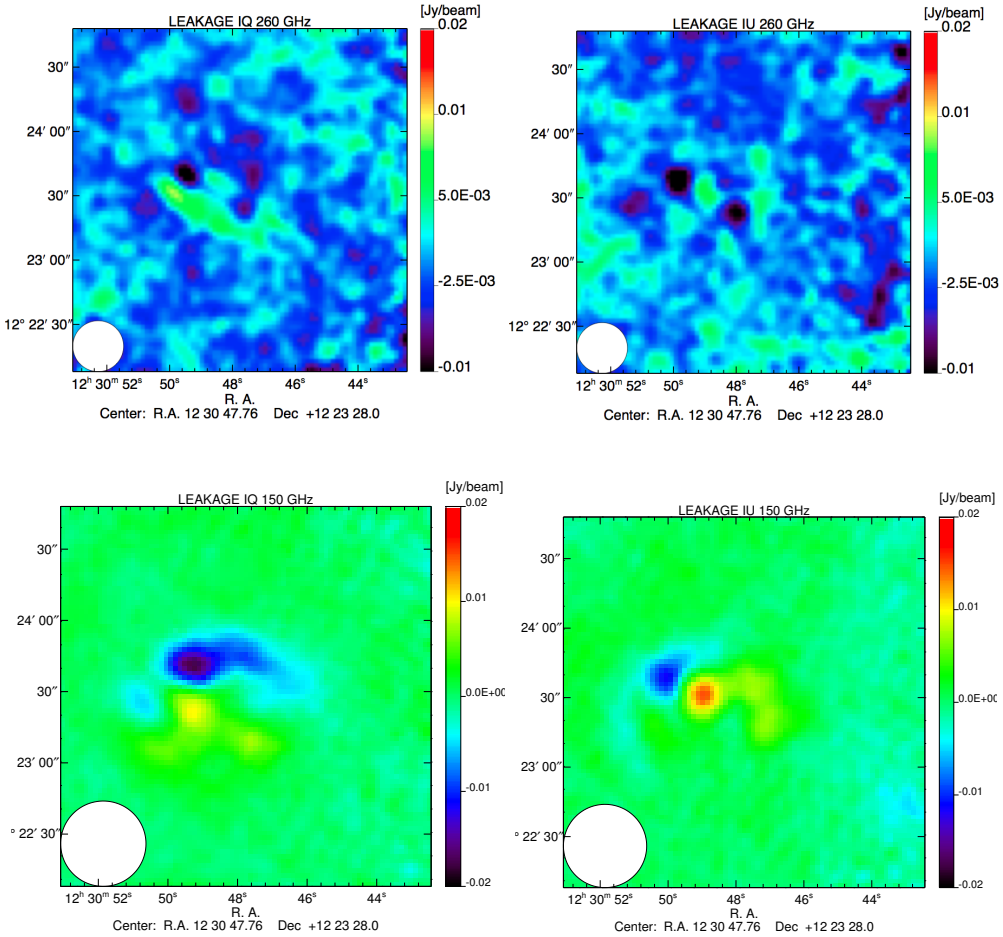

Figure 7.16: *M87 polarisation leakage maps $I \rightarrow Q$ (left) and $I \rightarrow U$ (right) at 260 GHz (top) and 150 GHz (bottom). We observe that the polarisation leakage is very small, lower than 1% of the intensity.*

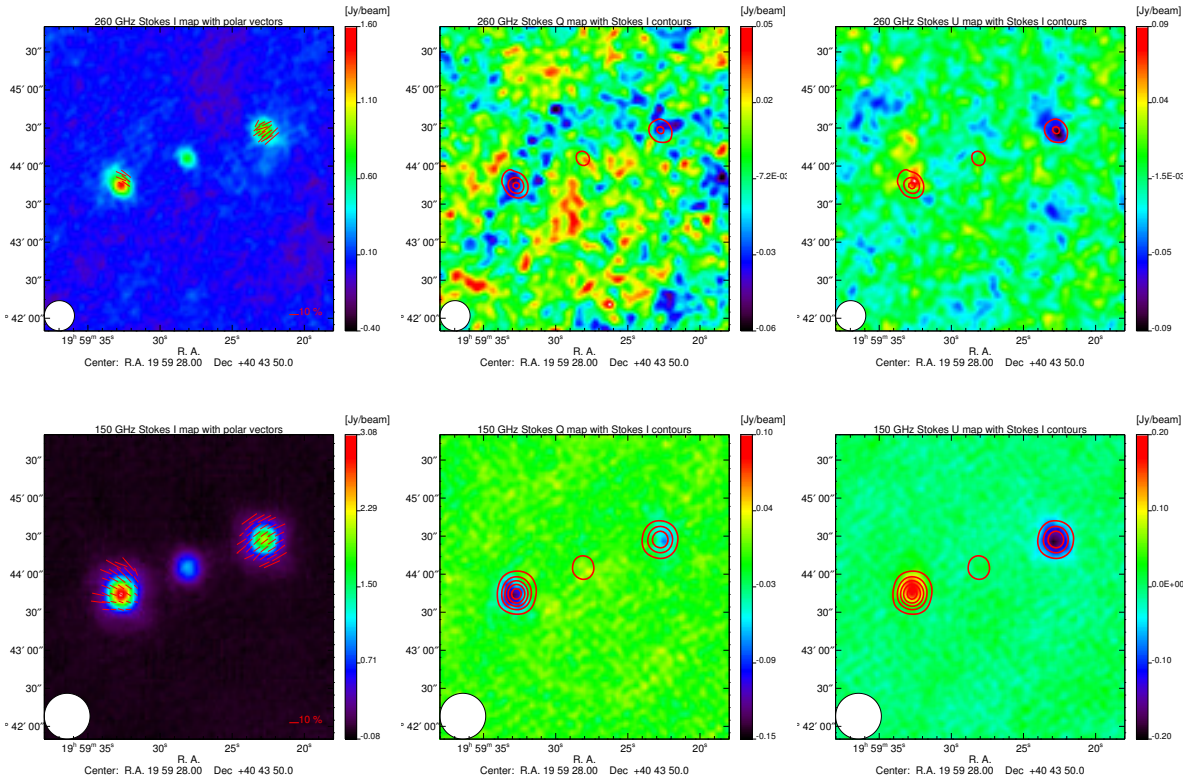

Figure 7.17: *Cygnus A leakage corrected Stokes I, Q and U maps at 260 GHz (top) and 150 GHz (bottom). The contours in Q, U represent the intensity map. They start from 0.2 Jy/beam with steps of 0.2 Jy/beam. Polarisation vectors are over-plotted in red on the intensity image when $I > 0$ and $P > 2\,\sigma_P$.*

7.3.2 Cygnus-A

Cygnus A is a typical radio galaxy with twin jets of plasma emanating from its nucleus and forming two extended, radio lobes. Cygnus A is the most powerful Fanaroff-Riley II (FRII) radio galaxy in the local environment. At low radio frequencies, the synchrotron emission from the two giant lobes dominate [Hargrave et Ryle, 1974]. At higher frequencies the radio hotspots and the galaxy core become more prominent. The southern and northern hotspots are at 50 and 70 arcsec from the core, respectively. The complex structure of Cygnus A can be well-explained by assuming that it consists of two components, which are polarized in opposite directions and of an unpolarized core ([Schraml et Turlo, 1967], [Soboleva, 1966] and [Mayer et Hollinger, 1968]). The leakage corrected *NIKA* Stokes I, Q, and U maps of Cygnus A at 260 (top row) and 150 (bottom row) GHz are presented on Fig. 7.17.

On the intensity maps the polarisation vectors are over-plotted in red. On the Q and U maps Stokes I map contours are also represented in red. As expected, on the intensity maps at 1.15 and 2.05 mm we clearly observe three compact sources corresponding to the central galaxy and two hotspots emitted by it. By contrast, the polarisation maps show only two polarised regions that correspond to the radio hotspots and nothing on the core, as expected. This is an unambiguous confirmation of the astrophysical origin of the observed polarisation: if it was due to instrumental polarisation, it would be proportional to total intensity (and therefore showed

Figure 7.18: *Polarisation intensity (a), degree (b) and angle (c) maps at 260 GHz (left) and 150 GHz (right) of the radio galaxy Cygnus A. Only the regions with $P > 2\ \sigma_P$ are plotted on (b) and (c).*

(a)

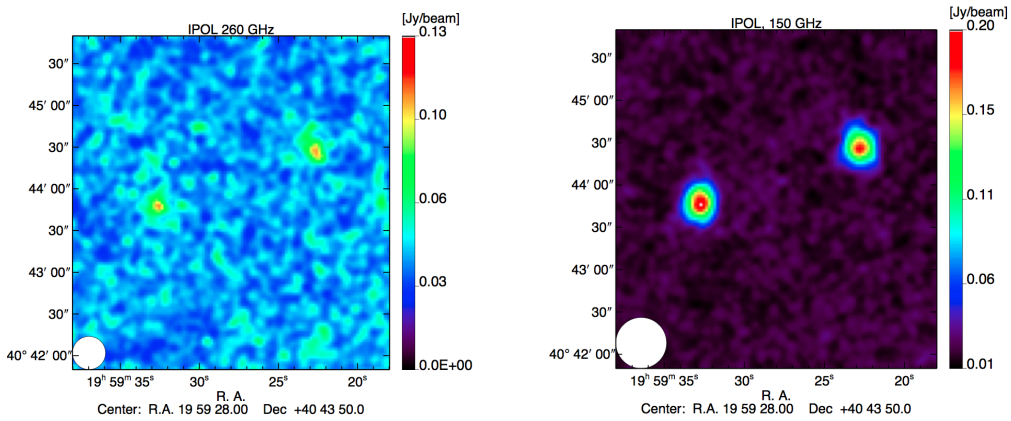

(b) Even if the polarisation is lower at 260 GHz, $\sim 10\%$ of polarisation is detected at both wavelengths.

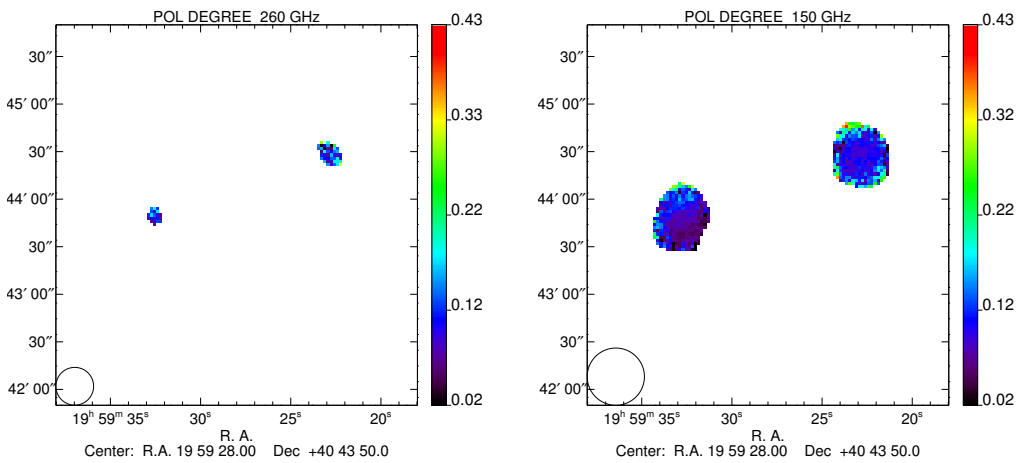

(c) The opposite direction of the polarisation of the two hotspots shows up at both wavelengths.

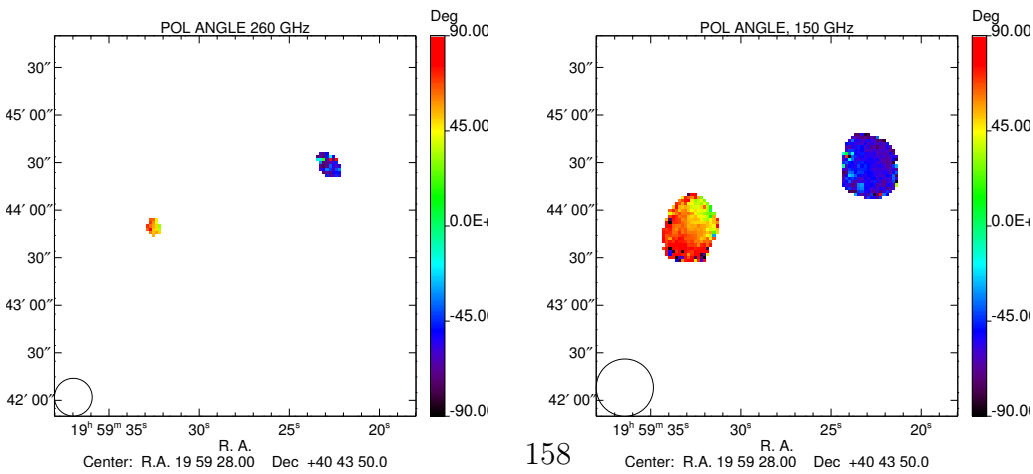

up also on the core) and with identical direction on the entire map. The polarisation intensity maps are reported on the top panel of Fig. 7.18 (a) showing a more polarised emission of the two radio hotspots at 2.05 mm than at 1.15 mm.

The polarisation degree maps are reported on the central panel of Fig. 7.18 (b) and the angle maps on the bottom panel (c), respectively. On the two radio hotspots emission of this source the polarisation degree reaches a level of $\sim 10\%$ at both wavelengths. For illustration, the leakage maps are shown on Fig. 7.19. The level of the polarisation leakage peak-to-peak reaches a value of $\sim 3\%$ at both wavelengths and we correct for it. This confirms the interpretation that on compact sources the intensity to polarisation leakage is larger than in diffuse sources. While Cygnus-A shows up a diffuse emission at radio frequencies, with *NIKA* we have not detected such emission. To our knowledge this is the first detection of this source in polarisation at these mm wavelengths.

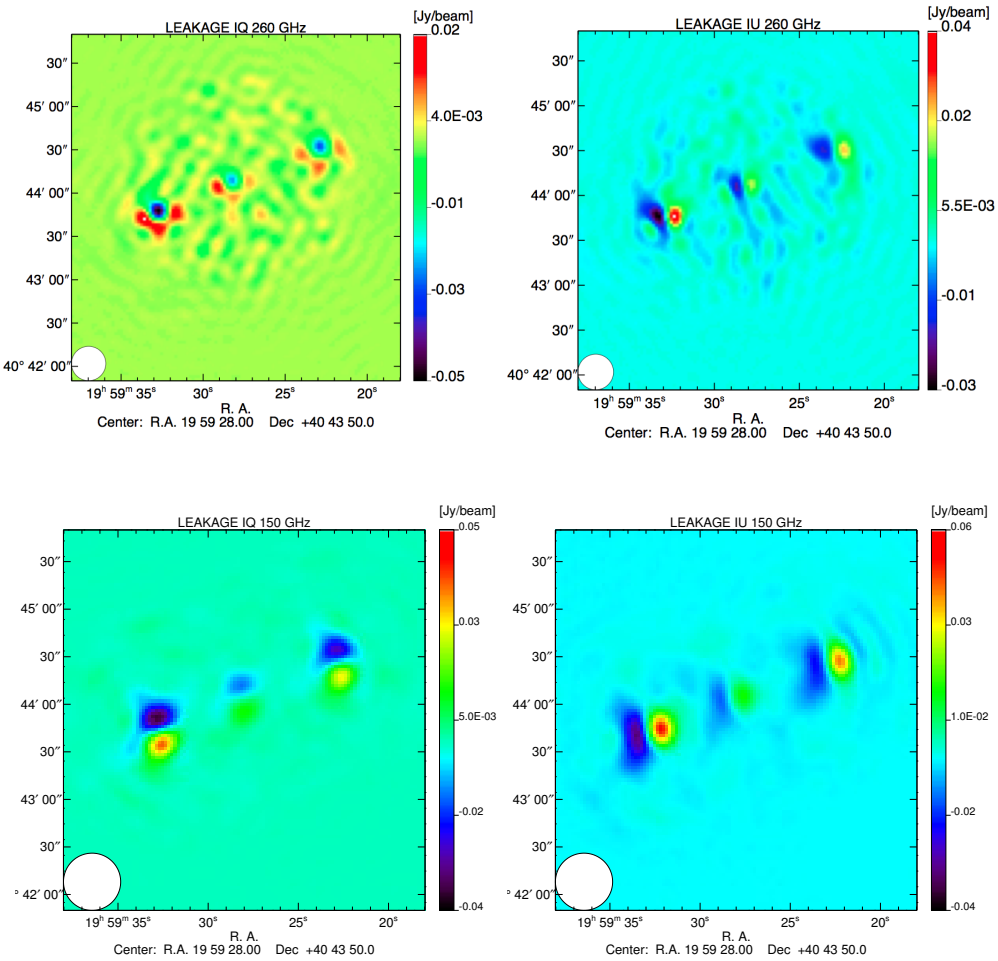

Figure 7.19: *From left to right Cygnus-A intensity to polarisation leakage maps IQ, IU at 260 GHz and at 150 GHz. We observe that the leakage maps show a bipolar pattern in the three sources, the two hotspots and the nucleus.*

7.3.3 Orion OMC-1 molecular cloud

The Orion Molecular Cloud (OMC-1) is the closest site of OB star formation. Fig. 7.20, extracted from [Schleuning, 1998], shows a general view of OMC-1. It reports observations of OMC-1 at 100

μm and 350 μm. The KL nebula, corresponding to the peak of the intensity flux from far infrared to millimetre wavelengths on the OMC-1 "ridge", is also represented in the figure. Mapping the polarisation of the thermal emission of dust at millimetre or sub-millimetre wavelengths (usually 850 μm or 1.3 mm) is the principal means of probing the magnetic field geometry in molecular cloud cores. A frequent characteristic of these observations is the decrease of polarisation degree p as a function of the total observed intensity I. This depolarisation effect (sometimes referred to as "polarisation hole") has been observed in many dense cores and filamentary clouds. [Schleuning, 1998] confirmed the weak polarisation and its orientation already measured by [Hildebrand *et al.*, 1984] towards the KL nebula. This strong emission observed in this region is thought to be powered by an explosive event [Zapata *et al.*, 2011]. Another region of interest is found 90 arcsec at south of KL along the ridge, it is a sub-millimetre peak called KHW [Keene *et al.*, 1982].

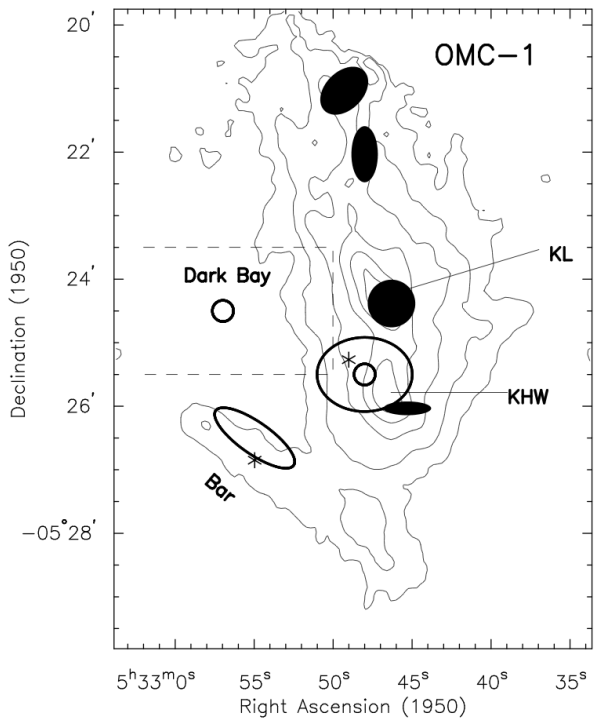

Figure 7.20: *Intensity OMC-1 map observed at 350 μm by [Schleuning, 1998].*

NIKA observations

Leakage corrected Stokes I, Q, U $8' \times 8'$ *NIKA* maps of OMC-1 are presented on Fig. 7.21. They correspond to the co-addition of 18 scans for a total observational time of $\sim$ 5h. The polarisation vectors are over-plotted on the intensity maps showing the polarisation fraction and its orientation. The peak of the flux is observed across the KL nebula where we observe a flux of 45.8 Jy/beam and 14 Jy/beam at 260 GHz and 150 GHz, respectively. The orientation of the polarisation vectors shows up well aligned following the intensity structures across the source and suggesting a well ordered magnetic field. They are consistent between the 260 and 150 GHz map, confirming the same physical origin of the observed polarisation.

In order to directly compare with the POLKA map observed at 870 μm we put on top of the POLKA map reported on Fig. 7.22 *NIKA* polarisation vectors (red line). Let us note that the orientation polarisation vectors is consistent with POLKA polarisation vectors. It also appears

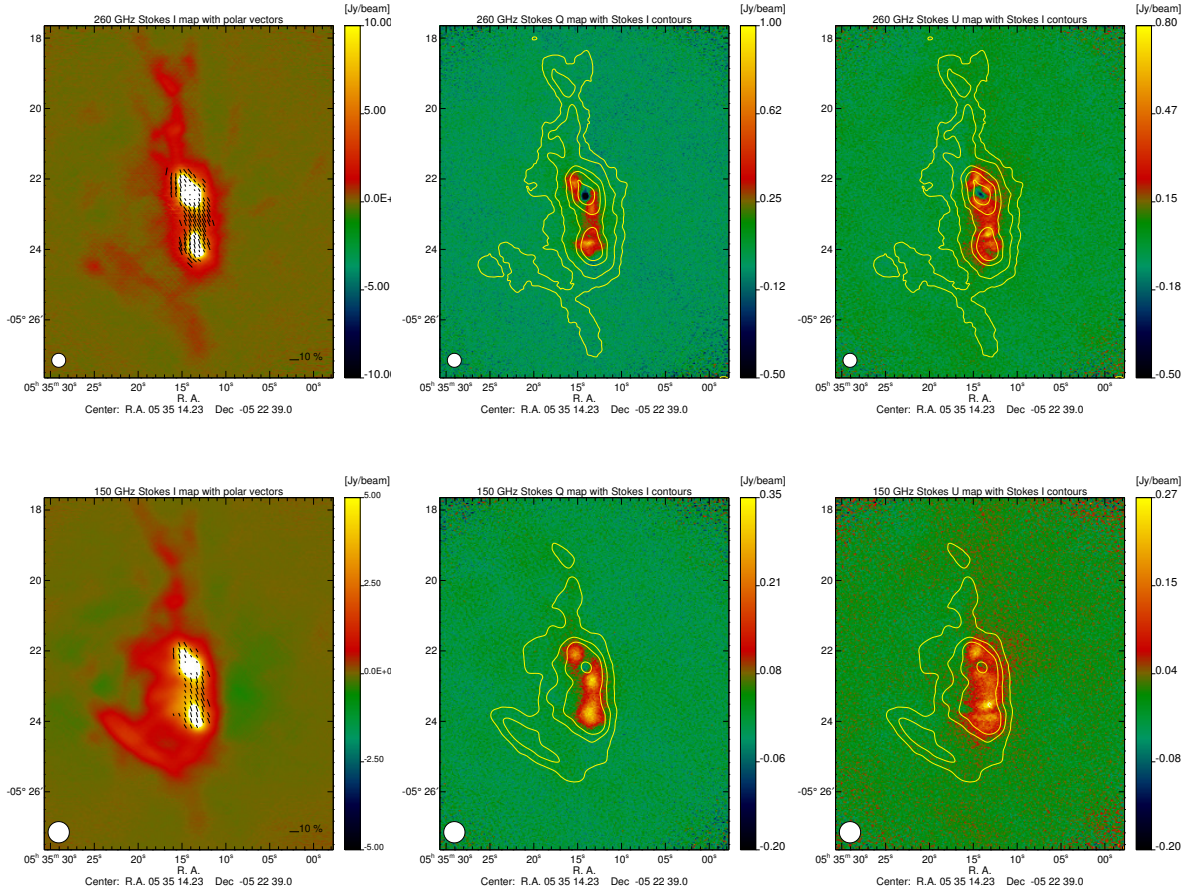

Figure 7.21: *Stokes leakage corrected I, Q and U maps of Orion OMC-1 at 260 GHz (top) and 150 GHz (bottom). The intensity contours over-plotted in the Q and U maps corresponds to [0.3, 1, 3, 6, 15, 48] Jy/beam at 260 GHz and [0.3, 1, 2, 10, 14] Jy/beam at 150 GHz. Polarisation vectors are plotted in red on the intensity image where $I > 0$ and $P > 2\,\sigma_P$.*

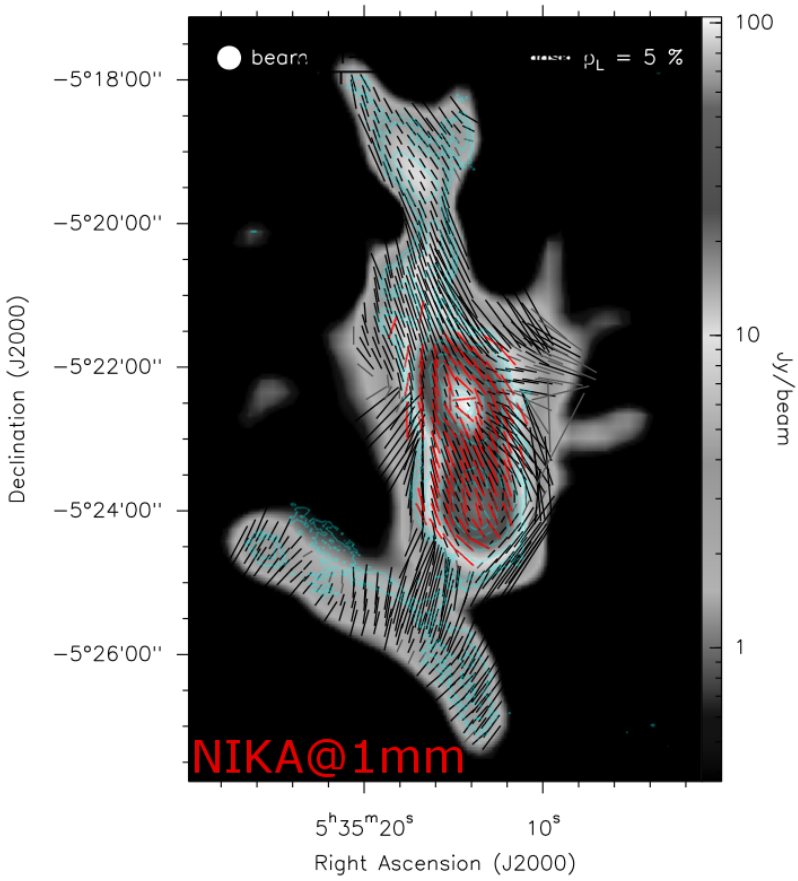

Figure 7.22: *Polarisation vectors measured by NIKA at 1.15 mm over plotted in red on the POLKA map [Wiesemeyer et al., 2014].*

an increase of the polarisation fraction in the diffuse emission regions. By contrast, we observe a decrease of the polarisation degree across KL nebula. Tab. 7.4 reports a summary of the results obtained by *NIKA* at both wavelengths to compare with SCUPOL [Matthews *et al.*, 2009] and POLKA [Wiesemeyer *et al.*, 2014] results. While the results found at 1.15 mm are well consistent with SCUPOL and POLKA, at 2.05 mm they are in agreement within the error bars only with SCUPOL [Matthews *et al.*, 2009].

For illustration, the intensity to polarisation leakage maps are reported on Fig. 7.23 showing a level of 2% of the intensity signal peak-to-peak. This effect is particularly intense in the most compact regions of the source where the intensity flux increases.

The polarisation degree maps p as observed at both *NIKA* frequencies are reported on the central panel of Fig. 7.24 (b). We observe on both maps a polarisation degree that reaches a level of about 10% of the total intensity in regions where the diffuse intensity emission is observed. This polarisation fraction decreases greatly near the KL nebula. The polarisation angle ψ is shown on the bottom panel of Fig. 7.24 (c). It shows up approximately constant on the extended emission reaching a value of $\sim$ 20-30°. Averaging across the KL nebula, the values obtained at 260 GHz of p and ψ are [0.6 $\pm$ 0.2] % and [37.73 $\pm$ 3.56]°, respectively. At 150 GHz $p = [1 \pm 0.2]$% and $\psi = [25.35 \pm 2.15]°$. The uncertainties reported here are purely statistical, for a more precise

Table 7.4: *Summary on KL nebula polarisation degree and angle results obtained by previous experiments and NIKA. An absolute uncertainty of 1.8° has to be added to the statistical angle uncertainties reported here.*

p [%]			ψ [°]		
POLKA	SCUPOL	*NIKA*	POLKA	SCUPOL	*NIKA*
[870 μ m]	[850 μ m]	[1.15 - 2.05 mm]	[870 μ m]	[850 μ m]	[1.15 - 2.05 mm]
0.7 ± 0.2	0.7 ± 0.1	(0.6 ± 0.2) - (1.0 ± 0.2)	32.8 ± 7.6	40.8 ± 5.4	[37.73 ± 3.56] - [25.35 ± 2.15]

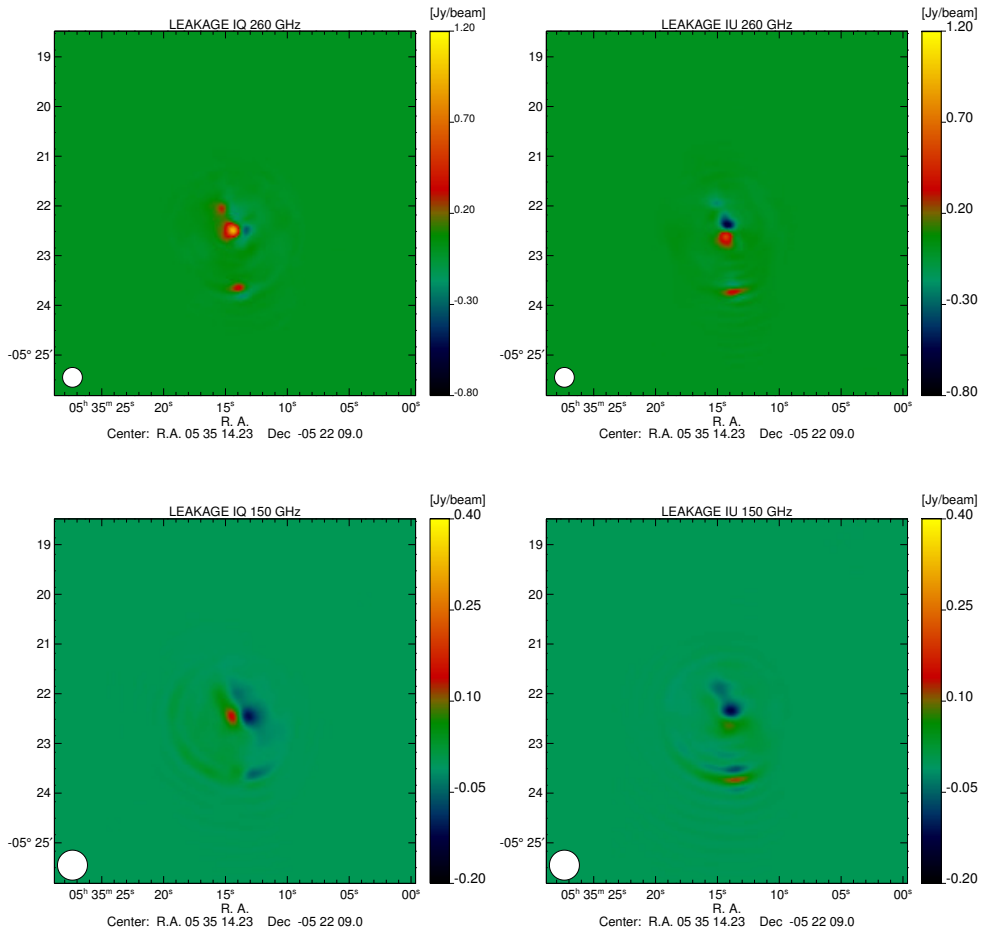

Figure 7.23: *From left to right Orion OMC-1 intensity to polarisation leakage IQ and IU maps at 260 GHz (top) and at 150 GHz (bottom).*

error estimation we have to consider the systematic uncertainty due to HWP zero position and corresponding to 1.8° as well as the calibration error calculated on Uranus, about ∼14% at 260 GHz and 5% at 150 GHz.

In order to observe the variation of the polarisation degree with the intensity structures of the source, already suggested by the polarisation vectors, we plot on Fig. 7.25 the polarisation degree as a function of the Stokes intensity I. Notice that here only the bias corrected values are represented. The uncertainties, represented in blue, have been calculated as the dispersion between the observational maps. The fraction of polarisation decreases towards high intensity flux regions confirming a depolarisation effect across the peak of the source. Whereas the faintest regions of the intensity flux map shows up a high level of polarisation. These regions correspond to the edges of the source. The total intensity emission is clearly underestimated in these regions because of the data processing, hence leading to an overestimation of p. Indeed, the atmosphere rejection is done by decorrelation as presented in Sec. 6.1.4. Because Orion is extended and of comparable size to *NIKA*'s field of view, it is not possible to mask it entirely during this process. The edges are therefore not excluded from the common mode estimation and they are filtered out to some extent. Atmosphere and correlated electronic noises are subdominant at high frequencies, such a decorrelation is not necessary on "pure"-Q and "pure"-U timelines and polarisation maps are therefore not affected. In order to quantify this effect, we compute the transfer function of the data processing on these observations.

Transfer function of OMC-1 The transfer function is somewhat hard to define exactly and to estimate as well, because it is linked to the scan pattern and it is then anisotropic. It may also depend on the input signal (and its anisotropy) and on the input noise as shown for example in [Adam, 2015] in the case of Sunyaev Zel'dovitch observations with *NIKA*. At this stage though, we shall see that an approximate definition of the transfer function is enough to explain what we observe. We therefore take its usual and simple definition as the ratio between the cross correlation spectrum of the input ($\mathcal{I}$) and output ($\mathcal{O}$) signal map and the auto correlation spectrum of the input map:

$$T_k = \frac{P_k^{\mathcal{IO}}}{P_k^{\mathcal{II}}}. \tag{7.25}$$

Where:

$$P_k^{\mathcal{IO}} = FT(M_{\mathcal{I}}) \times [FT(M_{\mathcal{O}})]^*; \tag{7.26}$$
$$P_k^{\mathcal{II}} = FT(M_{\mathcal{I}}) \times [FT(M_{\mathcal{I}})]^*. \tag{7.27}$$

In order to compute T_k, we simulate input I, Q and U maps and analyse them with the exact same mask and pipeline parameters as for real observations. We take a flat input angular power spectrum to produce the maps to be immune to a non periodic boundary effect when we will compute the angular power spectra of the maps[2]. A Gaussian noise with a $1/f$ correlated component between KIDs is taken to mimic the atmosphere. Results based on 30 simulations are presented on Fig. 7.26. As expected, the total intensity is suppressed up to three times as much as polarisation on large angular scales, clearly justifying the trend of the polarisation degree increase on the same angular scales as presented on Fig. 7.25. Note that Q and U are affected in the same way by the data processing and so the polarisation angle is less prone to be biased by the transfer function.

[2]We could in principle correct for this effect with tools developed in the context of *Planck* data analysis, but as we will consider ratios of output/input quantities, only the relative variations are important and suffice to minimise this extra complication.

Figure 7.24: *Polarisation intensity (a), degree (b) and angle (c) maps of Orion Molecular Cloud (OMC-1) at 260 GHz (left) and 150 GHz (right) with intensity contours overplotted. Only the regions with $P > 2\,\sigma_P$ are plotted on (b) and (c).*

(a)

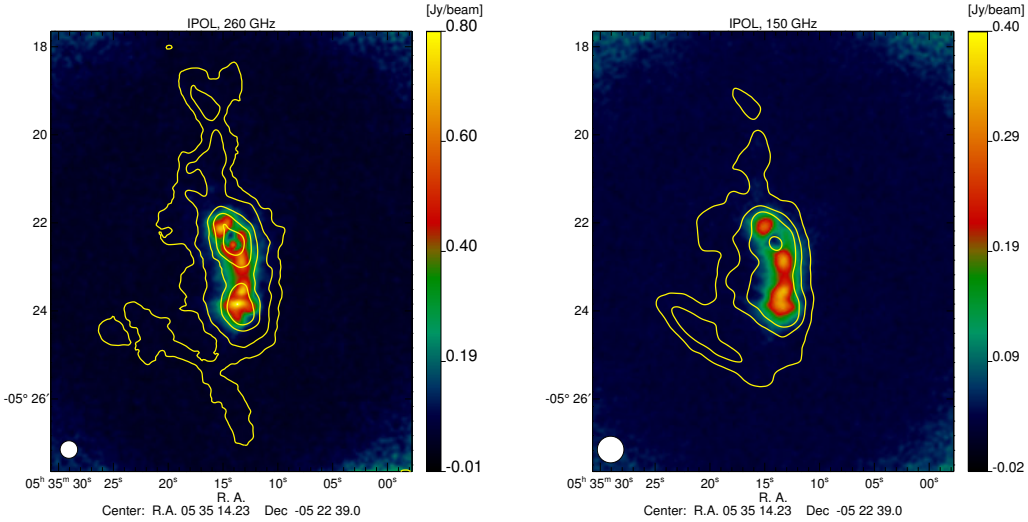

(b)

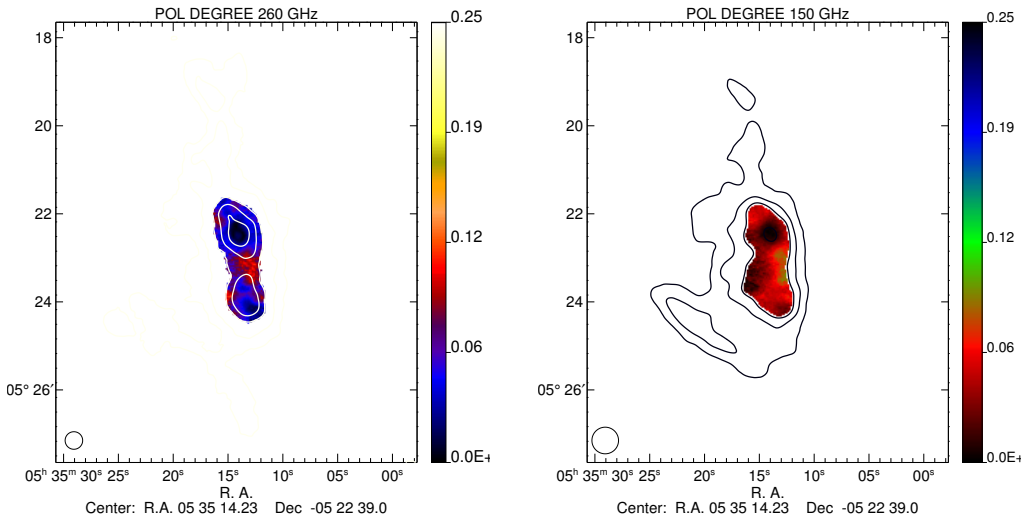

(c)

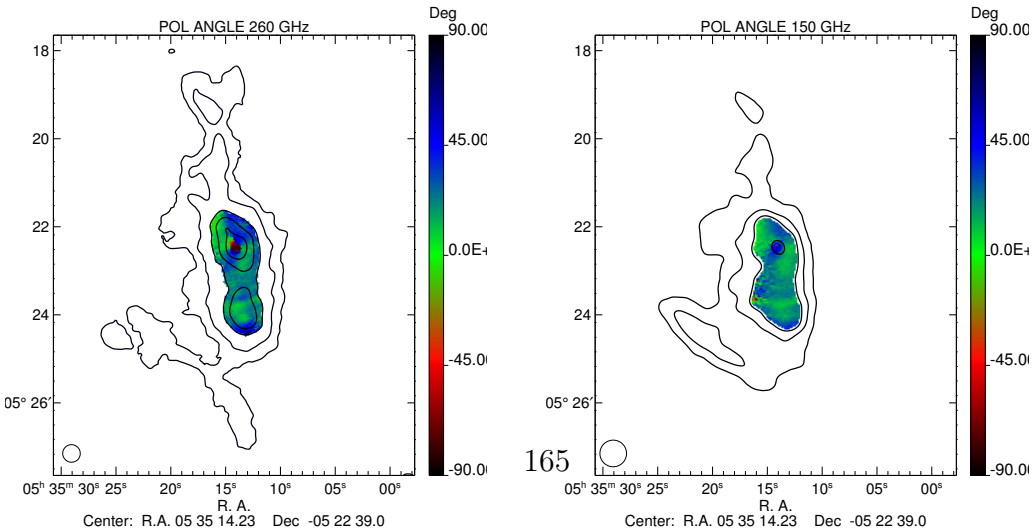

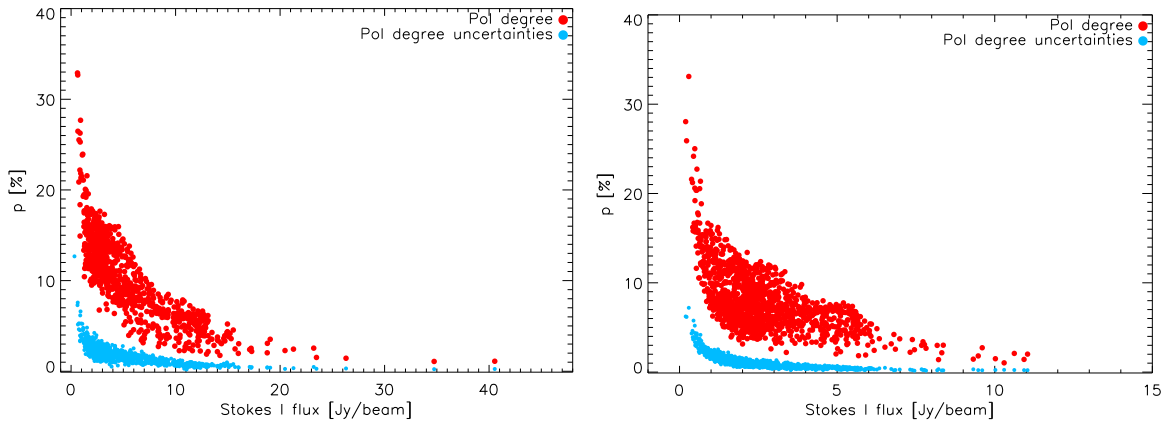

Figure 7.25: *Polarisation degree (red) as a function of the intensity observed at 1.15 mm on left and at 2.05 mm on right. Uncertainties are shown in blue in the figure.*

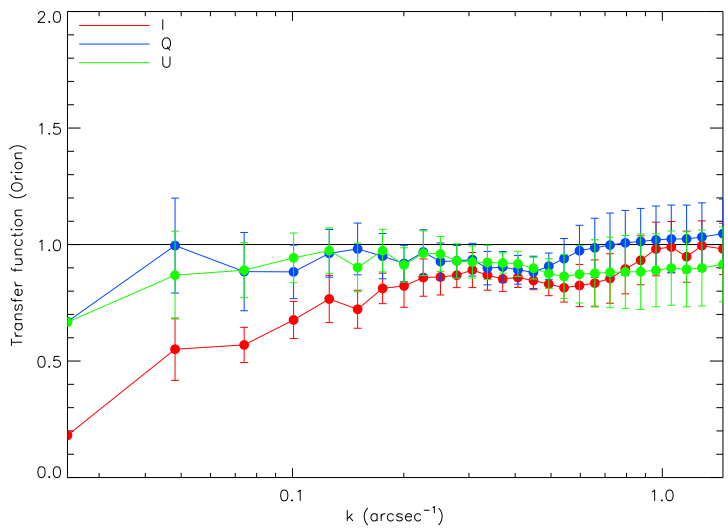

Figure 7.26: *Transfer function computed for the three Stokes parameters maps of Orion as a function of the wave number.*

7.3.4 Spectral index maps

The *NIKA* instrument, thanks to its simultaneous observation at two wavelengths, permits to recover the spatial distribution of the spectral index and draw information about the physical origin of the source emission in terms of *free-free*, synchrotron or dust emission. The spectrum of OMC-1 is expected to be described by a thermal dust emission spectrum:

$$I_\nu = I_0 \nu^{\beta_d} B_{\nu(T_d)}, \tag{7.28}$$

with β_d the spectral index of the dust emission and T_d is the dust temperature and $B_\nu(T_d)$ is the Planck spectrum. At the *NIKA* frequencies the approximation $h\nu << k_B T_d$ is valid and the Planck spectrum reduces to the Rayleigh-Jeans law:

$$B_\nu(T_d) = \frac{2\nu^2}{c^2} k_B T_{RJ}. \tag{7.29}$$

Consequently Eq. 7.28 becomes:

$$I_\nu = I_0 \frac{2}{c^2} k_B T_{RJ} \nu^{\beta_d + 2}. \tag{7.30}$$

We write $\beta' = \beta_d + 2$, the spectral index is therefore given by:

$$\beta' = \log\left(\frac{I_{\nu_1}}{I_{\nu_2}}\right) / \log\left(\frac{\nu_1}{\nu_2}\right). \tag{7.31}$$

The spectral index calculated on OMC1 is shown on the Fig. 7.27. The 1.15 mm and 2.05 mm maps have been convolved at the same resolution. We note that at 2.05 mm the extended emission along the bar, on the South of the source, is stronger than at 1.15 mm. This can be explained by the fact that the 1.15 mm intensity map is more affected by the atmospheric emission than the 2.05 mm intensity map. Consequently even if the mask used to decorrelate the two bands is the same it could be exposed to a filtering effect at large scales of the source during the common mode noise decorrelation as we have seen in Sec. 7.3.3. This difference could be also indicative of dust grain properties changing along the bar. β' reaches a value of ~ 2 in the region with a detection of $\mathrm{P} > 2\ \sigma_P$ on both spectral index maps, in intensity on left of the Fig. 7.27 and polarisation intensity P on right.

7.4 Summary and conclusions

The absolute calibration is crucial for high quality observations and to compare with other experiments. The comparison in terms of intensity flux I with other experiments reported in this chapter showed consistent results between *NIKA* and other experiments. Calibration uncertainties arises mainly from the variation of atmospheric conditions along the observation campaign and uncertainties in the opacity correction. This calibration error is generally estimated using the *NIKA* primary calibrator, Uranus.

To do observations in polarisation we need to calibrate the polarisation angle with respect to a well defined reference frame. The characterisation of the HWP in laboratory allowed us to characterise its zero position with a precision of 1.8° and to fix it with respect to the cabin reference frame at the telescope. Furthermore, to validate the accuracy in the determination of the linear polarisation signal we have compared our results with other experiments. Observations of stable and highly polarised quasars allowed us to verify the correct reconstruction of the polarisation angles. Further, a joint session of observations with XPOL experiment allowed the

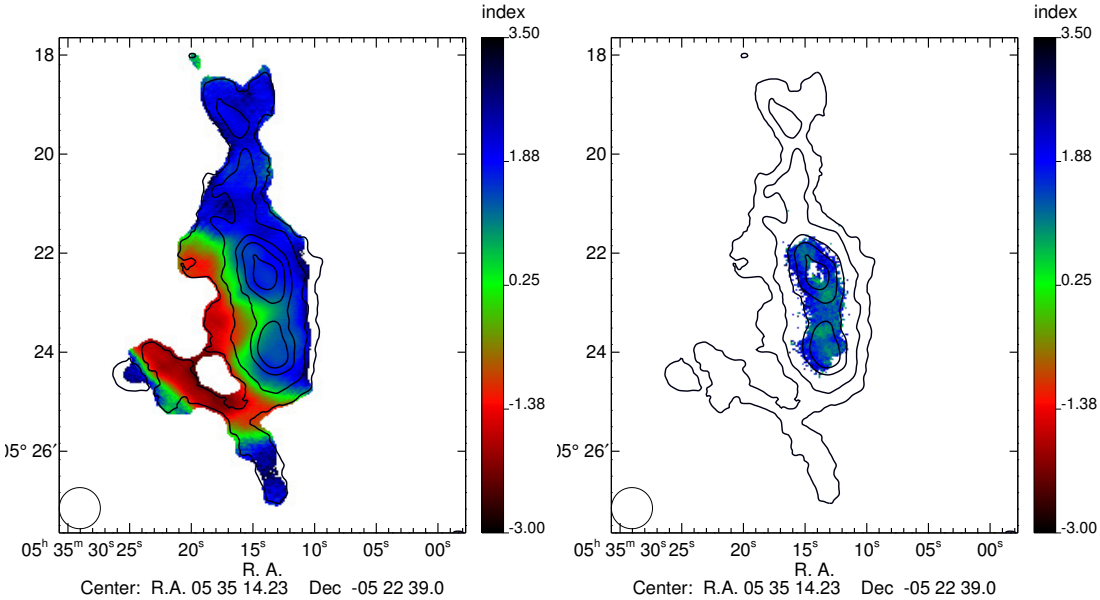

Figure 7.27: *Spectral index in intensity I (left) and polarisation intensity P for the OMC1 (right). The value of the spectral index in the region where $P > \sigma_P$ is consistent between the two maps confirming the same physical origin of the emission. It is consistent with a dust spectrum with spectral index $\beta' \simeq 2$.*

verification of the polarisation degree and angle reconstruction. Generally, we found a good agreement between *NIKA* and XPOL observations, and with other experiments, confirming the accuracy of our detection strategy and of the data analysis software developed in this thesis.

Finally we sought to probe the performance of our system in the reconstruction of the polarisation of extended sources. We have observed two radio galaxy, M87 and Cygnus-A, which have a strong synchrotron emission and the Orion molecular cloud, an interesting star forming region. All these observations established the accuracy of the detection strategy chosen, also observing astrophysical sources with fluxes of about a Jansky and degrees of polarisation as low as 3%. In particular, the observations of the different orientation of the polarisation on the two radio hotspots of Cygnus A is a striking feature and to our knowledge they are the first ones in polarisation at millimetre wavelengths.

Orion represents a typical astrophysical target for future *NIKA2* observations, aiming at characterising magnetic fields in star forming regions. It is a well known source at sub-millimetre and millimetre wavelengths. The comparison with other experiments, in particular with SCUPOL and POLKA, shows a good agreement with *NIKA* results revealing the observation of a well ordered magnetic field following the intensity structure of the source. We have started to evaluate the transfer function of the data processing on the map reconstruction and the local polarisation properties of Orion. First order approximations account for the overall trend of the degree of polarisation. In order to fully study the properties of Orion, we should go into further details, deriving transfer functions at the map level, per different scan orientation, with a more realistic simulation of the map and the atmosphere. This will be done in greater detail with *NIKA2* during the first phase of the polarisation commissioning performed in the early 2016.

Part IV

Polarisation properties of the Crab nebula

8

Millimeter polarisation properties of the Crab nebula

Contents

8.1 Polarisation angle calibration in CMB experiments 171

8.2 *NIKA* observations 172

8.2.1 Total intensity map estimation 172

8.2.2 Polarisation maps 175

8.2.3 Polarisation degree and angle estimation 178

8.2.4 A calibrator for CMB experiments 180

8.2.5 Extension to other frequencies 181

8.2.6 Polarisation intensity SED 182

8.2.7 Spectral index 183

8.3 Conclusions 184

8.1 Polarisation angle calibration in CMB experiments

The linear polarisation of the CMB anisotropies on the sky can be decomposed into a scalar and a pseudo-scalar field, respectively called E and B modes. The primordial density fluctuations (scalar perturbations) can only produce E CMB polarisation, while B CMB polarisation can only be produced by primordial (tensor perturbations) gravitational waves arising from the inflation epoch and by the gravitational lensing of the $E-$modes. Thus, the detection of the $B-$modes constitutes one of the most ambitious goals of the observational cosmology.

Recently, [BICEP2 Collaboration *et al.*, 2016] set a new upper limit for the detection of the tensor-to-scalar-ratio $r < 0.07$ at 95% confidence. Upcoming CMB experiments aiming at measuring the primordial $B-$modes require an accurate determination of the foreground contaminants to the CMB signal and a high control of systematic effects. Different instrument

parameters, if not precisely known, can induce significant systematic effects. One of the most important is the leakage of intensity to polarisation. Therefore, one needs an accurate understanding of the instrumental polarisation, which can be achieved by the study of unpolarised sources. The accuracy of the reconstructed polarisation is performed on a well-known, highly polarised source.

The Crab nebula, located at equatorial coordinates $\alpha = 5^h 34^m 32s$ and $\beta = 22°0'52''$, also known as Tau A, is a supernova remnant that emits a highly polarised signal due to the synchrotron emission of the central pulsar and its interaction with the surrounding gas. Since it is the most intense polarised source in the microwave sky at angular scales of few arcminutes, it represents one the best candidates for the calibration of the polarisation properties for CMB experiments.

For example, the *Planck* satellite mission used the Crab for polarisation cross-check in the frequency range from 30 to 353 GHz. The XPOL experiment [Thum *et al.*, 2008] mounted at the 30 meter IRAM telescope measured the spatial distribution of the Crab nebula in intensity and polarisation at 90 GHz with an absolute accuracy of 0.5° in polarisation angle [Aumont *et al.*, 2010]. The total intensity emission of the Crab exhibits a synchrotron emission spectrum decreasing with frequency with power law of spectral index $\beta = -0.296 \pm 0.06$ [Macías-Pérez *et al.*, 2010]; the polarisation angle has been shown to be constant at the degree-level, see WMAP [Weiland *et al.*, 2011] and *Planck* [Planck Collaboration *et al.*, 2015g].

The Crab nebula, together with the known quasars, represented the ideal verification source for the *NIKA* experiment. It was observed during the three *NIKA* observational campaigns in polarisation. A first report on this source has been presented in [Ritacco *et al.*, 2016a]. In this chapter I will discuss more in detail the results obtained.

8.2 *NIKA* observations

The Crab nebula maps presented in this chapter have been obtained, on February 2015, by a combination of 16 observational scans of 8×6 arcminutes for a total observation time of ~ 2.7 hours. In order to have the best coverage of the source surface, we performed on-the-fly maps oriented in equatorial coordinates according to 4 different scan direction: 0°, 90°, 120°, 150°. As usual, the observations have been acquired with a frequency sampling of 47.68 Hz and a HWP rotation frequency of 2.98 Hz.

8.2.1 Total intensity map estimation

In Chap. 6, I have presented the map-making algorithm developed and used for *NIKA* polarisation measurements. In particular Sec. 6.1.4 describes the impact of the pixel-to-pixel correlated noise due to the atmospheric emission and the methods adopted in the pipeline software to correct for this noise contribution. The Orion molecular cloud maps obtained with and without noise decorrelation showed the efficiency of the polarisation detection strategy chosen, which permits the determination of a polarised signal uncontaminated by the atmospheric noise.

Despite the fact that the polarised signal results are cleaned from the atmospheric noise, a correct measurement of the polarisation fraction also requires a good estimation of the total intensity map. For an extended source like the Crab nebula the decorrelation of the atmospheric and electronic noise is complicated by diffuse emission from small to large angular scales. Here, we will be presenting the estimation of the Stokes I intensity map provided by a common mode decorrelation masking the source, (see Sec. 6.1.4) and that provided by a new approach developed for observational targets with a stronger emission at 2.05 mm than at 1.15 mm.

For the Crab nebula a common mode decorrelation masking the source (Sec. 6.1.4) can produce significant filtering effects at large angular scales. To solve this problem we investigated the idea to use a more realistic "model" of the atmospheric based on the 1.15 mm observations. Indeed, the atmospheric emission is stronger in the 1.15 mm band than at 2.05 mm. Thus, we can use observations at 1.15 mm as a template to be subtracted from the 2.05 mm data. This approach is named "Dual band decorrelation" method and was developed for the reconstruction of the SZ signal in clusters of galaxies [Adam *et al.*, 2014b]. By contrast, the electronic noise is independent between *NIKA* channels. As a consequence, for this "Dual band decorrelation" method the electronic noise in the final maps is significantly larger than for the common mode decorrelation masking the source.

In the following we will compare these two methods using Crab nebula intensity observations. Let us formalise the "Dual band decorrelation" method using the Crab nebula as a target. Since this source is well described by a synchrotron spectrum we can write the signal detected at 1.15 mm ($m_{1\mathrm{mm}}$) and 2.05 mm ($m_{2\mathrm{mm}}$) as:

$$\begin{aligned} m_{1\mathrm{mm}} &= C\nu_1^{\beta} + A_{1\mathrm{mm}} + E_{1\mathrm{mm}}, \\ m_{2\mathrm{mm}} &= C\nu_2^{\beta} + A_{2\mathrm{mm}} + E_{2\mathrm{mm}}, \end{aligned} \tag{8.1}$$

where $A_{1\mathrm{mm}}$ and $A_{2\mathrm{mm}}$ represent the atmospheric emission terms and $E_{1\mathrm{mm}}$, $E_{2\mathrm{mm}}$ represent the electronic noise terms in the two mm *NIKA* bands. Using a well adapted mask on the source we can create a common mode template, which consists of an estimation of a mean calculated using all the detectors at 1.15 mm CM_1:

$$CM_1 = A_{1\mathrm{mm}} + \epsilon C\nu_{1\mathrm{mm}}^{\beta} + E_{1\mathrm{mm}}. \tag{8.2}$$

The $\epsilon C\nu_{1\mathrm{mm}}^{\beta}$ term represents any residual of the source signal, which could be present in the common mode template. Since the atmospheric signal is more important at 1.15 mm than at 2.05 mm it is always true that:

$$\gamma = \frac{A_{2\mathrm{mm}}}{A_{1\mathrm{mm}}} < 1. \tag{8.3}$$

We can write:

$$\begin{aligned} m_{2\mathrm{mm}} - \gamma CM_1 &= C\nu_2^{\beta} + A_{2\mathrm{mm}} - \gamma(A_{1\mathrm{mm}} + \epsilon C\nu_1^{\beta} + E_{1\mathrm{mm}}) + E_{2\mathrm{mm}} \\ &= C\nu_2^{\beta} - \gamma\epsilon C\nu_1^{\beta} + A_{2\mathrm{mm}} - \gamma A_{1\mathrm{mm}} - \gamma E_{1\mathrm{mm}} + E_{2\mathrm{mm}} \\ &= C\nu_2^{\beta}\left[1 - \gamma\epsilon\left(\frac{\nu_1}{\nu_2}\right)^{\beta}\right] + A_{2\mathrm{mm}} - \gamma A_{1\mathrm{mm}} + E_{2\mathrm{mm}} - \gamma E_{1\mathrm{mm}}. \end{aligned} \tag{8.4}$$

Since the spectral index for the Crab estimated by [Macías-Pérez *et al.*, 2010] is β = -0.296±0.006 the term $\left(\frac{\nu_1}{\nu_2}\right)^{\beta} < 1$. Moreover the residual atmospheric term $\epsilon << 1$ and $\gamma < 1$. As a consequence the term $\gamma\epsilon\left(\frac{\nu_1}{\nu_2}\right)^{\beta} << 1$ and it can be neglected. In the following, the term $A_{2\mathrm{mm}} - \gamma A_{1\mathrm{mm}}$ represents the residual of the atmosphere and $E_{2\mathrm{mm}} - \gamma E_{1\mathrm{mm}}$ the electronic terms left on the map.

The top left panel of Fig. 8.1 shows the 150 GHz Stokes I map obtained using the method described above. The bottom left panel of the figure shows the map obtained using a common mode decorrelation masking the source where the S/N > 3. The bottom right panel shows the difference map. This latter shows a diffuse signal reaching a level of $\simeq$ 0.7 Jy/beam in the centre. The comparison shows that the "Dual band decorrelation" permits us to better recover the diffuse emission. The right panel of Fig. 8.1 shows the integrated flux at 150 GHz calculated

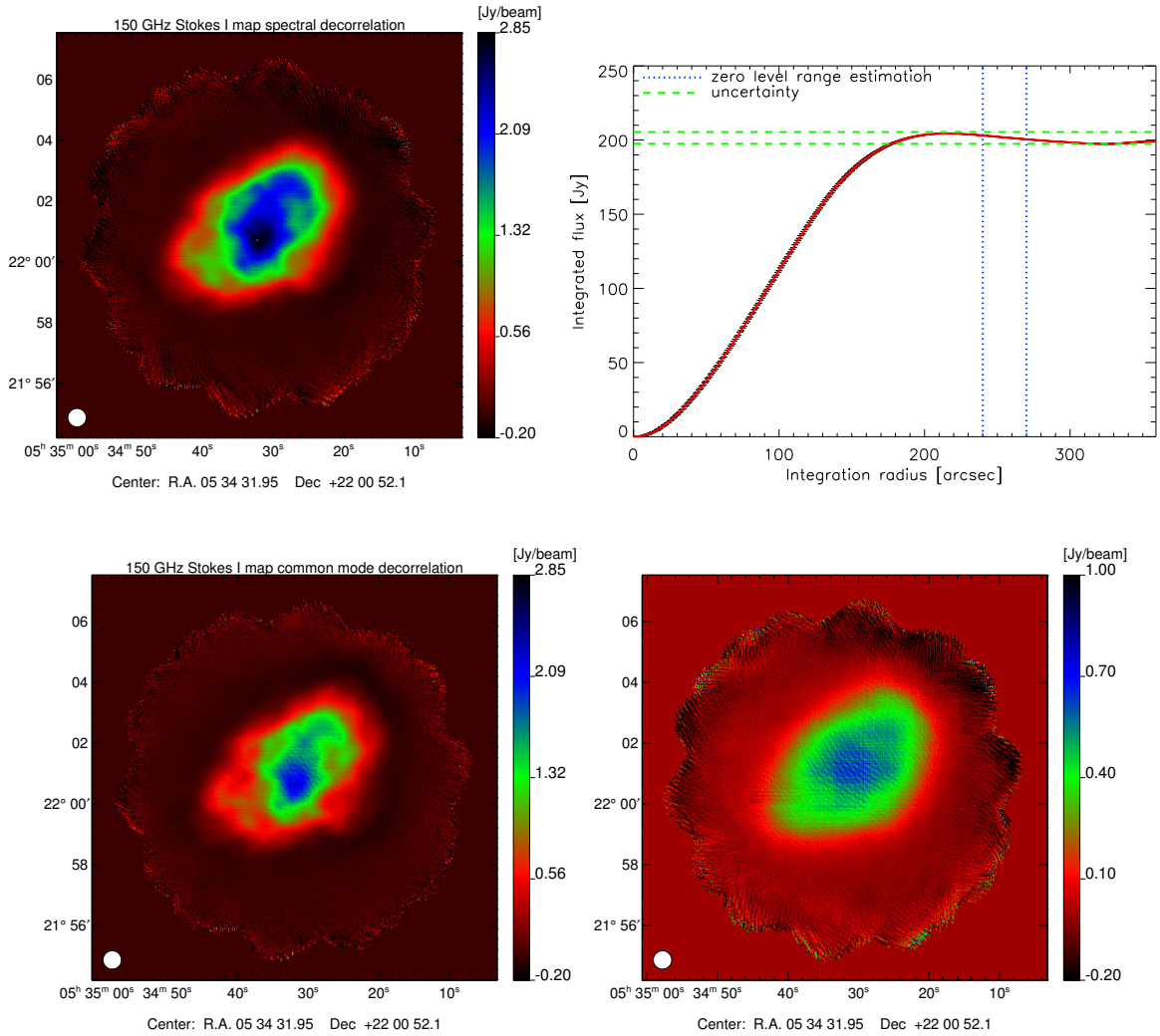

Figure 8.1: **Top**: *Stokes I map of the Crab nebula at 150 GHz (left) obtained using the "Dual band decorrelation" method. On right it is shown the integrated flux calculated up to 4′. The estimation of the flux has been corrected by a zero level, which corresponds to the mean of the signal calculated in an annular ring indicated by the blue dotted lines. The green dotted line represents the uncertainties measured at large radii.* **Bottom**: *Stokes I map at 150 GHz obtained using a common mode decorrelation masking the source (left). On the right panel it is reported the map obtained by the difference of the two previous maps (top and bottom left). This map shows significant diffuse signal that reaches a level of* $\sim$ *0.7 Jy beam*$^{-1}$ *in the centre of the source.*

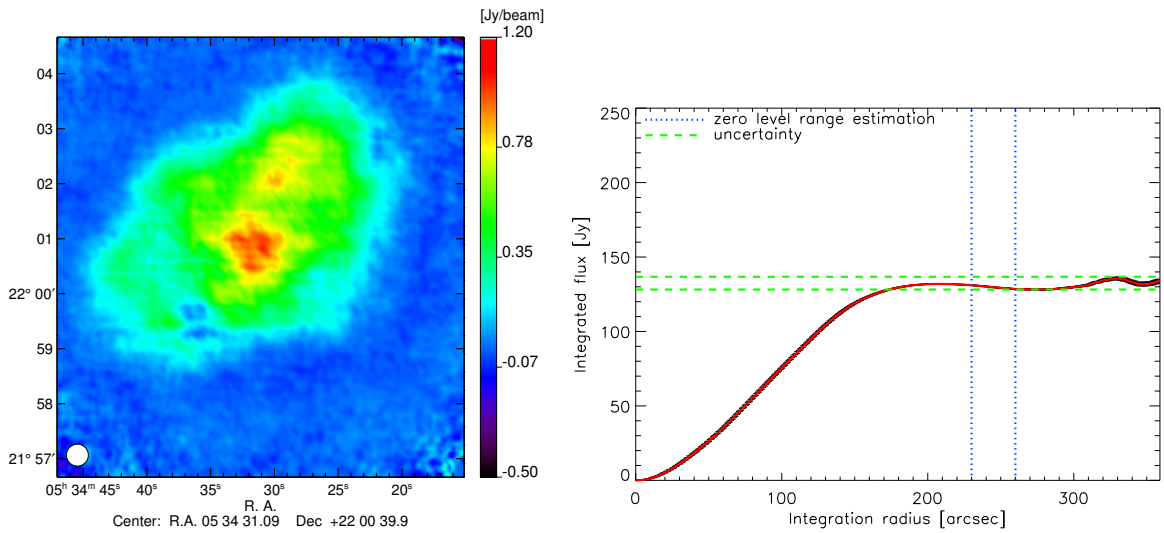

Figure 8.2: **Left** *Crab nebula Stokes I map at 260 GHz obtained using the common mode decorrelation masking the source.* **Right** *Integrated flux at 4′ radius, the estimation of the flux has been corrected by a zero level, corresponding to the mean of the signal calculated in an annular ring indicated by the blue dotted line. The green dotted line represents the uncertainties measured at large radii.*

on the left panel map. A zero level, calculated as the a mean of the signal measured on an external annular ring region (30 arcseconds), is subtracted from the flux. The maximum signal estimated up to 4 arcminutes corresponds to 204.4±7.9±10.2 Jy. The first uncertainty accounts for the fluctuations of the signal at large radii, where the noise is more important. In the figure the uncertainties are represented by green dotted lines. The second term of the uncertainty indicates the calibration error which corresponds to $\simeq$ 5% at 150 GHz.

The 1.15 mm intensity map has to be estimated by using the common mode decorrelation method masking the source, see Sec. 6.1.4. Fig. 8.2 presents the Stokes intensity map obtained at 260 GHz using this decorrelation method. Notice that in this case we expect the diffuse emission to be filtered. This will be discussed in more detail in the following.

On the right panel of Fig. 8.2 it is represented the integrated flux calculated up to 4 arcminutes of radius on the map at 260 GHz (reported on left). The maximum flux reaches a value of 136.7±8.6±13.7 Jy. The uncertainties are estimated in the same way that for the map at 150 GHz, but in this case the calibration error corresponds to $\simeq$ 14%. The results obtained are consistent within error bars with [Planck Collaboration *et al.*, 2015g] at 143 and 217 GHz.

8.2.2 Polarisation maps

In order to have the best estimation of the polarised maps, they have been corrected for the intensity to polarisation leakage as discussed in Sec. 6.4.1. For illustration, the intensity to polarisation leakage maps of Stokes Q and U are reported on Fig. 8.3 at 260 GHz (top) and 150 GHz (bottom). The intensity to polarisation leakage peak-to-peak reaches a value of $\sim$ 1% at 260 GHz and $\sim$ 0.5% at 150 GHz. This confirms the hypothesis of reduced effects in the case of extended sources.

The final Stokes I, Q, U maps obtained for the Crab nebula are reported on Fig. 8.4. The

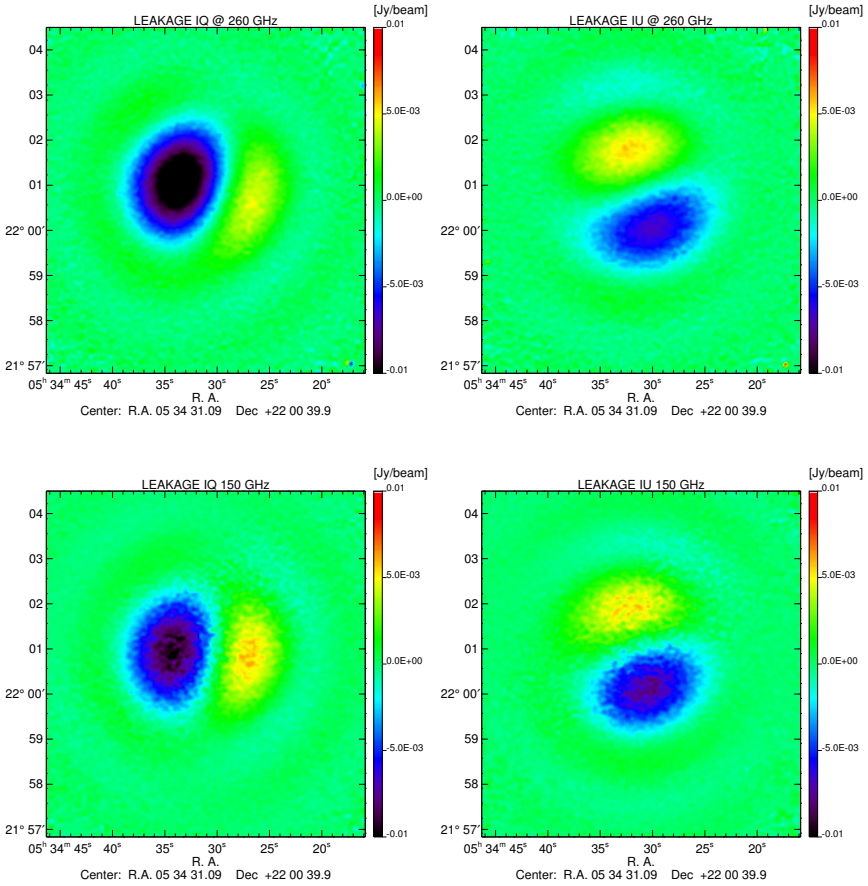

Figure 8.3: *Stokes Q and U intensity to polarisation eakage maps for the Crab nebula observations. At 260 GHz (top) the peak-to-peak estimation reaches a value of $\simeq$ 1% of the intensity flux. At 150 GHz it corresponds to $\simeq$ 0.5%.*

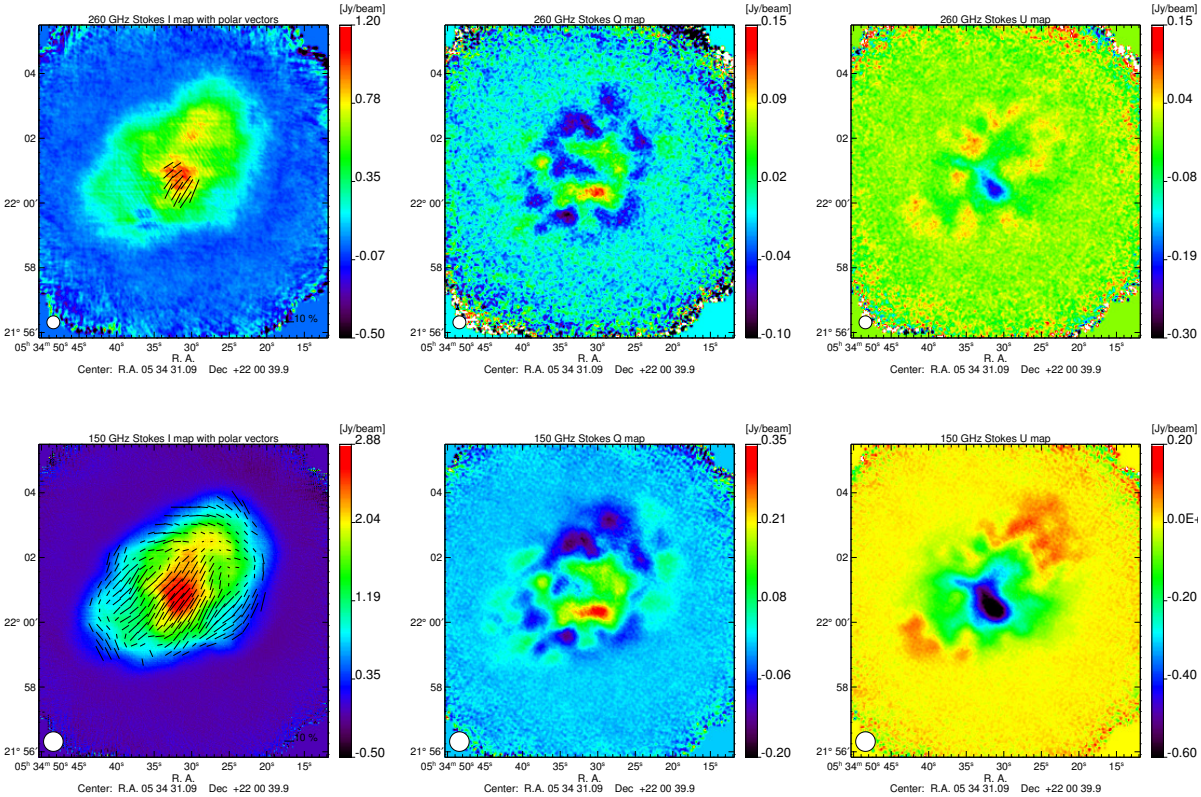

Figure 8.4: *Stokes I, Q, U maps obtained at 260 GHz (top) and 150 GHz (bottom). The polarisation vectors are over plotted in black on the intensity maps where $P > 3\ \sigma_P$.*

intensity maps are obtained as explained in Sec. 8.2.1. The polarisation maps (Q, U) are obtained from the common mode decorrelation method masking the source. As discussed in Sec. 6.3.3 the polarisation signal is well determined independently on the decorrelation method and we expect no significant filtering effects.

Polarisation vectors are over-plotted on Stokes I maps where P $> 3\ \sigma$. Comparing the polarisation maps (Q, U) at 260 and at 150 GHz we observe a consistant morphology of the signal even if the large scales of Q and U maps at 260 GHz have a very low S/N. The polarisation intensity P is displayed on Fig. 8.5 at both frequencies. These maps show a maximum of 0.25 Jy/beam at 260 GHz and 0.8 Jy/beam at 150 GHz. We can see that the Crab nebula is less extended in polarised intensity than in Stokes I.

For the maps, we used the naive estimator of P discussed in Sec. 7.2.1, which is conventionally used by other experiments [Matthews *et al.*, 2009] and [Aumont *et al.*, 2010]. Only the central region corresponding to values starting from to 0.1 Jy at both wavelengths has a significant S/N. The true values of polarisation intensity and degree given hereafter in the text have been estimated as explained in Sec. 7.2.1 and are corrected for noise bias. Comparing the polarised intensity flux measured at 150 GHz and at 260 GHz (Fig. 8.5) we observe a strong polarised emission coming from the most intense region of the source. In addition, the polarised diffuse emission appears to be more prominent at 150 than at 260 GHz. This is probably due to the fact that the 260 GHz maps have significantly less S/N.

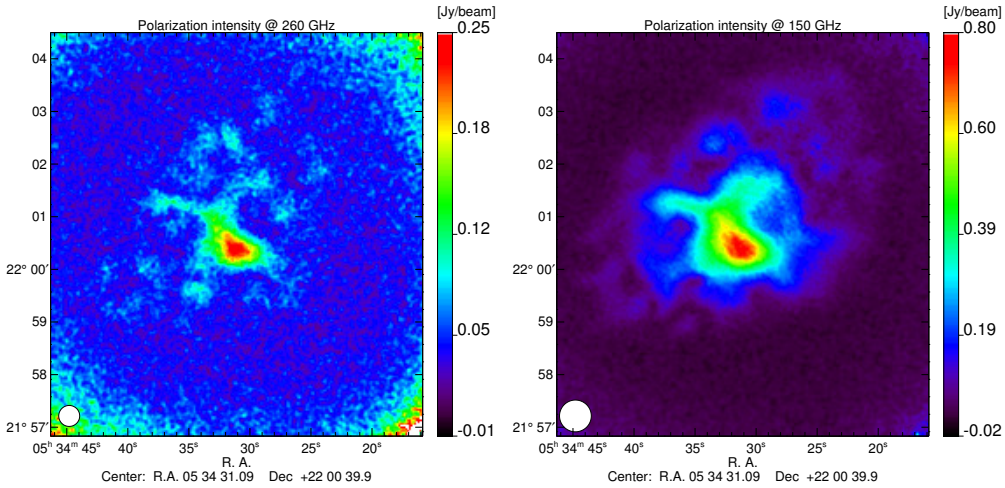

Figure 8.5: *Polarisation intensity maps at 260 GHz (left) and 150 GHz (right), respectively.*

8.2.3 Polarisation degree and angle estimation

In order to estimate the properties of the Crab nebula polarised emission we discuss here its polarisation fraction and orientation angle. This source exhibits a strong synchrotron emission [Macías-Pérez *et al.*, 2010] and it is expected to be more polarised at 150 GHz than at 260 GHz.

Polarisation degree maps are shown on the top panel of Figs. 8.6 and 8.7. As usual for the maps, we use the naive estimator of the polarisation intensity (Eq. 7.13). By contrast, the polarisation degree distributions represented on the right panels of the figures are corrected for noise bias using (Eq. 7.19).
The polarisation degree p distribution at 150 GHz has been calculated where P $> 5\ \sigma_P$. At 260 GHz, the polarised signal is limited by noise, so we constrain the projection of values where P $> 3\ \sigma_P$. The uncertainties represented by cyan dots on Fig. 8.6 and Fig. 8.7 are computed by using the Eq. 7.24, where the error in Q and U is obtained from the dispersion of different observational scans.
At 260 GHz, see top panel of Fig. 8.6, the polarisation is defined only across the peak intensity flux region reaching a value of $\sim$ 30$\pm$10%. Notice that this large degree of polarisation may result from the underestimation of the intensity signal due to the filtering effects. At 150 GHz, see Fig. 8.7, a more significant detection of the polarisation appears clear. The polarisation fraction distribution represented where P $> 5\ \sigma$ results highly dispersed around a polarisation degree value of $\sim$ 20-30$\pm$4%.

Polarisation angle maps estimated using Eq. 7.14 are presented at 260 and 150 GHz on the bottom of Fig. 8.6 and Fig. 8.7, respectively. The right panels present the polarisation angle as function of the Stokes I map. At 260 GHz the angle ψ appears approximatively constant across the most intense region, where the intensity flux is among [0.6 - 1.2] Jy. At 150 GHz, the spatial distribution of ψ presented on Fig. 8.7 shows a value of the angle $\simeq 150°$, which remains approximately constant in the central region of the source. On the map edges, ψ pixel-to-pixel deviation is high, except for the northern region where the average angle is around 220°. This was observed also by the XPOL 90 GHz map [Aumont *et al.*, 2010].

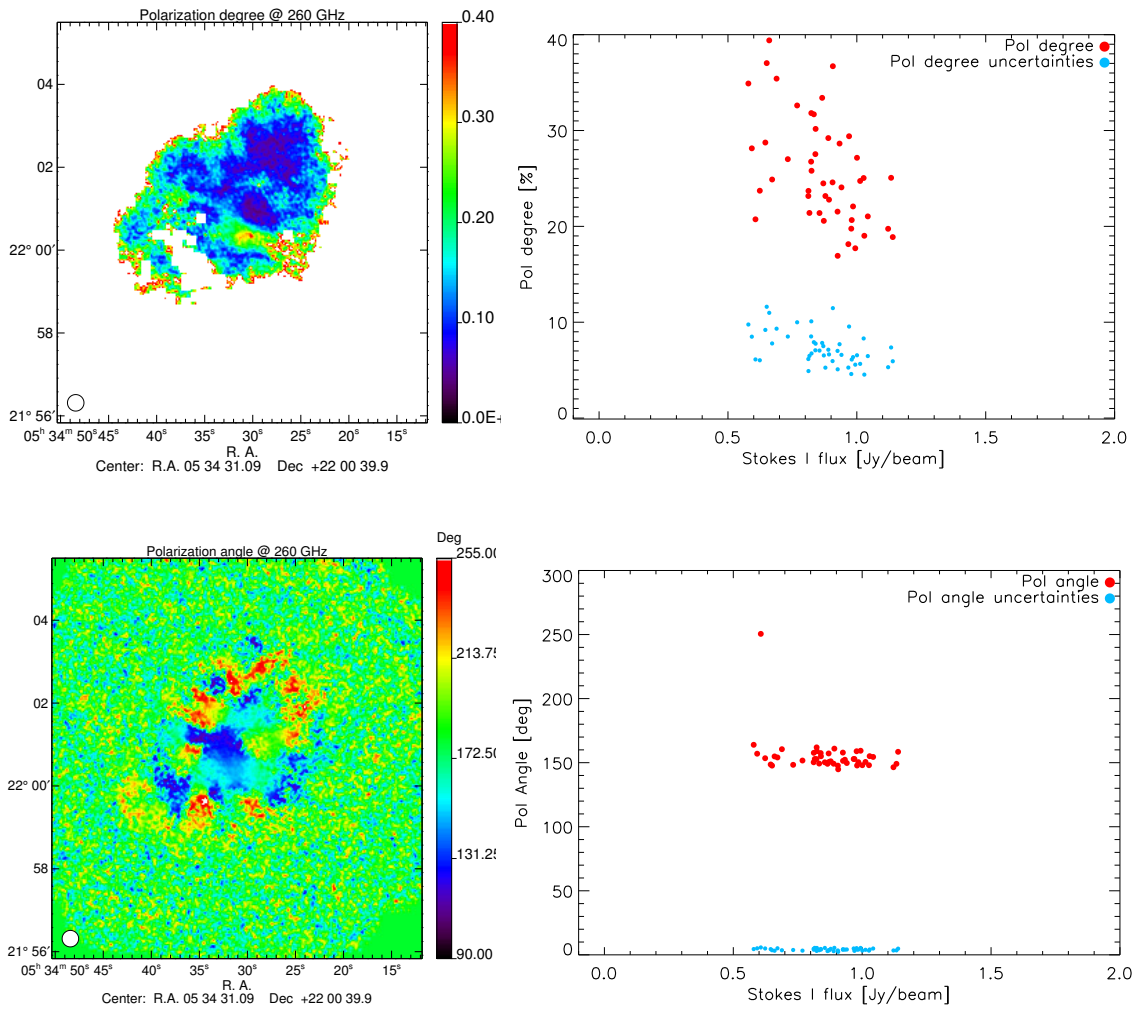

Figure 8.6: **Top** *On left panel we report the naive estimator of the polarisation degree map at 260 GHz, see Sec. 7.2.1 for details on the polarisation reconstruction accuracy. On the right panel we present the polarisation degree as a function of the total intensity. In this case the values have been noise bias corrected, i.e. calculated using Eq. 7.19.* **Bottom** *Polarisation angle map measured at 260 GHz (left) and polarisation angle as a function of total intensity (right) calculated where $P > 3\ \sigma_P$. The cyan dots on the top and bottom right panels represent the uncertainties calculated as the dispersion between different scans.*

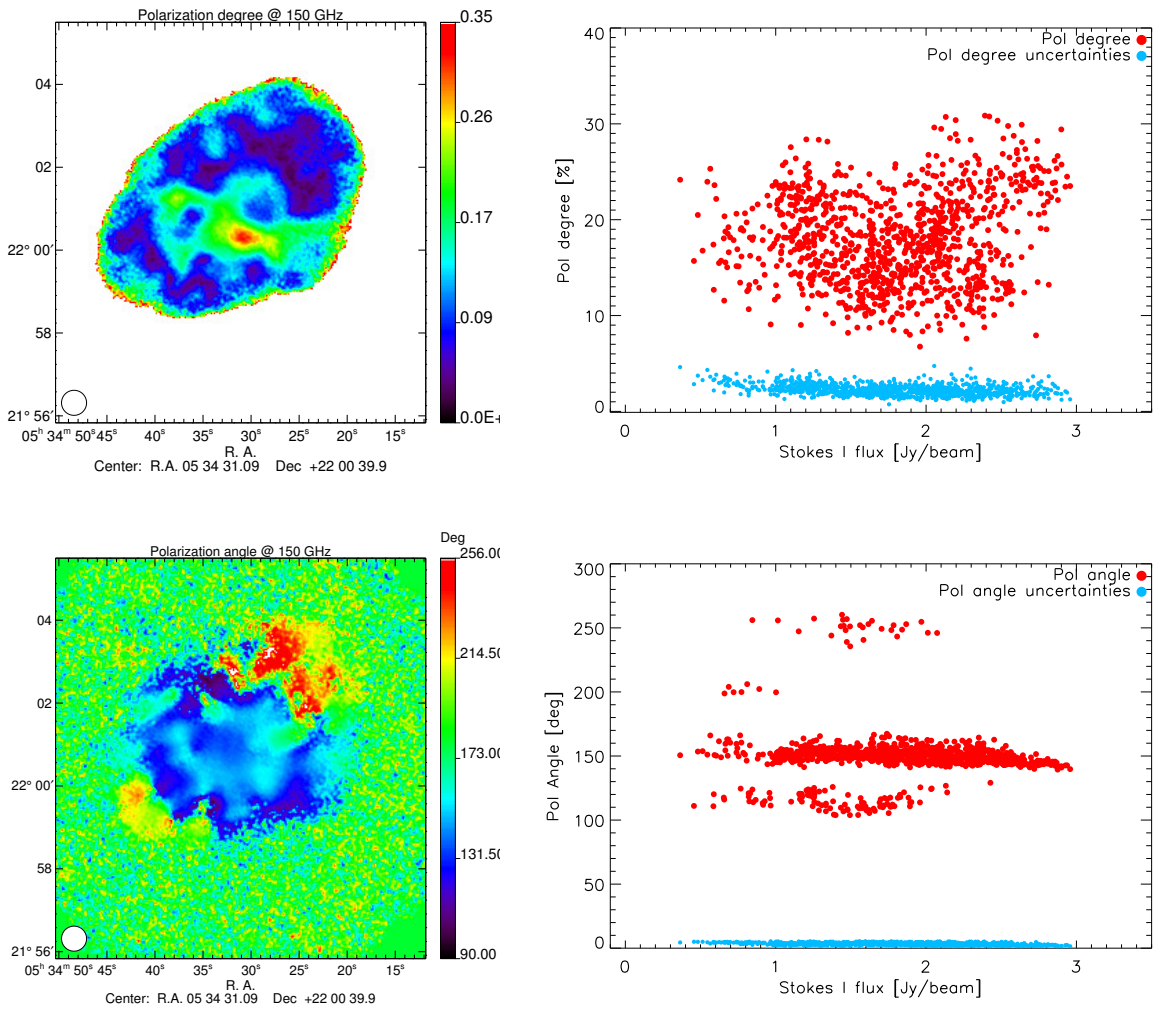

Figure 8.7: **Top** *On left panel we report the naive estimator of the polarisation degree map at 150 GHz, see Sec. 7.2.1 for details on the polarisation reconstruction accuracy. On the right panel we present the polarisation degree as a function of the total intensity. In this case the values have been noise bias corrected, i.e. calculated using Eq. 7.19.* **Bottom** *Polarisation angle map measured at 150 GHz (left) and polarisation angle as a function of total intensity (right) calculated where $P > 3\ \sigma_P$. The cyan dots on the top and bottom right panels represent the uncertainties calculated as the dispersion between different scans.*

8.2.4 A calibrator for CMB experiments

As discussed before the Crab Nebula is usually used to verify polarisation CMB observations in terms of polarisation degree and angle. Thus, to compare with low angular resolution CMB experiments we now calculate the polarisation degree p and angle ψ values in well defined regions. In particular, to compare with the *Planck* and XPOL experiments we calculate the average of p and ψ in high S/N region and in a beam of FWHM 5 and 10 arcminutes. These correspond to the *Planck* 's 100 GHz ($10'$), and 217 and 353 GHz ($5'$) resolutions.

	Frequency [GHz]	I [Jy]	P [Jy]	p [%]	ψ [°]
P $> 3\ \sigma_P$	150	84.61±0.02	10.51 ±0.01	12.42±0.01	144.8±4.3
	260	1.79±0.01	0.51±0.01	28.31 ±0.91	153.6±2.3
P $> 10\ \sigma_P$	150	15.68±0.01	3.52 ±0.01	22.46±1.01	150.1±4.8
	260	no detection			
seen by 10′	150	207.89±0.31	14.41 ±0.25	6.93±0.12	139.9±1.9
	260	157.78±1.36	4.58 ±1.21	2.91±0.79	156.3±7.7
seen by 5′	150	207.16±0.11	14.33 ±0.11	6.97±0.04	141.1±1.9
	260	151.53±0.39	1.36 ±0.35	0.89±0.24	123.1±7.6

Table 8.1: *Total intensity I flux and polarised intensity flux P, polarisation degree, p, and angle, ψ. The values have been calculated in the region with high S/N and within 5 and 10 arcminutes from the center of the source (RA,DEC). Color corrections corresponding to 1.08 at 260 GHz and 1.05 at 150 GHz have been applied assuming a power law spectrum for the Crab nebula with spectral index of* -0.296 *[Macías-Pérez* et al., *2010]. The uncertainties are computed from the dispersion between different scans. In addition a calibration error of* $\sim$ *14 % (260 GHz) and 5 %(150 GHz) have to be considered and propagated. The angle uncertainty takes into account for a systematic uncertainty of 1.8° on the position of the zero of the HWP.*

The flux values calculated in these regions are reported in Tab. 8.1. The uncertainties have been estimated considering the dispersion maps of the scans, both in total intensity and polarisation. Further, calibration errors of $\sim$ 14% at 260 GHz and $\sim$ 5% at 150 GHz have to be considered and propagated to the polarisation degree and angle uncertainties.
Transforming Q and U maps in galactic coordinates to compare with *Planck* satellite, the polarisation angle of the Crab Nebula at 150 GHz for a region of 5′ is -87.15±4.3, compatible within 1σ uncertainties with [Planck Collaboration *et al.*, 2015g]. At 260 GHz the S/N ratio is too low to have a significant detection of the polarisation angle. Indeed, the angle values reported on Tab. 8.1 present a significative variation between the cases considered.

At 150 GHz the polarisation angle values obtained in high S/N regions agree with those reported in Tab. 8.2 for the XPOL 90 GHz data. The polarisation degree values measured by *NIKA* (Tab. 8.1) and XPOL (Tab. 8.2) are generally not consistent. The difference observed can be explained by a not perfect determination of the intensity signal and/or by the fact that *NIKA* values have been noise bias corrected by contrast to the XPOL ones. The subtraction of the noise bias decreases the polarisation intensity and as a consequence the polarisation degree.

8.2.5 Extension to other frequencies

The intensity emission of the Crab nebula from 1 to 10^6 GHz is dominated by the well known synchrotron radiation observed at radio wavelengths [Macías-Pérez *et al.*, 2010]. This synchrotron emission shows a decrease of flux with increasing frequency that can be represented by a power law of spectral index β = -0.296±0.06 [Baars *et al.*, 1977; Macías-Pérez *et al.*, 2010]. Moreover, the flux is fading with time at a rate of α = 0.167±0.015 %yr^{-1} [Aller et Reynolds, 1985]. Further, from the visible to the X-rays the synchrotron emission evolves towards a much harder spectrum represented by a power law of spectral index $\beta = 0.698 \pm 0.018$ [Macías-Pérez *et al.*,

	p [%]	ψ [°]
P $> 3\ \sigma_P$	15.6±0.3	153.7±0.4
P $> 10\ \sigma_P$	23.8±0.6	152.1±0.3
seen by $10'$	7.7±0.2	148.8±0.2
seen by $5'$	8.8±0.2	149.9±0.2

Table 8.2: *Polarisation fraction and angle for the Crab nebula observed at 90 GHz and reported in [Aumont et al., 2010].*

2010]. These observations suggest a low frequency emission produced by particles accelerated by the same magnetic field. The direction of the polarisation is thus expected to be constant while the polarisation degree may vary. At submillimiter wavelength 10-100 μm a cold dust component is also observed.

Fig. 8.8 shows the intensity flux of the Crab nebula as a function of the frequency. The "radio experiments" in the plot refer to values reported in [Dmitrenko *et al.*, 1970; Vinogradova *et al.*, 1971]. We also include *Archeops* [Macías-Pérez *et al.*, 2007] *Planck* [Planck Collaboration *et al.*, 2015g] and WMAP [Weiland *et al.*, 2011] recent results. The *NIKA* data are reported on Fig. 8.8. The decrease of the flux is commonly interpreted by a power law of the form:

$$I_\nu = A\left(\frac{\nu}{1GHz}\right)^\beta \tag{8.5}$$

The best-fit model (yellow) is obtained by χ^2 minimisation on the ν<100 GHz:

$$A = 906.9 \pm 3.3 \quad \beta = -0.307 \pm 0.001 \tag{8.6}$$

Notice that fading has been accounted for. For comparison we report in Fig. 8.8 the power law (red line) obtained by using the fit values estimated by [Macías-Pérez *et al.*, 2010]. The difference observed between the two fits can be explained by considering the relative low value measured by *Planck* at 100 GHz that decreases the amplitude, A. The *NIKA* flux at 150 GHz is consistent within 1 σ uncertainty with the two models, while the flux at 260 GHz is well described by the "new" model (yellow line) suggesting a decrease of the flux with the frequency with respect to the previous model. Notice that the radio data seems to be badly represented by the new model.

8.2.6 Polarisation intensity SED

While total intensity observations of the Crab nebula have been performed for decades at different wavelengths, the amount of polarisation observations is significantly smaller. Recently, *Planck* published polarisation observations on this source [Planck Collaboration *et al.*, 2015g] that allows together with *WMAP* [Weiland *et al.*, 2011], XPOL [Aumont *et al.*, 2010] and *NIKA* data the estimation of its polarisation intensity SED.

Fig. 8.9 shows the polarisation intensity flux as a function of the frequency for the three experiments. We do not use the value estimated at 260 GHz by *NIKA* because we do not have a significant detection. The models considered to fit the data are based on only *WMAP* data in one case (red line) and only on *Planck* data in the other case (yellow line) accounting for fading the fitted amplitude and spectral indeces are:

$$A = 78.9 \pm 7.8 \quad \beta = -0.35 \pm 0.03 \quad WMAP \tag{8.7}$$

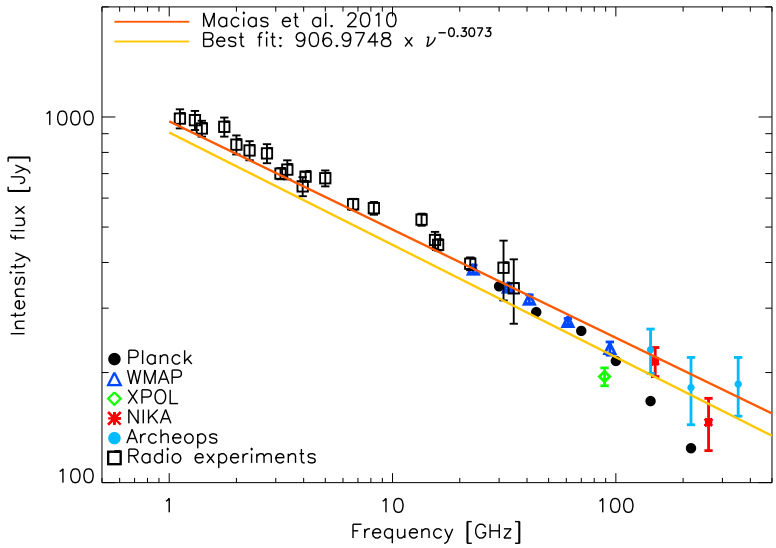

Figure 8.8: *Crab nebula total intensity spectral energy density SED. A fit considering a power law with values reported in [Macías-Pérez et al., 2010] is shown in red and the best-fit using the values at low frequency indicated in the text is shown in yellow. The discrepancy between the two models is explained by relative low intensity of the Planck data with respect of previous measurements.*

And

$$A = 179.1 \pm 15.4 \quad \beta = -0.54 \pm 0.02 \quad PLANCK \tag{8.8}$$

From the figure we note that the fit obtained using only *WMAP* data describe all the measurements except *Planck* high frequency data. The *NIKA* polarisation intensity at 150 GHz is also consistent with this model. By contrast, the *Planck* data have a significantly steeper spectral index. This model is not consistent with the *Planck* observation at 353 GHz reported in the plot.
New mm wavelengths observations are needed to clarify the polarisation intensity spectrum of the Crab nebula. Future *NIKA2* observations at 260 GHz could improve the accuracy of the model considered.

8.2.7 Spectral index

The two mm bands observations performed by *NIKA* gives the opportunity to explore the spatial distribution of the SED of galactic sources. Their emission can be due to three fundamentally important physical processes: thermal emission from dust, *free-free* emission from ionised gas and synchrotron emission from relativistic charged particles moving in the galactic magnetic field. We can estimate the spectral index β as:

$$\beta = \log\left(\frac{I_{\nu_1}}{I_{\nu_2}}\right) / \log\left(\frac{\nu_1}{\nu_2}\right) \tag{8.9}$$

Because of the low S/N in polarisation at 260 GHz we consider only total intensity maps in the following. The left panel of Fig. 8.10 reports the spectral index map obtained using the *NIKA* total intensity maps at 260 and 150 GHz. The value of β observed on the map varies between -0.26 and -0.5 reaching a value of -0.89 in the external regions. The right panel of the figure shows the total intensity map at 260 GHz as function of the total intensity map at 150 GHz. The

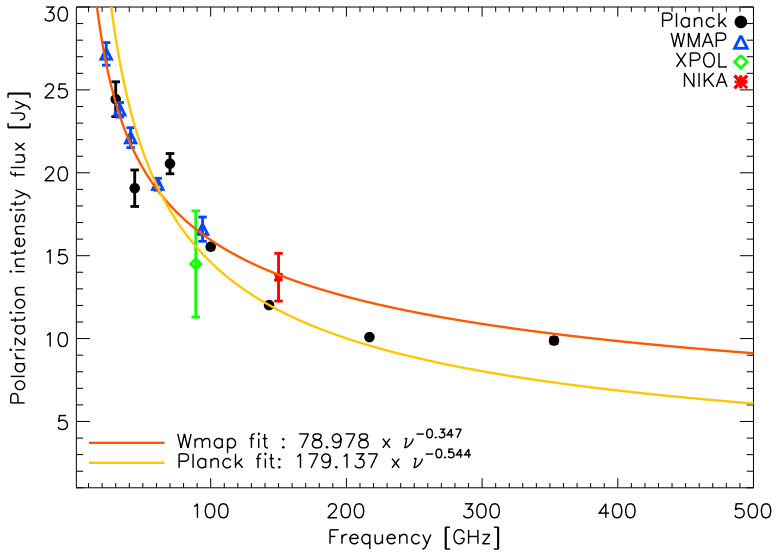

Figure 8.9: *Crab nebula polarisation intensity SED. The two best-fit models presented are calculated using only WMAP data (red line) or Planck data only (yellow line). NIKA polarisation flux measured at 150 GHz agrees with the WMAP model. Planck data suggest a steeper spectral index. However, the flux observed at 353 GHz is not explained by this model.*

correlation found between the two frequencies suggests a same physical origin of the emission. The value of the spectral index obtained by the fit is:

$$\beta = -0.566 \pm 0.003 \tag{8.10}$$

For comparison we calculate the β value using directly the integrated flux values calculated at both *NIKA* frequencies:

$$\beta_1 = -0.72 \pm 0.35 \tag{8.11}$$

In both cases the estimation does not agree with the measured spectral index indicated in Eq. 8.6. This discordance can be explained by considering the difference in the filtering effects of the two intensity maps that have been constructed using two different decorrelation methods. Further work is needed to account for filtering effects when computing spectral index with the *NIKA* maps.

8.3 Conclusions

In this chapter we presented *NIKA* Crab nebula observations performed in February 2015. Although polarisation maps show the same morphology of the signal at both *NIKA* frequencies, the polarisation intensity detected at 260 GHz is limited by low S/N. At 150 GHz the polarisation degree and angle agree the results obtained by XPOL and *Planck* experiments. Combining currently available data we estimated the SED of the total intensity $I_\nu = (906.975 \pm 3.347)\left(\frac{\nu}{1GHz}\right)^{-0.307\pm0.001}$.

In polarisation, we observe significant disagreement between the predicted *WMAP* and *Planck* SEDs. *NIKA* polarisation intensity flux measured at 150 GHz agrees with the *WMAP* model and it is consistent with *Planck* within 1 σ. According to the model based on *WMAP*

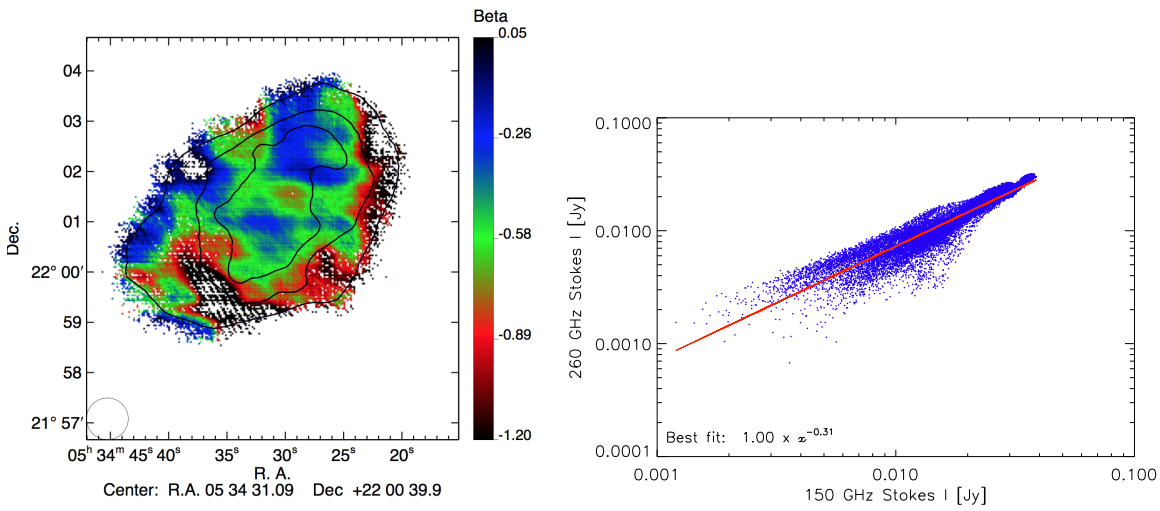

Figure 8.10: *Spectral index map (left) obtained using the two NIKA total intensity maps. The correlation between the two maps is shown on the right panel.*

data the spectral index is β = -0.347±0.026, slightly different with respect to total intensity estimation.

To give a complete interpretation of the polarisation spectrum of the Crab nebula we need further observations at mm wavelengths.

9
Conclusions

This thesis work has been dedicated to the development of a new polarimeter for millimetre wavelengths observations. The aim of the project was to study the optimal configuration for the polarisation system to be adopted in the *NIKA2* instrument. This camera recently installed at the IRAM 30 m telescope is well adapted for a large panel of scientific goals: mapping galaxy clusters via Sunyaev Zel'dovitch effect, probing the deep universe via the observation of dusty galaxies, mapping the interstellar medium in total intensity and polarisation. In particular, *NIKA2* will be able to obtain high sensitivity polarisation observations at 260 GHz of filamentary structures in galactic regions. This will allow the observation of small angular scales in nearest clouds in which magnetic fields may channel the matter of interstellar filaments into growing dense cores.

The validation of a new detection strategy, using a continuous rotation detection of the polarisation coupled to a new generation of millimetre wavelengths detectors, the KIDs, constitutes the core of my thesis. In this context I took advantage of the *NIKA2* prototype, *NIKA*, already installed at the telescope at the beginning of my thesis. The complementarity between instrumental characterisation in laboratory, observations at the telescope and a data analysis development gave me the unique opportunity to participate to each step of the experimental process.

In the first part of my work in the *NIKA* collaboration I have characterised the polarisation instrumental setup in laboratory. I have mainly studied two configurations, one using an Half Wave Plate (HWP) consisting of a single plate of sapphire and the other one using a multi-mesh HWP. The first configuration has been chosen to have a better control of the instrumental systematics at the telescope. Indeed, the first observational campaign in polarisation of *NIKA*, performed at the telescope on January 2014, helped us getting ready to face problems related to telescope polarisation observations.

The laboratory characterisation of the second HWP showed a polarised signal quasi-totally ($\sim 100\%$) transmitted in the large *NIKA* band. The high performance of this system allowed us to recover the polarisation of the sky without any performance loss. This system has perfectly worked at the telescope during the observational campaign of February 2015 allowing us to observe several polarised sources.

In addition of the instrumental characterisation I have developed a dedicated data analysis

pipeline to transform raw modulated data into Stokes I, Q, U maps. This pipeline has been implemented starting from the already existing total intensity pipeline. This polarised pipeline permits the realtime data analysis of polarised observations at the telescope. We have identified a major contribution to the noise due to a modulation of the background signal at harmonics of the rotation frequency of the HWP which required to be subtracted from the time ordered data.

Instrumental polarisation has been characterised using unpolarised source observations. For this purpose we have used the planet Uranus. These observations revealed a bipolar pattern detected on Stokes Q, U maps fixed in Nasmyth coordinates (*i.e.* cabin referential frame) and changing orientation in equatorial coordinates. This effect reaches an instrumental polarisation level of 3% peak-to-peak at both *NIKA* wavelengths. Assuming this due to intensity to polarisation leakage we model the leakage term as a convolution of the original intensity map with beam pattern kernels. These two kernels were directly estimated using an observational beam map performed on Uranus. We corrected for this effect directly on the time ordered data before projecting into maps. This algorithm permits to correct for the intensity to polarisation leakage polarised point and extended sources observations reducing the effect at a level below 1%.

The verification of the *NIKA* polarimeter accuracy in the reconstruction of the polarised signal has been performed via the observation of known quasars. In particular the polarisation observed on the primary calibrator for polarisation millimetre wavelengths observations, the quasar 3C 286, agrees with previous measurements, *e.g.* XPOL observations [Agudo *et al.*, 2012]. In addition to quasar measurements we have observed two radio galaxies M87 measured with 2% of polarisation at 150 GHz and Cygnus-A that shows a striking feature of the polarisation from the two hotspots of emission at both *NIKA* frequencies. Orion Molecular Cloud (OMC-1) represents a good verification source to probe the potentiality of the instrument in the reconstruction of the dust polarised emission. Observations performed with *NIKA* are in good agreement with other experiments, like POLKA and SCUBAPOL. The orientation of the polarisation vectors is well aligned with the intensity structures across the source suggesting an ordered magnetic field. Furthermore, Crab nebula observations confirm a good calibration within the error bars of the *NIKA* instrument polarisation angle. Finally, using *Planck*, *WMAP* and XPOL observations I have modelled the polarisation intensity spectrum according to a synchrotron power law. *NIKA* polarisation intensity flux at 150 GHz is well described by a model based on *WMAP* data, while *Planck* data show a steeper spectrum. Further work is needed to understand these discrepancies.

The results obtained with the *NIKA* instrument have validated the chosen detection strategy and produced the first polarisation observations with KIDs. These detectors represent now one of the candidates for the next generation of CMB experiments thanks to their easy manufacture and natural multiplexing capability. In addition, the efficiency of the *NIKA* polarimeter in the reconstruction of the polarisation supports the choice of this detection strategy in experiment like B-SIDE [Monfardini *et al.*, 2016], a balloon-borne experiment, which aims at constraining foreground emissions at galactic scales and the CORE satellite [The COrE Collaboration *et al.*, 2011] that aims at detecting B-mode signal of primordial gravitational waves.

The work that I have done during these three years has contributed to the development of the *NIKA2* instrument. During the last year, I had the opportunity to take part in the commissioning phase of this instrument at the telescope, during which I coordinated the first observations in polarisation. These observations are not reported in this work because time constraints prevented me to properly analyse the data, understand systematic effects and conclude about its polarisation performance. However, next year these observations will be completed by a dedicated commissioning of *NIKA2* in polarisation.

Conclusion

NIKA2, installé au télescope de 30 m de l'IRAM en Octobre 2015, et actuellement en phase de caractérisation, est optimisé pour plusieurs buts scientifiques : cartographier les amas de galaxie avec l'effet Sunyaev Zel'dovitch, sonder l'Univers profond à travers l'observation de galaxies lointaines, cartographier le milieu interstellaire en intensité et en polarisation. En particulier, *NIKA2* sera capable d'observer à haute résolution les structures filamentaires des régions galactiques à 260 GHz. Ceci permettra l'observation à petite échelle angulaire des nuages moléculaires les plus proches dans lesquels les lignes de champ magnétique peuvent réguler l'expansion des cœurs denses au sein des filaments de matière. La première originalité de cet instrument est l'utilisation de matrices de *Kinetic Inductance Detectors* (KIDs). La seconde tient à sa façon de moduler la polarisation incidente par une lame demi-onde en rotation continue et rapide devant l'entrée du cryostat.

Cette thèse a été dédiée à la caractérisation de ce système polarimétrique et au développement d'une chaîne d'analyse des données, en s'appuyant sur le protoype *NIKA*. La complémentarité entre la caractérisation de l'instrument au laboratoire, les observations au télescope et le développement du pipeline de traitement des données m'a permis de prendre part à chaque étape du processus expérimental.

J'ai tout d'abord caractérisé le polarimètre en laboratoire, en étudiant en particulier deux configurations, l'une utilisant une lame demi-onde composée d'une seule couche de saphir, l'autre composée de plusieurs grilles métalliques. La première configuration a été choisie pour sa simplicité qui permettait une meilleure interprétation de systématiques nouvelles qui auraient pu nous surprendre. La première campagne d'observation en polarisation de *NIKA*, effectuée au télescope en Janvier 2014, a montré que le systéme se comportait en fait comme on l'attendait et que l'on pouvait donc passer à un choix plus complexe mais plus performant d'une lame demi-onde à mèches. La caractérisation au laboratoire de cette deuxième lame demi-onde a permis de montrer son bon fonctionnement, avec en particulier une dépolarisation négligeable du signal incident.

Ce système a parfaitement marché au télescope pendant la campagne d'observation de Février 2015, nous permettant d'observer plusieurs sources polarisées et de trouver des résultats en accord avec des observations existantes de ces objets. Pour parvenir à ces résultats, j'ai développé le pipeline d'analyse des données pour produire les cartes des paramètres de Stokes I, Q et U. Ce travail s'est appuyé sur les développements du pipeline dans le cadre des observations non polarisées de *NIKA*. Outre la différence du signal à reconstruire, il fallu également traiter des bruits et effets instrumentaux nouveaux, comme un signal parasite synchrone avec la rotation de la lame demi-onde et une composante de polarisation instrumentale. Celle-ci a été caractérisée en utilisant des observations d'une source non polarisées : Uranus, brillante et ponctuelle pour la résolution angulaire de *NIKA*. Ces observations ont montré un pattern bipolaire sur les cartes en polarisation Q et U, fixe en coordonnées Nasmyth (c'est à dire le référentiel de la cabine). Cet effet contribue à hauteur de 3% environ pour les deux bandes. En le modélisant comme une conversion d'une fraction de l'intensité totale en polarisation, j'ai pu

le décrire comme un noyau de convolution, mettre en place une correction des cartes observées et réduire son effet à moins d'1%. L'étalonnage de l'orientation absolue de la polarisation reconstruite avec *NIKA* ainsi que sa précision s'est faite en observant des quasars connus. En particulier, nos observations de 3C286, considéré comme un calibrateur primaire en polarisation aux longueurs d'onde millimétriques, sont en très bon accord avec les mesures existantes comme celles d'XPOL par exemple [Agudo *et al.*, 2012]. Il en va de même pour une source plus diffuse comme le nuage moléculaire d'Orion (OMC-1) pour lequel nous avons pu valider le résultat de nos observations en les comparant à celles de POLKA et SCUBAPOL. L'orientation des vecteurs de polarisation est bien alignée avec les structures d'intensité de la source suggérant un champ magnétique ordonné. Les observations de la nébuleuse du Crabe confirment également la bonne compréhension de l'orientation du polarimètre. Enfin, en utilisant *Planck*, *WMAP* et XPOL j'ai reconstruit le spectre d'intensité de polarisation du Crabe et montré qu'il suivait un spectre de puissance typique du rayonnement synchrotron. Le flux en intensité polarisée mesuré à 150 GHz par *NIKA* est bien décrit par un modèle basé sur des données *WMAP*, tandis que les données *Planck* montrent un spectre plus raide. La résolution de cette incompatibilité nécessite davantage d'étude et sera l'un des sujets abordés lors des premières observations de *NIKA2* en mode polarisé prévues en 2017.

En conclusion, les résultats que j'ai obtenus avec l'instrument *NIKA* ont validé la stratégie de mesure de la polarisation avec une lame tournante continument, ainsi que les algorithmes de traitement des données et des effets instrumentaux. *NIKA* était déjà la première caméra à observer le ciel avec des KIDs, elle est à présent la première à observer le ciel avec ces détecteurs *et* en polarisation. Ceci démontre le potentiel de ces détecteurs pour les futurs instruments, en particulier un futur satellite dédié à la mesure de la polarisation du CMB. D'autre projets connexes reposant sur cette technologie sont également envisagés, comme B-SIDE [Monfardini *et al.*, 2016], une expérience ballon, qui vise à contraindre les émissions d'avant plan polarisées à une précision suffisante pour les soustraire au niveau requis pour détecter significativement les ondes gravitationnelles primordiales dans les modéles d'inflations dits "naturels".

Bibliography

[Abbas *et al.*, 2004] Abbas, M. M., P. D. Craven, J. F. Spann *et al.* (2004). Laboratory Experiments on Rotation and Alignment of the Analogs of Interstellar Dust Grains by Radiation. *ApJ*, 614:781–795.

[Abdo *et al.*, 2010] Abdo, A. A., M. Ackermann, M. Ajello *et al.* (2010). Fermi-Large Area Telescope Observations of the Exceptional Gamma-ray Outbursts of 3C 273 in 2009 September. *ApJ*, 714:L73–L78. arXiv, 1012.2980.

[Adam, 2015] Adam, R. (2015). *Observation des amas de galaxies par effet Sunyaev Zel'dovitch et la polarisation du fond diffus cosmologique.* Thèse de doctorat, Université de Grenoble.

[Adam *et al.*, 2014a] Adam, R., A. Adane, P. Ade *et al.* (2014a). High resolution SZ observations at the IRAM 30-m telescope with NIKA. *ArXiv e-prints.* arXiv, 1409.1137.

[Adam *et al.*, 2015] Adam, R., B. Comis, J.-F. Macías-Pérez *et al.* (2015). Pressure distribution of the high-redshift cluster of galaxies CL J1226.9+3332 with NIKA. *A&A*, 576:A12. arXiv, 1410.2808.

[Adam *et al.*, 2014b] Adam, R., B. Comis, J. F. Macías-Pérez *et al.* (2014b). First observation of the thermal Sunyaev-Zel'dovich effect with kinetic inductance detectors. *A&A*, 569:A66. arXiv, 1310.6237.

[Ade *et al.*, 2006] Ade, P. A., Giampaolo Pisano, Carole Tucker, et Samuel Weaver (2006). A review of metal mesh filters. *In SPIE Astronomical Telescopes+ Instrumentation*, pages 62750U–62750U. International Society for Optics and Photonics.

[Ade *et al.*, 2014] Ade, P. A. R., R. W. Aikin, D. Barkats *et al.* (2014). Detection of B-Mode Polarization at Degree Angular Scales by BICEP2. *Physical Review Letters*, 112(24):241101. arXiv, 1403.3985.

[Agudo *et al.*, 2012] Agudo, I., C. Thum, H. Wiesemeyer *et al.* (2012). 3C 286: a bright, compact, stable, and highly polarized calibrator for millimeter-wavelength observations. *A&A*, 541: A111. arXiv, 1201.2150.

[Aller et Reynolds, 1985] Aller, H., et SP Reynolds (1985). The decrease with time of the radio flux of the crab nebula. *The Astrophysical Journal*, 293:L73–L75.

[Andersson *et al.*, 2015] Andersson, B., A Lazarian, et John E Vaillancourt (2015). Interstellar dust grain alignment. *Annual Review of Astronomy and Astrophysics*, 53:501–539.

[André *et al.*, 2014] André, P., J. Di Francesco, D. Ward-Thompson *et al.* (2014). From Filamentary Networks to Dense Cores in Molecular Clouds: Toward a New Paradigm for Star Formation. *Protostars and Planets VI*, pages 27–51. arXiv, 1312.6232.

[André *et al.*, 2010] André, P., A. Men'shchikov, S. Bontemps *et al.* (2010). From filamentary clouds to prestellar cores to the stellar IMF: Initial highlights from the Herschel Gould Belt Survey. *A&A*, 518:L102. arXiv, 1005.2618.

[Arzoumanian *et al.*, 2011] Arzoumanian, D., P. André, P. Didelon *et al.* (2011). Characterizing interstellar filaments with Herschel in IC 5146. *A&A*, 529:L6. arXiv, 1103.0201.

[Aumont *et al.*, 2010] Aumont, J., L. Conversi, C. Thum *et al.* (2010). Measurement of the Crab nebula polarization at 90 GHz as a calibrator for CMB experiments. *A&A*, 514:A70.

[Austermann *et al.*, 2012] Austermann, J. E., K. A. Aird, J. A. Beall *et al.* (2012). SPTpol: an instrument for CMB polarization measurements with the South Pole Telescope. *In Millimeter, Submillimeter, and Far-Infrared Detectors and Instrumentation for Astronomy VI*, volume 8452 de *Proc. SPIE*, page 84521E. arXiv, 1210.4970.

[Baars *et al.*, 1977] Baars, J., R Genzel, IIK Pauliny-Toth, et A Witzel (1977). The absolute spectrum of cas a-an accurate flux density scale and a set of secondary calibrators. *Astronomy and Astrophysics*, 61:99–106.

[Baldry *et al.*, 2002] Baldry, I. K., K. Glazebrook, C. M. Baugh *et al.* (2002). The 2dF Galaxy Redshift Survey: Constraints on Cosmic Star Formation History from the Cosmic Spectrum. *ApJ*, 569:582–594. astro-ph/0110676.

[Bardeen *et al.*, 1957] Bardeen, J., L. N. Cooper, et J. R. Schrieffer (1957). Theory of superconductivity. *Physical Review*, 108:1175.

[Bastian *et al.*, 2010] Bastian, N., K. R. Covey, et M. R. Meyer (2010). A Universal Stellar Initial Mass Function? A Critical Look at Variations. *ARA&A*, 48:339–389. arXiv, 1001.2965.

[Basu et Roy, 2013] Basu, A., et S. Roy (2013). Magnetic fields in nearby normal galaxies: energy equipartition. *MNRAS*, 433:1675–1686. arXiv, 1305.2746.

[Beck, 2007] Beck, R. (2007). Magnetism in the spiral galaxy ngc 6946: magnetic arms, depolarization rings, dynamo modes, and helical fields. *Astronomy & Astrophysics*, 470(2):539–556.

[Beck, 2012] Beck, R. (2012). Magnetic fields in galaxies. *Space Science Reviews*, 166(1-4):215–230.

[Beckert *et al.*, 2000] Beckert, T., W. J. Duschl, et P. G. Mezger (2000). Free-free and recombination radiation from massive star-forming regions. *A&A*, 356:1149–1156.

[Benoît *et al.*, 2004] Benoît, A., P. Ade, A. Amblard *et al.* (2004). First detection of polarization of the submillimetre diffuse galactic dust emission by Archeops. *A&A*, 424:571–582. astro-ph/0306222.

[BICEP2 and Keck Array Collaborations *et al.*, 2015] BICEP2 and Keck Array Collaborations, P. A. R. Ade, R. W. Aikin *et al.* (2015). BICEP2/Keck Array. IV. Optical Characterization and Performance of the BICEP2 and Keck Array Experiments. *ApJ*, 806:206. arXiv, 1502.00596.

[BICEP2 Collaboration *et al.*, 2014] BICEP2 Collaboration, P. A. R. Ade, R. W. Aikin *et al.* (2014). Detection of B-Mode Polarization at Degree Angular Scales by BICEP2. *Physical Review Letters*, 112(24):241101. arXiv, 1403.3985.

[BICEP2 Collaboration *et al.*, 2016] BICEP2 Collaboration, Keck Array Collaboration, P. A. R. Ade *et al.* (2016). Improved Constraints on Cosmology and Foregrounds from BICEP2 and Keck Array Cosmic Microwave Background Data with Inclusion of 95 GHz Band. *Physical Review Letters*, 116(3):031302. arXiv, 1510.09217.

[BICEP2/Keck and Planck Collaborations *et al.*, 2015] BICEP2/Keck and Planck Collaborations, P. A. R. Ade, N. Aghanim *et al.* (2015). A Joint Analysis of BICEP2/Keck Array and Planck Data. *ArXiv e-prints*. arXiv, 1502.00612.

[Bierman *et al.*, 2011] Bierman, E., T Matsumura, CD Dowell *et al.* (2011). A millimeter-wave galactic plane survey with the bicep polarimeter. *The Astrophysical Journal*, 741(2):81.

[Boggess *et al.*, 1992] Boggess, N. W., J. C. Mather, R. Weiss *et al.* (1992). The COBE mission - Its design and performance two years after launch. *ApJ*, 397:420–429.

[Bourrion *et al.*, 2011] Bourrion, O., A. Bideaud, A. Benoit *et al.* (2011). Electronics and data acquisition demonstrator for a kinetic inductance camera. *Journal of Instrumentation*, 6:6012. arXiv, 1102.1314.

[Bourrion *et al.*, 2012] Bourrion, O., C. Vescovi, J. L. Bouly *et al.* (2012). NIKEL: Electronics and data acquisition for kilopixels kinetic inductance camera. *Journal of Instrumentation*, 7:7014. arXiv, 1204.1415.

[Calvo, 2008] Calvo, M. (2008). *Development of Kinetic Inductance Detectors for the study of the Cosmic Microwave Background Polarization*. Thèse de doctorat, Scuola di dottorato Vito Volterra - Università di Roma La Sapienza.

[Calvo *et al.*, 2012] Calvo, M., M. Roesch, F. X. Désert *et al.* (2012). Improved mm-wave photometry for Kinetic Inductance Detectors. *A&A*.

[Cantalupo *et al.*, 2010] Cantalupo, C. M., J. D. Borrill, A. H. Jaffe, T. S. Kisner, et R. Stompor (2010). MADmap: A Massively Parallel Maximum Likelihood Cosmic Microwave Background Map-maker. *ApJS*, 187:212–227. arXiv, 0906.1775.

[Carroll et Ostlie, 2007] Carroll, B., et D.A. Ostlie (2007). *An Introduction to Modern Astrophysics*. Pearson Addison-Wesley.

[Catalano *et al.*, 2014] Catalano, A., M. Calvo, N. Ponthieu *et al.* (2014). Performance and calibration of the NIKA camera at the IRAM 30 m telescope. *A&A*, 569:A9. arXiv, 1402.0260.

[Chapman *et al.*, 2014] Chapman, D., A. M. Aboobaker, P. Ade *et al.* (2014). EBEX: A Balloon-Borne CMB Polarization Experiment. *In American Astronomical Society Meeting Abstracts*, volume 223 de *American Astronomical Society Meeting Abstracts*, page 407.03.

[Cho et Lazarian, 2005] Cho, J., et A. Lazarian (2005). Grain Alignment by Radiation in Dark Clouds and Cores. *ApJ*, 631:361–370. astro-ph/0505571.

[C.Hunt, 2003] C.Hunt (2003). *Transition-Edge Superconducting Antenna-Coupled Bolometers*. Thèse de doctorat, California Institute of Technology, Pasadena, CA.

[Ciolek et Mouschovias, 1996] Ciolek, G. E., et T. C. Mouschovias (1996). Effect of Ambipolar Diffusion on Dust-to-Gas Ratio in Protostellar Cores. *ApJ*, 468:749.

[Clark *et al.*, 2014] Clark, S. E., J. E. G. Peek, et M. E. Putman (2014). Magnetically Aligned H I Fibers and the Rolling Hough Transform. *ApJ*, 789:82. arXiv, 1312.1338.

[Comastri et Brusa, 2007] Comastri, A., et Marcella Brusa (2007). Extragalactic surveys: Agn physics and evolution. *arXiv preprint arXiv:0710.0561.*

[Compiègne *et al.*, 2011] Compiègne, M., L. Verstraete, A. Jones *et al.* (2011). The global dust SED: tracing the nature and evolution of dust with DustEM. *A&A*, 525:A103. arXiv, 1010.2769.

[Crutcher, 2012] Crutcher, R. M. (2012). Magnetic Fields in Molecular Clouds. *ARA&A*, 50:29–63.

[Crutcher *et al.*, 2010] Crutcher, R. M., B. Wandelt, C. Heiles, E. Falgarone, et T. H. Troland (2010). Magnetic Fields in Interstellar Clouds from Zeeman Observations: Inference of Total Field Strengths by Bayesian Analysis. *ApJ*, 725:466–479.

[D'Addabbo, 2014] D'Addabbo, A. (2014). *Applications of Kinetic Inductance Detectors to Astronomy and Particle Physics.* Thèse de doctorat, Université Joseph Fourier - Sapienza Università.

[D'Addabbo *et al.*, 2013] D'Addabbo, A., R. Adam, A. Adane *et al.* (2013). The NIKA instrument: results and perspectives towards a permanent KID based camera for the Pico Veleta observatory. *ArXiv e-prints.* arXiv, 1312.4801.

[Davis et Greenstein, 1951] Davis, Jr., L., et J. L. Greenstein (1951). The Polarization of Starlight by Aligned Dust Grains. *ApJ*, 114:206.

[Day *et al.*, 2003] Day, P. K., H. G. LeDuc, B. A. Mazin, A. Vayonakis, et J. Zmuidzinas (2003). A broadband superconducting detector suitable for use in large arrays. *Nature*, 425:817–821.

[de Vaucouleurs *et al.*, 1976] de Vaucouleurs, G., A. de Vaucouleurs, et J. R. Corwin (1976). Second reference catalogue of bright galaxies. *In Second reference catalogue of bright galaxies, 1976, Austin: University of Texas Press.*, page 0.

[Dehnen et Binney, 1998] Dehnen, W., et J. Binney (1998). Mass models of the Milky Way. *MNRAS*, 294:429. astro-ph/9612059.

[Desert *et al.*, 1990] Desert, F.-X., F. Boulanger, et J. L. Puget (1990). Interstellar dust models for extinction and emission. *A&A*, 237:215–236.

[Dicke *et al.*, 1946] Dicke, R. H., R. Beringer, R. L. Kuhl, et A. B. Vane (1946). Atmospheric absorption measurements with a microwave radiometer. *Phys. Rev.*, 70:340–348.

[Dickinson *et al.*, 2003] Dickinson, C., R. D. Davies, et R. J. Davis (2003). Towards a free-free template for CMB foregrounds. *MNRAS*, 341:369–384. astro-ph/0302024.

[Dickinson *et al.*, 2011] Dickinson, C., M. Peel, et M. Vidal (2011). New constraints on the polarization of anomalous microwave emission in nearby molecular clouds. *MNRAS*, 418:L35–L39. arXiv, 1108.0308.

[Dmitrenko *et al.*, 1970] Dmitrenko, D., NM Tseitlin, LV Vinogradova, et Kh F Giterman (1970). Absolute measurements of the intensity of radio emission from cassiopeia-a, cygnus-a, and taurus-a in the 3–15 cm range of wavelengths. *Radiophysics and Quantum Electronics*, 13(6):649–654.

[Dolginov et Mitrofanov, 1976] Dolginov, A. Z., et I. G. Mitrofanov (1976). Orientation of cosmic dust grains. *Ap&SS*, 43:291–317.

[Doyle *et al.*, 2008] Doyle, S., P. Mauskopf, J. Naylon, A. Porch, et C. Duncombe (2008). Lumped Element Kinetic Inductance Detectors. *Journal of Low Temperature Physics*, 151:530–536.

[Draine et Lazarian, 1998] Draine, B. T., et A. Lazarian (1998). Diffuse Galactic Emission from Spinning Dust Grains. *ApJ*, 494:L19–L22. astro-ph/9710152.

[Draine et Weingartner, 1996] Draine, B. T., et J. C. Weingartner (1996). Radiative Torques on Interstellar Grains. I. Superthermal Spin-up. *ApJ*, 470:551. astro-ph/9605046.

[Draine et Weingartner, 1997] Draine, B. T., et J. C. Weingartner (1997). Radiative Torques on Interstellar Grains. II. Grain Alignment. *ApJ*, 480:633–646. astro-ph/9611149.

[Eadie *et al.*, 1971] Eadie, W. T., D. Drijard, et F. E. James (1971). *Statistical methods in experimental physics.*

[Einstein, 1916] Einstein, A. (1916). Die Grundlage der allgemeinen Relativitätstheorie. *Annalen der Physik*, 354:769–822.

[Elmegreen, 2000] Elmegreen, B. G. (2000). Star Formation in a Crossing Time. *ApJ*, 530:277–281. astro-ph/9911172.

[Errard, 2012] Errard, J. (2012). *A hunt for Cosmic Microwave Background B-modes in the systematic contaminants jungle.* Theses, Université Paris-Diderot - Paris VII.

[Ferriere, 2001] Ferriere, K. M. (2001). The interstellar environment of our galaxy. *Reviews of Modern Physics*, 73(4):1031.

[Fixsen, 2009] Fixsen, D. J. (2009). The Temperature of the Cosmic Microwave Background. *ApJ*, 707:916–920. arXiv, 0911.1955.

[Fomalont *et al.*, 2014] Fomalont, E., T. van Kempen, R. Kneissl *et al.* (2014). The Calibration of ALMA using Radio Sources. *The Messenger*, 155:19–22.

[Friedmann, 1922] Friedmann, A. (1922). Über die Krümmung des Raumes. *Zeitschrift fur Physik*, 10:377–386.

[Friedmann, 1924] Friedmann, A. (1924). Über die Möglichkeit einer Welt mit konstanter negativer Krümmung des Raumes. *Zeitschrift fur Physik*, 21:326–332.

[Gaensler *et al.*, 2005] Gaensler, B., M Haverkorn, L Staveley-Smith *et al.* (2005). The magnetic field of the large magellanic cloud revealed through faraday rotation. *Science*, 307(5715):1610–1612.

[Gamow, 1946] Gamow, G. (1946). Expanding Universe and the Origin of Elements. *Physical Review*, 70:572–573.

[Ginzburg et Syrovatskii, 1965] Ginzburg, V. L., et S. I. Syrovatskii (1965). Cosmic Magnetobremsstrahlung (synchrotron Radiation). *ARA&A*, 3:297.

[Gold *et al.*, 2009] Gold, B., C. L. Bennett, R. S. Hill *et al.* (2009). Five-Year Wilkinson Microwave Anisotropy Probe Observations: Galactic Foreground Emission. *ApJS*, 180:265–282. arXiv, 0803.0715.

[Goldberg *et al.*, 1967] Goldberg, J., AJ Macfarlane, Ezra T Newman, F Rohrlich, et ECG Sudarshan (1967). Spin-s spherical harmonics and ð. *Journal of Mathematical Physics*, 8(11):2155–2161.

[Gong et Ostriker, 2011] Gong, H., et E. C. Ostriker (2011). Dense Core Formation in Supersonic Turbulent Converging Flows. *ApJ*, 729:120. arXiv, 1101.2650.

[Gorter et Casimir, 1957] Gorter, C. J., et H. B. G. Casimir (1957). On superconductivity. i. *Physica*, 1:306–320.

[Greve *et al.*, 1996] Greve, A., J.-F. Panis, et C. Thum (1996). The pointing of the IRAM 30-m telescope. *A&AS*, 115:379.

[Griffin *et al.*, 2010] Griffin, M. J., A. Abergel, A. Abreu *et al.* (2010). The Herschel-SPIRE instrument and its in-flight performance. *A&A*, 518:L3. arXiv, 1005.5123.

[Guth, 1981] Guth, A. H. (1981). Inflationary universe: A possible solution to the horizon and flatness problems. *Physical Review D*, 23(2):347.

[Hall, 1949] Hall, J. S. (1949). Observations of the Polarized Light from Stars. *Science*, 109:166–167.

[Hargrave et Ryle, 1974] Hargrave, P. J., et M. Ryle (1974). Observations of Cygnus A with the 5-km radio telescope. *MNRAS*, 166:305–327.

[Heiles, 2000] Heiles, C. (2000). 9286 Stars: An Agglomeration of Stellar Polarization Catalogs. *AJ*, 119:923–927. astro-ph/9910303.

[Heiles et Troland, 2005] Heiles, C., et T. H. Troland (2005). The Millennium Arecibo 21 Centimeter Absorption-Line Survey. IV. Statistics of Magnetic Field, Column Density, and Turbulence. *ApJ*, 624:773–793. astro-ph/0501482.

[Heitsch *et al.*, 2005] Heitsch, F., A. Burkert, L. W. Hartmann, A. D. Slyz, et J. E. G. Devriendt (2005). Formation of Structure in Molecular Clouds: A Case Study. *ApJ*, 633:L113–L116. astro-ph/0507567.

[Hennebelle, 2013] Hennebelle, P. (2013). On the origin of non-self-gravitating filaments in the ISM. *A&A*, 556:A153. arXiv, 1306.5452.

[Hennebelle et Chabrier, 2008] Hennebelle, P., et G. Chabrier (2008). Analytical Theory for the Initial Mass Function: CO Clumps and Prestellar Cores. *ApJ*, 684:395–410. arXiv, 0805.0691.

[Hildebrand *et al.*, 1984] Hildebrand, R. H., M. Dragovan, et G. Novak (1984). Detection of submillimeter polarization in the Orion nebula. *ApJ*, 284:L51–L54.

[Hiltner, 1949] Hiltner, W. A. (1949). Polarization of Radiation from Distant Stars by the Interstellar Medium. *Nature*, 163:283.

[Hinderks *et al.*, 2009] Hinderks, J. R., P. Ade, J. Bock *et al.* (2009). Quad: A high-resolution cosmic microwave background polarimeter. *The Astrophysical Journal*, 692(2):1221.

[Hinshaw *et al.*, 2013] Hinshaw, G., D. Larson, E. Komatsu *et al.* (2013). Nine-year Wilkinson Microwave Anisotropy Probe (WMAP) Observations: Cosmological Parameter Results. *ApJS*, 208:19. arXiv, 1212.5226.

[Hlavacek-Larrondo *et al.*, 2012] Hlavacek-Larrondo, J., A. C. Fabian, A. C. Edge *et al.* (2012). Extreme AGN feedback in the MAssive Cluster Survey: a detailed study of X-ray cavities at z>0.3. *MNRAS*, 421:1360–1384. arXiv, 1110.0489.

[Houde *et al.*, 2013] Houde, M., Andrew Fletcher, Rainer Beck *et al.* (2013). Characterizing magnetized turbulence in m51. *The Astrophysical Journal*, 766(1):49.

[Hu et White, 1997] Hu, W., et Martin White (1997). Tensor anisotropies in an open universe. *The Astrophysical Journal Letters*, 486(1):L1.

[Hu et White, 1997] Hu, W., et M. White (1997). The Damping Tail of Cosmic Microwave Background Anisotropies. *ApJ*, 479:568–579. astro-ph/9609079.

[Hubble, 1929] Hubble, E. (1929). A Relation between Distance and Radial Velocity among Extra-Galactic Nebulae. *Proceedings of the National Academy of Science*, 15:168–173.

[Hull et Plambeck, 2015] Hull, C. L. H., et R. L. Plambeck (2015). The 1.3mm Full-Stokes Polarization System at CARMA. *Journal of Astronomical Instrumentation*, 4:50005. arXiv, 1506.04771.

[Hull *et al.*, 2014] Hull, C. L. H., R. L. Plambeck, W. Kwon *et al.* (2014). TADPOL: A 1.3 mm Survey of Dust Polarization in Star-forming Cores and Regions. *ApJS*, 213:13. arXiv, 1310.6653.

[Ichiki, 2014] Ichiki, K. (2014). Cmb foreground: A concise review. *Progress of Theoretical and Experimental Physics*, 2014(6):06B109.

[Inutsuka et Miyama, 1997] Inutsuka, S.-i., et S. M. Miyama (1997). A Production Mechanism for Clusters of Dense Cores. *ApJ*, 480:681–693.

[Jeans, 1902] Jeans, J. H. (1902). The Stability of a Spherical Nebula. *Philosophical Transactions of the Royal Society of London Series A*, 199:1–53.

[Johnson *et al.*, 2007] Johnson, B. R., J. Collins, M. E. Abroe *et al.* (2007). MAXIPOL: Cosmic Microwave Background Polarimetry Using a Rotating Half-Wave Plate. *ApJ*, 665:42–54. astro-ph/0611394.

[Jones et Spitzer, 1967] Jones, R. V., et L. Spitzer, Jr. (1967). Magnetic Alignment of Interstellar Grains. *ApJ*, 147:943.

[Jorstad *et al.*, 2005] Jorstad, S. G., Alan P Marscher, Matthew L Lister *et al.* (2005). Polarimetric observations of 15 active galactic nuclei at high frequencies: jet kinematics from bimonthly monitoring with the very long baseline array. *The Astronomical Journal*, 130(4):1418.

[Jorstad *et al.*, 2001] Jorstad, S. G., A. P. Marscher, J. R. Mattox *et al.* (2001). Multiepoch Very Long Baseline Array Observations of EGRET-detected Quasars and BL Lacertae Objects: Connection between Superluminal Ejections and Gamma-Ray Flares in Blazars. *ApJ*, 556: 738–748. astro-ph/0102012.

[Kauffmann, 2005] Kauffmann, J. (2005). Column densities and masses from dust emission.

[Keck Array *et al.*, 2016] Keck Array, T., BICEP2 Collaborations, : *et al.* (2016). BICEP2 / Keck Array VIII: Measurement of gravitational lensing from large-scale B-mode polarization. *ArXiv e-prints*. arXiv, 1606.01968.

[Keene *et al.*, 1982] Keene, J., R. H. Hildebrand, et S. E. Whitcomb (1982). A high resolution sub-millimeter map of OMC-1. *ApJ*, 252:L11–L15.

[Kellermann *et al.*, 2004] Kellermann, K. I., M. L. Lister, D. C. Homan *et al.* (2004). Sub-Milliarcsecond Imaging of Quasars and Active Galactic Nuclei. III. Kinematics of Parsec-scale Radio Jets. *ApJ*, 609:539–563. astro-ph/0403320.

[Kinman, 1967] Kinman, T. D. (1967). Optical Polarization Measures of Five Radio Sources. *ApJ*, 148:L53.

[Kogut *et al.*, 2007] Kogut, A., J. Dunkley, C. L. Bennett *et al.* (2007). Three-Year Wilkinson Microwave Anisotropy Probe (WMAP) Observations: Foreground Polarization. *ApJ*, 665:355–362. arXiv, 0704.3991.

[Kramer *et al.*, 2013] Kramer, C., J. Penalver, et A. Greve (2013). Improvement of the iram 30m telescope pattern. Rapport technique, IRAM. available from http://www.iram-institute.org/EN/content-page-161-7-66-161-0-0.html.

[Krolik, 1999] Krolik, J. H. (1999). Book Review: Active galactic nuclei : from the central black hole to the galactic environment / Princeton U Press, 1999. *The Observatory*, 119:306.

[Kurtz *et al.*, 1994] Kurtz, S., E. Churchwell, et D. O. S. Wood (1994). Ultracompact H II regions. 2: New high-resolution radio images. *ApJS*, 91:659–712.

[Lacki et Thompson, 2010] Lacki, B. C., et Todd A Thompson (2010). The physics of the far-infrared-radio correlation. ii. synchrotron emission as a star formation tracer in high-redshift galaxies. *The Astrophysical Journal*, 717(1):196.

[Lanzetta *et al.*, 2002] Lanzetta, K. M., N. Yahata, S. Pascarelle, H.-W. Chen, et A. Fernández-Soto (2002). The Star Formation Rate Intensity Distribution Function: Implications for the Cosmic Star Formation Rate History of the Universe. *ApJ*, 570:492–501. astro-ph/0111129.

[Lazarian, 2003] Lazarian, A. (2003). Magnetic Fields via Polarimetry: Progress of Grain Alignment Theory. *J. Quant. Spec. Radiat. Transf.*, 79:881. astro-ph/0208487.

[Lazarian *et al.*, 2015] Lazarian, A., BG Andersson, et Thiem Hoang (2015). Grain alignment: Role of radiative torques and paramagnetic relaxation. *arXiv preprint arXiv:1511.03696*.

[Lazarian *et al.*, 2014] Lazarian, A., G. Eyink, E. Vishniac, et G. Kowal (2014). Reconnection in Turbulent Astrophysical Fluids. *In* Pogorelov, N. V., E. Audit, et G. P. Zank, éditeurs : *8th International Conference of Numerical Modeling of Space Plasma Flows (ASTRONUM 2013)*, volume 488 de *Astronomical Society of the Pacific Conference Series*, page 23. arXiv, 1408.3134.

[Lazarian et Hoang, 2007] Lazarian, A., et T. Hoang (2007). Subsonic Mechanical Alignment of Irregular Grains. *ApJ*, 669:L77–L80. arXiv, 0707.3805.

[Lee *et al.*, 2015] Lee, S.-S., S. Kang, D.-Y. Byun *et al.* (2015). First Detection of 350 Micron Polarization from a Radio-loud AGN. *ApJ*, 808:L26. arXiv, 1507.03310.

[Liddle et Lyth, 2000] Liddle, A. R., et David H Lyth (2000). *Cosmological inflation and large-scale structure*. Cambridge University Press.

[Lilly *et al.*, 1996] Lilly, S. J., O. Le Fevre, F. Hammer, et D. Crampton (1996). The Canada-France Redshift Survey: The Luminosity Density and Star Formation History of the Universe to Z approximately 1. *ApJ*, 460:L1. astro-ph/9601050.

[Linde, 2014] Linde, A. (2014). Inflationary Cosmology after Planck 2013. *ArXiv e-prints*. arXiv, 1402.0526.

[Linde *et al.*, 1994] Linde, A., Dmitri Linde, et Arthur Mezhlumian (1994). From the big bang theory to the theory of a stationary universe. *Physical Review D*, 49(4):1783.

[Linde, 1982] Linde, A. D. (1982). A new inflationary universe scenario: a possible solution of the horizon, flatness, homogeneity, isotropy and primordial monopole problems. *Physics Letters B*, 108(6):389–393.

[Macellari *et al.*, 2011] Macellari, N., E. Pierpaoli, C. Dickinson, et J. E. Vaillancourt (2011). Galactic foreground contributions to the 5-year Wilkinson Microwave Anisotropy Probe maps. *MNRAS*, 418:888–905. arXiv, 1108.0205.

[Macías-Pérez *et al.*, 2007] Macías-Pérez, J., G Lagache, Bruno Maffei *et al.* (2007). Archeops in-flight performance, data processing, and map making. *Astronomy & Astrophysics*, 467(3):1313–1344.

[Macías-Pérez *et al.*, 2010] Macías-Pérez, J. F., F. Mayet, J. Aumont, et F.-X. Désert (2010). Global Spectral Energy Distribution of the Crab Nebula in the Prospect of the Planck Satellite Polarization Calibration. *ApJ*, 711:417–423. arXiv, 0802.0412.

[Madau *et al.*, 1996] Madau, P., H. C. Ferguson, M. E. Dickinson *et al.* (1996). High-redshift galaxies in the Hubble Deep Field: colour selection and star formation history to z˜4. *MNRAS*, 283:1388–1404. astro-ph/9607172.

[Madsen *et al.*, 2015] Madsen, K. K., F. Fürst, D. J. Walton *et al.* (2015). 3C 273 with NuSTAR: Unveiling the Active Galactic Nucleus. *ApJ*, 812:14.

[Martin et Puplett, 1970] Martin, D. H., et E. Puplett (1970). Polarised interferometric spectrometry for the millimeter and submillimeter spectrum. *Infrared Physics*, 10:105–109.

[Mathis, 1990] Mathis, J. S. (1990). Interstellar dust and extinction. *Annual Review of Astronomy and Astrophysics*, 28:37–70.

[Matthews *et al.*, 2009] Matthews, B. C., C. A. McPhee, L. M. Fissel, et R. L. Curran (2009). The Legacy of SCUPOL: 850 μm Imaging Polarimetry from 1997 to 2005. *ApJS*, 182:143–204.

[Matthews *et al.*, 2001] Matthews, B. C., Christine D Wilson, et Jason D Fiege (2001). Magnetic fields in star-forming molecular clouds. ii. the depolarization effect in the omc-3 filament of orion a. *The Astrophysical Journal*, 562(1):400.

[Matthews *et al.*, 2014] Matthews, T. G., Peter AR Ade, Francesco E Angilè *et al.* (2014). Lupus i observations from the 2010 flight of the balloon-borne large aperture submillimeter telescope for polarimetry. *The Astrophysical Journal*, 784(2):116.

[Mayer et Hollinger, 1968] Mayer, C. H., et J. P. Hollinger (1968). Polarized Brightness Distribution Over Cassiopeia a, the Crab Nebula, and Cygnus a at 1.55 cm Wavelength. *ApJ*, 151:53.

[McKee et Ostriker, 2007] McKee, C. F., et E. C. Ostriker (2007). Theory of Star Formation. *ARA&A*, 45:565–687. arXiv, 0707.3514.

[Meny *et al.*, 2007] Meny, C., V. Gromov, N. Boudet *et al.* (2007). Far-infrared to millimeter astrophysical dust emission. I. A model based on physical properties of amorphous solids. *A&A*, 468:171–188. astro-ph/0701226.

[Molinari *et al.*, 2010] Molinari, S., B. Swinyard, J. Bally *et al.* (2010). Clouds, filaments, and protostars: The Herschel Hi-GAL Milky Way. *A&A*, 518:L100. arXiv, 1005.3317.

[Monfardini *et al.*, 2014] Monfardini, A., R. Adam, A. Adane *et al.* (2014). Latest NIKA Results and the NIKA-2 Project. *Journal of Low Temperature Physics*, 176:787–795. arXiv, 1310.1230.

[Monfardini *et al.*, 2016] Monfardini, A., J. Baselmans, A. Benoit *et al.* (2016). Lumped Element Kinetic Inductance Detectors for space applications. *ArXiv e-prints*. arXiv, 1606.00719.

[Montier *et al.*, 2015] Montier, L., S. Plaszczynski, F. Levrier *et al.* (2015). Polarization measurement analysis. II. Best estimators of polarization fraction and angle. *A&A*, 574:A136. arXiv, 1407.0178.

[Moreno, 2010] Moreno, R. (2010). Neptune and uranus planetary brightness temperature tabulation. Rapport technique, ESA Herschel Science Center. available from ftp://ftp.sciops.esa.int/pub/hsc-calibration/PlanetaryModels/ESA2.

[Motte *et al.*, 1998] Motte, F., P. Andre, et R. Neri (1998). The initial conditions of star formation in the rho Ophiuchi main cloud: wide-field millimeter continuum mapping. *A&A*, 336:150–172.

[Mould *et al.*, 1980] Mould, J., M. Aaronson, et J. Huchra (1980). A distance scale from the infrared magnitude/H I velocity-width relation. II - The Virgo cluster. *ApJ*, 238:458–470.

[Mouschovias et Ciolek, 1999] Mouschovias, T. C., et G. E. Ciolek (1999). Magnetic Fields and Star Formation: A Theory Reaching Adulthood. *In* Lada, C. J., et N. D. Kylafis, éditeurs : *NATO Advanced Science Institutes (ASI) Series C*, volume 540 de *NATO Advanced Science Institutes (ASI) Series C*, page 305.

[Mouschovias et Morton, 1991] Mouschovias, T. C., et S. A. Morton (1991). Ambipolar diffusion, cloud cores, and star formation: Two-dimensional, cylindrically symmetric contraction. I - The issues, formulation of the problem, and method of solution. *ApJ*, 371:296–316.

[Naghizadeh-Khouei et Clarke, 1993] Naghizadeh-Khouei, J., et D. Clarke (1993). On the statistical behaviour of the position angle of linear polarization. *A&A*, 274:968.

[Nakamura *et al.*, 2008] Nakamura, M., H. Li, S. Diehl, et S. Li (2008). Numerical Modeling of AGN Jets: Formation of Magnetically Dominated Lobes and Stability Properties of Current-Carrying Jets. *In* Rector, T. A., et D. S. De Young, éditeurs : *Extragalactic Jets: Theory and Observation from Radio to Gamma Ray*, volume 386 de *Astronomical Society of the Pacific Conference Series*, page 373. arXiv, 0707.1537.

[Nartallo *et al.*, 1998] Nartallo, R., W. K. Gear, A. G. Murray, E. I. Robson, et J. H. Hough (1998). A Millimetre/Submillimetre Polarization Survey of Compact Flat-Spectrum Radio Sources. *MNRAS*, 297:667–686. astro-ph/9712219.

[Netzer, 2013] Netzer, H. (2013). *The Physics and Evolution of Active Galactic Nuclei*. Cambridge University Press.

[Newman et Penrose, 1966] Newman, E. T., et Roger Penrose (1966). Note on the bondi-metzner-sachs group. *Journal of Mathematical Physics*, 7(5):863–870.

[Nozawa *et al.*, 1998] Nozawa, S., N. Itoh, et Y. Kohyama (1998). Relativistic Thermal Bremsstrahlung Gaunt Factor for the Intracluster Plasma. *ApJ*, 507:530–557. astro-ph/9802096.

[Offner *et al.*, 2014] Offner, S. S. R., P. C. Clark, P. Hennebelle *et al.* (2014). The Origin and Universality of the Stellar Initial Mass Function. *Protostars and Planets VI*, pages 53–75. arXiv, 1312.5326.

[Omont *et al.*, 2001] Omont, A., Pierre Cox, Frank Bertoldi *et al.* (2001). A 1.2 mm mambo/iram-30 m survey of dust emission from the highest redshift pss quasars. *Astronomy & Astrophysics*, 374(2):371–381.

[Palmeirim *et al.*, 2013] Palmeirim, P., P. André, J. Kirk *et al.* (2013). Herschel view of the Taurus B211/3 filament and striations: evidence of filamentary growth? *A&A*, 550:A38. arXiv, 1211.6360.

[Pancharatnam, 1955] Pancharatnam, S. (1955). Achromatic combinations of birefringent plates. *In Proceedings of the Indian Academy of Sciences-Section A*, volume 41, pages 137–144. Springer.

[Pardo *et al.*, 2002] Pardo, J. R., J. Cernicharo, et E. Serabyn (2002). Atmospheric transmission at microwaves (ATM): an improved model for millimeter/submillimeter applications. *IEEE*, 49:1683 – 1694.

[Patriarchi et Perinotto, 1999] Patriarchi, P., et M. Perinotto (1999). Interstellar extinction. *Mem. Soc. Astron. Italiana*, 70:637–651.

[Peretto *et al.*, 2012] Peretto, N., P. André, V. Könyves *et al.* (2012). The Pipe Nebula as seen with Herschel: formation of filamentary structures by large-scale compression? *A&A*, 541:A63. arXiv, 1203.3403.

[Pereyra et Magalhães, 2004] Pereyra, A., et A. M. Magalhães (2004). Polarimetry toward the Musca Dark Cloud. I. The Catalog. *ApJ*, 603:584–594.

[Perley, 1982] Perley, R. A. (1982). The positions, structures, and polarizations of 404 compact radio sources. *AJ*, 87:859–880.

[Perley et Butler, 2013] Perley, R. A., et B. J. Butler (2013). Integrated Polarization Properties of 3C48, 3C138, 3C147, and 3C286. *ApJS*, 206:16. arXiv, 1302.6662.

[Pisano, 2000] Pisano, G. (2000). *Realizzazione e calibrazione di un Polarimetro per misure della Radiazione di Fondo Cosmico nel lontano infrarosso.* Thèse de doctorat, Università La Sapienza.

[Pisano *et al.*, 2014] Pisano, G., B. Maffei, M. W. Ng *et al.* (2014). Development of large radii half-wave plates for CMB satellite missions. *In Millimeter, Submillimeter, and Far-Infrared Detectors and Instrumentation for Astronomy VII*, volume 9153 de *Proc. SPIE*, page 915317. arXiv, 1409.8516.

[Pisano *et al.*, 2008] Pisano, G., Giorgio Savini, Peter A. R. Ade, et Vic Haynes (2008). Metal-mesh achromatic half-wave plate for use at submillimeter wavelengths. *Appl. Opt.*, 47(33):6251–6256.

[Pisano *et al.*, 2006] Pisano, G., G. Savini, P. A. R. Ade, V. Haynes, et W. K. Gear (2006). Achromatic half-wave plate for submillimeter instruments in cosmic microwave background astronomy: experimental characterization. *Appl. Opt.*, 45:6982–6989.

[Planck Collaboration, 2013] Planck Collaboration (2013). VizieR Online Data Catalog: Planck Catalog of Compact Sources Release 1 (Planck, 2013). *VizieR Online Data Catalog*, 8091:0.

[Planck Collaboration *et al.*, 2014a] Planck Collaboration, A. Abergel, P. A. R. Ade *et al.* (2014a). Planck 2013 results. XI. All-sky model of thermal dust emission. *A&A*, 571:A11. arXiv, 1312.1300.

[Planck Collaboration *et al.*, 2014b] Planck Collaboration, R. Adam, P. A. R. Ade *et al.* (2014b). Planck intermediate results. XXXII. The relative orientation between the magnetic field and structures traced by interstellar dust. *ArXiv e-prints.* arXiv, 1409.6728.

[Planck Collaboration *et al.*, 2015a] Planck Collaboration, R. Adam, P. A. R. Ade *et al.* (2015a). Planck 2015 results. X. Diffuse component separation: Foreground maps. *ArXiv e-prints*. arXiv, 1502.01588.

[Planck Collaboration *et al.*, 2015b] Planck Collaboration, R. Adam, P. A. R. Ade *et al.* (2015b). Planck 2015 results. VIII. High Frequency Instrument data processing: Calibration and maps. *ArXiv e-prints*. arXiv, 1502.01587.

[Planck Collaboration *et al.*, 2015c] Planck Collaboration, P. A. R. Ade, N. Aghanim *et al.* (2015c). Planck intermediate results. XIX. An overview of the polarized thermal emission from Galactic dust. *A&A*, 576:A104. arXiv, 1405.0871.

[Planck Collaboration *et al.*, 2015d] Planck Collaboration, P. A. R. Ade, N. Aghanim *et al.* (2015d). Planck intermediate results. XIX. An overview of the polarized thermal emission from Galactic dust. *A&A*, 576:A104. arXiv, 1405.0871.

[Planck Collaboration *et al.*, 2015e] Planck Collaboration, P. A. R. Ade, N. Aghanim *et al.* (2015e). Planck intermediate results. XXI. Comparison of polarized thermal emission from Galactic dust at 353 GHz with interstellar polarization in the visible. *A&A*, 576:A106. arXiv, 1405.0873.

[Planck Collaboration *et al.*, 2014c] Planck Collaboration, P. A. R. Ade, N. Aghanim *et al.* (2014c). Planck 2013 results. XIII. Galactic CO emission. *A&A*, 571:A13. arXiv, 1303.5073.

[Planck Collaboration *et al.*, 2016a] Planck Collaboration, P. A. R. Ade, N. Aghanim *et al.* (2016a). Planck intermediate results. XXXV. Probing the role of the magnetic field in the formation of structure in molecular clouds. *A&A*, 586:A138. arXiv, 1502.04123.

[Planck Collaboration *et al.*, 2015f] Planck Collaboration, P. A. R. Ade, N. Aghanim *et al.* (2015f). Planck 2015 results. XXV. Diffuse low-frequency Galactic foregrounds. *ArXiv e-prints*. arXiv, 1506.06660.

[Planck Collaboration *et al.*, 2014d] Planck Collaboration, P. A. R. Ade, N. Aghanim *et al.* (2014d). Planck intermediate results. XV. A study of anomalous microwave emission in Galactic clouds. *A&A*, 565:A103. arXiv, 1309.1357.

[Planck Collaboration *et al.*, 2015g] Planck Collaboration, P. A. R. Ade, N. Aghanim *et al.* (2015g). Planck 2015 results. XXVI. The Second Planck Catalogue of Compact Sources. *ArXiv e-prints*. arXiv, 1507.02058.

[Planck Collaboration *et al.*, 2013] Planck Collaboration, P. A. R. Ade, N. Aghanim *et al.* (2013). Planck 2013 results. XVI. Cosmological parameters. *ArXiv e-prints*. arXiv, 1303.5076.

[Planck Collaboration *et al.*, 2014e] Planck Collaboration, P. A. R. Ade, N. Aghanim *et al.* (2014e). Planck 2013 results. XII. Diffuse component separation. *A&A*, 571:A12. arXiv, 1303.5072.

[Planck Collaboration *et al.*, 2015h] Planck Collaboration, P. A. R. Ade, N. Aghanim *et al.* (2015h). Planck 2015 results. XIX. Constraints on primordial magnetic fields. *ArXiv e-prints*. arXiv, 1502.01594.

[Planck Collaboration *et al.*, 2015i] Planck Collaboration, P. A. R. Ade, N. Aghanim *et al.* (2015i). Planck 2015 results. XIII. Cosmological parameters. *ArXiv e-prints*. arXiv, 1502.01589.

[Planck Collaboration *et al.*, 2016b] Planck Collaboration, P. A. R. Ade, N. Aghanim *et al.* (2016b). Planck 2015 results. XV. Gravitational lensing. *A&A*, 594:A15. arXiv, 1502.01591.

[Purcell et Spitzer, 1971] Purcell, E. M., et L. Spitzer, Jr. (1971). Orientation of Rotating Grains. *ApJ*, 167:31.

[Rice, 1945] Rice, S. O. (1945). Mathematical analysis of random noise. *Bell System Technical Journal*, 24(1):46–156.

[Ritacco *et al.*, 2016a] Ritacco, A., R. Adam, A. Adane *et al.* (2016a). First Polarised Light with the NIKA Camera. *Journal of Low Temperature Physics*, 184:724–732. arXiv, 1508.00747.

[Ritacco *et al.*, 2016b] Ritacco, A., Ponthieu N., Catalano A. *et al.* (2016b). Polarimetry at millimeter wavelenghts with the nika camera: calibration and performance. *A&A*.

[Roesch *et al.*, 2012] Roesch, M., A. Benoit, A. Bideaud *et al.* (2012). Development of Lumped Element Kinetic Inductance Detectors for NIKA. *ArXiv e-prints*. arXiv, 1212.4585.

[Rubiño-Martín *et al.*, 2012] Rubiño-Martín, J. A., C. H. López-Caraballo, R. Génova-Santos, et R. Rebolo (2012). Observations of the Polarisation of the Anomalous Microwave Emission: A Review. *Advances in Astronomy*, 2012:351836.

[Rybicki et Lightman, 1979] Rybicki, G. B., et A. P. Lightman (1979). Book-Review - Radiative Processes in Astrophysics. *Astronomy Quarterly*, 3:199.

[Sachs et Wolfe, 1967] Sachs, R. K., et Arthur M Wolfe (1967). Perturbations of a cosmological model and angular variations of the microwave background. *The Astrophysical Journal*, 147(1):73–90.

[Savini *et al.*, 2006] Savini, G., Giampaolo Pisano, et Peter AR Ade (2006). Achromatic half-wave plate for submillimeter instruments in cosmic microwave background astronomy: modeling and simulation. *Applied Optics*, 45(35):8907–8915.

[Savini *et al.*, 2006] Savini, G., G. Pisano, et P. A. R. Ade (2006). Achromatic half-wave plate for submillimeter instruments in cosmic microwave background astronomy: modeling and simulation. *Appl. Opt.*, 45:8907–8915.

[Schleuning, 1998] Schleuning, D. A. (1998). Far-Infrared and Submillimeter Polarization of OMC-1: Evidence for Magnetically Regulated Star Formation. *ApJ*, 493:811–825.

[Schraml et Turlo, 1967] Schraml, J., et Z. Turlo (1967). Polarization of Cygnus a at 1.95 CM Wavelength. *ApJ*, 150:L15.

[Shu, 1977] Shu, F. H. (1977). Self-similar collapse of isothermal spheres and star formation. *ApJ*, 214:488–497.

[Shu, 2007] Shu, F. H. (2007). Magnetohydrodynamics of Star Formation. *In AAS/Division of Dynamical Astronomy Meeting #38*, volume 38 de *AAS/Division of Dynamical Astronomy Meeting*, page 1.01.

[Shu *et al.*, 1987] Shu, F. H., F. C. Adams, et S. Lizano (1987). Star formation in molecular clouds - Observation and theory. *ARA&A*, 25:23–81.

[Silk, 1968] Silk, J. (1968). Cosmic Black-Body Radiation and Galaxy Formation. *ApJ*, 151:459.

[Simmons *et al.*, 1980] Simmons, J. F. L., C. Aspin, et J. C. Brown (1980). A critique of the polarimetric evidence on the nature of Cygnus X-1. *A&A*, 91:97–107.

[Simmons et Stewart, 1985] Simmons, J. F. L., et B. G. Stewart (1985). Point and interval estimation of the true unbiased degree of linear polarization in the presence of low signal-to-noise ratios. *A&A*, 142:100–106.

[Smoot *et al.*, 1992] Smoot, G. F., CL Bennett, A Kogut *et al.* (1992). Structure in the cobe differential microwave radiometer first-year maps. *The Astrophysical Journal*, 396:L1–L5.

[Soboleva, 1966] Soboleva, N. S. (1966). Observations of Polarized Radio Emission of Cygnus-A at 3.95 cm. *Soviet Ast.*, 10:214.

[Soler *et al.*, 2013] Soler, J. D., P. Hennebelle, P. G. Martin *et al.* (2013). An Imprint of Molecular Cloud Magnetization in the Morphology of the Dust Polarized Emission. *ApJ*, 774:128. arXiv, 1303.1830.

[Spitzer, 1968] Spitzer, Jr., L. (1968). Diffuse matter in space. *Interscience Tracts on Physics and Astronomy*, 28.

[Starobinsky, 1982] Starobinsky, A. A. (1982). Dynamics of phase transition in the new inflationary universe scenario and generation of perturbations. *Physics Letters B*, 117(3-4):175–178.

[Sunyaev et Zeldovich, 1972] Sunyaev, R. A., et Y. B. Zeldovich (1972). The Observations of Relic Radiation as a Test of the Nature of X-Ray Radiation from the Clusters of Galaxies. *Comments on Astrophysics and Space Physics*, 4:173.

[The COrE Collaboration *et al.*, 2011] The COrE Collaboration, C. Armitage-Caplan, M. Avillez *et al.* (2011). COrE (Cosmic Origins Explorer) A White Paper. *ArXiv e-prints*. arXiv, 1102.2181.

[The Polarbear Collaboration: P. A. R. Ade *et al.*, 2014] The Polarbear Collaboration: P. A. R. Ade, Y. Akiba, A. E. Anthony *et al.* (2014). A Measurement of the Cosmic Microwave Background B-mode Polarization Power Spectrum at Sub-degree Scales with POLARBEAR. *ApJ*, 794: 171. arXiv, 1403.2369.

[Thum *et al.*, 2008] Thum, C., H. Wiesemeyer, G. Paubert, S. Navarro, et D. Morris (2008). XPOL-the Correlation Polarimeter at the IRAM 30-m Telescope. *PASP*, 120:777–790. arXiv, 0806.1666.

[Tucker et Ade, 2006] Tucker, C. E., et Peter AR Ade (2006). Thermal filtering for large aperture cryogenic detector arrays. *In SPIE Astronomical Telescopes+ Instrumentation*, pages 62750T–62750T. International Society for Optics and Photonics.

[Ulrich, 1967] Ulrich, R. (1967). Far-infrared properties of metallic mesh and its complementary structure. *Infrared Physics*, 7(1):37–55.

[Urry et Padovani, 1995] Urry, C. M., et Paolo Padovani (1995). Unified schemes for radio-loud active galactic nuclei. *Publications of the Astronomical Society of the Pacific*, 107(715):803–890.

[van Engelen *et al.*, 2015] van Engelen, A., B. D. Sherwin, N. Sehgal *et al.* (2015). The Atacama Cosmology Telescope: Lensing of CMB Temperature and Polarization Derived from Cosmic Infrared Background Cross-correlation. *ApJ*, 808:7. arXiv, 1412.0626.

[Vinogradova *et al.*, 1971] Vinogradova, L. V., D. A. Dmitrenko, et N. M. Tsejtlin (1971). Absolute measurements of the intensity of radiation from Cas A, Cyg A, Tau A at wavelengths from 15 - 30 cm. *Izvestiia Vysshaia Uchebn. Zaved., Radiofizika*, 14:157–159.

[Wagner *et al.*, 2015] Wagner, J., A. L. Roy, T. P. Krichbaum *et al.* (2015). First 230 GHz VLBI fringes on 3C 279 using the APEX Telescope. *A&A*, 581:A32. arXiv, 1506.03244.

[Weiland *et al.*, 2011] Weiland, J. L., N. Odegard, R. S. Hill *et al.* (2011). Seven-year Wilkinson Microwave Anisotropy Probe (WMAP) Observations: Planets and Celestial Calibration Sources. *ApJS*, 192:19. arXiv, 1001.4731.

[Weingartner et Draine, 2003] Weingartner, J. C., et B. T. Draine (2003). Radiative Torques on Interstellar Grains. III. Dynamics with Thermal Relaxation. *ApJ*, 589:289–318. astro-ph/0211342.

[White et Hu, 1997] White, M., et W. Hu (1997). The Sachs-Wolfe effect. *A&A*, 321:8–9. astro-ph/9609105.

[Wiesemeyer *et al.*, 2014] Wiesemeyer, H., T. Hezareh, E. Kreysa *et al.* (2014). Submillimeter Polarimetry with PolKa, a Reflection-Type Modulator for the APEX Telescope. *PASP*, 126:1027–1047. arXiv, 1408.5100.

[Wilson *et al.*, 1970] Wilson, R. W., K. B. Jefferts, et A. A. Penzias (1970). Carbon Monoxide in the Orion Nebula. *ApJ*, 161:L43.

[Zaldarriaga, 1998] Zaldarriaga, M. (1998). *Fluctuations in the Cosmic Microwave Background.* Thèse de doctorat, Thesis (PhD). MASSACHUSETTS INSTITUTE OF TECHNOLOGY, Source DAI-B 59/09, p. 4876, Mar 1999, pages.

[Zaldarriaga, 2004] Zaldarriaga, M. (2004). The Polarization of the Cosmic Microwave Background. *Measuring and Modeling the Universe*, page 309. astro-ph/0305272.

[Zaldarriaga et Seljak, 1997] Zaldarriaga, M., et U. Seljak (1997). All-sky analysis of polarization in the microwave background. *Phys. Rev. D*, 55:1830–1840. astro-ph/9609170.

[Zapata *et al.*, 2011] Zapata, L. A., J. Schmid-Burgk, et K. M. Menten (2011). Orion KL: the hot core that is not a "hot core". *A&A*, 529:A24. arXiv, 1009.1426.

Abstract

Magnetic fields play a crucial role in a large number of astrophysical processes from Galactic to Cosmological scales. They can be traced via observations of dust polarisation as demonstrated by several experiments like Archeops, SCUBA, ALMA and the *Planck* satellite. In particular, low resolution observations of dust polarisation have demonstrated that Galactic filamentary structures, where star formation takes place, are associated to well organised magnetic fields. High angular resolution polarisation observations could probe the physics at small angular scales and complete the current understanding of the star formation process: this is one of the main objectives of the *NIKA2* camera. In *NIKA2* as well as in its prototype, *NIKA*, the polarisation reconstruction consists in a quasi-simultaneous detection of the Stokes parameters Q and U, describing the linear polarisation of the light. This is achieved thanks to the continuous rotation of a modulator, a Half Wave Plate (HWP) and a polariser coupled to the fast response of the Lumped Element Kinetic Inductance Detectors (LEKIDs). This PhD thesis focuses on the development of the *NIKA* polarimeter and consequently that of *NIKA2*, which observes the sky in intensity and polarisation from the IRAM 30 m telescope located in the Sierra Nevada (Spain). It presents the instrumental characterisation of the instrumental setup, the dedicated data analysis pipeline to reconstruct the polarisation properties of the observed source at the telescope and the science verification using known compact and extended sources observations.

Key-words: Polarization: Instrumentation - Data analysis - NIKA: kinetic inductance detectors

Résumé

Les champs magnétiques jouent un role cruciale dans un grand nombre de processus astrophysiques aux échelles Galactiques et Cosmologiques. On peut les mettre en évidence grace à l'observation de la polarisation de la poussière comme montré par les expériences Archeops, SCUBA, ALMA et *Planck*. Les observations obtenues par *Planck* en polarisation montrent une structure bien organisée des champs magnétiques à grande échelle dans les filaments Galactiques, là où a lieu la formation stellaire. Des observations à haute résolution angulaire de ces régions Galactiques pourraient clarifier le rôle des champs magnétiques dans le processus de formation stellaire. Ceci est un des objectifs scientifiques de la caméra *NIKA2*. Pour *NIKA2* comme pour son prototype, *NIKA*, la polarisation est mesurée par la detection quasi-simultanée des paramètres de Stokes Q et U qui décrivent la polarisation linéaire de la lumière. Cela grâce à la rotation continue d'un modulateur, une lame demi-onde (*Half Wave Plate, HWP*) et un polariseur couplé à la rapidité des détecteurs à inductance cinétique (LEKIDs). Cette thèse décrit le développement du polarimètre de *NIKA* et par conséquence celui de *NIKA2*, qui observe le ciel en intensité et polarisation du telescope de 30 m de l'IRAM situé dans la Sierra Nevada (Espagne). Elle présente : la caractérisation instrumentale au laboratoire du polarimètre, l'analyse des données dediée à la reconstruction de la polarisation des sources observées au telescope et la validation de la stratégie de detection en utilisant l'observation de sources connues compactes et étendues.

Mots-clefs: Polarisation : Instrumentation - Analyse des données - NIKA : détecteurs à inductance cinétique